THE UNIVERSITY *of* EDINBURGH

Investigating the protective properties of dimethyl fumarate and Nrf2 signalling in response to drug toxicity

Jose Meseguer Ripollés

M.Sc

THE UNIVERSITY *of* EDINBURGH

This dissertation is submitted for the degree of

Doctor of Philosophy

-2019-

Declaration

This thesis contains my work and results acquired and analysed with our collaborators.

The RNA sequencing studies were performed during an internship at Novo Nordisk Research Centre Oxford in collaboration with Dr. Nicola Beer. Ms. Esther Mellado helped in the RNA library preparation and sequencing and Dr. Enrique Toledo performed part of the RNA sequencing analysis.

Apart from these results performed during my internship, the project has been performed by myself.

The work in this thesis has not been submitted for any other degree or professional qualification.

Jose Meseguer Ripollés

Abstract

Liver disease represents a major cause of mortality and morbidity. Despite the regenerative capacity of the liver, maintained injury or acute injury can lead to loss of liver function and disease. The most common cause of acute liver damage is drug-induced liver injury (DILI). This can lead to organ failure and possible death. Therefore, new therapies to reduce the severity of the injury are required. Stimulation of anti-inflammatory and anti-oxidative stress pathways during the resolution of the injury have been proposed as powerful approaches to reduce organ injury and to enhance regeneration.

A main transcription factor which regulates anti-inflammatory and anti-oxidative stress is 'nuclear factor erythroid-derived 2-like 2' (Nrf2). Therefore, pharmacological activation of the Nrf2 pathway offers the potential to exert a cytoprotective effect promoting tissue regeneration. Dimethyl fumarate (DMF) is a drug approved for some forms of multiple sclerosis.

DMF's protection is due in part by activation of the Nrf2 pathway. We hypothesize that DMF could be used to reduce the severity of DILI via Nrf2 activation. This thesis explores the protective effects of DMF and Nrf2 signalling during paracetamol-induced hepatotoxicity using *in vitro* and *in vivo* models.

For the *in vitro* studies, a semi-automated platform to produce hepatocytes-like cells (HLCs) from human pluripotent stem cells was employed. Single-cell high content image analysis was performed to understand Nrf2 nuclear translocation dynamics following DMF administration. The protective properties of DMF were tested in three different combinations: pre-treatment prior to paracetamol incubation, co-treatment or post-treatment following paracetamol injury. In all cases, DMF protected HLCs from paracetamol exposure. These findings were validated in a Zebrafish model of paracetamol injury. A

zebrafish liver GFP reporter line was employed to detect fluorescence changes upon paracetamol exposure. Pre-treatment with DMF prior to paracetamol injury reduced the level of GFP loss.

RNA sequencing from both models identified that DMF protection was mediated via Nrf2 pathway stimulation. This was mainly by an increase in cell metabolism and oxidative stress management as well as reducing pro-inflammatory pathways activation. In summary, the findings of this work provide new understanding on the effects of DMF in the modulation of the Nrf2 pathway during paracetamol-induced liver injury. These studies may provide a platform to develop new treatment regimes for patients with acute liver disease.

Lay abstract

Liver disease represents a major cause of mortality and morbidity. Despite the regenerative capacity of the liver, maintained injury or acute injury can lead to loss of liver function and disease. The most common cause of acute liver damage is drug-induced liver injury (DILI). This can lead into hepatocyte death (the main cell type of the liver) and organ failure.

Therefore, new therapies to reduce the severity of the injury are required. Inflammation and stress are responsible for cell death and injury development. Stimulation of anti-inflammatory and anti-cell stress pathways during the resolution of the injury have been proposed as powerful approaches to reduce organ injury and to enhance regeneration.

Our body has a mechanism that can manage and reduce inflammation and cell stress called 'nuclear factor erythroid-derived 2-like 2' (NRF2). Therefore, pharmacological activation of the NRF2 pathway offers the potential to promote organ regeneration. Dimethyl fumarate (DMF) is a drug approved for some forms of multiple sclerosis. DMF's protection is based in part by activation of the NRF2 pathway.

We hypothesize that DMF could be used to reduce the severity of DILI via NRF2 activation. This thesis explores the protective effects of DMF and Nrf2 signalling during DILI. First, we tested the effects of DMF in a human stem cell derived hepatocytes (HLCs) model of DILI. DMF protected HLCs from injury via NRF2 activation. A zebrafish model of DILI was used to validate the findings on HLCs in a whole organism. In both models DMF protected hepatocytes from injury.

This was mediated by NRF2 activation boosting the capacity of cells to resist injury and by stopping the development of the inflammation process. In summary, the findings of this work provide an

understanding on the effects of DMF in the modulation of the Nrf2 pathway in liver injury. These studies may provide a platform for translation to patients with acute liver disease.

Table of contents

List of figures and tables

Abbreviations

AALD	Alcohol-associated liver diseases
ABCA1	ATP Binding Cassette Subfamily A Member 1
AFP	Alpha-fetoprotein
ALB	Albumin
ALF	Acute liver failure
ALP	Alkaline phosphatase
ALS	Amyotrophic Lateral Sclerosis
ALT	Aminotransferase
APOC3	Apolipoprotein C3
APOD	Apolipoprotein D
apoda.1	Apolipoprotein Da, duplicate 1
ARE	Antioxidant response element
aSMA	Alpha-smooth muscle actin
ATP	Adenosine Triphosphate
BMP	Bone morphogenetic protein
BMS	Bristol-Myers Squibb
bp	Base pairs
BSA	Bovine Serum Albumin
B2M	Beta-2 Microglobulin
CCL3L1	C-C Motif Chemokine Ligand 3 Like 1
CFA	Common factor analysis
CLDN6	Claudin 6
CNC	Cap'n'collar
crygm	Crystallin family
Cull3	Cullin 3
CYP	Cytochrome
Cys	Cysteine residues
d.p.f	Days post fertilisation
DE	Definitive Endoderm
DEGs	Differential expression genes
DHRS7	Dehydrogenase/Reductase 7

DILI	Drug-induced liver injury
DMF	Dimethyl fumarate
DMSO	Dimethylsulfoxide
DPBS	Dulbecco's phosphate-buffered saline
DUOX2	Dual oxidase 2
DUSP9	Dual specificity phosphatase 9
EBs	Embryoid bodies
EMA	European Medicines Agency
EMPs	Extracellular matrix proteins
EMT	Epithelial–mesenchymal transition
ETFB	Electron Transfer Flavoprotein Subunit Beta
ETS1	ETS Proto-Oncogene 1 Factor
FACS	Fluorescence activated cell sorting
fbxo32	F-Box Protein 32
FDA	Food and drug administration
FGF	Fibroblast growth factor (
GFP	Green fluorescent protein
GGT	Gamma-glutamyl transferase
GMP	Good Manufacturing Practice
GSEA	Gene Set Enrichment Analysis
GSH	GLutathione
GSR	Glutathione reductase
GST	Glutathione S-transferase
H_2O_2	Hydrogen peroxide
haao	3-hydroxyanthranilate 3,4-dioxygenase
HCA	High content analysis
HCA2	Hydroxycarboxylic acid receptor 2
HCC	Hepatocellular carcinoma
HE	Hepatic endoderm
hESC	Human embryonic stem cell
HGD	Homogentisate 1,2-dioxygenase
HGF	Hepatocyte growth factor
HIF-1a	Hypoxia-inducible factor 1-alpha
HLCs	Hepatocytes-like cells

HMOX1	Heme oxygenase-1
HNF4a	Hepatocyte Nuclear Factor 4 Alpha
HTRA2	HtrA serine peptidase 2
ICC	Immunocytochemistry
IL	Interleukine
iPSC	Induced pluripotent stem cell
ITGA2	Integrin a2
Keap1	Kelch-like ECH-associated protein 1
KOSR	Knock-Out Serum Replacement
KRT/CK	Keratin/cytokeratin
LFABP	Liver-type fatty acid-binding protein
LPO	Lactate, pyruvate and octanoic acid
LPS	Lipopolysaccharide
MDA	Malondialdehyde
mg	Milligram
ml	Millilitre
mM	Millimolar
MMF	Monoethyl fumarate
MPT	Membrane permeability transition
MRP	Multidrug resistance-associated protein
MSigDB	Molecular signatures database
NAC	N-Acetylcysteine
NAFLD	Non-alcoholic fatty liver disease
NAPQI	N-acetyl-p-benzoquinone imine
NASH	Non-alcoholic steatohepatitis
NEAT1	Nuclear Enriched Abundant Transcript 1
Nf-kb	Nuclear factor kappa-light-chain-enhancer of activated B cells
NIDI1	Nidogen 1
nM	NanoMolar
NPPB	Natriuretic Peptide B
NQO1	NAD(P)H quinone reductase 1
Nrf2	Nuclear factor erythroid-derived 2-like 2
NRGN	Neurogranin

Nup160	Nucleoporin 160
NUPR1	Nuclear Protein 1
OCT	Octamer-binding transcription factor
OSM	Oncostatin M
PBS	Phosphate Buffered Saline
PCA	Principal Component Analysis
PDFG	Platelet-derived growth factor
PHH	Primary human hepatocytes
PSC	Pluripotent stem cells
PTGR1	Prostaglandin reductase 1
qPCR	Quantitative polymerase chain reaction
QUIN	Quinolinic acid
RAS	Renin-angiotensin system
Rbx1	RING box protein 1
RIN	RNA integrity number
ROCK	Rho-Associated Protein Kinase
ROS	Reactive oxygen species
rpe65a	Retinoid Isomerohydrolase
RPMI	Roswell Park Memorial Institute (Medium)
SCNN1A	Sodium Channel Epithelial 1 Alpha Subunit
SD	Standard Deviation
SE	Standard Error
SEMA7A	Semaphorin7A
SERPINB8	Serpin Family B Member 8
SGOT	Serum glutamic oxaloacetic transaminase
SGPT	Serum glutamic pyruvic transaminase
SLC2A3	Solute carrier family 2 member 3
sMAF	Small musculoaponeurotic fibrosarcoma oncogene homologue
SMOX	Spermine Oxidase
SSEA	Stage-specific embryonic antigen
STM	Septum transversum mesenchyme
SULT	Sulfotransferase
TACSTD2	Tumor Associated Calcium Signal Transducer 2

TAGLN	Transgelin
TCA	Tricarboxylic acid
tcnba	Transcobalamin beta a
TFPI2	Tissue Factor Pathway Inhibitor 2
TGF	Transforming Growth Factor
TGF-b	Transforming growth factor b
TNF-a	Tumour necrosis factor aplha
TPM1	Tropomyosin 1
TRIM71	Tripartite Motif Containing 71
TTC37	Tetratricopeptide Repeat Domain 37
UBR	Ubiquitin Protein Ligase E3 Component N-Recognin
UGT	UDP-glucuronosyltransferase
VEGF	Vascular endothelial growth factor
WB	Western Blot
WT	Wild Type
µm	Micrometer
µM	Micromolar

Acknowledgments

I would like to thank everyone who has helped me over the last few years for making the completion of this thesis a more bearable task. I am also really grateful for the Tissue Repair PhD programme for funding me and for creating such a great group to share this journey.

I am especially grateful to my supervisor Prof. Dave Hay for taking me into his lab and for his guidance and support during these years. It has been a pleasure to work under his supervision. In addition, I would like to thank my second supervisor Prof. Jeremy Hughes for his great ideas, supervision and feedback during my project.

I would also like to thank the members of my PhD committee: Prof. Lesley Forrester for her supervision and training, Dr. David Ferenbach for his support and Dr. James Dear for his supervision and collaboration during this project.

I am also thankful to my collaborators at Novo Nordisk, especially to Dr. Nicola Beer for giving me the chance to undertake an internship with her team. Thanks to her scientific vision, the level of depth on this project increased.

Many thanks to all the people I had the pleasure to work with during my studies, especially Baltasar and Celine for their help and training and for making the lab a welcoming and entertaining place to work. Thanks also go to the many friends I had the pleasure to meet throughout my time in Edinburgh, in particular though the SCRM, the tissue repair programme and many others. And despite the distance I could never forget my friends back in Spain, whose friendship and support has been invaluable to get me to where I am today.

Special thanks to my family, firstly to my parents for their support in all my decisions (albeit not always the smartest). I will always be thankful to them for making me who I am today. To my sister, for always being a support and inspiration and for laughing at the same silly things as me. Last but not least, I would like to thank my partner Sam, for bringing fun and new adventures to my life; her support and kindness made this journey much easier.

Publications

The following publications were published during my PhD studies

1. Semi-automated Production of Hepatocyte Like Cells from Pluripotent Stem Cells. **Jose Meseguer-Ripolles**, Baltasar Lucendo-Villarin, Yu Wang, David C. Hay. J. Vis. Exp. (137), e57995, doi:10.3791/57995 (2018).

2. Pluripotent Stem Cell-Derived Human Tissue: Platforms to Evaluate Drug Metabolism and Safety. **Jose Meseguer-Ripolles**, Salman R. Khetani, Javier G. Blanco, Miari Iredale, David C. Hay. Review, AAPS J (2018) 20: 20. https://doi.org/10.1208/s12248-017-0171-8

3. Modelling non-alcoholic fatty liver disease in human hepatocyte-like cells. Lyall Marcus J., Cartier Jessy, Thomson John P., Cameron Kate, **Meseguer-Ripolles Jose**, O'Duibhir Eoghan, Szkolnicka Dagmara, Villarin Baltasar Lucendo, Wang Yu, Blanco Giovanny Rodriguez, Dunn Warwick B., Meehan Richard R., Hay David C. ,and Drake Amanda J. Philosophical Transactions B DOI: 10.1098/rstb.2017.0362

4. A human iPSC line capable of differentiating into functional macrophages expressing ZsGreen: a tool to study and track therapeutic cells *in vivo*. Martha Lopez Yrigoyen*, Antonella Fidanza*, Luca Cassetta, Richard A. Axton, A. Helen Taylor, **Jose Meseguer-Ripolles**, Anestis Tsakiridis, Val Wilson, David Hay, Jeff W. Pollard, Lesley M. Forrester. Philosophical Transactions B DOI: 10.1098/rstb.2017-02195

5. Modelling foetal exposure to maternal smoking using hepatoblasts from pluripotent stem cells. Baltasar Lucendo-Villarin, Panagiotis Filis, Madeleine J. Swortwood, Marilyn A. Huestis, **Jose Meseguer-Ripolles**, Kate Cameron, John P. Iredale, Peter J. O'Shaughnessy, Paul A. Fowler, David C. Hay. Arch Toxicol (2017) 91: 3633. https://doi.org/10.1007/s00204-017-1983-0

6. Defined and Scalable Generation of Hepatocyte-like Cells from Human Pluripotent Stem Cells, Yu Wang, Sharmin Alhaque, Kate Cameron, **Jose Meseguer-Ripolles**, Baltasar Lucendo-Villarin, Hassan Rashidi, David C. Hay. J. Vis. Exp. (121), e55355, doi:10.3791/55355 (2017).

7. Serum Free Production of Three-Dimensional Human Hepatospheres from Pluripotent Stem Cells. Balta Lucendo-Villarin, Hassan Rashidi, Sharmin Alhaque, Lena Fischer, **Jose Meseguer-Ripolles**, Yu Wang, Cliona O'Farrelly, Michael Themis, David C. Hay. J. Vis. Exp. In-press (2019)

8. Genome editing in pluripotent stem cells provides new understanding of protein SUMOylation during stem cell specification. Yu Wang, Michael H. Tatham, Wolfgang Schmidt-Heck, Carolyn Swann, Karamjit Singh-Dolt, **Jose Meseguer-Ripolles**, Baltasar Lucendo-Villarin, Tilo Kunath, Timothy R. Rudd, Andrew Smith, Jan G. Hengstler, Patricio Godoy, Ronald T. Hay, David C. Hay. iScience, 2019.

CHAPTER ONE

INTRODUCTION

1.1 The Liver

1.1.1 Liver function and architecture

The liver is the largest internal organ in the body exhibiting multiple functions. The main endocrine functions include the secretion of hormones such as thrombopoietin, angiotensinogen and insulin-like growth factor; with bile secretion as the main exocrine function. In addition, the liver is also essential for several functions including drug detoxification, metabolism regulation, urea metabolism, cholesterol synthesis and transport, glycogen storage and secretion of serum plasma proteins such as albumin or apolipoproteins (1). Organ structure is key to maintaining the multifunctional properties of the liver. The main structural unit of the liver is the liver lobule. The lobule is formed by single-cell layers of hepatocytes, the main cell type of the liver, lined by sinusoidal capillaries and connected to a network of blood vessels. The lobule displays a hexagon shape with a central vein in the centre of the lobule and the portal triad at each of the corners (**Figure 1**).

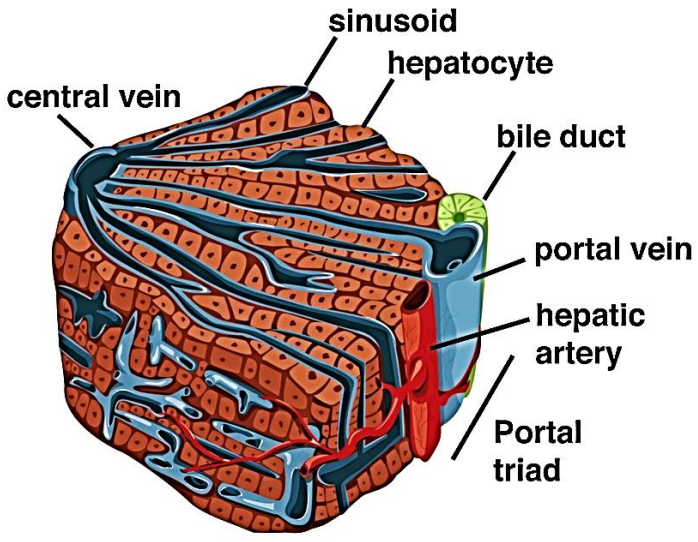

Figure 1. Liver structure. Schematic illustration of part of a liver lobule. From Si-Tayeb et al., 2010 (1)

The portal triad consists of the hepatic artery, hepatic portal vein and the bile duct (1). Blood enters the lobule through both the hepatic artery and hepatic portal vein flowing through the sinusoidal space to the central vein. During this flow, blood is exposed to the basal surface of the hepatocytes allowing the protein secretion and the absorption of components from the blood. Hepatocytes secrete bile acids into the canaliculi and then into the bile ducts. The blood flow creates distinct microenvironments within the liver, with gradients in oxygen and nutrient concentrations. These creates three zones with distinct metabolic functions (1,2) (**Figure 2A**). The first zone or periportal zone is responsible for gluconeogenesis, oxidative metabolism and ureagenesis. The third zone or pericentral zone is responsible for metabolism of xenobiotics, lipogenesis and glycolysis. Zone two or the intermediate zone displays a mixture of zone one and zone three function (3).

Although the hepatocyte is the main cell type of the liver, their function is coordinated by other cell types that regulate blood and bile flow and maintain liver homeostasis (**Figure 2B**). Cholangiocytes represent the second major cell type. Cholangiocytes are the epithelial cells from the bile duct. In addition, endothelial cells from the sinusoid vasculature required for blood flow. Within the sinusoid, Kupffer cells, the resident macrophages of the liver. Stellate cells reside in between the hepatocytes and the sinusoid (4).

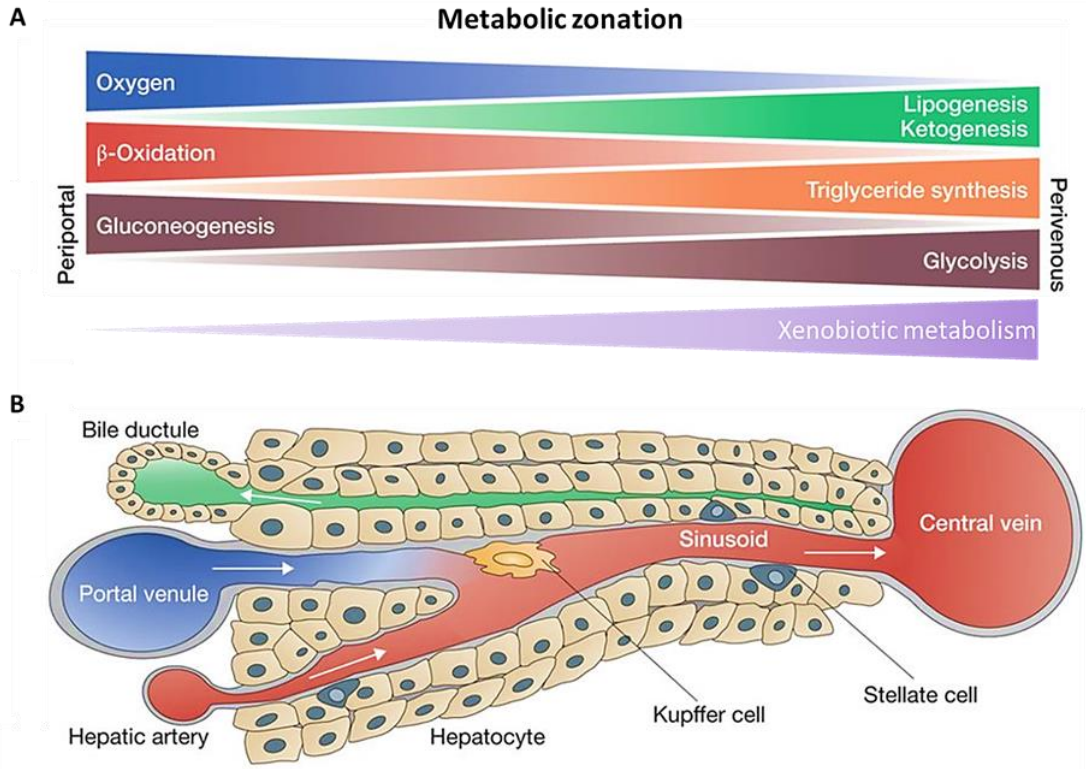

Figure 2. Liver zonation and cell organisation. (**A**) Diagram of hepatocyte metabolic zonation. (**B**) In each lobule, several sinusoids carry blood from the portal triads to the central vein. Hepatocytes form single-cell sheet cords separated by sinusoids. Cholangiocytes are the epithelial cells forming the bile duct. Stellate cells reside in the space of Disse which integrates the space between the hepatocyte and the sinusoid. Kupffer cells reside in the sinusoid which it is form by endothelial cells. Adapted from Birchmeier 2016 (5).

Understanding how the different cell types interact in health and disease is key to develop new cell-based models for regenerative medicine. Liver development studies provide knowledge of the origin and interaction of the different cell types or the liver.

1.1.2 Liver development overview

Liver development is a complex process requiring the precise coordination of many steps. Studies from animal models have identified several phases during liver development, including endoderm specification, liver bud specification and hepatic differentiation (4). These phases are controlled by multiple signalling pathways. Given their complexity, I will deal with those in turn.

1.1.2.1 Endoderm specification

The Early embryo is composed of three primary germ layers: ectoderm, mesoderm and endoderm. During gastrulation, endoderm is specified from mesoderm and forms the primitive gut tube. This can be divided into foregut, midgut and hindgut (6). The foregut develops into the liver, biliary tree, stomach, pancreas, lungs, oesophagus and thyroids. Midgut development gives rise to the small intestine whereas hindgut develops into the large intestine (7).

Definitive endoderm formation is controlled by multiple signalling pathways. Transforming growth factor b (TGF-b) has been reported to be critical for endoderm formation. Within TGF-b growth factors, Nodal has been shown to orchestrate endoderm and mesoderm development in a concentration dependent manner. Increased levels of Nodal induce endoderm where reduced levels are required for mesoderm induction (8). Endoderm specification is controlled by an autoregulatory loop where Nodal expression controls fibroblast growth factor (FGF) and bone morphogenetic protein (BMP) signalling. In addition, definitive endoderm separation is controlled by the Wnt/b-catenin signalling pathway (9). All these signalling gradients lead to the primitive gut tube formation which can be divided into foregut, midgut and hindgut. Foregut development requires low levels of Wnt and BMP, where FGF signalling keeps cells susceptible to Wnt and BMP proteins (**Figure 3**).

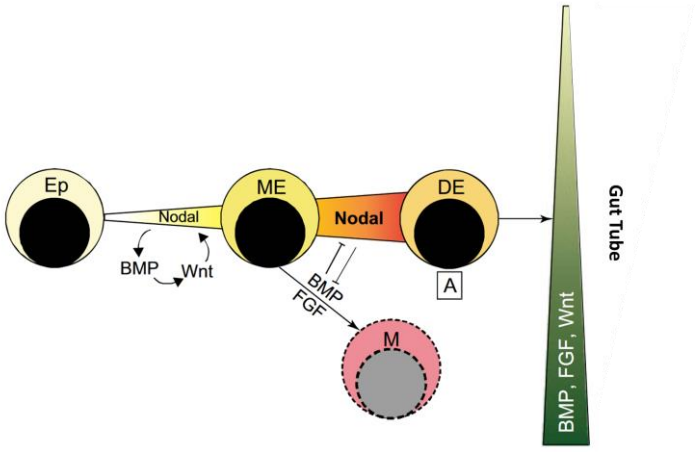

Figure 3. Endoderm specification. Nodal signalling is required for mesendoderm (ME) formation from the embryonic epiblast (Ep). This is increased by a reinforcing loop of Nodal, Wnt and BMP signalling. High levels of Nodal signalling promote definitive endoderm (DE) formation, while increase in BMP and FGF and reduction of Nodal are required for mesoderm commitment. The BMP, FGF and Wnt gradient patterns the DE forming the gut tube. From Gordillo et al., 2015 (4)

1.1.2.2 Liver bud specification

The liver bud originates from a newly specified ventral endodermal cell called hepatoblast. By E9.0 in mice, the ventral area of the foregut thickens to form the liver bud. During the liver bud formation, the ventral endodermal cells transition into a multilayer of pseudostratified cells called hepatoblasts (10). Between E9.0 and E9.5, hepatoblasts expand and break down the basal layer surrounding the developing hepatic endoderm. The basal layer is composed mainly by laminin and collagen IV, the hepatoblasts delaminate this layer and migrate into the adjacent septum transversum mesenchyme (STM) to form the liver bud (10). At this stage, endothelial cells are required for liver bud formation. Studies in mice showed endothelial infiltration between E8.25 and E10 (4). Conversely, the removal of the endothelial cells prior to vascularisation impaired liver bud development (11). Due to endothelial cell integration the liver bud is vascularised, permitting a continuous growth (**Figure 4**). Vascularisation of the liver bud permits the colonisation of hematopoietic cells, making the liver bud a driver of foetal haematopoiesis (4).

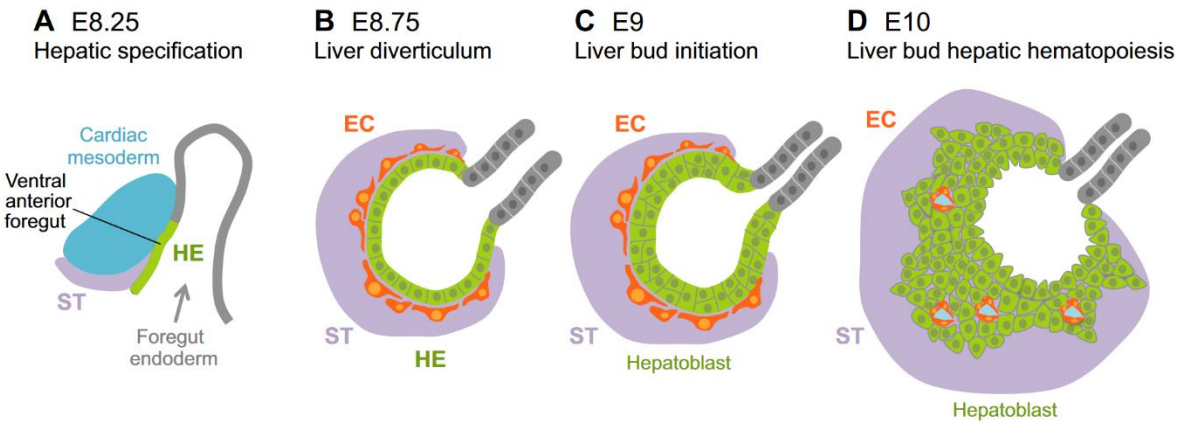

Figure 4. Mouse liver bud development. (**A**) Sagittal section of the mouse hepatic endoderm at E8.25 (HE, green), resting adjacent to the convergence of the cardiac mesoderm (blue) and septum transversum (ST, purple). (**B-D**) Transverse sections of the mouse liver bud development from E8.75 until E10. Diverticulum progressing to the liver bud stage. At E8.75, the hepatic endoderm thickens and forms the liver diverticulum, endothelial cells (ECs, orange) are surrounding the hepatic endoderm. At E9, hepatoblast are originated from the hepatic endoderm. Hepatoblast then proliferate and migrate into the ST forming the liver bud. From Gordillo et al., 2015 (4).

Hepatic specification from the foregut is controlled mainly by FGF, BMP and Wnt signalling. FGF is produced by the cardiac mesoderm. Impaired liver bud development it has been observed by both inhibition of FGF signalling as well as removal of the cardiac mesoderm (12). FGF hepatic induction is regulated by the MAPK pathway (13). BMP signalling is originated from the mesoderm and STM and has hepatic induction properties. BMP2a is required to induce the expression of key genes involved in liver development (14). In addition, inhibition of BMP4 in mice stopped liver bud formation (15). Finally, the role of Wnt/b-catenin signalling in hepatic specification is not fully understood. In zebrafish, loss of Wnt2 and Wnt2b leads to liver organogenesis failure (16). On the contrary, in mice Wnt2 and Wnt2b loss caused lung agenesis but it did not impair liver development or other endoderm-derived organs (17). The role of canonical and non-canonical Wnt signalling pathway in hepatic induction is still requires

further investigation. In addition, the interactions of BMP, FGF and Wnt pathways are still unclear. FGF signalling is not a target of BMP and Wnt signalling is not activated by BMP or FGF signalling (4).

1.1.2.3 Hepatoblast expansion and maturation

Hepatoblasts originate from the liver bud and its expansion is regulated by interactions with endothelial and mesenchymal cell in the septum transversum. Wnt signalling promotes liver expansion and hepatoblast proliferation. Chicken studies showed how overexpression of β-catenin activation increased liver size at E15, as well as inhibition of the Wnt pathway resulted in liver shrinkage (18). In addition, Wnt acts in collaboration with FGF signalling and hepatocyte growth factor (HGF) to promote hepatoblasts proliferation (19). Hepatoblasts are proliferative cells with the bipotential ability to differentiate into hepatocytes and cholangiocytes (**Figure 5**). Hepatoblasts expresses a combination of hepatocyte markers such as albumin, Hepatocyte Nuclear Factor 4 Alpha (HNF4a) and keratin 18 (KRT18) as well as the cholangiocyte marker keratin 19 (KRT19) (4).

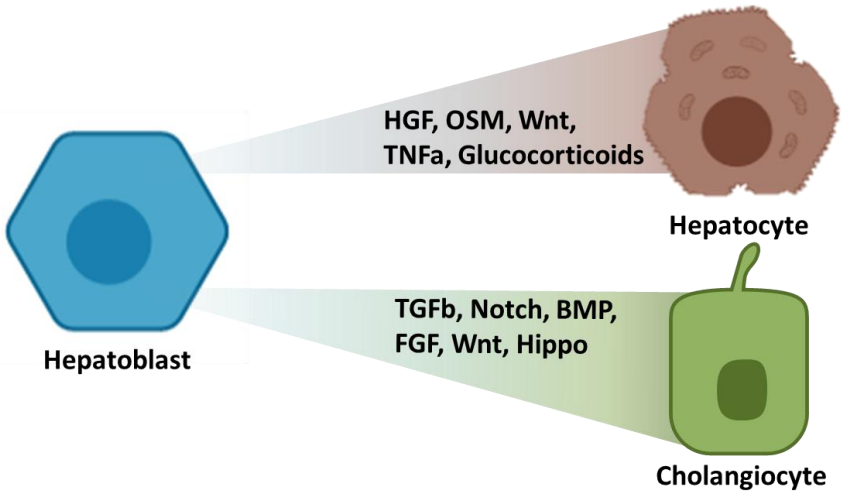

Figure 5. Hepatoblast bipotential differentiation. The differentiation potential of the hepatoblast (Hb) into hepatocytes (H) and cholangiocytes (Ch) is regulated by multiple signalling pathways.

The differentiation process is regulated by TGF-b, Wnt, BMP, Notch and FGF. TGF-b signalling is originated around the portal mesenchyme and promotes bile duct development (20). In addition to TGF-b, Notch signalling is essential for bile duct differentiation, while Notch inhibition results in reduced bile duct differentiation (21). Wnt signalling is required for both cholangiocytes and hepatocytes, and b-catenin promotes biliary differentiation while its deletion impairs bile duct formation in mice (22). Hepatocyte differentiation is also regulated by Wnt signalling. B-catenin deletion from hepatoblasts led to a decrease in HNF4a reducing hepatocyte differentiation (23). Working with Wnt signalling, HGF, oncostatin M (OSM) and glucocorticoids promote hepatocyte differentiation and maturation (12,24).

1.1.3 Liver diseases

Liver disease is a major problem in society as it is responsible for approximately 2 million deaths worldwide per year (25). Common causes of liver injury include non-alcoholic fatty liver disease (NAFLD), alcohol-associated liver diseases (AALD), viral hepatitis and drug-induced liver injury (DILI) and liver cancer such as hepatocellular carcinoma (HCC) and cholangiocarcinoma.

The liver is a highly regenerative organ that can adapt to injury through tissue repair by hepatocyte proliferation. Maintained or acute injury can reduce the regeneration capacity of the liver leading to liver fibrosis by extracellular matrix proteins (EMPs) accumulation. Chronic liver disease develops if this process continues. Chronic liver disease is characterised by fibrosis accumulation, reduction of liver function and regenerative properties leading to liver cirrhosis. Once liver cirrhosis is established, the potential to reverse disease decreases (**Figure 6**). At the point of end-stage disease, the only effective therapy is liver transplant (26). Chronic injuries are commonly caused by viral infection, alcohol consumption, NAFLD and immune or metabolic disorders.

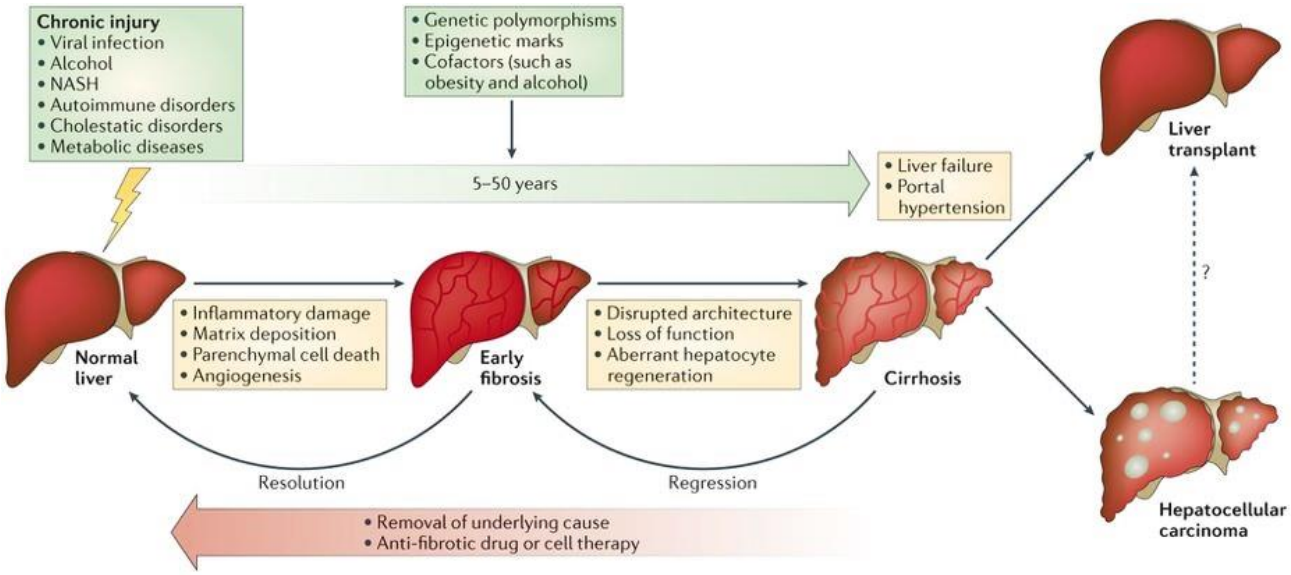

Figure 6. Ethicology of chronic liver disease. Fibrosis originates from an unbalanced wound-healing process. Injury can be caused by viral infection, alcohol consumption, NAFLD or metabolic disorders. Chronic disease originates from a maintained fibrosis over the years. Unless stopped, this process leads to cirrhosis and organ failure. From Pellicoro et al. 2014 (26).

Most types of liver injury are caused by hepatocyte and/or choanocyte death. Cell death generates a pro-injury microenvironment caused by the release of reactive oxygen species (ROS) as well as pro-inflammatory cytokines such as interleukin-6 (IL-6), Il-1b and tumour necrosis factor alpha (TNF-a) (27). These factors stimulate immune cells and stellate cells, the major effectors of disease progression. The activation of both stellate cells and macrophages results into the secretion of pro-fibrotic signals such as TGF-b, platelet-derived growth factor (PDGF) or angiotensin II. TGF-b is one of the major pro-fibrotic mediators by upregulating type I collagen and alpha-smooth muscle actin (aSMA) production in hepatic stellate-derived myofibroblasts (28). PDGF induces myofibroblasts proliferation via ERK and nuclear factor kappa-light-chain-enhancer of activated B cells (Nf-kb) (29). Angiotensin II is a vasoactive cytokine and induces fibrosis via renin-angiotensin system (RAS) activation in stellate cells (30). If this process is not stopped, TGF-b, PDGF and angiotensin II activation can generate

a positive feedback loop which will maintain fibrosis leading into cirrhosis (26).

In contrast to chronic liver disease, acute liver failure (ALF) is a life-threating disease characterised by a rapid loss of hepatocytes. ALF can be caused by prolonged ischemia, DILI or metabolic disorders, amongst others (31). Within the different origins of injury, hepatocyte death typically occurs by either apoptosis or necrosis. Apoptosis is a controlled cell death process that occurs following DNA damage, metabolism alterations or by death receptor ligands (32,33). This process is regulated by caspases, a family of proteases that cleave proteins involved in cellular homeostasis. During this process mitochondria permeability is compromised, releasing proapoptotic proteins like cytochrome c or Smac/Diablo (34). Following mitochondrial leakage, the activation of the caspase cascade will activate apoptosis. Ultimately, apoptotic cells shrink and fragment into apoptotic bodies that are phagocytosed by macrophages and adjacent cells, minimising the development of a pro-inflammatory environment (35). Necrosis in contrast, is a non-controlled cell death mechanism in response to acute injury (36). Necrosis is characterised by ATP depletion as a consequence of mitochondrial permeabilization by the opening of the mitochondrial membrane permeability transition (MPT) pore. Mitochondrial leakage leads to release of intermembrane protein, DNA fragmentation and ROS generation. These changes generate cellular swelling, forming large cellular membrane protrusions called blebs. Finally, bleb rupture causes cell death and release of the cellular components into the extracellular space leading to inflammation (37).

1.1.3.1 Drug-induced liver injury

Drug-induced liver injury (DILI) is one of the most common causes of ALF in most developed countries at an estimated annual rate of 10 - 15 patients per 100,000 (38–40). Paracetamol (acetaminophen) induced hepatotoxicity is the most common cause of DILI, causing over 50% of ALF cases in the United States in 2003 (38). Paracetamol toxicity is caused via a dose-dependent mechanism. Under non-toxic concentration, paracetamol exhibits analgesic properties. This process generates low levels of toxic metabolites that the liver can metabolise. On the contrary, paracetamol overdose induces major hepatocyte death causing life-threatening acute liver damage (41,42); hepatoxicity is characterised by the generation in excess of N-acetyl-p-benzoquinone imine (NAPQI) by cytochrome (CYP) P450 proteins (43,44). NAPQI is a highly reactive toxic metabolite that will induce ROS generation and inflammation (42).

Following administration, 90% of the paracetamol is metabolised by UDP-glucuronosyltransferase (UGT) and sulfotransferase (SULT) and excreted with urine. The remaining paracetamol is metabolised by CYP P450 proteins, mainly CYP 2E1 as well as CYP 2A6, CYP 2D6 AND CYP 3A4, into NAPQI (44–48). NAPQI is conjugated with glutathione (GSH) forming paracetamol-GSH - a non-toxic conjugate that can be excreted with the urine (49).

The common method of paracetamol toxicity is by overdose. Paracetamol-induced hepatotoxicity is developed through ingestion in single dose of more than 10 g in adults and 150 mg/kg in children, but lower doses or repeated administration of paracetamol can also lead to hepatotoxicity (38,50,51). During an overdose, NAPQI is produced in excess by CYP P450 proteins resulting in GSH depletion. After GSH depletion, NAPQI forms protein adducts by binding sulfhydryl groups of cellular proteins including mitochondrial proteins (52,53). This leads

to mitochondrial dysfunction and disruption, generation of ROS, lipid peroxidation, DNA fragmentation, ATP depletion and cell death by necrosis or apoptosis as explained previously (49). The depth of the injury can be further amplified by the immune response by the release of pro-inflammatory cytokines including TNF-a and Il-1b (54,55). Organ failure occurs when the remaining hepatocytes fail to proliferate and regenerate the liver (56). A recent study showed how injury-induced senescence in hepatocytes following paracetamol injury inhibited liver regeneration (57). Necrotic cells induce the spread of senescence to the remaining hepatocytes, blocking regeneration. This process is regulated by a positive-feedback loop that spreads senescence from both necrotic cells and macrophage-dependent TGF-b signalling.

The only current treatment for paracetamol-induced hepatotoxicity is N-Acetylcysteine (NAC). The main effect of NAC is to increase the production and availability of hepatic glutathione which neutralises NAPQI and reduces hepatocyte death (58–60). NAC treatment is only effective if it is administrated within the first 8-10 hrs following paracetamol overdose consumption (58). Therefore, new treatments that increase the treatment window or block the spread of senescence could be potential approaches to reduce the level of injury and/or promote liver regeneration.

1.1.4 Liver biology and disease modelling

There is a need to develop models that recapitulate liver physiology during health and disease. Current approaches use *in vitro* and *in vivo* tools to study liver biology. To date, *in vitro* models rely heavily on immortalised cell lines, usually derived from human tumours. These models have advantages, such as cost-effective scale-up and well-to-well reproducibility. Additionally, these cell lines can be easily genetically engineered, allowing the expression or suppression of key

genes of interest. While these models demonstrate advantages, they offer limited biological relevance when compared to the intact organ or the cancer they were derived from (61,62). Currently, primary human hepatocytes (PHH) are considered the gold standard for drug discovery and regenerative medicine. There are however drawbacks with PHH. The main disadvantages of using primary cell types are their labour-intensive isolation from diseased organs, the scarcity of donor tissue, the rapid loss of cell phenotype, and significant batch-to-batch variation (63,64).

1.1.5 Stem cells as a renewable model for liver research

Stem cell technology has been proposed as a suitable alternative to overcome the limitations of primary and immortalised cell types. Current advances in human embryonic stem cell (hESC) and induced pluripotent stem cell (iPSC) differentiation protocols into hepatocyte-like cells (HLCs) better mimic primary cells than the immortalised lines (65). Through model refinement and cost-effective scale-up it is now possible to prototype systems from defined genetic backgrounds to study and better understand the biology behind drug-induced liver injury and other forms of liver diseases (66–71).

Human pluripotent stem cells (hPSC) exhibit self-renewal and pluripotency, the potential to differentiate into the three germ layers (72). hESC are derived from the inner cell mass of blastocytes unsuitable for implantation (73). iPSC were first produced by overexpressing key transcription factors: Oct 3/4, Sox2, Klf4 and c-Myc (74). hPSC express the pluripotent transcription factors Oct4, Nanog and Sox2 (75–77) and the cell surface markers like tumour rejection antigens TRA-1-60 and TRA-1-81, stage-specific embryonic antigen 3 (SSEA3) and 4 (SSEA4).

Over the last two decades, several groups have established differentiation protocols that allow the efficient differentiation of hPSC HLCs. Hepatocyte differentiation attempts to recreate aspects of a human liver development *in vitro* by using growth factors and small molecules (for a review of the different protocols for HLCs production see (78)). To date, most of the work has focused on monolayer hepatocyte systems.

Hepatocyte monolayer differentiation systems usually consist of a stagewise approach where the stem cell populations are driven to definitive endoderm using activin and Wnt signalling (79,80). This is followed by hepatic progenitor cell specification (81,82) and hepatocyte maturation (83–87). These protocols produce HLCs that express mature hepatocyte markers such as HNF4a, albumin, and cytochrome P450 proteins, exhibit metabolic activity and secrete serum proteins such as albumin (88,66). Successful differentiation of the different stages of the protocol can be assessed using a panel of protein markers (**Figure 7**).

Advantages of the monolayer systems include the ease and cost of scale-up, and relatively reduced batch-to-batch variation, making them ideal for regenerative medicine research (89). However, current systems face some limitations such as a mixture of foetal and adult hepatocyte traits and limited organisation, and as a consequence cannot recapitulate all situations that occur *in vivo* (90). Recent advances in HLCs differentiation protocols have been proven to model liver diseases. HLCs have been used to model human metabolic liver disease (70,71), non-alcoholic fatty liver disease (67,69), drug-induced liver injury (68,91) and foetal hepatotoxicity (92). Another advantage is the ability to create HLCs from multiple libraries to capture genetic diversity offering new resources to study mechanism of action and to develop better models to study idiosyncratic reactions (93).

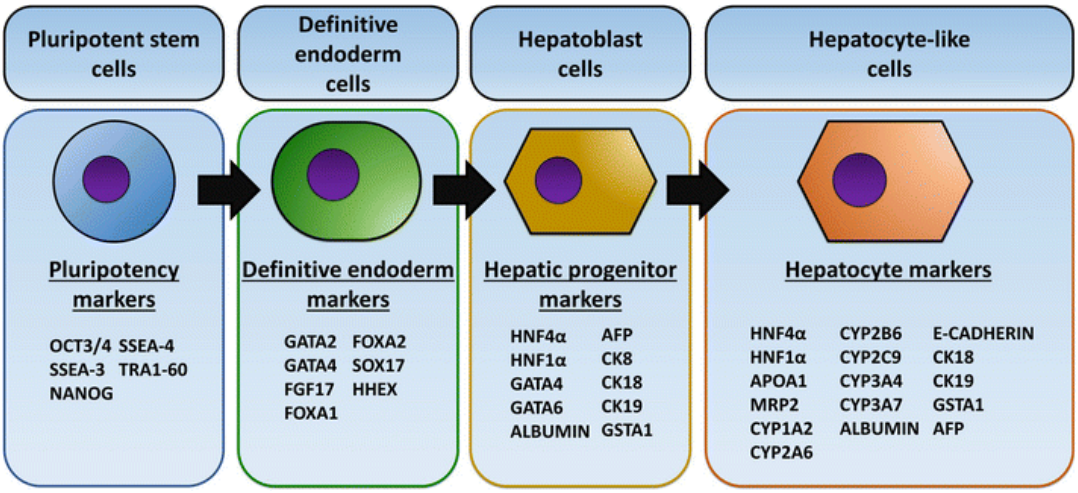

Figure 7. HLCs markers during the differentiation process. Pluripotent stem cells are differentiated to definitive endoderm, then primed to the hepatoblast stage. Following this, the progenitors are matured to hepatocyte-like cells. A panel of markers can be employed to assess successful differentiation at each stage of the process. OCT - octamer-binding transcription factor, SSEA - stage-specific embryonic, GATA - GATA binding protein, FOXA - forkhead box protein A, FGF17 - Fibroblast growth factor 17, hHex—hematopoietically-expressed homeobox, HNF - Hepatocyte nuclear factor, AFP - Alpha-fetoprotein, CK - cytokeratin, GSTA1 - glutathione S-transferase A1, APOA1- apolipoprotein A1, MRP2 - Multidrug resistance-associated protein 2, CYP - Cytochrome P450. Adapted from Meseguer-Ripolles et al, 2018 (78).

1.2 The Nrf2 pathway

As described previously, therapies that increase the antioxidant and anti-inflammatory capacity of the hepatocytes or block the spread of senescence could reduce the severity of acute liver injury and enhance regeneration. The transcription factor 'nuclear factor erythroid-derived 2-like 2' (Nrf2) is a major regulator of a large battery of cytoprotective genes involved in multiple processes such as oxidative stress management, glutathione synthesis, detoxification, drug excretion and NADPH synthesis (94). Therefore, pharmacological activation of Nrf2 during acute liver injury may provide a successful therapy for patients.

1.2.1 Regulation of Nrf2

Nrf2 is a member of the cap'n'collar (CNC) basic-region leucine zipper transcription factor family and it was discovered in 1994 (95). It regulates the expression of more than 200 genes that contain an enhancer region in their promotor named antioxidant response element (ARE) (96). Nrf2 is able to regulate the expression of the ARE depended genes in response to multiple forms of stress.

The main regulation of Nrf2 is through its interaction with Kelch-like ECH-associated protein 1 (Keap1). Keap1 was firstly described in 1999 as the main Nrf2 repressor (97). Keap1 is an E3 ubiquitin ligase that targets Nrf2 for proteasomal degradation via the cullin 3 (Cul3) and RING box protein 1 (Rbx1) complex (98,99). Therefore, under non-stress conditions, Keap1 interacts with Nrf2 and undergoes a rapid proteasomal degradation, this mechanism limits the half-life of Nrf2 to 15-40 minutes (96). However, oxidative stress and electrophilic molecules can limit the binding capacity of Keap1 by interacting and covalently modifying Keap1 cysteine residues (Cys) (100). Keap1 is a cysteine-rich protein, with Cys-151, Cys-226, Cys-273, Cys-288 and Cys-613 as the most common modified residues with Cys-151 the preferable residue for interaction with electrophile compounds (101). Following Keap1 inhibition, Nrf2 is rapidly accumulated into the cytoplasm. This is followed by a nuclear translocation of Nrf2 where it forms a heterodimer with small musculoaponeurotic fibrosarcoma oncogene homologue (sMAF) proteins inducing the ARE-dependent gene expression (96).

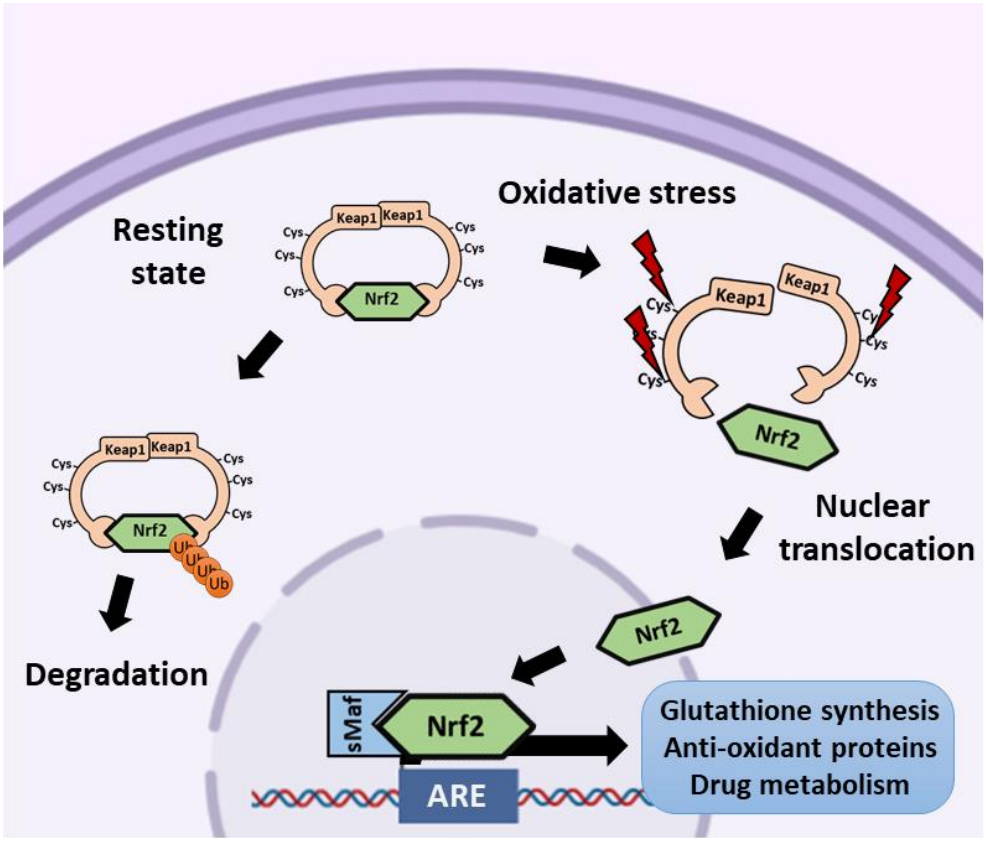

Figure 8. Overview of the Nrf2-Keap1 pathway regulation. Upon cell stress Keap1 structure changes allowing the dissociation of the Nrf2–Keap1 complex allowing Nrf2 to undergo nuclear translocation initiating the expression of the ARE mediated genes. ARE = antioxidant response element, Cys = cysteine groups, sMAF = small Maff protein, Ub = ubiquitin. Figure drawn by author.

1.2.2 The role of Nrf2 in DILI modulation

In hepatocytes, Nrf2 is highly expressed to maintain organ homeostasis (102). Nrf2 regulates the expression of several proteins involved in drug metabolism including phase I, phase II and phase III proteins. Nrf2 regulates the expression of several processes involved in paracetamol metabolism (**Figure 9**). Nrf2 also controls the expression of proteins that control glutathione and NAPDH homeostasis. NAPDH is an essential cofactor for multiple drug metabolising enzymes and to the antioxidant machinery. Lipid metabolism and heme and iron metabolism is also regulated by Nrf2 (for a detailed review of the Nrf2 regulatory network in drug metabolism see (94)).

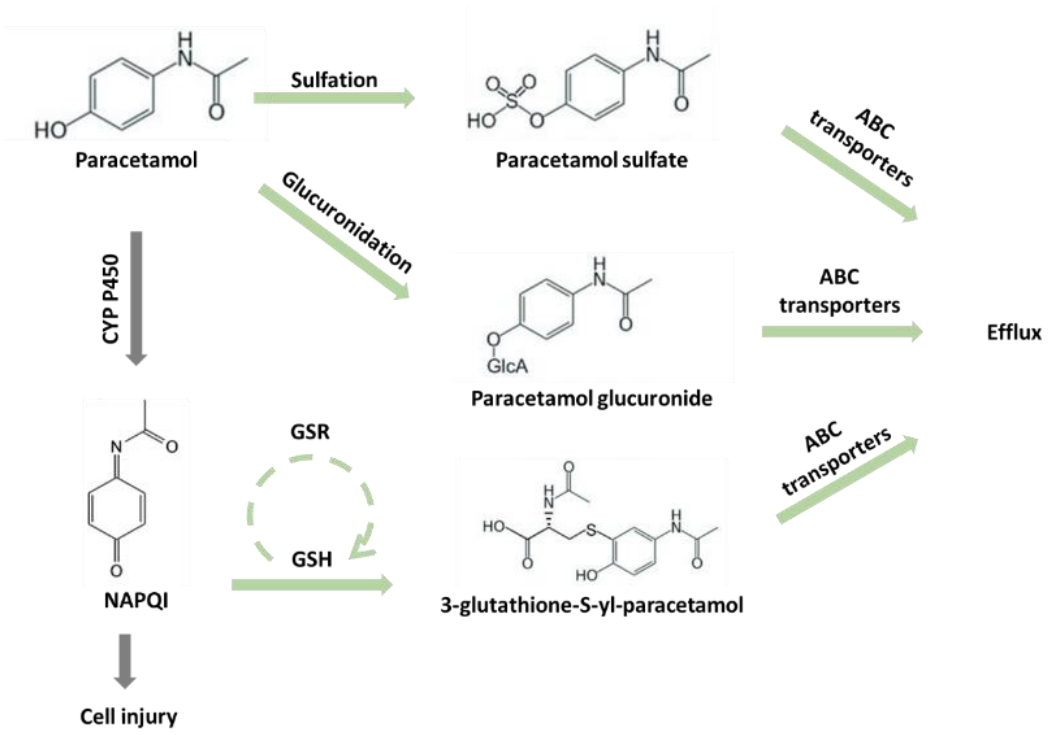

Figure 9. Role of Nrf2 in paracetamol metabolism. In green are all the processes regulated in part by the Nrf2 pathway. Nrf2 can regulate the UGT and SULT enzymes responsible for the non-toxic paracetamol metabolism. In addition, Nrf2 also regulates glutathione (GSH) recycling by the induction of GSR as well as the glutathione-S-transferases responsible for NAPQI neutralisation. Finally, Nrf2 can also regulate the ABC transporters responsible for metabolite efflux (103–106).

In addition, Nrf2 displays anti-inflammatory properties by a crosstalk with Nf-kb and direct inhibition of pro-inflammatory genes. Nrf2 can inhibit Nf-kb transcription. Treatment with lipopolysaccharide (LPS) in a Nrf2 knockout mice model of sepsis exhibited an increased expression of the Nf-kb signature when compared to control mice. In Nrf2 knockout mice, the inhibitor of Nf-kb (IκB) was highly phosphorylated and undergoing proteasomal degradation, reducing the inhibition of the Nf-kb pathway (107). Another mechanism where Nrf2 can suppress Nf-kb is by the competition to bind the transcriptional cofactor p300 (108). Finally, the activation of Nrf2 suppresses the macrophage inflammatory response by blocking the

transcription of pro inflammatory cytokines (Il-6, IL-1b, IL-1a and Nos2) via an ARE non-dependent mechanism (109).

The protective role of Nrf2 in paracetamol-induced hepatoxicity was demonstrated in a study with Nrf2-knockout mice. Nrf2 knockout mice exhibited an increased paracetamol-induced injury due to a reduction in the detoxification enzymes expression (106,110,111). Opposite results were observed where Keap1-knockout mice were exposed to paracetamol (112). Moreover, a different study reported Nrf2 activation following paracetamol administration in a mouse model. Nrf2 nuclear translocation was observed in both toxic and non-toxic paracetamol concentrations (113). In this study, upregulation of Nrf2 target genes was not detected at the toxic concentrations despite the nuclear translocation of Nrf2. Recent work in mouse liver cells probed the direct interaction of NAPQI and Nrf2. In this study, NAPQI activated Nrf2 nuclear translocation by depleting cellular glutathione and by modifying the cysteine residues of Keap1 (114). Therefore, the cytoprotective potential of Nrf2 following paracetamol overdose might be dependent of the level of injury; where higher concentrations of NAPQI could activate Nrf2 nuclear translocation but fail to induce transcription (113). This could be due to a significant dysregulation of cellular processes involved in cellular homeostasis from paracetamol overdose. Following injury, Nrf2 has been shown to play an important role in liver regeneration; it is required to maintain hepatocyte identity during the regenerative process by regulating the expression of Notch1 and HNF4a (115,116).

1.2.3 Therapeutic activation of Nrf2

Pharmacological activation of Nrf2 following paracetamol-induced hepatotoxicity might represent a potential therapy to enhance hepatocyte health and liver regeneration. The majority of Nrf2 inducers are electrophile compounds that covalently modify the cysteine residues of Keap1 (117). Keap1 inhibition is mainly by changing the conformational structure of Keap1 or by blocking the interaction between Keap1 and the CUL3/RBX1 complex (118–120). Fumaric acid compounds are potential Nrf2 activators; Dimethyl fumarate (DMF) is a fumaric acid compound approved by the food and drug administration (FDA) and the European Medicines Agency (EMA) for relapsing multiple sclerosis and psoriasis (121,122). DMF is metabolised by hydrolysis to monoethyl fumarate (MMF) by esterases (123). Both DMF and MMF can interact directly with Keap1 cysteine residues activating Nrf2 (124). MMF is further metabolised through the tricarboxylic acid (TCA) cycle with no CYP P450 involvement. MMF is mainly eliminated by CO_2 exhalation (60%) followed by renal (16%) and fecal (1%) elimination (125).

Even though the mechanism of action of DMF is not fully understood, DMF presents some immunomodulatory and oxidative stress management properties (124). To date, most of the work has been focused in understanding the mechanism of action of DMF in multiple sclerosis and psoriasis. The main effects observed by DMF treatment are: activation of Nrf2 pathway, indirect inhibition of Nf-kb and hypoxia-inducible factor 1-alpha (HIF-1a), modulator of intracellular GSH and modulation of the immune system.

DMF induces the expression of multiple Nrf2 target genes including Heme oxygenase-1 (HMOX1), NAD(P)H quinone reductase 1 (NQO1) or glutathione reductase (GSR) as well as by inhibiting the expression of pro-inflammatory signalling such as Il-1b, TNFa, nitric oxide and Il-6

(126–129). DMF inhibits Nf-kb activation by a covalent modification of p65, a member of the Nf-kb transcription factor family. DMF inhibits the nuclear translocation and DNA biding activity of phosphorylated p65 (130,131). Inhibition of HIF-1a by DMF treatment has also been reported; DMF can interact with HIF-1a and promote its degradation reducing the expression of HIF-1a target genes such as vascular endothelial growth factor (VEGF) and Il-8 (132). In addition, there is complex interaction between DMF and GSH;

In vitro work in astrocytes and peripheral blood monocytes reported GSH depletion followed by an upregulation of HMOX-1 following DMF treatment (133,134). Interestingly, the initial decrease of GSH was accompanied with an increase in total basal levels of GSH after 24 h of DMF treatment; this could be controlled by GSR upregulation after DMF treatment (134,135). In contrast, Kramer et al. showed how DMF prevented glutathione depletion and Nrf2 activation in a mouse model of traumatic brain injury (136). Finally, several immunomodulation properties of DMF have been reported. First, DMF can activate the hydroxycarboxylic acid receptor 2 (HCA2) expressed in neutrophils reducing their neutrophil adhesion, activity and recruitment capacity (137,138). In addition, work in multiple sclerosis patients showed that long term treatment of DMF induces reduction in peripheral memory T-cells, natural killer cells and B cells with a relative increase in Th2 and naïve T-cells with a higher anti-inflammatory activity (139,140). Further research to fully understand the immunomodulatory properties of DMF is required. Therefore, pharmaceutical repurposing of the use of DMF could potentially lead to a successful treatment to reduce the severity of acute liver injury.

1.3 The objective of the thesis

The focus of this study is to investigate the cytoprotective properties of dimethyl fumarate and Nrf2 signalling during drug-induced hepatotoxicity in both *in vitro* an *in vivo* models. For the *in vitro* studies, (HLCs) from human pluripotent stem cells were employed. The *in vitro* findings were validated in a zebrafish liver-GFP reporter line.

1.4 Hypothesis of the thesis

Short term stimulation of Nrf2 by dimethyl fumarate will protect hepatocytes from drug-induced oxidative stress and toxicity.

CHAPTER TWO

MATERIALS AND METHODS

2.1 Materials and reagents

2.1.1 Cell culture medium

Table 1 Cell culture medium used for hESC maintenance and differentiation

Cell culture	Medium	Medium supplements	Supplier
Human embryonic stem cells	mTeSR1	10 µM ROCK inhibitor only for differentiation and resuscitation	Stem Cell Technologies
Embryoid bodies	Knockout DMEM	20% FBS 1% Glutamax 1% Penicillin Streptomycin	Thermo Fisher Scientific
hESC-derived hepatic endoderm medium	RPMI 1640	B27 100ng/ml Activin A 50ng/ml Wnt3a 1% Penicillin Streptomycin	Thermo Fisher Scientific R & D System Peprotech Thermo Fisher Scientific
hESC-derived hepatoblast medium	Knockout DMEM	20% Knockout Serum Replacement (KSR) 0.5% Glutamax 1% Non-Essential Amino Acids 1% Penicillin Streptomycin 0.1mM β-Mercaptoethanol 1% DMSO	Thermo Fisher Scientific Sigma Aldrich
hESC-derived hepatocyte-like cell medium	HepatoZYME medium	1% Glutamax 1% Penicillin Streptomycin 10ng/ml hepatocyte growth factor (HGF) 20ng/ml oncostatin M (OSM) 10 µM hydrocortisone 21-hemisuccinate	Thermo Fisher Scientific Peprotech Sigma Aldrich

2.1.2 Antibodies

Table 2. Primary antibodies used for immunostaining

Primary antibodies			
Antibody	**Host species**	**Dilution**	**Supplier**
Oct4	Rabbit Poly	1/200	Abcam
NANOG	Rabbit Poly	1/200	Abcam
AFP	Mouse Mono	1/400	Abcam
a-SMA	Mouse Mono	1/200	DAKO
b-tubulin	Mouse Mono	1/1000	Sigma Aldrich
Sox17	Goat Poly	1/400	R & D Systems
Foxa2	Mouse Mono	1/200	R & D Systems
HNF4a	Rabbit poly	1/200	Santa Cruz
CK19	Mouse Mono	1/50	DAKO
E-cadherin	Mouse Mono	1/200	Abcam
CYP2D6	Sheep Poly	1/200	University of Dundee
CYP3A4	Sheep Poly	1/4200	University of Dundee
MRP1	Mouse Mono	1/100	Abcam
Nrf2	Rabbit poly	1/100	Abcam
Nrf2	Mouse Mono	1/100	Santa Cruz
IgG	Rabbit Poly	1/400	DAKO
IgG	Mouse Mono	1/400	DAKO
IgG	Goat Poly	1/400	DAKO
IgG	SHeep Poly	1/400	DAKO

Table 3. Secondary antibodies used for immunostaining

Secondary antibodies			
Antibody	**Host species**	**Dilution**	**Supplier**
Anti-Rabbit 568	Donkey	1/400	Life Technologies
Anti-Rabbit 488	Donkey	1/400	Life Technologies
Anti-Mouse 488	Rabbit	1/400	Life Technologies
Anti-Mouse 568	Goat	1/400	Life Technologies
Anti-Sheep 488	Donkey	1/400	Life Technologies
Anti-Goat 488	Rabbit	1/400	Life Technologies
Anti-Goat 568	Rabbit	1/400	Life Technologies
Anti-Rabbit 568	Donkey	1/400	Life Technologies
Hoechst 350 nm (DNA staining)		1/1000	Invitrogen

Table 4. Antibodies used for flow cytometry

Antibody	Fluorophore	Host species	Dilution	Supplier
SSEA-1	FITC	Mouse	1/50	Biolegend
SSEA-4	PE	Mouse	1/50	Biolegend
TRA-1-60	PE	Mouse	1/50	Biolegend
Mouse IgG	FITC/PE	Rabbit	1/50	Biolegend

Table 5. Antibodies used for western blot

Antibody	Host species	Dilution	Supplier
Nrf2	Mouse Mono	1/1000	R & D Systems
b-actin	Mouse Mono	1/10000	Sigma

2.1.3 Cell Painting assay

Table 6. Fluorescent staining used for the cell painting assay.

Compound	Florescence (nm)	Dilution	Supplier
HCS CellMask	488	1/50000	Invitrogen
MitoTracker Deep Red	647	1/4000*	Invitrogen
Hoechst 33342	350	1/1000	Invitrogen

2.1.4 Oligonucleotides

Only TaqMan probes from applied biosystems were used for this study.

Table 7. List of TaqMan primers used

Gene	Primer
Glutathione reductase	Hs00167317_m1
NADPH quinone dehydrogenase 1	Hs01045993_g1
Heme oxygenase 1	Hs01110250_m1
Beta 2 microglobulin	Hs00187842_m1

2.1.4.1 Chemical reagents

Table 8. List of reagents used

Reagent	Supplier	Catalogue number
Dimethyl fumarate	Sigma Aldrich	242926
H_2O_2	Sigma Aldrich	H1009
Paracetamol	Sigma Aldrich	P0300000
Brusatol	Sigma Aldrich	SML1868
N-Acetylcysteine	Sigma Aldrich	PHR1098

2.1.4.2 Semi-automated platform equipment

Equipment	Supplier
Multidrop	Thermo Fisher Scientific
ViaFlo	Integra
Automatic plate washer	Biotek
Operetta high throughput microscope	Perkin Elmer
GloMax explorer multiplex plate reader	Promega

2.2 Stem cell culture and differentiation

All cell culture reagents were GIBCO products supplied by Thermo Fisher Scientific unless stated otherwise. Corning (UK) supplied the plastic ware utilised throughout the cell culture. For high throughput imaging, specific μClear 96-well plates from Greiner Bio-one were used. Cell culture medium used in this study is described in **Table 1**.

2.2.1 Stem cell culture

H9 human embryonic stem cells were cultured on 5μg/cm^2 of laminin 521 (BioLamina) with mTser1 media (STEMCELL Technologies). Medium was changed daily. The cells were incubated at 37 °C in 5 % (v/v) CO2, 95 % (v/v) air, for optimal growth.

2.2.2 Stem cell passaging

hESC were passaged when they reached 80% of confluency. Medium was aspirated and the cells were washed with Dulbecco's phosphate-buffered saline (DPBS) (Life Technologies) once. Gentle cell dissociation reagent (STEMCELL Technologies) was added to the cells. For regular passaging, cells were incubated for 5 minutes until the edges of the colonies were rounded up. The Gentle cell dissociation regent was

aspirated and fresh mTser1 medium was added. Using a cell scraper, a homogeneous suspension of cells was formed. Cell split ratio was 1:3 for regular PSC colonies maintenance.

2.2.3 Stem cell freezing and thawing

Stem-cellbanker (Amsbio) was used as a freezing solution. hESC at 80-90 % confluence were dissociated and collected, cells were centrifuged at 200xg for 3 minutes in a 15 ml tube. Supernatant was removed and the cell pellet was resuspended in 1 ml of the freezing solution and transferred to -80 °C freezer for one night and then to the liquid nitrogen tank. Cells were thawed by warming the cryotube in a 37 °C water bath. Once thawed, cell suspension was transferred into a 15 ml tube with 5 ml of fresh mTeSR1 medium to resuscitate the cells. The cells were then centrifuged at 200xg for 3 minutes. The supernatant was removed, and the cells were resuspended in 2 ml of mTeSR1 medium supplemented with 10 µM ROCK inhibitor Y27632 and seeded onto a laminin 521 coated 6 well-plate well.

2.2.4 Embryoid body formation

Embryoid bodies (EBs) were generated from the hESCs. At 80-90 % confluence, hESCs were dissociated briefly for 2-3 minutes and collected with 4 ml of EB media. The whole 4 ml cell suspension was then plated in low attachment plates to promote cell self-aggregation. The media was changed every other day for 7 days until the EBs were defined and vacuolated. At day 7, EBs were transferred to 0.5 % gelatin coated 24-well plates. The EBs were allowed to differentiate spontaneously for 14 days and fed every other day with EB media. On day 14, the differentiated cells were fixed with 100% ice-cold methanol at -20 °C for 30 minutes. Cells were washed after fixation three times with DPBS at room temperature. Cells were then stained with specific antibodies of markers for the three germ layers.

2.2.5 Hepatocyte-like cell differentiation

For HLCs differentiation, cells were incubated for 7-9 minutes with gentle cell dissociation regent until all cells were rounded up while still attached at the plate. Using a cell scraper, a homogeneous suspension of single cells was formed. Single cells at 50,000 cells/cm^2 were plated on 5µg/cm^2 of laminin 521, when they reached 30 – 40 % of confluency the differentiation protocol was initiated. Once the cells reach the correct confluence, mTseR media was replaced with the endoderm differentiation medium. On day 4, the second stage, hepatoblast differentiation medium was added for 5 days changing the media every two days. On day 9, the HLCs medium was added. The medium was changed every second day.

2.2.6 High throughput culture of HLCs

The semi-automated platform was used to differentiate and characterize the cells. An automatic liquid handling dispenser (multidrop) was used to coat matrix and seed single cells. Cellular differentiation was initiated when the cells reached 40% confluency (Day 0). Media changes were performed using an automatic hand-held electronic channel pipette (ViaFlo) system to remove medium and the liquid handling dispenser for medium addition. Cell fixation and staining were performed using the automatic liquid handling dispenser in combination with the automatic plate washer (Biotek).

2.3 Cell characterisation

2.3.1 Fluorescence activated cell sorting (FACS)

Fluorescence activated cell sorting (FACS) was performed to characterise the expression of cell surface proteins in hESCs. hESCs were washed once with 2 ml DPBS and then dissociated with 1ml TrypLE. Cells were collected as single cells. Post centrifugation, cells

were resuspended in DPBS and filtered through a 0.22 µM filter. The single cell suspension was then incubated for 30 minutes at 4 °C with the fluorochrome conjugated antibodies (for antibody details, see **Table 4**). IgG controls were used for antibody specificity. After incubation, cells were then washed twice with DPBS, and spun down at 200xg for 5 minutes. Cells were then resuspended in 300 µl of DPBS. Only single live cells were used for quantification: dead cells were excluded by labelling them using DNA staining prior to acquisition. The analysis was carried out by using a live gate on forward scatter and side scatter parameters. Data for 20,000-50,000 'live' events were acquired for each sample using a BD LSR Fortessa (4 laser) analyser. The data was analysed using FlowJo software.

2.3.2 CYP P450 activity

CYP 3A and CYP 1A2 activity were measured on HLCs at day 18 by using the P450-Glo™ assay (Promega). CYP 3A (1:20) and CYP 1A2 (1:50) substrates were diluted in hepatocyte maturation medium and added to the HLCs for 5 37 °C in 5 % (v/v) CO2, plain medium with substrate was incubated in parallel to subtract background. After incubation, 50 µl of supernatant was collected and mixed with 50 µl of luciferin detection reagent in a white 96-well plate at room temperature in the dark for 20 minutes. Luminescence was measured using a multiplex plate reader (GloMax Explorer, Promega) and normalised per mg of protein (RLU/ml/mg).

2.3.3 Protein content quantification

The Pierce bicinchoninic acid (BCA) assay kit (Thermo Fisher Scientific) was used to quantify the protein content in HLCs. Protein supernatant was obtained by adding 50 µl of RIPA buffer (Thermo Fisher Scientific) per well of a 96-well plate. 10 µl per sample were analysed in duplicates added into a 96-well plate. A standard curve was generated using

bovine serum albumin standards at concentrations ranging from 0-2000 µg/ml. Reagents A and B from the kit were mixed at a 1:50 ratio for a final volume of 200 µl per well. Samples were incubated at room temperature in the dark for 30 minutes and absorbance was read at 562 nm using a multiplex plate reader (GloMax Explorer, Promega). Concentrations were calculated using standard curve.

2.3.4 High-content imaging and analysis

Image acquisition was performed using the automated Operetta fluorescent microscope. In brief, plates were placed in the Operetta and several random fields of view were imaged per well. Cell segmentation for image analysis was performed using the Columbus image analysis software. Cell segmentation is a process were the different organelles of the cells are identified for feature identification. Cell segmentation was performed by a first identification of the nuclei followed by cytoplasm identification. Details in Chapter 3.

2.3.5 Cell viability assay

Cell viability was determined by the amount of ATP in HLCs differentiated in 96-well plate format measured using CellTiter-Glo® Luminescent Cell Viability assay (Promega). 100 µl of CellTiter-Glo luciferase substrate were mixed with 100 µl of culture medium in the plate containing the HLCs. After incubation 100 µl of the mixture was transferred into a white 96-well plate and luminescence was measured using a multiplex plate reader (GloMax Explorer, Promega).

2.3.6 Cell Paint assay and morphological profiling

Cell Paint was developed by Bray et all, 2016 (141), The idea of this assay is to create an imaged cell-based profiling using specific dyes to stain cellular organelles. After a 4% paraformaldehyde fixation, cells were stained for cytoplasm (CellMask 488nm, ThermoFisher),

mitochondria (Mitotracker 665nm, ThermoFisher) and nuclei (NucBlue 460 nm, ThermoFisher) according to manufacturers' instructions.

Morphological profiling was performed by image cell segmentation. First cell nuclei are defined using Dapi channel. Next, cytoplasm was identified using CellMask staining from the nuclei identified previously. After cells have been identify automatically, a quality control step is performed to remove incorrect object segmentations. Then, by measuring the cell number, intensities, morphologies and pixel texture from the different channels a morphological profile was created using 86 different features. This was used to define changes in cells upon different stimuli.

2.3.7 ELISA assay

HLCs supernatant was collected after 24 h of culture at day 18. Albumin or AFP protein secretion was determined using commercially available micro-well plates pre-coated with immobilized human albumin or AFP antibodies (Alpha Diagnostic Intl. Inc, San Antonio, USA). The enzyme-linked immunosorbent assay (ELISA) was carried out according to the manufacturer's instructions. The supernatant was diluted 1:3 or 1:10 using the working sample diluent and pipetted into the wells in duplicate. Samples for the standard curve were pipetted in parallel. After one-hour incubation at room temperature, the micro-wells were washed four times with working wash solution. Anti-human albumin or AFP HRP-conjugated secondary antibody was then diluted in working sample diluent and added to the micro-wells followed by 30 minutes incubation at room temperature. After incubation, the micro-wells were washed five times using working wash solution. The substrate for the HRP enzyme TMB was then added and incubated for 15 minutes in the dark at room temperature. Stop solution was added directly to the wells in order to stop the enzymatic reaction. The plates were then read at 450 nm with a reference wavelength of 630nm with

the multiplex plate reader. The data was then normalised to per ml per mg protein as determined by BCA assay (Pierce, UK).

2.4 Molecular techniques

2.4.1 Immunofluorescence

Cell cultures in 96-well plates were fixed in 4% paraformaldehyde in H_2O for 15 minutes at room temperature. Subsequently, fixed cells were washed twice with PBS at room temperature. Cell were blocked with 0.1% PBS-Tween containing 10% BSA for one hour, followed by an incubation with primary antibodies diluted in PBS-0.1% Tween/1% BSA at 4°C overnight. Then the cells were washed three times with PBS-0.1% Tween/1% BSA. Secondary antibody was diluted in PBS/0.1% Tween/1% BSA and incubated for 1 hr at room temperature in the dark. Finally, the cells were washed three times with PBS and the nuclei was stained using Hoechst for 5 minutes.

2.4.2 Western blotting

Proteins for Western blotting were collected after one cell wash with DPBS, cell lysis was performed using RIPA buffer (Sigma Aldrich) supplemented with proteinase and phosphatase inhibitors (Sigma-Aldrich) at 1 %. After cell lysis, protein suspension was spun down for 15 min at 12,000 rpm at 4 °C and supernatant was transferred into a new 1.5 ml tube. Protein concentration was quantified by BCA.

2.4.2.1 SDS-NuPAGE polyacrylamide gel electrophoresis

The SDS-NuPAGE polyacrylamide gel electrophoresis (SDS-PAGE) was used to separate proteins based on their sizes. 50 µg protein supernatant was denatured at 100 °C for 10min in 1 x NuPAGE LDS (Thermo Fisher Scientific) sample buffer supplemented with 10 mM DTT before being used for electrophoresis. 4-12 % Bis-Tris precast

polyacrylamide gels (Thermo Fisher Scientific) were used with the XCell SureLock Mini-Cell System (Thermo Fisher Scientific) for the electrophoresis. After placing the gel in the chamber, the tank was filled with 1x NuPAGE MES-SDS running buffer with 0.5 ml of NuPAGE Antioxidant (Thermo Fisher Scientific) added into the inner chamber. The samples were loaded along with a SeeBlue Plus 2 Pre-Stained Standard (Invitrogen). A current of 200 V was applied and the samples were run for 1.5 hours. The gels containing proteins were carefully removed from the cassette for further use in western blotting

2.4.2.2 Protein transfer

Following the protein separation using SDS-PAGE gels, the proteins were then transferred from the gels to the Polyvinylidene fluoride (PVDF) membrane. The transfer sack was assembled from cathode to anode as follows: 3x sponge; 2x filter paper soaked in 1x NuPAGE Transfer Buffer; SDS-PAGE gel; PVDF membrane activated in 100 % ice-cold methanol; 2x filter paper soaked in 1x NuPAGE Transfer Buffer; 3x sponge. No bubbles between the gel and the membrane were created. After stack assembly, it was placed into the XCell Blot II module, the module was tightly sealed and placed into the transfer SureLock tank and 1x transfer buffer in the inner chamber and ice-cold water in the outer chamber was added. The tank was then placed on ice for the entire protein transfer process. A constant current of 160mA was applied for 90-120 min.

2.4.2.3 Immunoblotting

Following protein transfer into the PVDF membrane, the membrane was blocked in 10 % skimmed milk at room temperature with gentle agitation for at least one hour to reduce non-specific antibody binding. After blocking, the membrane was probed with desired primary antibody diluted in 5 ml 10 % skimmed milk/PBST at 4 °C overnight

with gentle rolling. The dilution ratios were optimised specifically for each primary antibody as listed in **Table 5**. Unbound antibody was removed by three washes with 0.1 % PBST at room temperature with agitation for 5 minutes. After primary antibody incubation, the membrane was then incubated with corresponding horseradish peroxidase (HRP)-conjugated secondary antibody diluted in 5 ml 10 % skimmed milk at room temperature for at least one hour with gentle rolling. Unbound secondary antibody was then removed by three washes with 0.1 % PBST at room temperature with agitation for 5 minutes. B-actin was used for loading control (142).

2.4.2.4 Enhanced Chemiluminescence (ECL)

Finally, protein content was quantified using enhanced chemiluminescence (ECL). Proteins bands were visualised using the Pierce Enhanced Chemiluminescence Kit (Pierce, UK). Peroxidase buffer and the Luminol/Enhancer solution were mixed at a 1:1 ratio and spread evenly onto the membrane (2 ml for each membrane), followed by a 5-minute incubation at room temperature. The HRP substrate reacts with the conjugated HRP group presented on the secondary antibody, specifying the target protein. The membrane was developed in the dark room using a film developer. Protein quantification was performed using FIJI software.

2.4.3 RNA extraction

RNA was extracted using RNeasy kit (Qiagen), accordingly to manufacturer's instructions. The cells were washed with PBS and 350 µl of lysis buffer was added into the cells (buffer RTL, RNEasy MiniKit, Qiagen) containing β-mercaptoethanol (Gibco, UK). The suspension was collected and placed in a 1.5 ml. Cell lysis was ensured by vortexing the samples for 30 seconds before addition of an equal volume of 70 % Ethanol. The suspension was transferred into a RNeasy

Spin Column placed with a collection tube. Column was centrifuged at 10,000 rpm for 20 seconds, flow through was discarded and 700 µl Buffer RW1 was added. Next, centrifugation at 10,000 rpm for 20 seconds was performed and the flow-through was discarded. Following this, 500 µl of Buffer RPE was added. After centrifugation at 10,000 rpm for 30 seconds, 500 µl buffer RPE was added followed by centrifugation at 10,000 rpm for 2 minutes. Then the RNeasy Spin Column was transferred to a new collection tube and centrifuged at 16,000 rpm for 1 minute. The spin column was placed into an RNAse free 1.5 mL tube and 30 µl RNAse free H2O was added to the membrane. After 3 minutes incubation at room temperature, the tube was centrifuged at 10,000 rpm for 1 minute and stored at -80 °C for later use. RNA concentration and integrity were quantified using the Nanodrop. Both 260/280 and 260/230 rations were quantified and only samples with ratios > 1.8 – 2 were used for downstream analysis. 260/280 ratio measures the purity of RNA from proteins, phenol or other contaminants that absorb at 280 nm. 260/230 ratio measures RNA purity from contaminants such as TRIzol, EDTA or carbohydrates that absorb at 230 nm.

2.4.4 Reverse transcription

400 ug of RNA was converted into cDNA using the QuantiTect Reverse Transcription Kit (Qiagen) accordingly to manufacturer's instructions. Genomic DNA contamination removal was performed by adding 7 µl of gDNA Wipeout Buffer to the purified RNA and RNase-free water up to 14 µl. The reaction was incubated at 42 °C for 5 minutes and then placed on ice. Next, 1 µl Quantiscript Reverse Transcriptase, 4 µl 5x Quantiscript RT Buffer and 1 µl RT Primer Mix were added to the reaction. Mix was incubated at 42 °C for 30 minutes, followed by a 95 °C heat treatment for 5 minutes, finishing with a final cool down to 4 °C for 5 minutes.

2.4.5 Quantitative polymerase chain reaction (qPCR)

qPCR was performed by using Taqman Fast Advance Mastermix and Taqman compatible primers (**Table 7**). Reaction mix was prepared by using 0.5 µl of primers, 5.5 µl of Taqman Fast Advance Mastermix and 5.5 µl of nuclease-free water containing 12 ng of cDNA per reaction. Reactions were prepared in triplicate. qPCR reaction consisted of: an initial denaturation step at 95 °C for 10 minutes, then 40 cycles of denaturation at 95 °C with an annealing/extension at 60 °C for 1 minute in accordance with the manufacturer's instructions. qPCR was performed using Roche LightCycler 480 Real-Time PCR System and data analysis was performed using Roche LightCycler 480 Software (version 1.5) in the form of cycle threshold (Ct) values. This value represents the point at which fluorescence intensity generated in the PCR reaction reaches a set threshold above the background signal. Relative expression was calculated by the ΔΔCt method and normalised to the housekeeping gene Beta-2 Microglobulin (B2M) (143).

2.4.6 RT2 PCR array

For the RT2 PCR array, 500 ug of RNA were converted into cDNA using T2 First Strand Kit (Qiagen) and the real time PCR was performed using the PAHS-065ZG-4 – RT2 Profiler PCR Array Human Oxidative Stress.

cDNA was synthesized using the RT2 First Strand Kit (Quiagen) according to the manufacturer's instructions. Genomic DNA contamination removal was performed by adding to the RNA 84µl of Buffer GE and RNase-free water up to 20 µl. The reaction was incubated at 42 °C for 5 minutes and then place on ice. 16 µl of 5x Buffer BC3, 4 µl of Control P2, 8 µl of RE3 Reverse Transcriptase Mix and 12 µl of RNase-free water were added to the reaction and incubated at 42 °C for 15 minutes, followed by a 95 °C heat treatment for 5 minutes. Finally, 182 µl of RNase-free water was added to each

reaction. The mix was placed on ice until PCR array immediately was performed.

Per sample, a qPCR reaction mix containing 1,300 µl of 2x RT2 SYBR Green Mastermix, 1,096 µl of RNase-free water and 204 µl of cDNA was prepared. Following this 10 µl of the master mix reaction was added to each well of the RT2 Profile PCR Array. Real-time reactions were performed Roche LightCycler 480 Real-Time PCR System. The qPCR reaction consisted of: an initial denaturation step at 95 oC for 5 minutes, 40 cycles of denaturation at 95 °C with annealing/extension at 60 °C for 1 minute. Four biological replicates per condition were used. The gene expression was analysed by RT2 Profiler PCR array Data Analysis using the cycle threshold (Ct) values.

2.4.7 RNA sequencing

RNA sequencing was performed during a 3-week internship at the Novo Nordisk Research Centre Oxford (NNRCO)

2.4.7.1 RNA isolation

RNA used for sequencing was isolated using the Dynabeads mRNA DIRECT Purification Kit (Thermo Fisher Scientific) according to manufacturer's instructions. This protocol is designed for a simple and rapid isolation of intact polyadenylated (polyA) mRNA by using Oligo(dT)$_{25}$ magnetic beads. Following treatment, cells were washed once with DPBS. Cells were frozen without medium at – 80 °C prior to RNA extraction. 50 µl of Lysis /Binding Buffer was added to each well of a 96-well plate. Pipetting of the solution was performed to obtain a complete lysis. Replicates from different treatments were combined in 1.5 ml tubes. DNA-shear was performed by passing the solution through a 21 gauge needle 3–5. In parallel, 50 µl of the Dynabeads solution were placed in a 1.5 ml tube and placed on a

magnet. After 30 seconds the supernatant was removed and 100 µl of Washing buffer A was added. Beads were placed on the magnet and supernatant was removed. The tube was separated from the magnet and the RNA suspension was pipetted and mixed with the beads. Lysate mix was incubated with continuous mixing for 5 minutes for hybridation. Next, tubes were placed on the magnet for 5 minutes. Beads with the RNA were washed two times with 600 µl of Washing buffer A and one time with 300 µl of Washing buffer B. Finally, the tube was placed on the magnet and supernatant was removed. 10 µl of Elution buffer was added and incubated at 70 °C for 2 minutes. Immediately after, the tube was placed on the magnet and the supernatant containing the mRNA transferred to a new RNase-free tube. Samples were stored at – 80 °C until downstream applications.

2.4.7.2 RNA integrity and quantification

RNA was quantified using the Qubit RNA HS Assay Kit (Thermo Fisher Scientific) according to manufacturer's instructions. Qubit working solution was prepared by diluting the Qubit RNA HS Reagent 1:200 in Qubit RNA HS Buffer. The final volume per reaction was 200 µl per sample. For samples, 1 µl of RNA and 199 µl of Qubit Mix were added in a 0.5 ml tube. For standards 10 µl of standard and 190 µl of Qubit Mix were added in a 0.5 ml tube. Samples and standards were mixed by vortexing for 2–3 seconds. The Qubit 3.0 Fluorometer was calibrated with the standards and samples were acquired next. The RNA concentration was calculated automatically by the Qubit 3.0 Fluorometer. RNA integrity was determined by RNA ScreenTape Assay (Agilent) according to manufacturer's instructions. 1 µl of RNA sample or RNA ladder were mixed with 5 µl of sample buffer in a 0.2 ml tube strip (Agilent). The samples were mixed using the IKA vortex at 2000 rpm for 1 min. Samples and ladder were spun and denaturalised by incubating the samples and ladder at 72 °C for 3 minutes and placing

the tubes on ice immediately for 2 minutes. Following denaturalisation, samples and ladder were placed in the Agilent 4200 TapeStation instrument. The RNA ScreenTape and tips were loaded into the TapeStation instrument and the electrophoresis was run. Only samples that have a RIN > 7 were used for subsequent analysis.

2.4.7.3 Library preparation and sequencing

Following RNA quality control, library preparation was performed using the QUANT SEQ 3' mRNA-seq Library Prep Kit FWD HT for Illumina (Lexogen) according to manufacturer's instructions. 15 ng of RNA was used to prepare the libraries.

Library generation

5 µl containing 15 ng of RNA was mixed with 5 µl of FS1 and incubated for 3 minutes at 85 °C and then cooled to 42 °C. In the meantime a master mix with 9.5 µl of FS2 and 0.5 µl of E1 per reaction was prepared, mixed and pre-warmed at 42 °C for 2-3 minutes. 10 µl of mix per reaction was added. The mix was incubated for at 42 °C for 15 minutes to generate the first cDNA strand. Remaining RNA was removed by adding 5 µl of RS and incubated at 95 °C for 10 minutes and then cooled to 25 °C. Synthesis of the second cDNA strand was performed by adding 10 µl to the mix with an incubation at 98 °C for 1 minute. After the incubation, slowly ramp down to 25 °C (0.5 °C / sec) and the mix was incubated 30 min at 25 °C. In the meantime, the master mix with 4 µl of SS2 and 1 µl of E2 per reaction was prepared. Following incubation 5 µl of the SS2/E2 mix was added into each sample and incubated at 25 °C for 15 minutes. Next step of the protocol was to purify the double stranded cDNA. To do so, 16 µl of purification beads (PB) were added, mixed well and incubated for 5 min. Samples were placed on a magnet for 2 – 5 minutes and the supernatant was discarded. 40 µl of EB was added and the mixture was removed from the magnet. Samples were mixed and incubated for 2 min at room

temperature (RT). Beads were washed twice for 30 seconds with 20 µl 80 % EtOH and air dried for 5 - 10 min. Next 20 µl EB was added into the tubes, samples were removed from the magnet, mixed well and incubated for 2 min at RT. Samples were placed on a magnet for 2 - 5 min. Finally, 17 µl of the supernatant was transferred into a fresh PCR plate.

Library amplification

Following library purification, amplification of the library was performed. A master mix was prepared by adding with 7 µl PCR and µl E3 per reaction. 8 µl of the master mix was added to the 17 µl of each purified library. 5 µl of i7 primer was added for sample identification and PCR was performed by a first incubation at 98 °C for 30 seconds followed by 20 cycles of incubation at 98 °C for 10 seconds then 65 °C for 20 and 72 °C for 30 seconds with a final step of 72 °C for 1 minute followed by a maintenance step of 10 °C. Following library amplification, a final purification step was performed to prepare samples for sequencing. For this, 30 µl of PB was added, mixed well and incubated for 5 minutes. Samples were placed on a magnet for 2 - 5 minutes, supernatant was removed and discarded. Next, 30 µl EB was added to the samples and removed from the magnet, mixed well and incubated 2 min at RT. Then, 30 µl PS was added, mixed well and incubated 5 min at RT. Mix was placed on a magnet for 2 - 5 min, and supernatant was removed and discarded. Beads were washed twice for 30 seconds with 120 µl 80 % EtOH. Beads were air dried for 5 - 10 min and 20 µl EB were added. Samples were removed from the magnet, mixed well and incubated for 2 min at RT. Finally, samples were placed on magnet for 2 - 5 min and 15 - 17 µl was transferred into a fresh PCR plate

Sequencing

Following library preparation, library size and concertation were calculated using the Qubit dsDNA HS Assay Kit (Thermo Fisher scientific) and DNA ScreenTape (Aligent) as described before. Samples were pooled in a 10 mM library for long-term storage. Library sequencing was performed using the NextSeq 500/550 High Output Kit (Illumina) on the NextSeq 500 (Illumina) according to the manufacturer's instructions. Reagents for sequencing were thawed at least 1 hour before running the sequencing, including the reagent cartridge, HT1 and the flow cell. Sample and PhiX (internal control library) libraries need to be denatured before sequencing. A 0.5 mM starting library was prepared by diluting the 10 mM stock library. Next, 40 µl of the library was mixed with 40 µl of 0.2N NaOH, vortexed the mixed and spun down. The mix was incubated at RT for 5 minutes, immediately after 40 µl of 200 mM Tris-HCL (pH 7) was added to the mix. Libraries were vortexed, spun and 880 µl of prechilled HT1 was added generating a 20 pM library. The PhiX was denatured by adding 2 µl of PhiX 10 nM, 3 µl of elution buffer and 10 µl of NaOH 0.2N. After mixing, PhiX was vortexed, spun and incubated for 5 minutes. Next, 5 µl of 200 mM Tris-HCL (pH 7) was added. Following vortex and spin, 985 µl of 200 mM Tris-HCL (pH 7) was added to generate a denatured library at 20 pM. Libraries were placed on ice until next step. The library loading concentration was prepared by adding 117 µl of the denatured library 20 pM, 1181 µl of HT1 and 2 µl of PhiX to generate a library between 2 and 2.5 pM. Library is then prepared for sequencing. The NextSeq cartridge and flow cell were placed into the NextSeq 500 sequencer and the run was stated. Cluster generation and sequencing were performed on the instrument. The instrument will use the required reagents provided in the cartridge. Following sequencing, data transfer and sequence alignment were performed by our collaborators at NNRCO.

2.5 Reagent preparation

2.5.1 Dimethyl fumarate

Dimethyl fumarate (Sigma) stock solutions of 50mM were prepared freshly for each experiment in DMSO (Sigma).

2.5.2 H_2O_2 preparation

H_2O_2 (Sigma) 30 % (w/w) (molar concentration of 9.79 mol/l) was diluted in HepatoZYME medium to obtain a final concentration of 1 mM, concentration used to induce ROS damage (144,145). A fresh solution was prepared for every experiment.

2.5.3 Paracetamol preparation

Paracetamol 2 M (Sigma) was prepared freshly for each experiment in DMSO.

2.6 Zebrafish work

2.6.1 Zebrafish lines and husbandry

Experiments were conducted in accordance with the United Kingdom Animals (Scientific Procedures) Act 1986 in a United Kingdom Home Office-approved establishment. Zebrafish (Danio rerio) were maintained at 28.5 °C, as previously described by Westerfield (Westerfield, 2007). Established lines used were WIK and Tg(-2.8 lfabp:GFP)), where GFP is green fluorescent protein (146,147). All experiments were terminated at day 5 days post-fertilization (d.p.f.).

2.6.2 Zebrafish chemical exposure

The wild-type WIK line was used for paracetamol-induced toxicity and dimethyl fumarate dosage. Unless otherwise stated, larvae were maintained at 28.5 °C in 50 ml conditioned water (CW), treatments

were carried out for 48 h (3–5 d.p.f.). Single Tg(-2.8lfabp:GFP)) Zebrafish larvae per well were positioned into a black V-shape 96-well plate for 48 h (3–5 days postfertilization (dpf)). At day 5, total fluorescence was measured using a fluorescence plate reader (ex/em 485 /520).

2.6.3 Zebrafish high throughput live imaging

Single larvae were oriented into a 96-well plate with 150 µl agar (0.75%, wt/vol) containing 84 mg/l MS-222. An orientation tool was 3D printed. Briefly, 0.75%, wt/vol agar was added into the 96-well plate following the positioning of the orientation tool. Once the agar was set, removal of the orientation tool creating an agar V shape where the larvae could be positioned. Imaging was performed using the operetta microscope, and image analysis was performed using Colomus software where supervised machine learning was used for automatic fish and liver recognition and analysis.

2.6.4 Orientation tool for zebrafish imaging 3D printing

3D printing of the orientation tool was done following the available files from Wittbrodt et al (148). Base plate and columns pins were printed by 'CNCvac 3D Printing' in generic Standard ABS using 100 µM layers to ensure high quality finish.

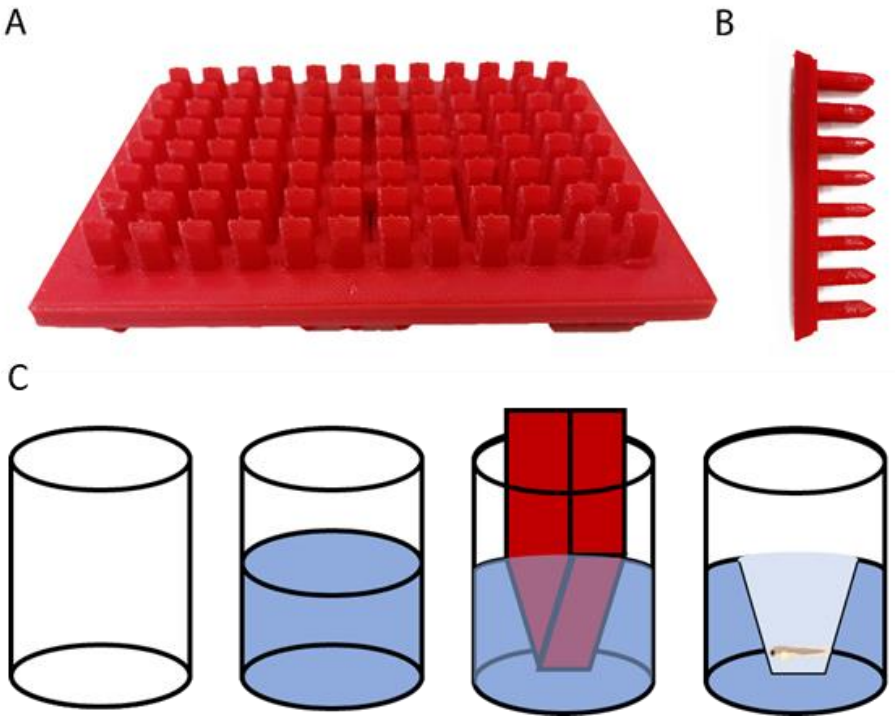

Figure 10. 3D designs of the orientation tool for zebrafish positioning. (**A**) 3D printed orientation tool to facilitate the zebrafish orientation. Pins are inserted in a 96-well-plate embedded with agarose 0.75% wt/vol. (**B**) Pin shape creates a 'V' shape that allows the zebrafish positioning. (**C**) Schematic representation of the agarose mold. First, 150 µl of agarose 0.75% wt/vol was added into a well of a 96-well plate. The orientation tool was positioned inside the 96-well plate while the agarose was not solidified. Upon solidification, the orientiation tool was removed creating a 'V' shaped incision where Zebrafish were positioned.

2.6.5 Zebrafish plate reader fluorescence quantification

Total fluorescence was detected using a fluorescence plate reader was used to detect changes in GFP signal. Paracetamol 10mM for 48 hours was used to quantify fluorescence decrease upon liver damage. Single larvae were introduced into a well of a black 96-well plate after treatment for fluorescence quantification. Wild type larvae were used to subtract larvae autofluorescence.

2.7 Bioinformatic analysis

Data formatting from the screening was performed using Python programming language. Following data organisation, analysis was performed by a combination of Spotfire and HC StratomineR software. Single cell imaging analysis for the Nrf2 nuclear translocation quantification was performed using Spotfire software. Data analysis from the Cell Pain assay was performed using Python. RNA-seq analysis was performed in R using with the DEseq2 packages. Details of each analysis are described throughout the thesis.

2.8 Statistical analysis

One-way ANOVA test and post-hoc Tukey multiple-comparison test was used for experiments that contained more than two groups. All data is represented as means with SEM. Statistical analysis was performed using GraphPad Prism software.

CHAPTER THREE

SEMI-AUTOMATED DIFFERENTIATION OF HUMAN STEM CELL-DERIVED HEPATOCYTES

3.1 Introduction

3.1.1 Current cell-based methods to study liver biology

Current cell-based models to study liver biology rely heavily on immortalized cell lines or primary cells. Despite their advantages, immortalized cell lines offer limited biological relevance when compared to the intact organ. Primary human hepatocytes (PHHs) are currently viewed as the gold standard to study liver biology (149). The disadvantages of their use include: their labour-intensive isolation from diseased organs, the scarcity of donor tissue, the rapid loss of cell phenotype in culture and significant batch-to-batch variation. Therefore, more stable, reproducible and cost-effective models that recapitulate liver physiology are required. Human pluripotent stem cell (hPSC) have been proposed as an alternative cell source to study liver biology. Advances in pluripotent stem cell differentiation protocols better mimic primary cells than the immortalised lines (65). In addition, hPSC-derived models exhibit drug sensitivity patterns similar to primary cells (150).

3.1.1.1 Human pluripotent stem cells

Human pluripotent stem cells are capable of self-renewal and retain pluripotency. Their ability to differentiate into any cell in the body render them a powerful tool to study human biology, model disease, high reproducibility and on defined genetic background.

hPSCs can be derived from early-stage embryos called human embryonic stem cells (hESC) (73) or induced pluripotent stem cells (iPSC), produced from somatic cells by overexpressing key transcription factors: Oct 3/4, Sox2, Klf4 and c-Myc (74). iPSCs have been produced in many different ways (for a review, see (151)).

hESC cell lines are derived from the inner cell mass (ICM) of grade B blastocysts not suitable for implantation (73). Current protocols allow the generation of hESC from blastomeres without affecting the development of the embryo. This process can be performed under the current good manufacturing practice (cGMP) conditions providing translational promise for the clinic (152). iPSC technology created a new tool for personalised medicine for both research and clinical applications. However, detailed analysis of the reprogramming process for iPSC generation showed an epigenetic memory in iPSCs when compared to ESCs (153) rising some issues about the quality of iPSCs. On the whole, both systems are powerful tools for research and medicine.

In the last decade, hPSCs have been successfully used for disease modelling, drug screening and cell therapy studies. Current clinical trials using hPSC as a treatment include: dry age-related macular degeneration (154), Parkinson's disease (155), Amyotrophic Lateral Sclerosis (ALS) (156) and ischemic heart disease (157) among others (158).

Under culture, hPSC colonies display packed cell colonies with marked edges, cells have a distinct nucleoli and high nuclei to cytoplasm ratio. In addition, hPSCs express a range of proteins markers, which include transcription factors such as OCT4 (75), NANOG (76) and SOX2 (77); Cell surface markers like tumour rejection antigens TRA-1-60 and TRA-1-81 and stage-specific embryonic antigen 3 (SSEA3) and 4 (SSEA4). SSEA1 can be used as a negative marker. in humans SSEA1 is expressed in some myeloid cells and tumours but not in undifferentiated hPSC (159,160). To assess the pluripotency capacity of hPSC, hPSC can be differentiated into the three germ layers *in vivo* by teratoma formation or *in vitro* embryoid bodies. Teratoma formation is considered the gold standard for demonstrating pluripotency on hPSC. Transplanting hPSC to immunodeficient mice leads into tumour

development of all three germ layers (72). Teratoma formation varies from 4 to 15 weeks and methods to assess are not fully standardised (161). Teratoma formation is a great tool to test pluripotency in newly produced hPSC lines but not a technique suitable for regular pluripotency confirmation of established hPSC lines. *In vitro* generation of embryoid bodies allows the spontaneous differentiation into the three germ layers. This process takes under 4 weeks (162). EBs formation can be used routinely as a tool for pluripotency confirmation of well-characterised hPSC lines.

3.1.1.2 Hepatocyte differentiation from hPSC

The self-renewal and pluripotency properties of hPSC creates a potentially unlimited source of hepatocytes to study liver biology. Several groups have established differentiation protocols that allow the efficient differentiation of human pluripotent stem cells (ES and iPSC) into hepatocyte-like cells (HLCs) (78). Hepatocyte differentiation attempts to recreate aspects of human liver development using growth factors and small molecules. Our approach has three key stages. First, hPSC are driven to definitive endoderm by using several growth factors such as activin A and Wnt3A. At definitive endoderm, cells display triangular morphology and by the expression of SOX17 and FOXA2. Definitive endoderm is followed by hepatic progenitors specification or hepatoblasts. Hepatoblasts are characterised by a distinct cobblestone-like morphology and expression of several markers which include hepatocyte nuclear factor 4 α (HNF4α), alpha fetoprotein (AFP) and cytokeratin 19 (CK19). Finally, hepatoblasts are matured into HLCs. They express hepatocyte markers such as HNF4a, albumin and cytochrome P450 proteins and exhibit metabolic function, protein secretion, glycogen storage and urea synthesis. However, current HLCs protocol do face some limitations, such as the mixture of foetal and adult hepatocyte traits and limited tissue structure (90). Work in the

last decade has been focused on improving phenotype, standardisation and large-scale production.

3.1.2 Semi-Automation of the HLCs differentiation protocol

Standardisation of somatic cell differentiation protocols are required to develop robust tools that accurately model human biology in the dish. Traditional cell culture techniques rely heavily on manual pipetting, which is both time consuming and error prone. This limits the throughput of the assay and the plate format one can work with. To date, most studies describing the generation of HLCs are labour intensive in nature and therefore small scale in size. Recent advances in liquid handling and pipetting systems have made possible the high throughput production of HLCs in multi-well plates (96- or 384- well plates) with reduced well-to-well and plate-to-plate variation (89). In combination with automated microscopy and high throughput analysis, it is possible to develop automated procedures which minimize the requirement for human intervention. This allows the user to create multi-parametric profile data sets to profile changes in human liver biology and model disease (67).

Platform assessment was performed in collaboration with AstraZeneca; a training compound library was employed to validate platform sensitivity and specificity to detect hepatotoxic compounds. First, a 96-well plate screen was performed and high throughput analysis was performed. After data analysis, results were validated in collaboration with AstraZeneca. Finally, a 384-well plate screen was performed for platform comparison.

3.1.3 Cell segmentation and high content analysis

Automated microscopy and high content analysis are powerful tools when combined with high throughput culture of HLCs. Automated microscopy allows an unbiased and reproducible image acquisition and analysis. Image-based cell profiling, uses these image-datasets to extract several morphological features per image creating a morphological profile, these profiles can be used to distinguish different cell traits (163). The image analysis begins with cell segmentation, which consists of set algorithms that will automatically identify the cells in the image. This is done by grouping pixels from one channel to distinguish cells from the background. A common procedure for cell segmentation is to first identify the nuclei, followed by cytoplasm identification. Next, a quality control of the segmentation based to discard incorrectly segmented cells can be performed (**Figure 11**).

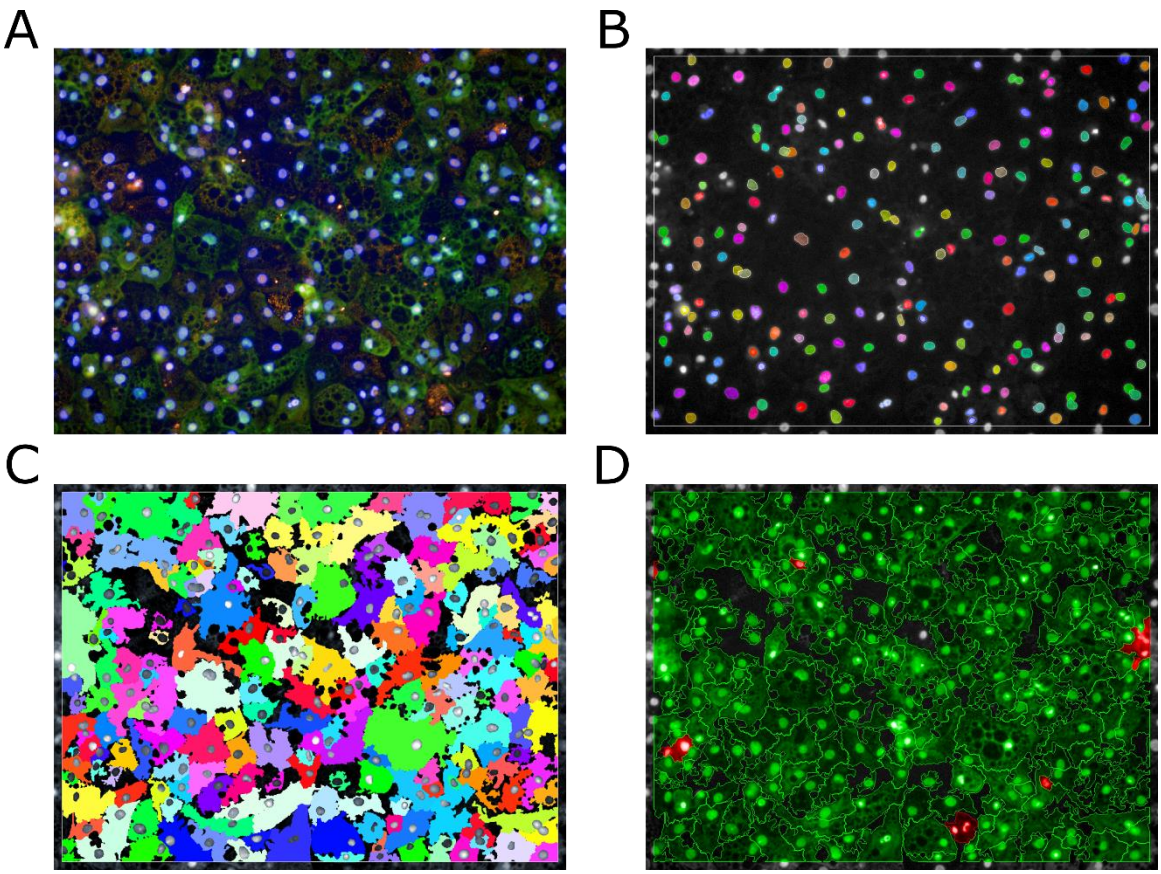

Figure 11. Cell Segmentation overview. (**A**) Raw image used for cell segmentation, the DAPI channel is used to automatically detect nuclei (**B**). Next, nuclei previously identified are used for cytoplasm detection (**C**). Finally, different features are used to perform a quality control to discard incorrectly segmented cells (**D**). Image consists of three channels: DAPI (Blue): stains nuclei; Cell Mask (Green): unspecific cytoplasmic stain, used for cytoplasmic recognition and protein of interest (orange) to quantify.

Following cell segmentation, images are prepared for feature extraction. Several morphological features per channel and cell are extracted, which can be divided into the following:

Shape features - features such as roundness and area can be quantified for the whole cell, nuclei, cytoplasm and any other different segmented parts.

Intensity- Intensity from each channel at the different regions of the cells is quantified.

Texture- texture features are quantified by mathematical functions measuring changes in pixel distribution and intensity structure of a region (e.g. nuclei or cytoplasm) to find patters e.g. spots, holes or edges (**Figure 12**).

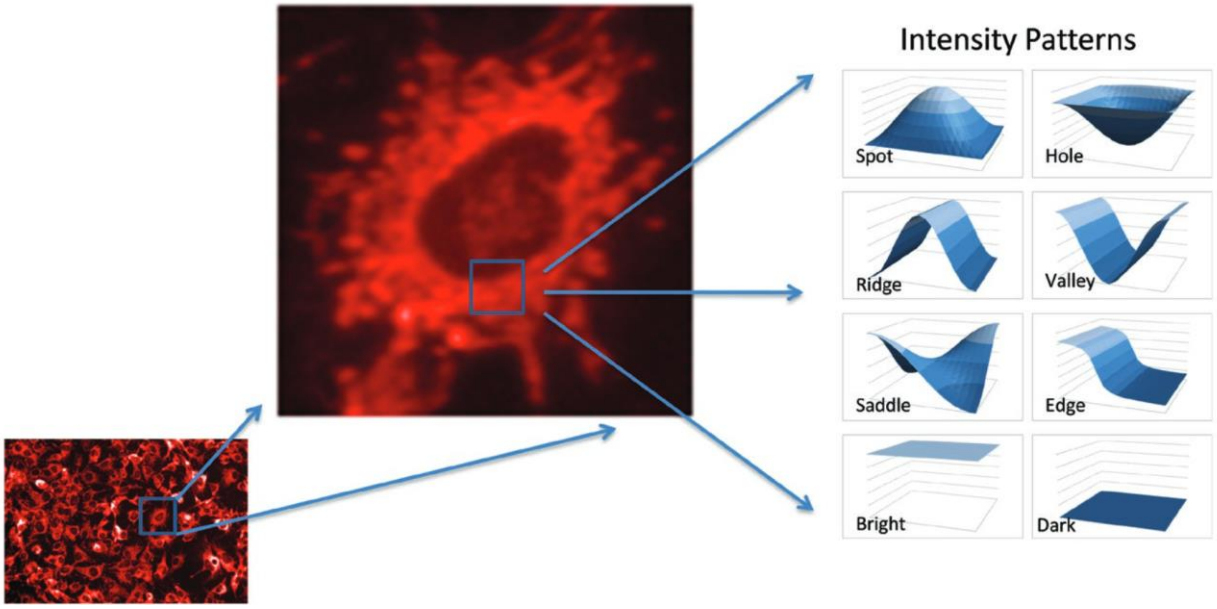

Figure 12. Texture features. Example of the 'SER Features' (Saddles, Edges, Ridges) generated on the Harmony software. Image obtained from PerkinElmer.

3.1.4 Multiparametric dataset analysis

High content analysis generates large multiparametric datasets. Without the correct pre-processing or tools for analysis, large multiparametric data sets can be underutilised. However, by using suitable data mining tools, it is possible to combine multiparametric data sets and distil the valuable information for downstream applications. A recent review summarises some of the best strategies for image acquisition, data processing and analysis to create high-quality image-based profiles (163). These pipelines have been successfully applied to drug screening (164) and morphological profiling of gene function (165). Multiple tools have been developed in recent years for standardised and unbiased analysis. Those include

CellProfiler (166), Ilastik (167) or Columbus (PerkinElmer) for image analysis and feature extraction and HC StratomineR (168), Spotfire (TIBCO), CellHTS2 (169) for data mining.

For my studies I used a combination of Python programming codes and commercially available software. Python was used for data preparation prior to analysis; software used was TIBCO Spotfire Data Visualisation and Analytics Software and HC StratoMineR (168). TIBCO Spotfire was used for data visualisation and annotation; HC StratoMineR is an easy-to-use data mining tool which follows the best practices as described in (163) for large multiparametric datasets analysis. I used Spotfire for quick visualisations of large data sets to assess plate-to-plate variations as well as for data annotation. HC StratoMineR allowed an in-depth data mining analysis. Thanks to a web-based tool it can be used with non-workstation computers. In addition, it is easy-to-use and its interactivity makes this a perfect tool for non-specialised users as no previous coding experience is required to perform the analysis.

3.2 Results

3.2.1 Characterisation of human embryonic stem cells

Current cell culture technologies allow standardised and reproducible hPSC culture. This is achieved by using defined matrices and media. Examination of hPSC culture includes morphological validation, expression of pluripotent markers and cell surface markers. Assessment of pluripotency was carried out by developing the PSC into the three germ layers (endoderm, mesoderm and ectoderm) and is determined by embryoid body (EB) formation into the three germ layers.

For my studies, a female human ESC line H9 was used. Cell culture was performed using a commercial matrix (laminin 521) and commercial maintenance medium (cGMP-mTeSR1). Spontaneous differentiation was minimised by regular passaging. Cell colonies were formed by packed colonies with marked edges. Cells displayed a distinct nucleoli and high nuclei to cytoplasm ratio (**Figure 13**). H9 expressed pluripotent markers Nanog and Oct4 as shown by immunocytochemistry (**Figure 14**). Pluripotent markers were also checked by cell surface protein expression using flow cytometry. H9 expressed SSEA-4 and TRA-1-60 and displayed a negative expression for SSEA1(**Figure 15**). Finally, embryonic body formation was performed to test the pluripotent capacity of the hESC. Results show that H9 can differentiate into the three germ layers (**Figure 16**).

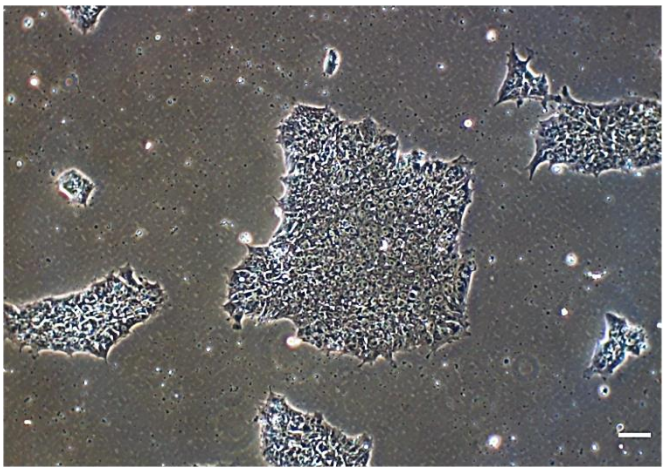

Figure 13. hPSC morphology in culture. Representative images of Human PSC, hPSC were cultured using mTseR1 medium and laminin 521. (A) hESC line H9 passage 42 and a hiPSC line, P106 passage 36 (B), Scale bar 100 µm.

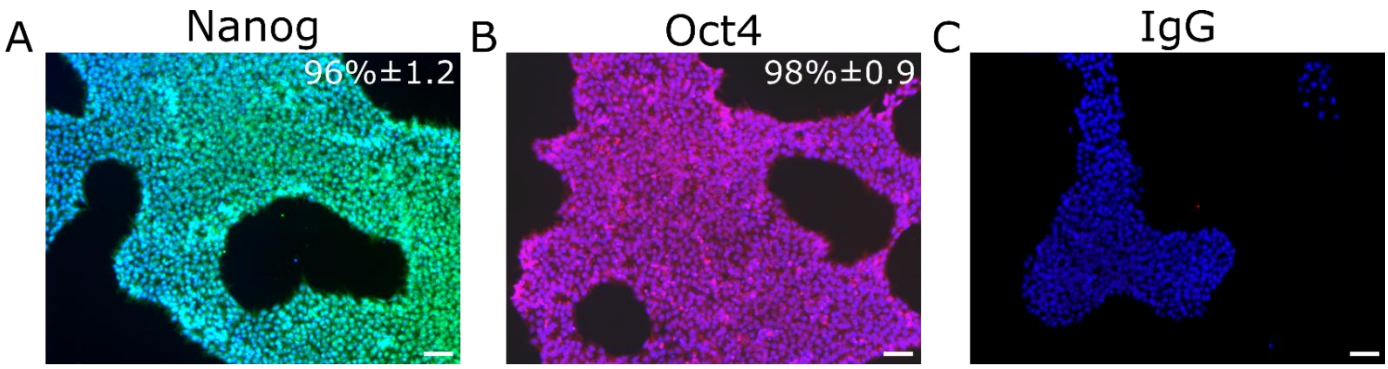

Figure 14. Pluripotent marker expression in PSC. Pluripotent markers were detected by immunofluorescence in both hESC (H9) and hiPSC (P106). Nanog (green) and Octamer 4 (Oct4) (red) were expressed at 96% (**A**) and 98% (**B**) in H9 and 97% (**D – E**) in P106, Immunoglobulin G was used as a negative control (**E, F**). The percentage is the average of three experiments. Images were taken at 10x magnification. Nuclei were stained with DAPI (blue) for cell detection. Scale bar = 100µm. The data represents six biological replicates +/- SEM.

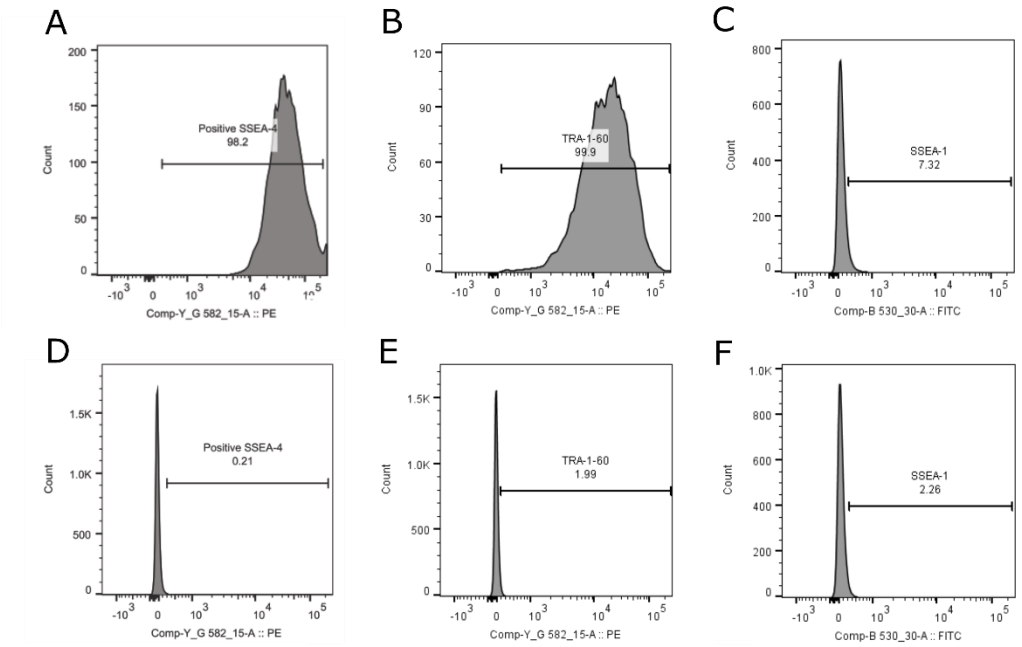

Figure 15. H9 express cell surface markers of pluripotency detected by flow cytometry. Flow cytometry analysis was performed to assess pluripotent marker expression in H9. H9 expressed the pluripotent markers (**A**) SSEA-4 and (**B**) TRA-1-60, H9 were negative for a marker of cell differentiation (**C**) SSEA1. (**D-F**) IgG controls were used for antibody specificity. Figure shows a representative sample distribution. n=3 biological replicates.

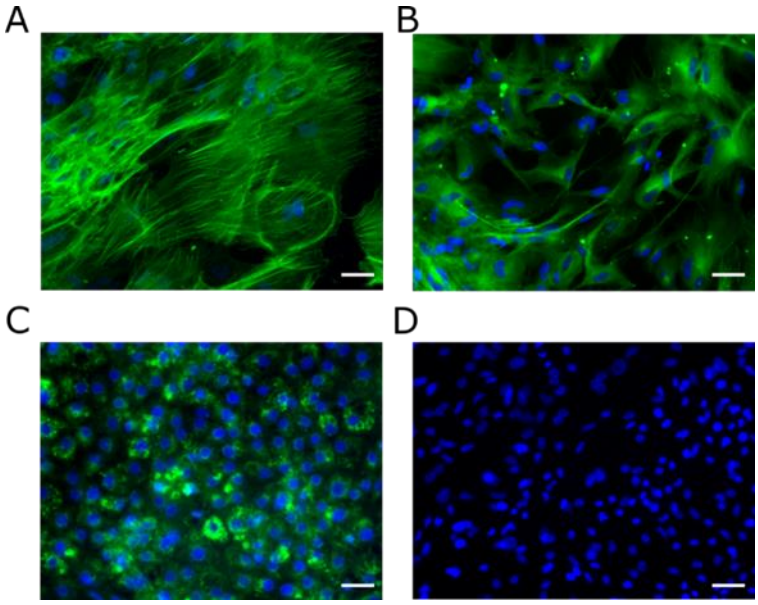

Figure 16. Characterisation of embryoid body pluripotency by immunostaining. Pluripotency markers were detected by immunostaining, (**A**) mesoderm cell lineage was detected by a-SMA (green), (**B**) ectoderm lineage by β-Tubulin (green) expression and (**C**) endoderm lineage by AFP staining (green). (**D**) IgG control was used for staining specificity. Nuclei were stained with DAPI (blue) for cell detection. Scale bar = 100 µm.

3.2.2 Differentiation of hPSC-derived hepatocyte like cells

For hepatic differentiation, I used a defined and serum-free protocol that drives human hepatocyte differentiation in the dish (**Figure 17**) (87,89). Single hPSCs seeded into laminin-521 coated plates at 50,000 cells/cm^2 and cultured with mTseR1. 24 h after seeding and once the right confluency was reached differentiation was started (**Figure 18**). H9 were primed into definitive endoderm using Wnt3a and Activin A for three days with daily media change. Following this, hepatoblast specification was achieved by culturing the definitive endoderm with media supplemented with DMSO and Knock-Out Serum Replacement (KOSR) for an extra five days with media change every other day. Finally, hepatocyte-like cells maturation was obtained by culturing hepatoblast with medium containing oncostatin M (OSM) and hepatocyte growth factor (HGF) for ten days with medium change every other day. Assessment of cell differentiation was examined by change in morphology, protein expression and cell function at the different stages of the differentiation process.

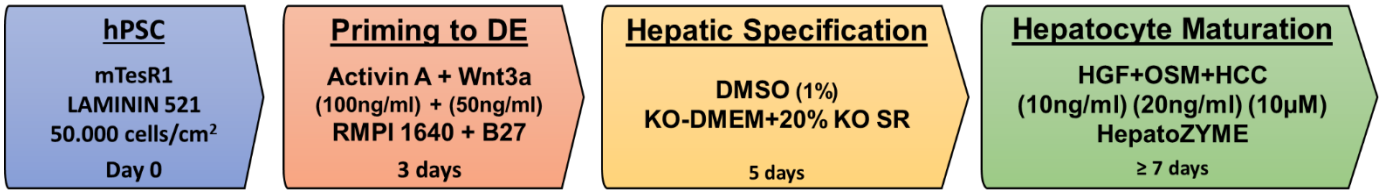

Figure 17. Diagram of the hepatocyte-like cell differentiation protocol. Three stage differentiation protocol from single cell seeding hPSC (Day 0) to definitive endoderm (Day 3), hepatoblast specification (Day 8) and hepatocyte maturation (Day 18). Abbreviations: hPSCs = human pluripotent stem cells; RPMI = Roswell Park Memorial Institute (RPMI) 1640 medium; B27 = B27 medium supplement: DMSO = dimethyl sulfoxide; KOSR = knockout serum replacement; KO-DMEM = knockout Dulbecco's Modified Eagle's Medium; HGF = hepatocyte growth factor; OSM = oncostatin M; HCC = hydrocortisone.

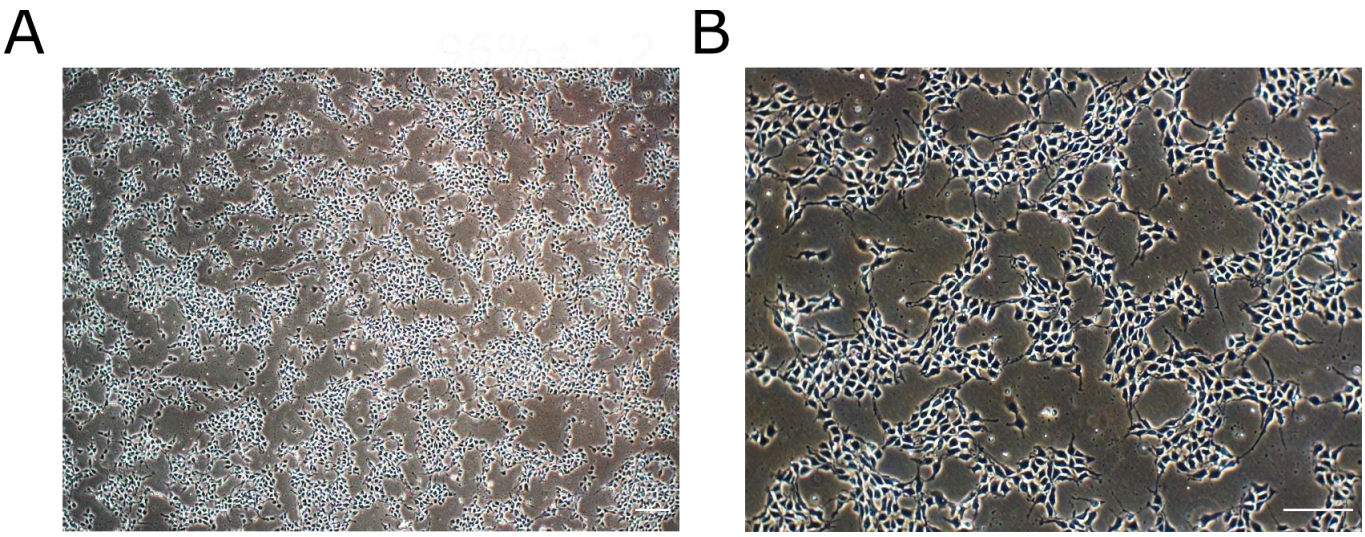

Figure 18. Representative confluency for HLCs differentiation. PSC cell confluency after 24h single cell seeding, cell confluency should be around 30 – 40% prior to differentiation. Images were taken at 10x (**A**) and 20X (**B**) magnification. Scale bar = 100µm.

3.2.2.1 hPSC differentiation to definitive endoderm

24 h after seeding and when hPSC cell confluency reached 30-40% differentiation was started. This was deemed optimal for H9 (66). Differentiation was started by replacing the medium with definitive endoderm differentiation medium supplemented with Wnt3a and Activin A. After 72 h hPSC lines acquired triangular shape (**Figure 19**), induction of definitive endoderm markers Sox17 and FoxA2 was confirmed by immunofluorescence (**Figure 20**). H9 hESCs expressed Sox17 at 92.8% and FoxA2 at 90%.

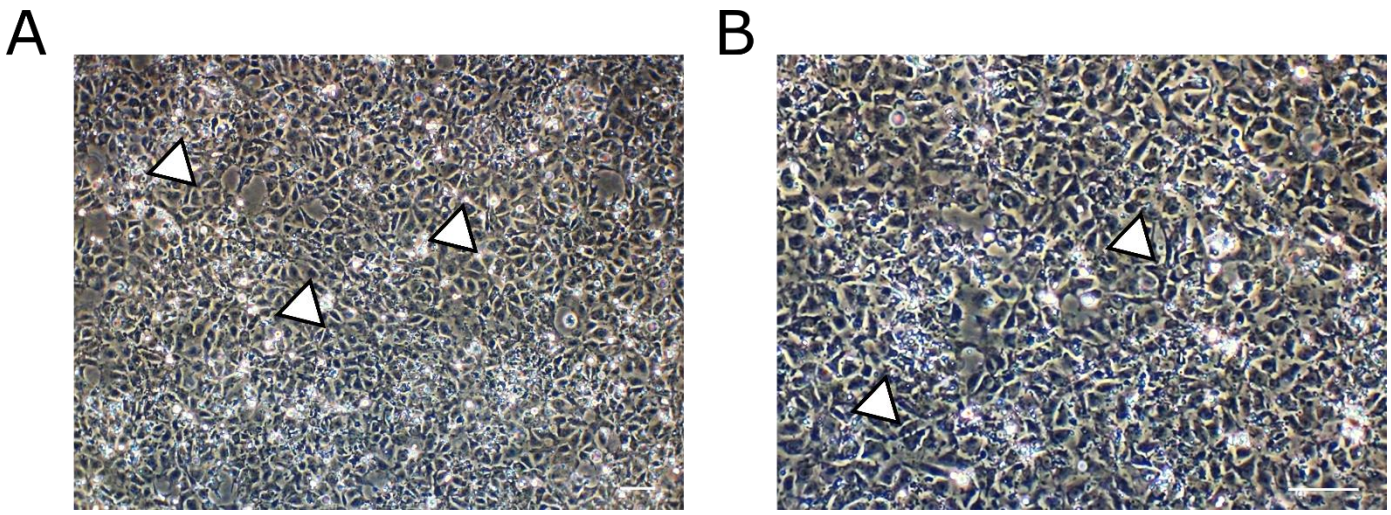

Figure 19. Definitive endoderm morphological characterisation. After 72 hours of definitive endoderm induction, a monolayer is formed and cells display a distinct triangular shape as marked by the arrows. Images were taken at 10x (**A**) and 20X (**B**) magnification. Scale bar = 100µm.

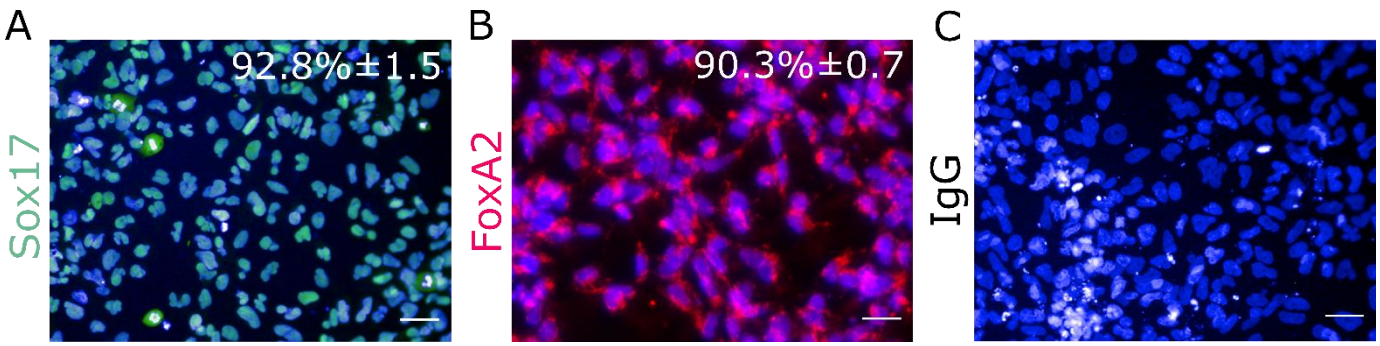

Figure 20. Definitive endoderm immunofluorescence characterisation. Cells at after 72 hours of definitive endoderm induction were fixed and stained for definitive endoderm markers (**A**) Sox17 in green and (**B**) FoxA2 in red. (**C) IgG** controls for antibody specificity staining. Nuclei were stained with DAPI for cell detection. Scale bar = 50µm. The data represents three biological replicates +/- SEM.

3.2.2.2 Hepatic progenitor specification from hPSC

Following definitive endoderm, hepatic progenitors were induced by culturing the cells with KO-DMEM supplemented with 1% DMSO and 20% KOSR for 5 days. Cells acquired hepatoblast morphology by the formation of cobblestone-like cells with well-defined cell-to-cell edges (**Figure 20**). A panel of protein markers was used to assess hepatoblast differentiation efficiency by immunofluorescence. AFP, HNF4α and CK19 expression were expressed ubiquitously (**Figure 22**).

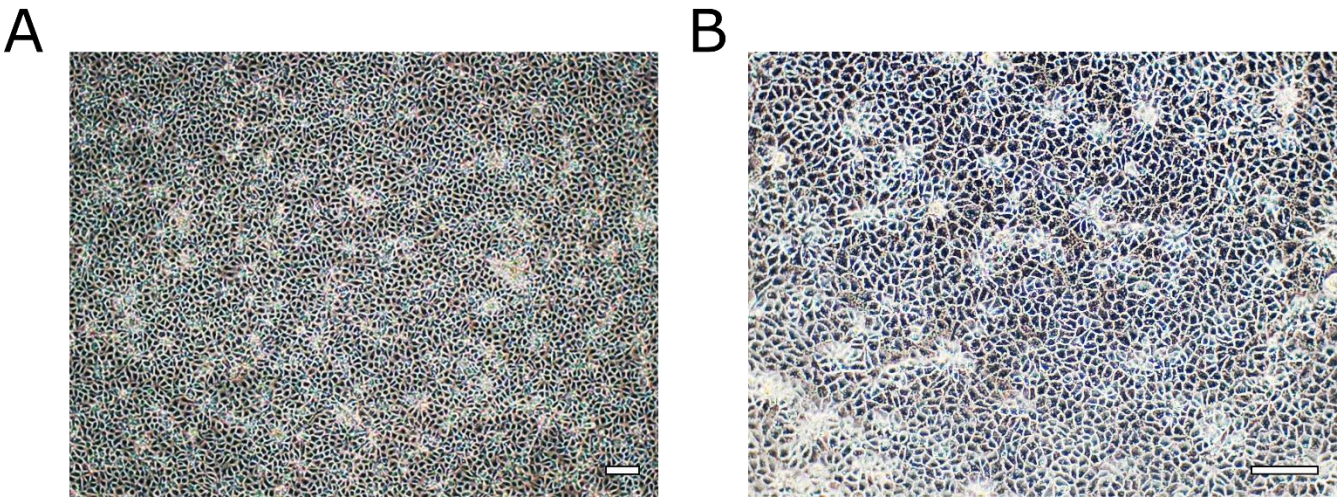

Figure 21. Hepatoblast morphological characterisation. After five days of hepatoblast differentiation, day nine of differentiation. hepatoblast display cobblestone-like morphology with marked cell-to-cell edges. Phase contrast Images were taken at 10x (**A**) and 20X (**B**) magnification. Scale bar = 100µm.

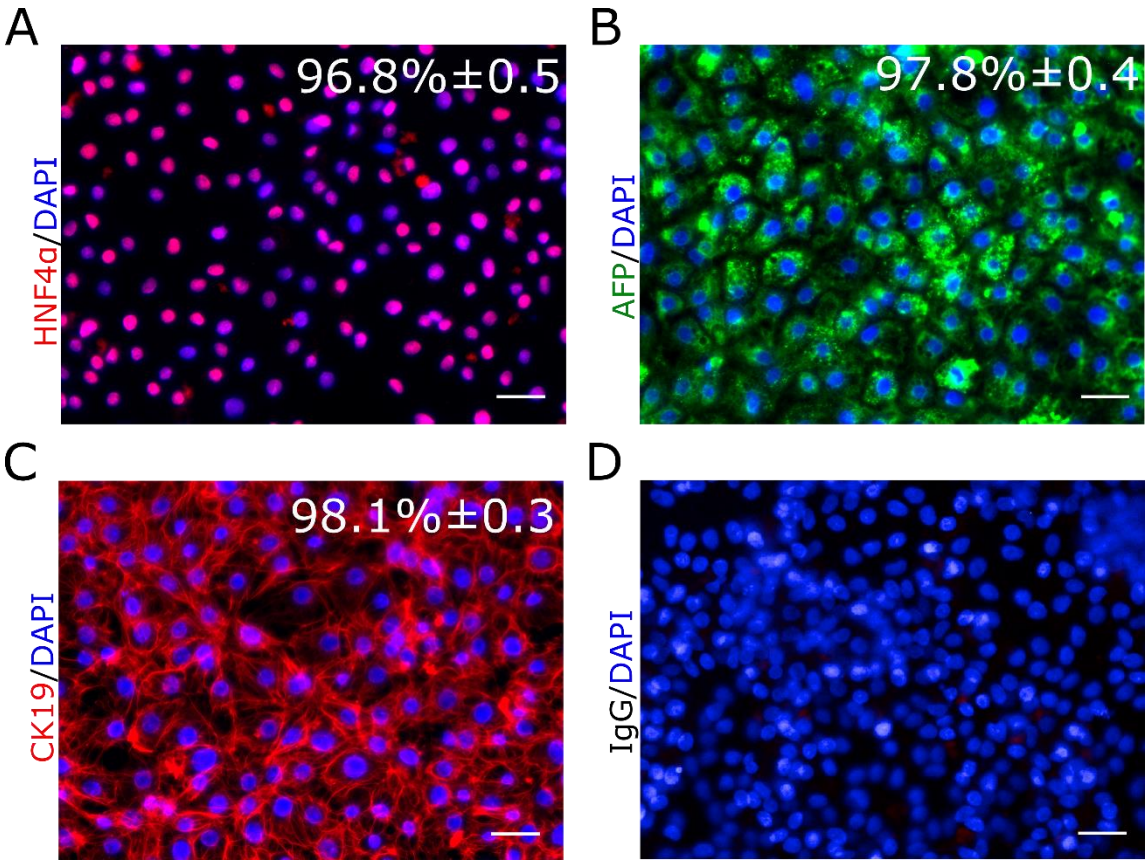

Figure 22. Hepatoblast markers characterisation. Hepatoblast markers were detected by immunofluorescence. HNF4α in red (**A**), AFP in green (**B**) and CK19 in red (**C**). IgG was used as negative control (**D**). Nuclear staining was used for cell identification (Blue). Abbreviations: HNF4α: Hepatocyte nuclear factor 4 α, AFP: Alpha fetoprotein and CK19: Cytokeratin 19. Scale bar = 50µm. The data represents three biological replicates +/- SEM, >300 cells counted per replicate.

3.2.2.3 Hepatocyte-like cells maturation

Finally, hepatoblasts were matured into hepatocyte-like cells, this process requires an extra ten days in culture. Hepatoblast were cultured with HepatoZYME medium supplemented with hepatocyte growth factor (HGF) and oncostatin M (OSM). At day 18, HLCs resemble some of the key features of hepatocytes. HLCs derived from H9 exhibit polygonal-shape and defined cell-to-cell contact. At day 18, HLCs were fixed and stained for typical hepatocyte markers (**Figure 24 A-G**) and tested for CYP P450 activity. HLCs expressed hepatocyte markers such as HNF4α (89.2% ±2 positive cells), ALB (92.8% ±6 positive cells), AFP (61.8% ±2 positive cells). HLCs also expressed CYP P450 proteins, CYP 2D6 and CYP 3A4 as well as MRP1, a drug transporters protein (**Figure 24**).

HLCs also displayed a distinct polygonal appearance as shown by E-Cadherin protein expression and phase contrast. CYP 1A2 and CYP 3A4 basal activity for H9 was measured at day 18. H9 exhibited CYP 1A2 activity at 295,906 ±45,828 RLU/mL/mg of protein and CYP 3A at 1,066,112 ±177,416 RLU/mL/mg of protein (**Figure 25**).

In addition, specific CYP P450 metabolic activity was determined by Bristol-Myers Squibb (BMS) compound incubation. Each of the BMS compounds are metabolised into toxic metabolites by a specific CYP P450 protein. Toxic metabolite generation can be correlated into CYP P450 activity (170). Therefore, ATP depletion is an indirect measure of CYP P450 activity. Hepato-sensitivity was detected on BMS compounds 1, 4 and 5 which relate to CYP 2C19, CYP 2C9 and CYP 2D6 activity respectively (**Figure 26**).

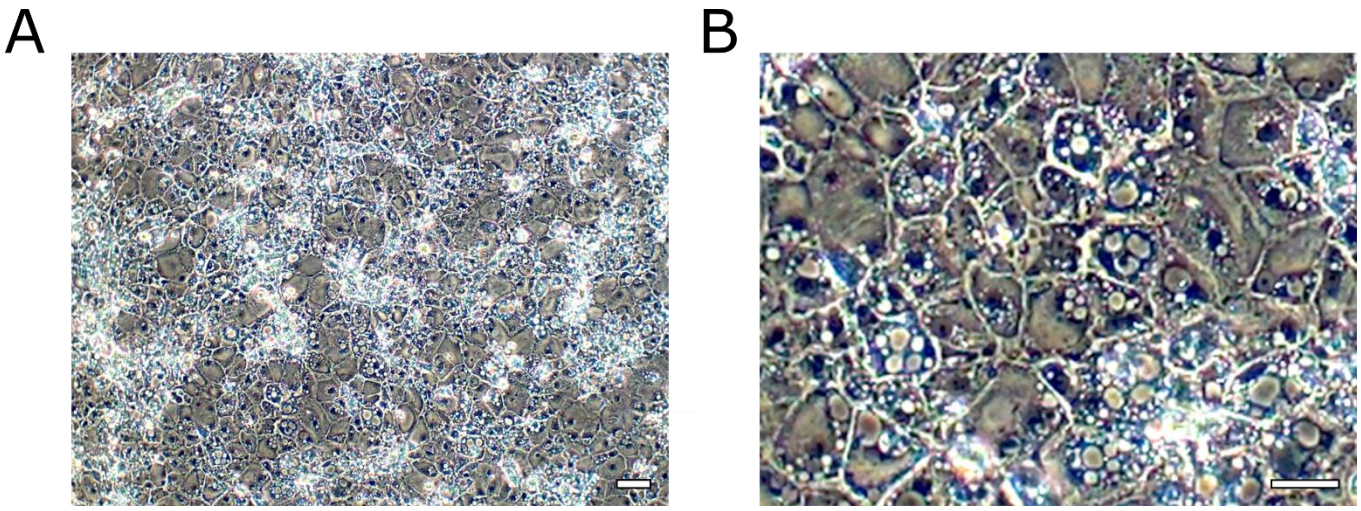

Figure 23. Morphological characterisation of HLCs. Images of HLCs at day 18, cells displayed a distinct polygonal appearance with marked cell-to-cell contact. Images were taken at 10X (**A**) and 20X (**B**). Scale bar 50µm.

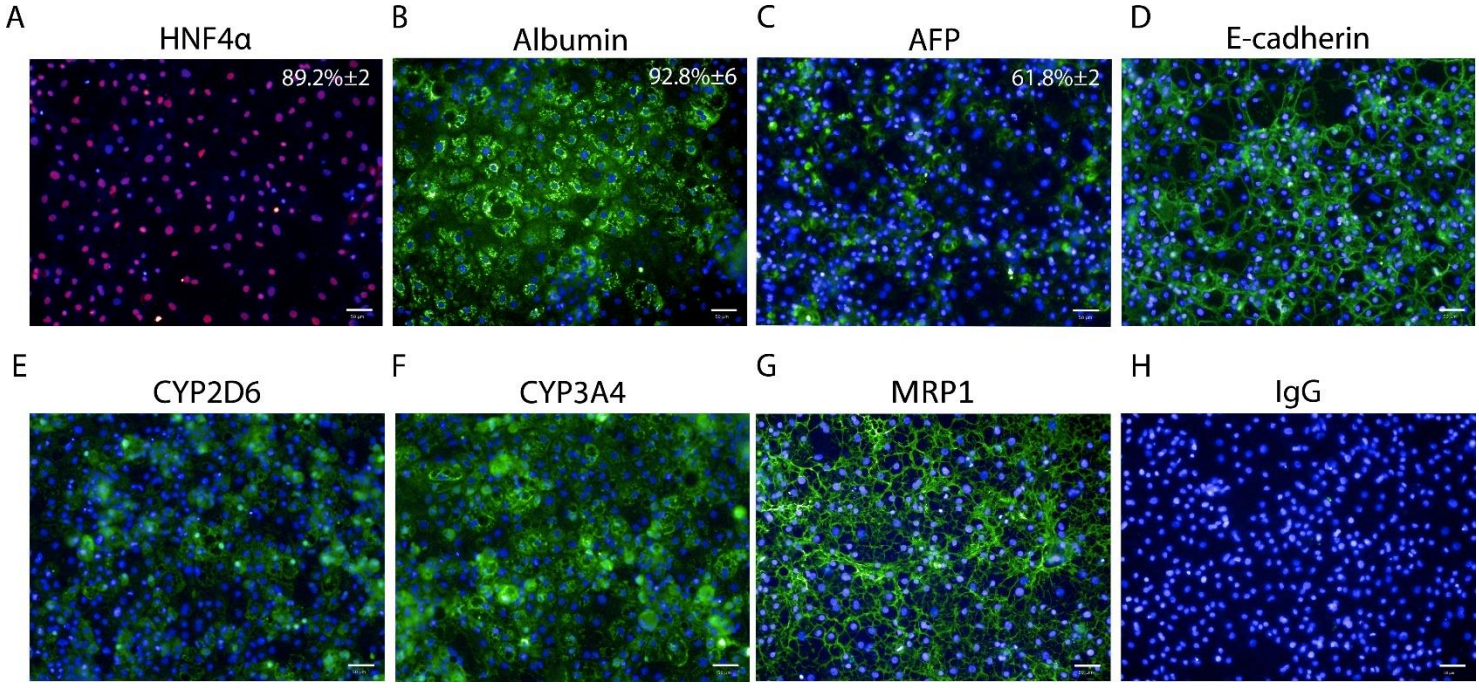

Figure 24. H9 derived hepatocyte-like cells marker expression at day 18. (A) The percentage of hepatocyte nuclear factor 4 alpha (HNF4α) expression ± SEM is based on thirty wells with ten fields of view per well. **(B)** The percentage of albumin (ALB) expression +/- SEM, is based on 3 separate wells with ten fields of view per well. **(C)** The percentage of alpha fetoprotein (AFP) +/- SEM is based on 3 separate wells with ten fields of view per well. **(D)** E-cadherin staining. **(E)** CYP2D6 staining. **(F)** CYP3A4 staining. **(G)**. Multidrug resistance-associated protein 1 (MRP1) **(H)** Immunoglobulin G (IgG) staining control. Scale bar = 50 µm. The data represents six biological replicates +/- SEM.

.

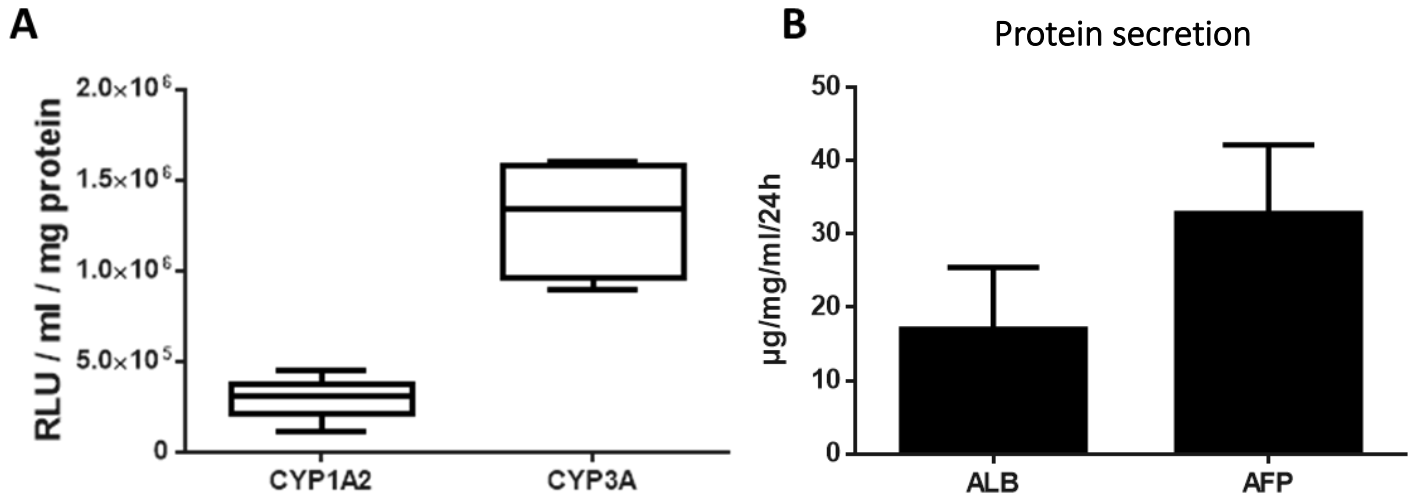

Figure 25. Metabolic activity characterisation of HLCs. (**A**) Basal CYP P450 activity of HLCs at day 18, CYP 3A and CYP 1A2 activity were measured. Activity is quoted as relative light units (RLUs)/mL per 1 mg of protein. (**B**) Albumin and AFP protein secretion was quantified by ELISA. Protein secretion produced during 24 h was quantified by µg of protein secreted/ml per 1 mg of protein. Box plots represents six biological replicates +/- SEM.

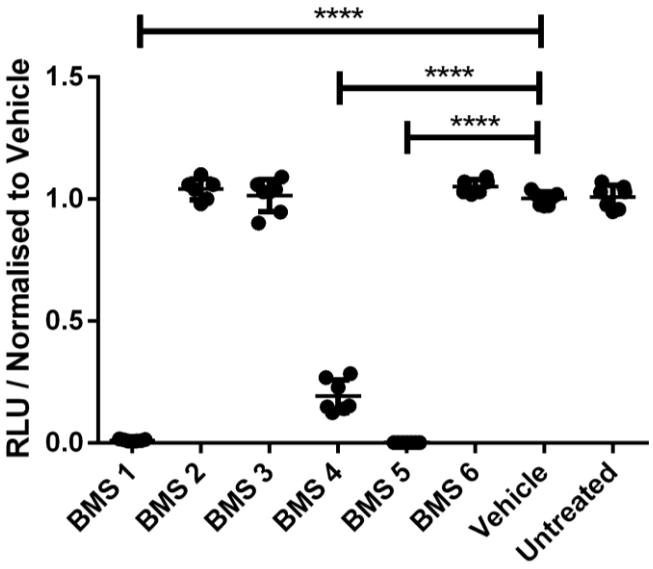

Figure 26. HLCs ATP depletion after BMS compounds exposure. HLCs differentiated from H9 (**A**) and P106 (**B**) at day 18 were incubated with BMS compounds for 48 hours. Following incubation, ATP was quantified. ATP levels are represented as relative light units (RLUs) normalised to the vehicle. Dot plot represents six biological replicates +/- SEM, p <0.0001.

3.2.3 Semi-automated differentiation of HLCs from hPSC

The ability to generate large quantities of multi-well plates for screening or for basic research has been limited by labour intensive procedures and batch-to-batch variation. To tackle this issue, I have developed a semi-automated high throughput platform to differentiate pluripotent stem cells into HLCs (**Figure 27**). Stem cell seeding and HLCs differentiation were performed using liquid handling and automatic pipetting systems in 96-well and 384-well plate format. Following the differentiation, a high throughput pipeline was developed for sample processing and analysis. For sample processing, liquid handling systems and automatic plate washer were used. Cell phenotype was analysed using automated microscopy and a multi-well luminometer.

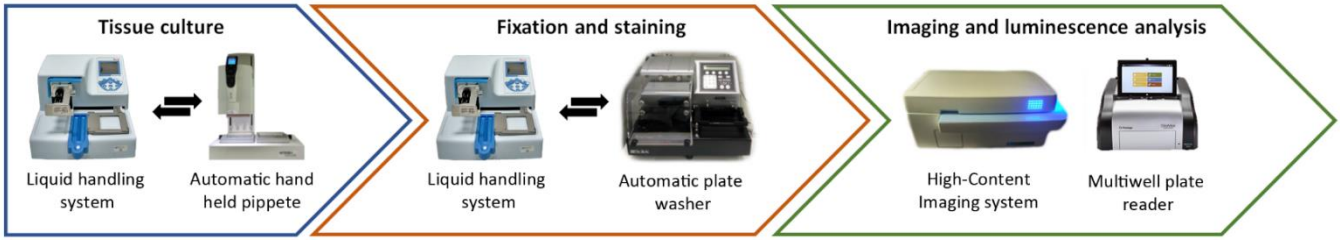

Figure 27. Schematic representation of the semi-automated high throughput platform. For tissue culture, a combination of a liquid handling system (Multidrop – ThermoFisher) and an automatic hand held pipette (ViaFlo - Integra) were used. For sample processing, the multidrop and an automatic plate washer (BioTek405) were used. Sample analysis was performed using a high content imaging system (Operetta - Perkinelmer) and a multi well plate reader (GloMax Explorer – Promega).

3.2.3.1 Tissue culture of HLCs using liquid handling systems

hPSC single cell suspension was dispensed using the Multidrop liquid handling system. Cell number per well was 50,000 cells/cm^2. Once cell confluency reached 30-40% differentiation was started. Medium changes were performed using automatic handheld pipette (ViaFlo). On day 18, the variability in HLCs number between wells was examined following DAPI staining, seven fields of view were captured per well and the number of nuclei quantified with no statistical differences between wells. Cell number was 41,662 ±3,366 cells per well for the 96-well plate format (**Figure 28**) and 16,290 ± 236 cells per well for 384-well plate (**Figure 29**).

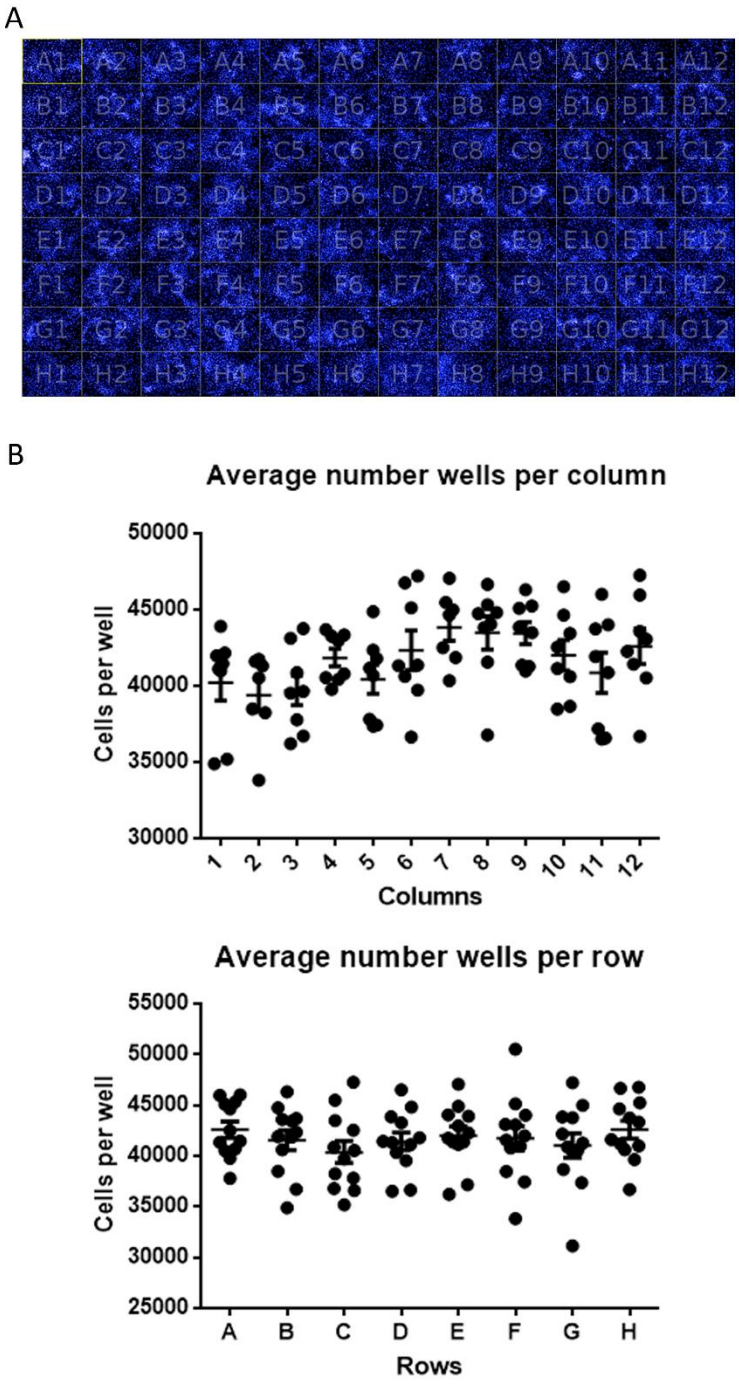

Figure 28. Assessment of HLCs well-to-well variability in 96-well format. (**A**) Representation of a 96-well plate view of HLCs stained with DAPI. Scale bar = 1 mm. **(B**) Quantification of cell number per well. Average of cell number per wells in columns (top) and rows (bottom), from seven fields of viewsper well and quantified using Columbus software. Average cell number across the plate is 41,662 ± 3,366 SEM cells per well. No statistically significant differences were observed between wells. A One-way ANOVA with Tukey's post-hoc statistical tests was employed.

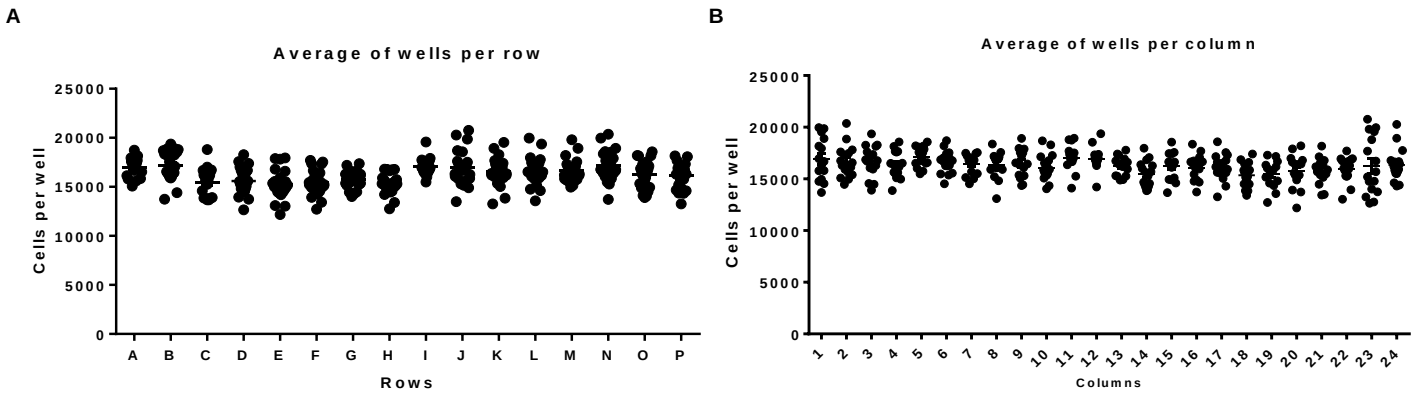

Figure 29. Assessment of HLCs well-to-well variability in 384-well format. Quantification of cell number per well. Average of cell number per wells in (**A**) columns and (**B**) rows from seven fields of views per well and quantified using Columbus software. Average cell number across the plate is 16,290 ± 236 cells per well. No statistically significant differences were observed between wells. A One-way ANOVA with Tukey's post-hoc statistical tests was employed.

3.2.4 Validation of the platform

In collaboration with AstraZeneca, a training compound library was employed to validate the drug sensitivity and specificity of the semi-automated differentiation system (**Table 9**). Screens were performed in both 96 and 384-well plate format using H9-derived HLCs. For the 96-well format, a total of 88 compounds were tested in the range of 0.002μM, 0.02μM, 0.2μM, 2μM, 20 μM, 200 μM in triplicate plates. 48h following compound incubation, assay performance was assessed. 200 μM as the highest concentration was selected to keep DMSO concentration below 1%. Higher DMSO concentration would increase the effect of the toxic compounds as it can induce cell toxicity (171).

Sensitivity of the screen was determined by the efficiency of the HLCs produced from this platform to detect correctly hepatotoxic compounds from the training library. In addition, sensitivity was determined by the ability of the platform to metabolise non-toxic compounds without causing toxicity.

To quantify the effect of the compounds into the cells, a combination of commercial assays were used to measure cell viability: ATP depletion (CellTiter-Glo®, Promega) and CYP3A metabolic activity (CellTiter-Glo®, Promega) were used. Parallel plates were used for high content imaging. Cells were stained for mitochondria, cytoplasm and nuclei following a modified version of the cell painting assay (141). After staining, plates for Cell Paint were imaged using the Operetta high-throughput microscope and ~90 features were extracted using Columbus image analysis software. Combination of the three different assays created a multiparametric data set. Data mining was performed to detect hits. Following this, sensitivity and sensitivity of the platform was determined in collaboration with AstraZeneca.

In the 384-well plate screen a concentration range of 17.5 µM, 25 µM, 35 µM, 50 µM, 70 µM, 100 µM, 140 µM, 180 µM, 200 µM was used with four replicates per plate. 72h following compound high content imaging assay was performed. Changes in the design of the screen were made following AstraZeneca feedback from the 96-well plate screen.

Drug Name	AZ Number	FDA toxicity
Lapatinib	AZ10402704	vMost-DILI-Concern
Pravastatin	AZ10154396	vLess-DILI-Concern
Nevirapine	AZ12307889	vMost-DILI-Concern
Flutamide	AZ10003185	vMost-DILI-Concern
Propylthiouracil	AZ10006157	vMost-DILI-Concern
Sulindac	AZ10173856	vMost-DILI-Concern
Pargyline	AZ10065948	N/A
Phenytoin	AZ10246255	vMost-DILI-Concern
Clotrimazole	AZ10235889	vLess-DILI-Concern
Ketoconazole	AZ12014276	vMost-DILI-Concern
Zafirlukast	AZ10027291	vMost-DILI-Concern
Furosemide	AZ10130507	Ambiguous DILI-concern
Coumarin	AZ10246257	N/A
Tacrine	AZ10050561	N/A
nomifensine	AZ10154702	vMost-DILI-Concern
alendronate	AZ10001115	vLess-DILI-Concern
Carbamazepine	AZ10089511	vMost-DILI-Concern
Naproxen	AZ10222853	vLess-DILI-Concern
Propranolol	AZ10015679	N/A
Meclizine	AZ10611097	vNo-DILI-Concern
Clofibrate	AZ10007325	vLess-DILI-Concern
epinephrine	AZ10453071	vNo-DILI-Concern
leflunomide	AZ10042615	vMost-DILI-Concern
Amiodarone	AZ10131427	vMost-DILI-Concern
Tamoxifen	AZ10009015	vMost-DILI-Concern
Erythromycin	AZ12201437	vMost-DILI-Concern
Felbamate	AZ10130800	vMost-DILI-Concern
Chlorpromazine	AZ10000853	vLess-DILI-Concern
Fenofibrate	AZ10116192	vLess-DILI-Concern
Fluoxetine	AZ10166761	vLess-DILI-Concern
Labetalol	AZ10337779	vMost-DILI-Concern
Ibuprofen	AZ10005713	vLess-DILI-Concern
Acetylsalicylic acid	AZ10015436	N/A
isoproterenol	AZ10064045	vNo-DILI-Concern
Imipramine	AZ10120857	vLess-DILI-Concern
Zileuton	AZ10757796	vMost-DILI-Concern
Stavudine	AZ10129833	vMost-DILI-Concern
Perhexilene	AZ10466355	vMost-DILI-Concern
Methotrexate	AZ10403554	vMost-DILI-Concern
Piroxicam	AZ10133063	vLess-DILI-Concern
cromoglicic acid (cromolyn)	AZ10005214	N/A
streptomycin	AZ12121615	vNo-DILI-Concern

Drug Name	AZ Number	FDA toxicity
Pioglitazone	AZ10080838	vLess-DILI-Concern
betaine	AZ10003728	vNo-DILI-Concern
Nitrofurantoin	AZ10430483	vMost-DILI-Concern
Dexamethasone	AZ10168612	Ambiguous DILI-concern
haloperidol	AZ10047978	vLess-DILI-Concern
Benzbromarone	AZ10132264	vMost-DILI-Concern
Diclofenac	AZ10194317	vMost-DILI-Concern
Mercaptopurine	AZ10184621	vMost-DILI-Concern
Methyldopa	AZ10712845	vMost-DILI-Concern
folic acid	AZ10013790	vNo-DILI-Concern
Busulfan	AZ10072216	vMost-DILI-Concern
Disulfiram	AZ10001511	vMost-DILI-Concern
Troglitazone	AZ10308701	vMost-DILI-Concern
Ticlopidine	AZ10025601	vMost-DILI-Concern
Iproniazid	AZ10013584	vMost-DILI-Concern
Buspirone	AZ10047343	Ambiguous DILI-concern
Clozapine	AZ10030042	vMost-DILI-Concern
Colchicine	AZ12064467	Ambiguous DILI-concern
Diphenhydramine	AZ10009895	vNo-DILI-Concern
Simvastatin	AZ10410259	vLess-DILI-Concern
Dantrolene	AZ11874538	vMost-DILI-Concern
Ximelagatran	AZ11942255	vMost-DILI-Concern
Indomethacin	AZ10003646	vMost-DILI-Concern
Isoniazid	AZ10012730	vMost-DILI-Concern
Acetaminophen	AZ10009025	vMost-DILI-Concern
Nefazodone	AZ10150878	vMost-DILI-Concern
sunitinib	AZ11755299	vMost-DILI-Concern
BOSENTAN	-	vMost-DILI-Concern
Donepezil	AZ10087366	vLess-DILI-Concern
Tienilic acid/Ticrynafen	AZ10256496	N/A
Procyclidine	AZ10620821	vNo-DILI-Concern
Metformin	AZ10046538	vLess-DILI-Concern
Nimesulide	AZ10491890	vMost-DILI-Concern
Alpidem	AZ11636409	vMost-DILI-Concern
Fluconazole	AZ10456348	vMost-DILI-Concern
Dacarbazine	AZ10523577	vMost-DILI-Concern
Oxybutynin	AZ10491901	vNo-DILI-Concern
MACITENTAN	-	vNo-DILI-Concern
DMSO	-	Negative control
20UM APAP	-	Positive control
200UM APAP	-	Positive control

Table 9. Astrazeneca compound library. Library of known hepatotoxic compounds to assess specificity and sensitivity of the semi-automated HLCs culture. Clinical and experimental concern to develop DILI was used for compound classification as shown on the FDA toxicity comlumn. N/A = no data available. APAP = Acetaminophen. DMSO= Dimethyl sulfoxide.

3.2.4.1 High content analysis

High content analysis was performed using the cell painting assay. HLCs were stained with NucBlue for the nuclei, Cell Mask green for the cytoplasm and Mitotracker for the mitochondrial activity (**Figure 30A**). After imaging, image analysis was performed using the Colombus image analysis software. Prior to cell segmentation, an extra quality control step was implemented to only analyse in-focused areas. The cell segmentation algorithm is not trained to distinguish from in-focused to out-focused areas (**Figure 31A**). This can lead to incorrect segmentation and feature extractions from out-of-focus regions which can lead to inaccurate results. To reduce this, a supervised machine learning package from Colombus image analysis software was used. This package can train an algorithm to distinguish in-focused from out-of-focused cells by using the texture features from these regions (**Figure 12**, **Figure 31B**). This creates a region of interest which only contains in-focus cells which are used for cell segmentation (**Figure 31C-D**). Following the quality control, cell segmentation was performed. ~90 morphological features such as fluorescence intensity, size, morphology or pixel texture were extracted.

These features were combined to create a cell profile, which can be used to distinguish between toxic and non-toxic compounds. Effects of compounds can be visualised on **Figure 30B**, a representation of a 96-well of the screen, where a rectangle represents a well with Cell Paint staining. It is possible to visualise intensity variation between wells which can be quantified by high throughput analysis. A correlation matrix of all the features was created to visualise the correlation between the features used to create the cell profile (**Figure 30C**).

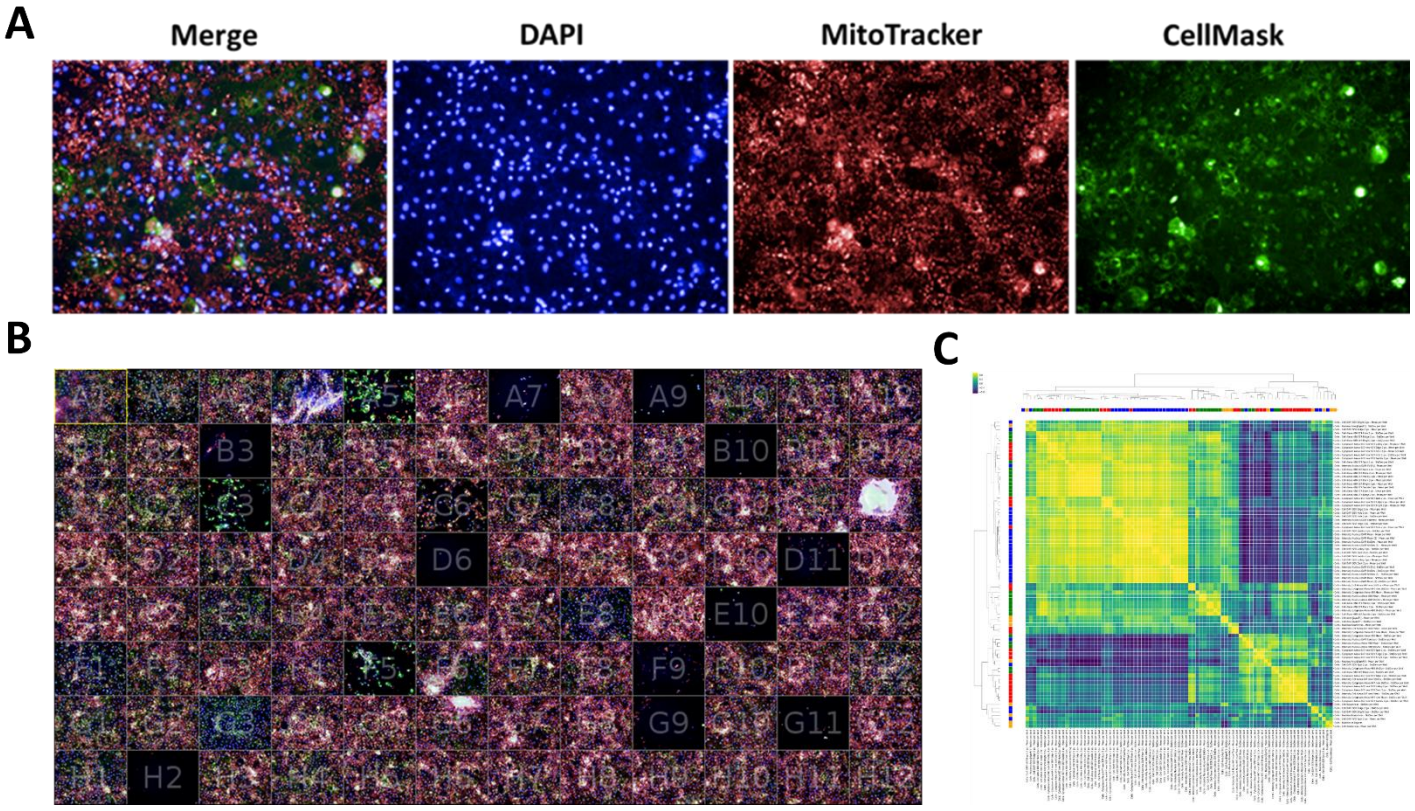

Figure 30. Cell Painting staining in HLCs. (**A**) HLCs were stained for nuclei (NucBlue), cytoplasm (Cell Mask green) and mitochondria (Mitotracker deep red). (**B**) Representation of a 96-well plate from the AstraZeneca compound screen at the higher concentration (200 µM). **C.** Correlation matrix of the 89 different features extracted from each image.

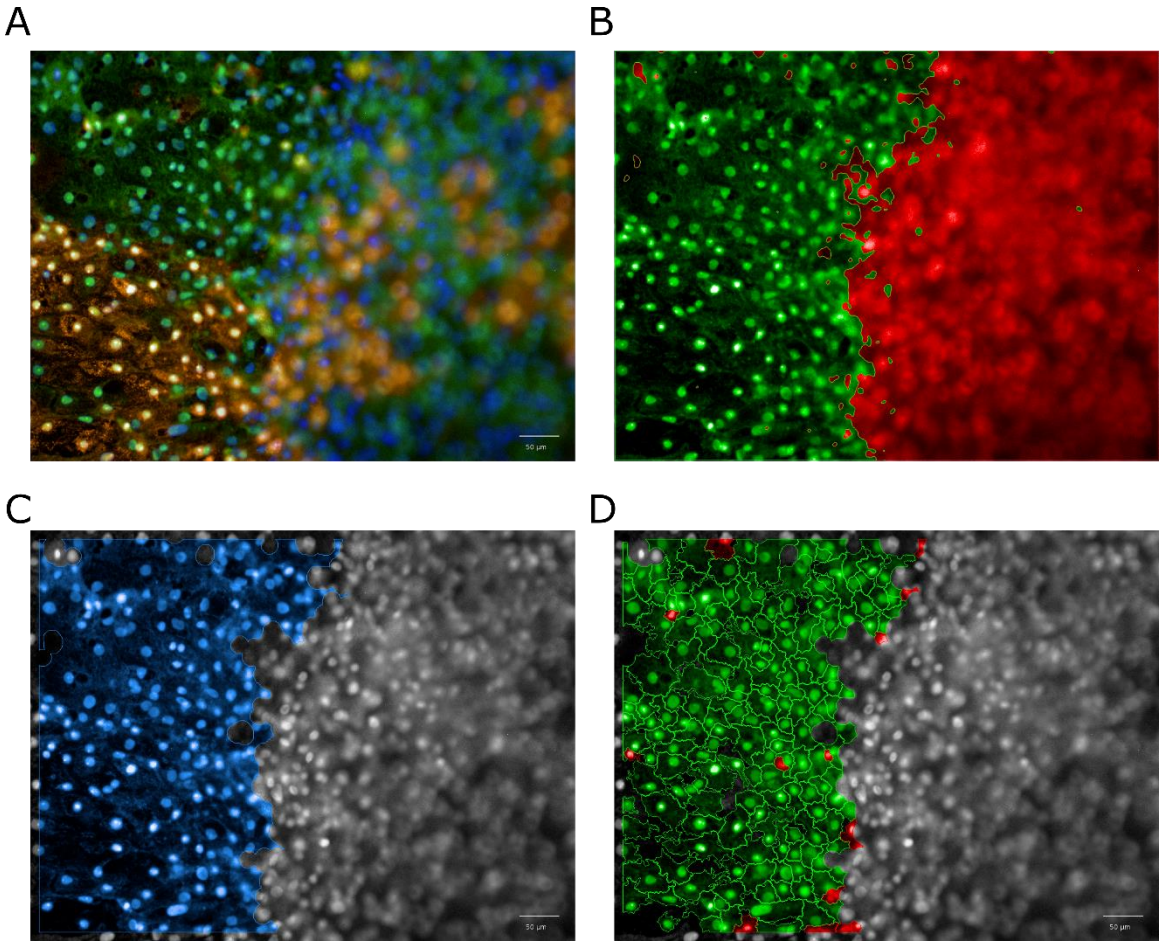

Figure 31. Supervised machine learning for cell segmentation. Following imaging, some areas of the well can be out of focus (**A**) leading to incorrect feature extraction. (**B**) A supervised machine learning algorithm was trained to distinguish between in-focused and out-of-focus cells based on image texture properties. (**C**) Areas with cells correctly focused are selected for subsequent (**D**) quality control and cell segmentation analysis.

3.2.4.2 Multiparametric data analysis

Data annotation and visualisation

Following data acquisition from the 96-well plate screen the different data sets (ATP quantification data, CYP 3A metabolic activity and the Cell Paint data) were combined creating a multiparametric data set for each drug at the different concentrations. Each data set was obtained from multiple sources with different file formatting and spatial data distribution. Data conversion was required to standardise the different file formats in order to combine them into one unique file. To solve this,

I developed a Python programming code which allowed me to standardise formats and combine the different data sets into one unique file; as well as adding important metadata required for data mining such as well location or plate number.

Following data combination, TIBCO Spotfire software was used for data visualisation and compound annotation. Spotfire allows a rapid and interactive visualisation of the combined data. Plate-to-plate visualisation using heatmaps allows the annotation of compounds, plate triplicates and compound concentrations (**Figure 32**). Spotfire can be used for data normalisation and analysis. This is be done by manually coding the functions for normalisation for each feature. Due to the large quantity of features, this software does not allow an efficient and interactive analysis.

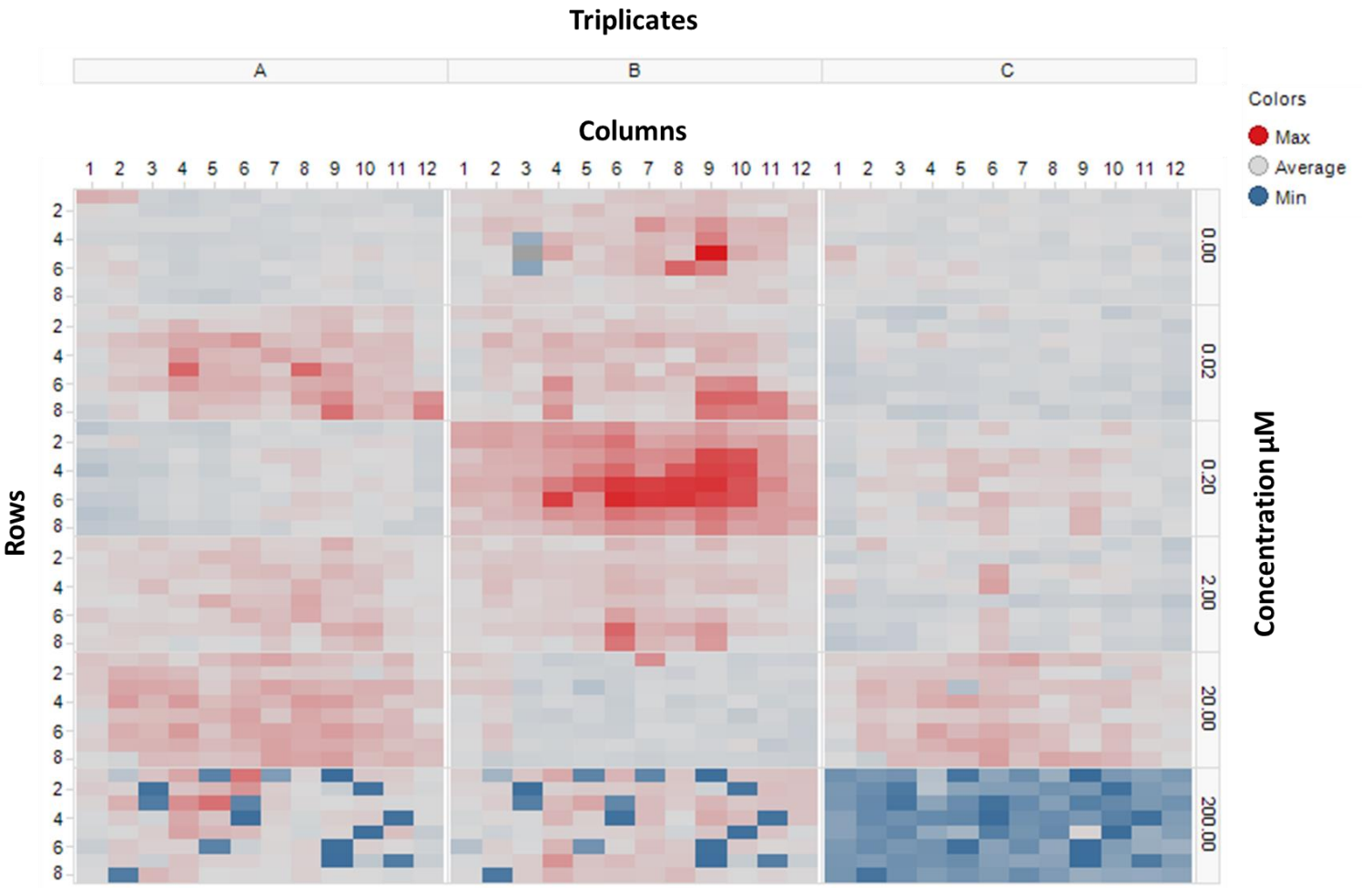

Figure 32. Representation of the screen data in a heatmap. Heat map representing the number of nuclei per well in triplicates in an increasing concentration. Each square of the heatmap represents a well of a 96-well plate. Triplicate plates are represented on the X-axis. The different concentrations were plotted on the Y-axis at increasing concentrations.

Data normalisation

Data analysis was performed using HC StratoMineR. This software provides a web-based easy-to-use pipeline for data mining. Per plate, each parameter was normalised by the median value of the negative control (**Figure 33**). Performing consistent normalisation using the median of the negative control in a plate-to-plate basis, plate effects can be normalised, allowing plates to be compared for analysis.

Data transformation

For subsequent analysis of multiparametric data sets, each parameter should approximate a normal distribution to reduce underrepresentation of the data (29,33). Mathematical functions can be applied to transform features with non-normal distribution to approximate them into a normal distribution. For this reason, HC StratoMineR has a step for data transformation. In this step, the distribution of each feature is automatically checked. If the software detects a feature which does not have normal distribution, it will suggest several mathematical functions to transform and approximate the data into normal distribution (**Figure 34**).

Data standardisation

Following data transformation, data standardisation is recommended to avoid a bias toward a parameter that has a larger range. Min-Max scalation was performed for each parameter at a screen level distribution (**Figure 35**).

A

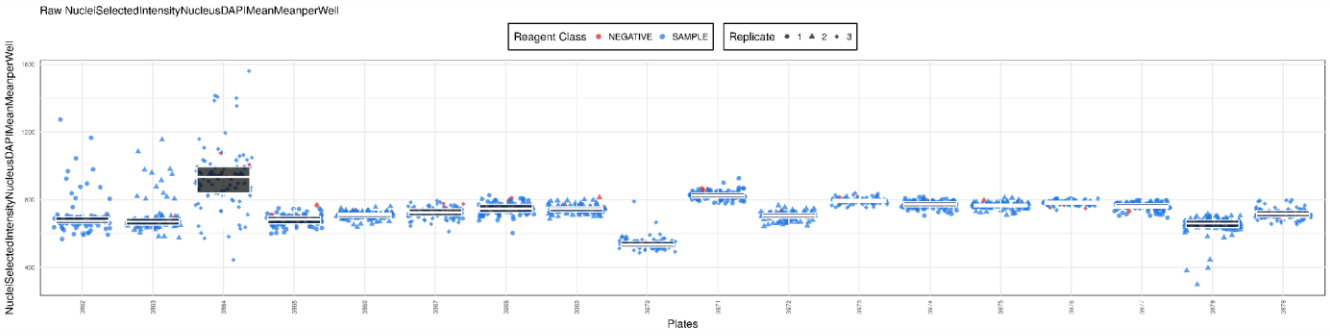

B

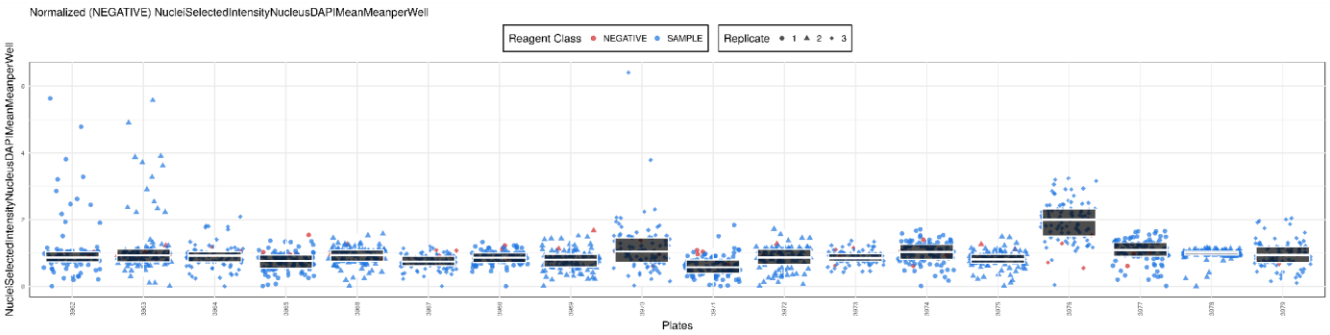

Figure 33. Data normalisation. Dapi nuclei intensity data plotted per plate in a box plot, each column represents a plate, dots represent the wells, shape of the dots represents the replicate and the colour the reagent classes. (**A**) Dapi nuclei intensity raw data. (**B**) Box plot of Dapi nuclei intensity where data has been normalised by the mean value of the negative controls in a plate-to-plate basis.

Data reduction

Following data normalisation, transformation and standardisation, the data set is prepared for analysis. Data reduction is performed to reduce the complexity of the multiparametric data set. Common factor analysis (CFA) is performed based in a correlation matrix (**Figure 36A**). Number of factors was determined automatically by the Kaiser's method to avoid bias in number of factors (**Figure 36B**). Eight factors were created and each factor was visualised in a polar plot, which indicates the loadings for each parameter in the generation of the factors for data reduction. In each plot, the angles display the different parameters, and the radius represents the factor loading of the parameter (**Figure 37**). The effect of the data reduction can be visualised when comparing the signature from plotting all the parameters across the wells (**Figure 38A**) versus the factors from the data reduction across the wells (**Figure 38B**). The sample variability is maintained after the data reduction from the eight factors generated during the data reduction.

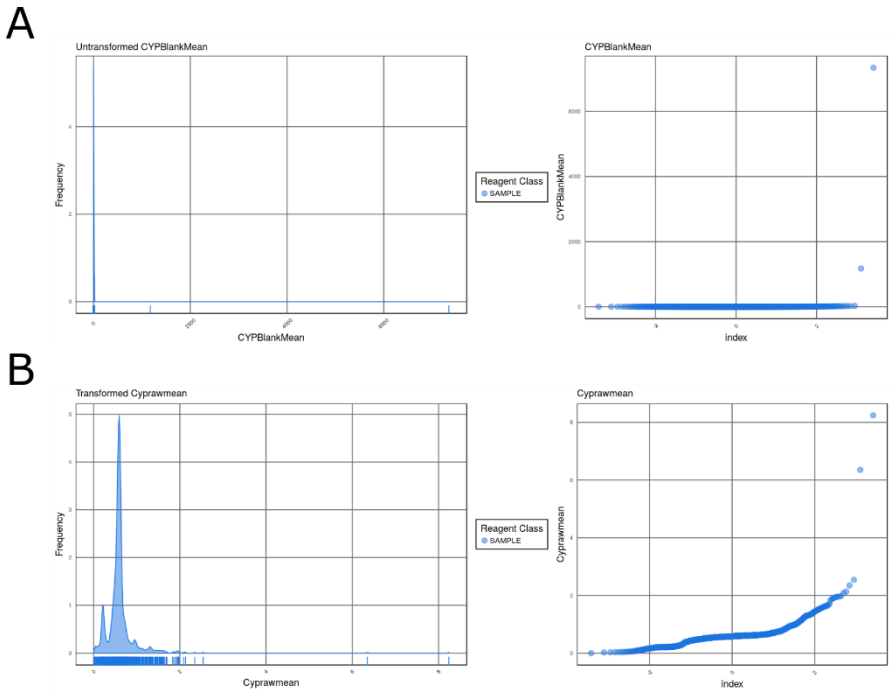

Figure 34. Data transformation. Data distribution was automatically checked using HC StratoMineR, in this example, the untransformed histogram plots data of CYP 450 activity (**A**) shows a non-normal distribution. HC StratoMineR suggests a log2 transformation (**B**) approximating the data into a normal distribution facilitating any further analysis.

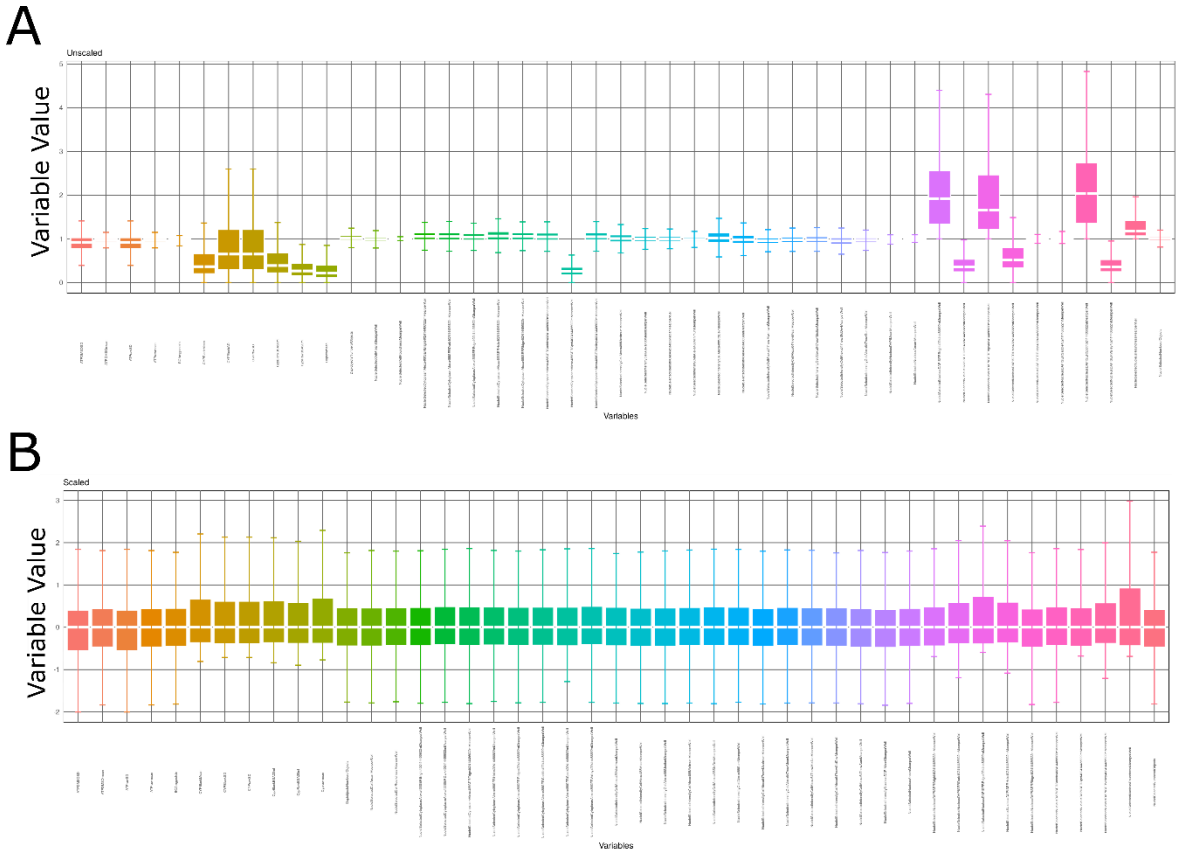

Figure 35. Data standardisation. (**A**) Non-standardised plot, on the x-axis, each column represents a parameter. The y-axis represents the value parameter, whic shows the range difference. (**B**) Standardised data plot, all the data set is in a similar range with a mean close to 0 reducing the bias based on range differences.

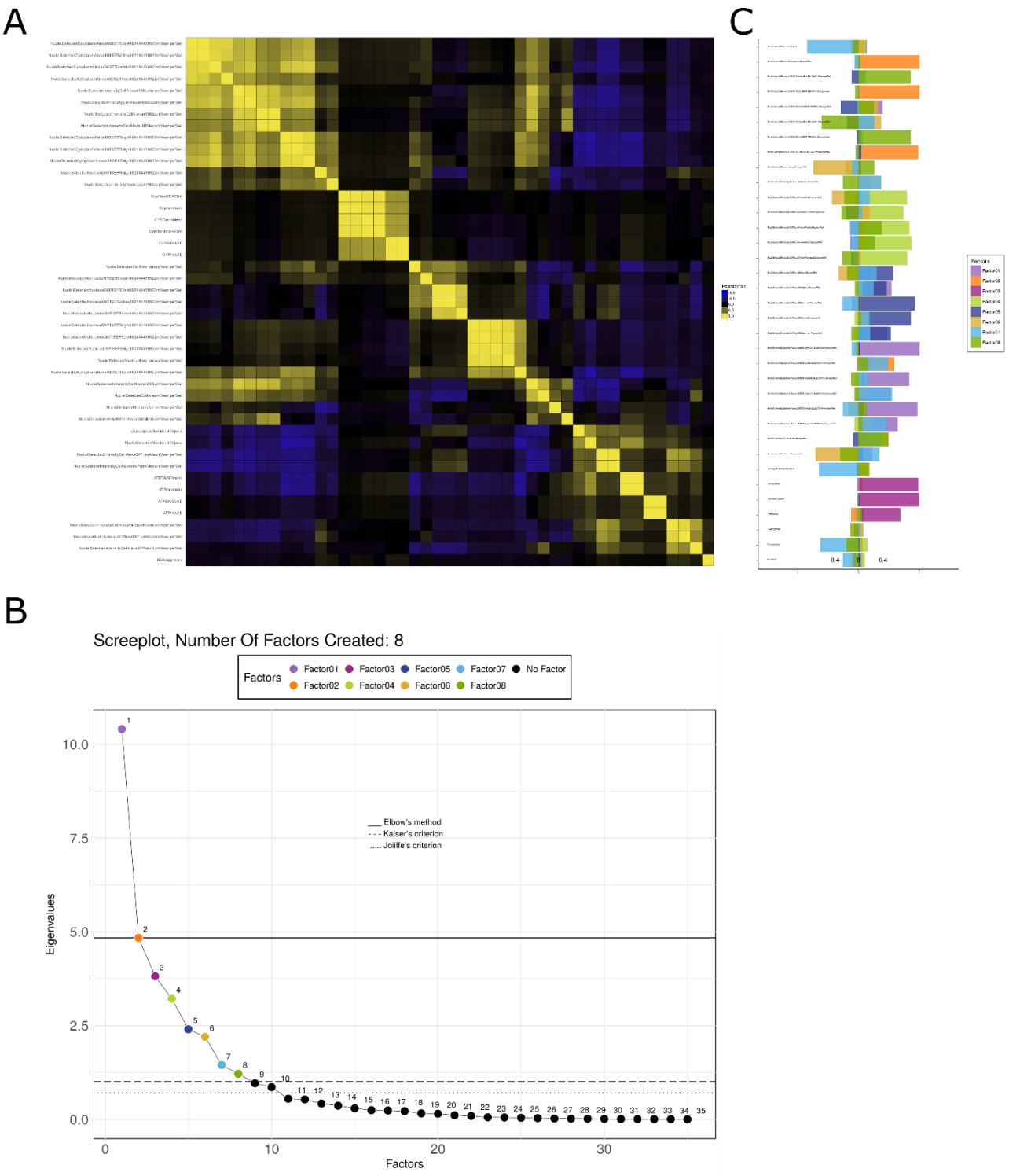

Figure 36. Parameter correlation matrix and data reduction from the 96-well plate dataset. (**A**) Hierarchical correlation matrix. The x-axis and y-axis represent the parameters. Each square represents a parameter compared to another parameter, the colour represents a Pearson's correlation between 1 and -1. Number of factors are determined automatically by the Kasier's method (**B**). (**C**) Loading plot representing which parameter contribute to each factors and how strong its contribution is. Values represent a Pearson's correlation between 1 and -1.

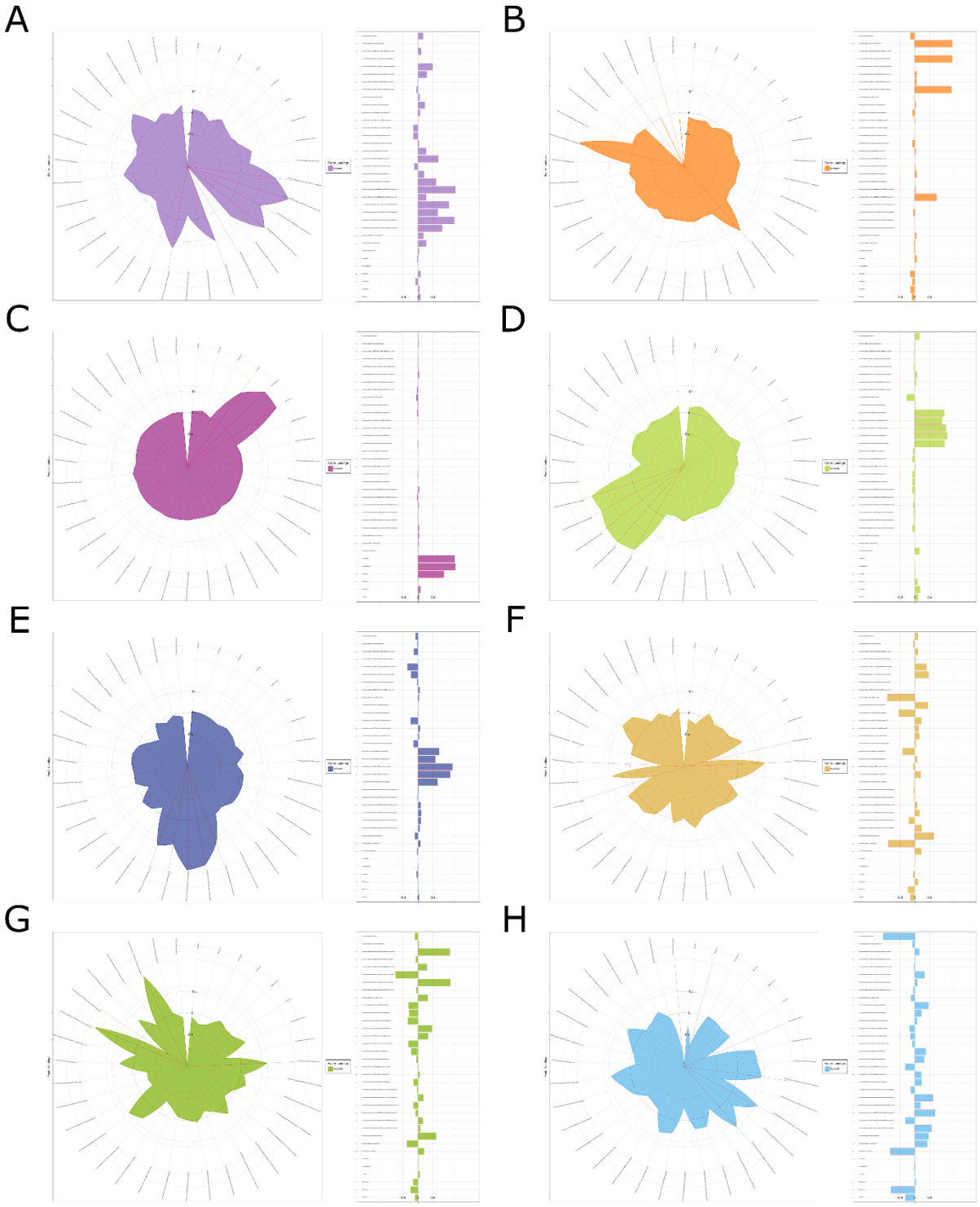

Figure 37. Polar plots from the 96-well plate dataset. The polar angles of each factor generated from the data reduction display the parameters from the data set, the radius represents the factor loading of the parameter. A significant contribution is considered if >0.4 or <-0.4 and is indicated with a red line. Every factor is visualized in this manner. (**A**) Factor 1, (**B**) Factor 2, (**C**) Factor 3, (**D**) Factor 4, (**E**) Factor 5, (**F**) Factor 6, (**G**) Factor 7 and (**H**) Factor 8. Values represent a Pearson's correlation between 1 and -1.

Figure 38. Data reduction comparison from the 96-well plate dataset. (**A**) Multiparametric plot from the pre-processed data, X-axis show all the wells of the plate where y-axis shows the values of the different parameters each represented in a different colour. (**B**) Multiparametric plot from the factors generated from the CFS on the y-axis instead of the parameter values. Comparison of (**A**) and (**B**) displays the effect of the data reduction step.

Hit selection

Finally, hit selection was performed. HC StratoMineR calculates a distance score from the eight factors generated by the data reduction. The result is one final distance factor where distance from controls will be close to 0 and distance from compounds will increase depending on their feature profile (**Figure 39A**). This is performed in a plate-to-plate basis for each replicate (**Figure 39C**). HC StratoMineR transforms the

distance factor into p-value and statistically significant hits can be identified. Compound was called a hit when $p < 0.05$ when compared to the negative control (**Figure 39B**).

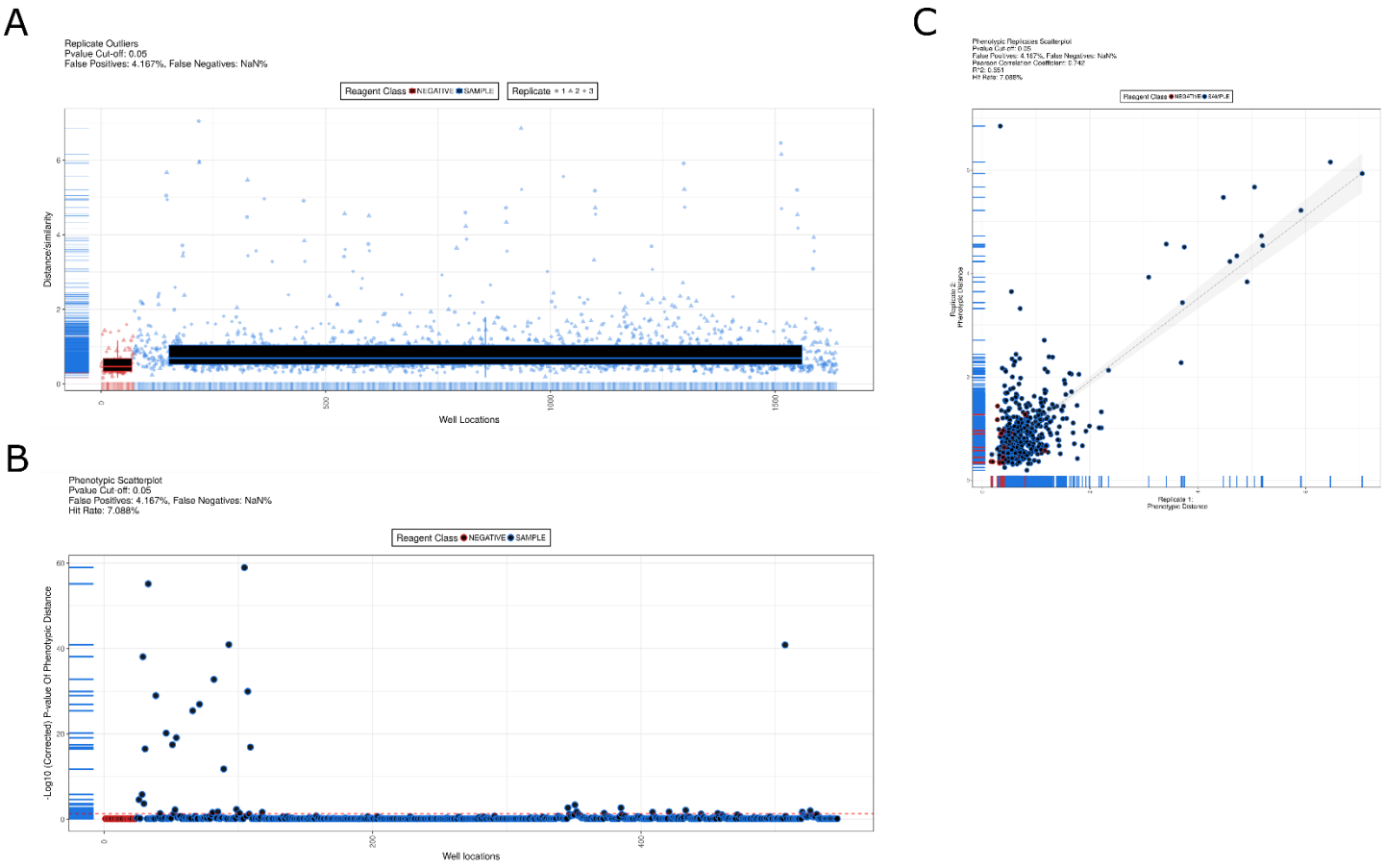

Figure 39. Hit picking parameter from the 96-well plate dataset. (**A**) Distribution of the screen to detect possible outliers. Each box in the box plot represents a condition (negative in blue or sample in red), the three replicates are combined to see the variation between plates and to detect outliers in the data set. On the x-axis are plotted all the wells and on the y-axis the distance from the negative control. (**B**) Scatter plot showing the hits detected from the screen. On the x-axis are plotted all the wells and on the y-axis the log10 p-value value, the red dotted line marks the value when a compound is marked as a hit. (**C**) Hit selection plot, x-axis represents replicate 1 and y-axis represent replicate 2. The plots shows the distance score from the negative controls in the replicates.

From the 96-well plate screen, 26 compounds were called as hits, see **Table 10** for details. Results were sent to AstraZeneca for results validation. The training compound library was composed of 64 hepatotoxic compounds and 19 non-hepatotoxic compounds. From the 26 compounds detected as hits, 23 compounds were related to DILI. Three compounds (Clotrimazole, Oxybutynin, Colchicine) were annotated as negative in AstraZeneca's data. After validating the results, the sensitivity and specificity of the assay were determined, giving a sensitivity of 35.9% and specificity of 84.2%. Sensitivity was determined as the ability of the system to detect compounds annotated as toxic by AstraZeneca's as hits or true positives. The specificity was determined as the ability of the system to not detect compounds annotated as non-toxic by AstraZeneca's as hits or true negatives.

Similar analysis was performed for the 384-well plate dataset. Common factor analysis (CFA) (**Figure 40A**) generated twelve factors. Number of factors was determined automatically by the Kaiser's method to avoid bias in number of factors (**Figure 40B**). Each factor is visualised in a polar plot, which indicates the loadings for each parameter in the generation of the factors for data reduction. In each plot, the angles display the different parameters, and the radius represents the factor loading of the parameter (**Figure** 41). The effect of the data reduction can be visualised when comparing the signature from plotting all the parameters across the wells (**Figure 42A**) versus the factors from the data reduction across the wells (**Figure 42B**). The sample variability is maintained after the data reduction from the twelve factors generated during the data reduction. Following this, hit selection was performed as explained before (**Figure 43**). Compound was called a hit when $p < 0.05$ when compared to the negative control. From the 384-well plate screen, 66 compounds were called as hits, see **Table 11** for details. From the 66 hits; 51 compounds belonged to the hepatotoxic group and 15 to the non-hepatotoxic. After validating the

results, the sensitivity and specificity of the assay were determined, giving a sensitivity of 79.7% and specificity of 21.1%. Due to its specificity, I selected the 96-well plate format for my studies.

Drug name	AZ Compound Name	FDA	Pos/Neg
Haloperidol	AZ10047978	vLess-DILI-Concern	Pos
Imipramine	AZ10120857	vLess-DILI-Concern	Pos
Fluoxetine	AZ10166761	vLess-DILI-Concern	Pos
Acetylsalicylic acid	AZ10015436	#N/A	Pos
Amiodarone	AZ10131427	vMost-DILI-Concern	Pos
Simvastatin	AZ10410259	vLess-DILI-Concern	Pos
Perhexilene	AZ10466355	vMost-DILI-Concern	Pos
Chlorpromazine	AZ10000853	vLess-DILI-Concern	Pos
Tamoxifen	AZ10009015	vMost-DILI-Concern	Pos
Clotrimazole	AZ10235889	vLess-DILI-Concern	Neg
Clozapine	AZ10030042	vMost-DILI-Concern	Pos
Ketoconazole	AZ12014276	vMost-DILI-Concern	Pos
Sunitinib	AZ11755299	vMost-DILI-Concern	Pos
Lapatinib	AZ10402704	vMost-DILI-Concern	Pos
Nefazodone	AZ10150878	vMost-DILI-Concern	Pos
Alpidem	AZ11636409	vMost-DILI-Concern	Pos
Oxybutynin	AZ10491901	vNo-DILI-Concern	Neg
Colchicine	AZ12064467	Ambiguous DILI-concern	Neg
Nimesulide	AZ10491890	vMost-DILI-Concern	Pos
Flutamide	AZ10003185	vMost-DILI-Concern	Pos
Troglitazone	AZ10308701	vMost-DILI-Concern	Pos
Disulfiram	AZ10001511	vMost-DILI-Concern	Pos
Fenofibrate	AZ10116192	vLess-DILI-Concern	Pos
Labetalol	AZ10337779	vMost-DILI-Concern	Pos
Tienilic acid/Ticrynafen	AZ10256496	#N/A	Pos
Dantrolene	AZ11874538	vMost-DILI-Concern	Pos

Table 10. 96-well plate screen hit list. Compound hits obtained from the screening. To detect specificity and sensitivity our hits were compared with AstraZeneca's results as shown on the Pos/Neg column. The results of this screen were a sensitivity of 35.9% and a specificity of 84.2%. Pos = positive, Neg = Negative.

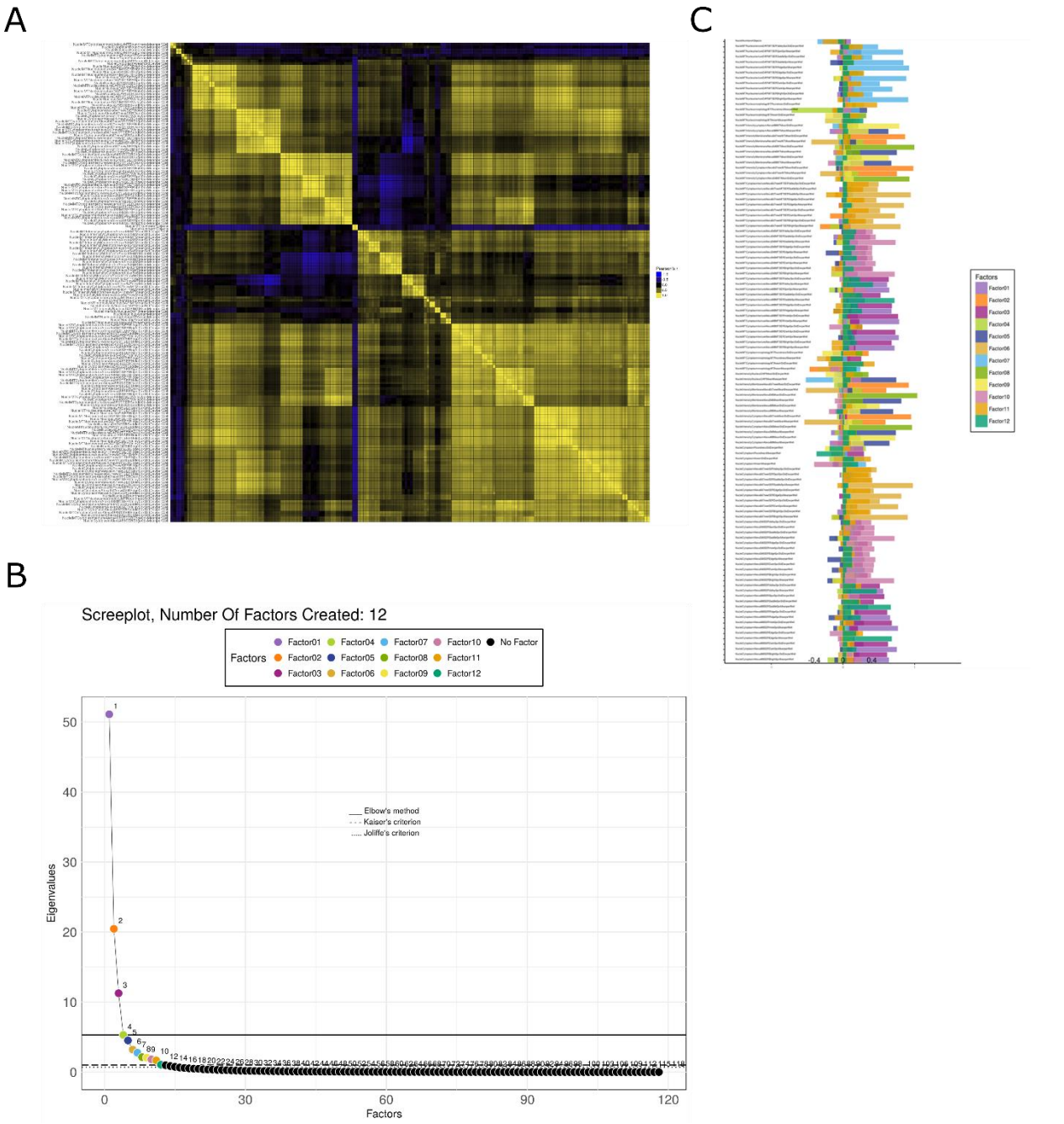

Figure 40. Parameter correlation matrix and data reduction from the 384-well plate screen. (**A**) Hierarchical correlation matrix. The x-axis and y-axis represent the parameters. Each square represents a parameter compared to another parameter, the colour represents a Pearson's correlation between 1 and -1. Number of factors are determined automatically by the Kasier's method (**B**). (**C**) Loading plot representing which parameter contribute to each factor and how strong its contribution is. Values represents a Pearson's correlation between 1 and -1.

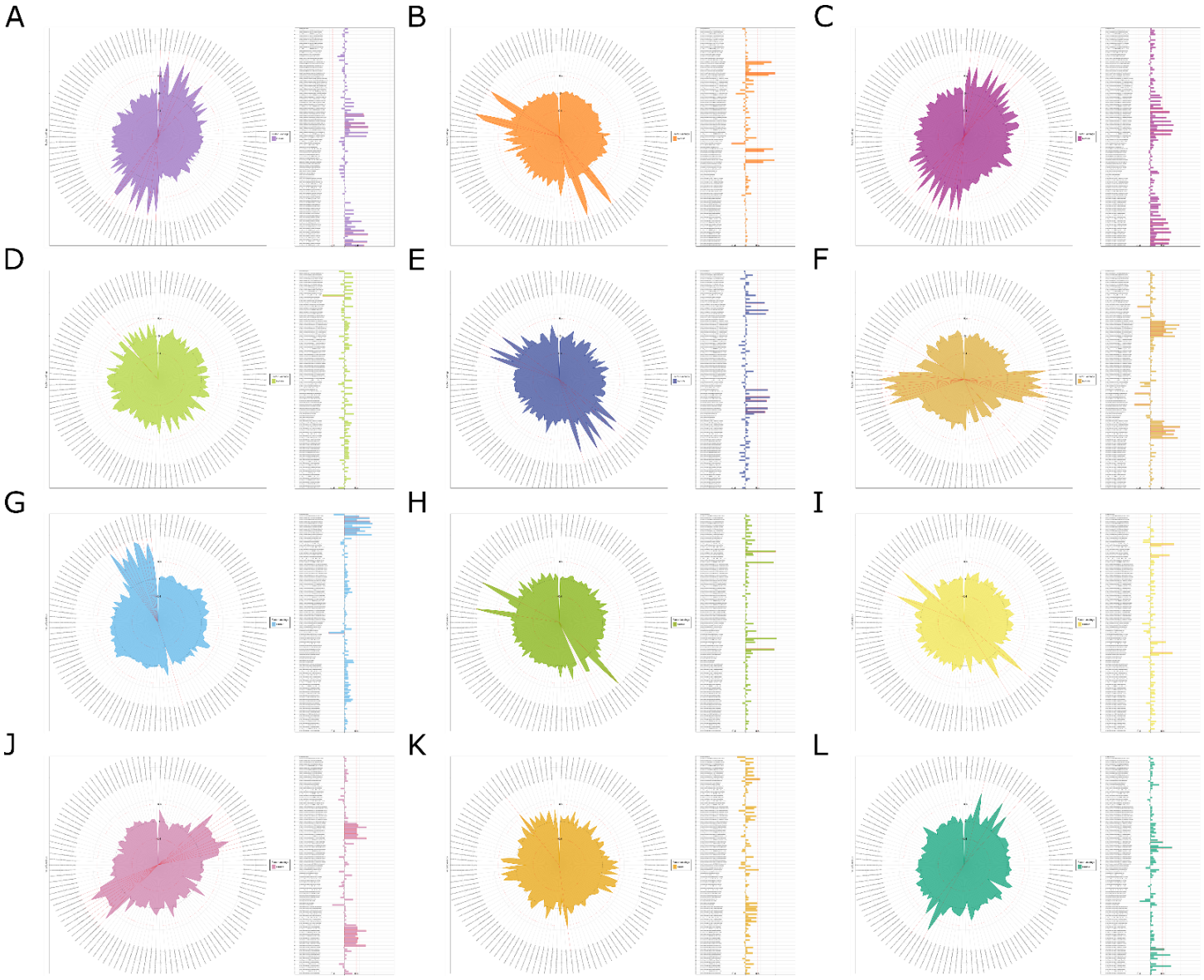

Figure 41. Polar plots from the 38-well plate dataset. The polar angles of each factor generated from the data reduction display the parameters from the data set, the radius represents the factor loading of the parameter. A significant contribution is considered if >0.4 or <-0.4 and is indicated with a red line. Every factor is visualized in this manner. (**A**) Factor 1, (**B**) Factor 2, (**C**) Factor 3, (**D**) Factor 4, (**E**) Factor 5, (**F**) Factor 6, (**G**) Factor 7, (**H**) Factor 8, (**I**) Factor 9, (**J**) Factor 10, (**K**) Factor 11 and (**L**) Factor 12. Values represents a Pearson's correlation between 1 and -1.

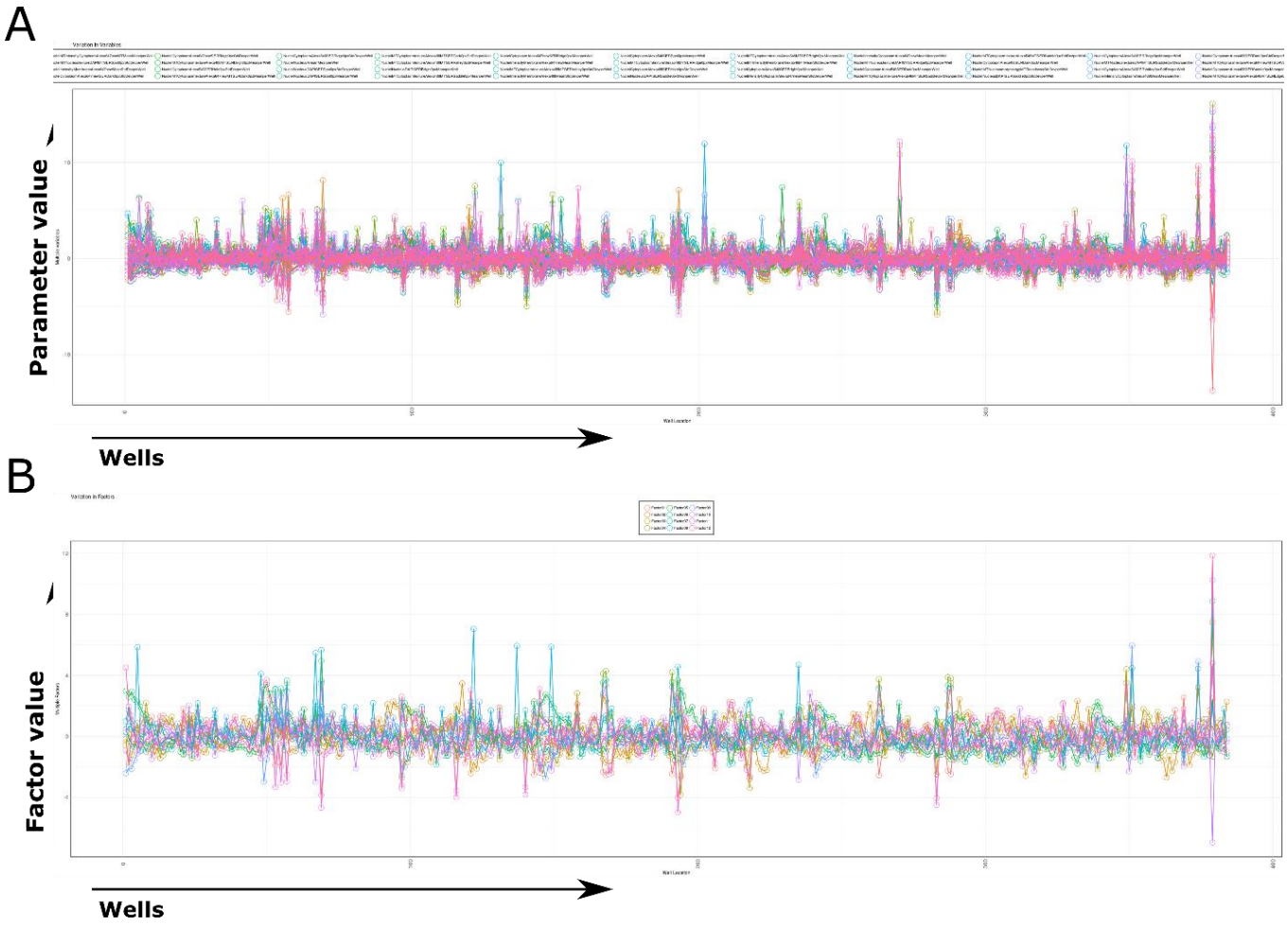

Figure 42. Data reduction comparison from the 384-well plate dataset. (**A**) Multiparametric plot from the pre-processed data, X-axis show all the wells of the plate where y-axis shows the values of the different parameters each represented in a different colour. (**B**) Multiparametric plot from the factors generated from the CFS on the y-axis instead of the parameter values. Comparison of (**A**) and (**B**) displays the effect of the data reduction step.

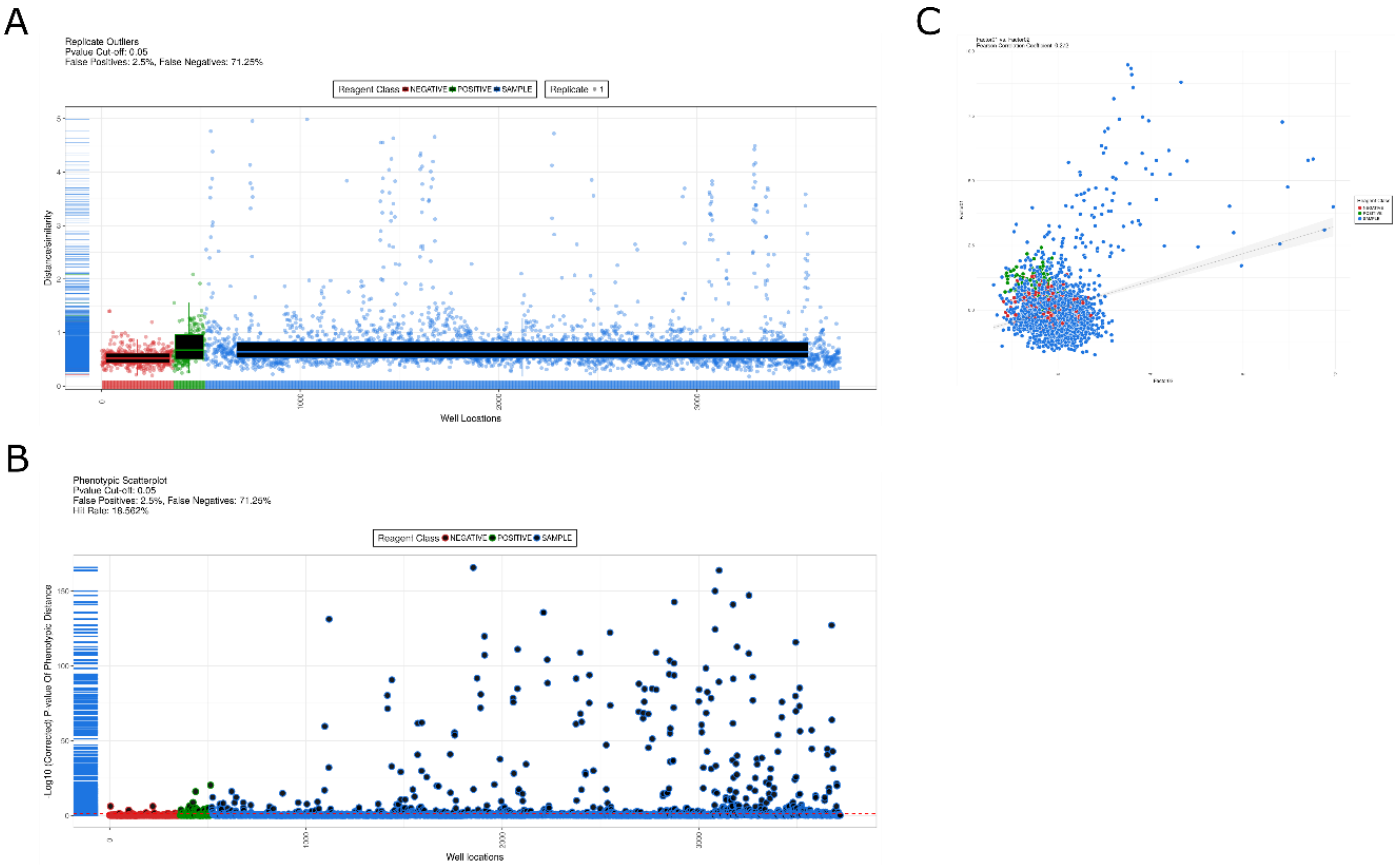

Figure 43. Hit picking parameter from the 384-well plate dataset. (**A**) Distribution of the screen to detect possible outliers. Each box in the box plot represents a condition (negative in blue or sample in red), the three replicates are combined to see the variation between plates and to detect outliers in the data set. On the x-axis are plotted all the wells and on the y-axis the distance from the negative control. (**B**) Scatter plot showing the hits detected from the screen. On the x-axis are plotted all the wells and, on the y-axis, the log10 p-value value, the red dotted line marks the value when a compound is marked as a hit. (**C**) Hit selection plot, x-axis represents replicate 1 and y-axis represent replicate 2. The plots show the distance score from the negative controls in the replicates.

Drug Name	AZ Copound Name	FDA	Pos/Neg
Piroxicam	AZ10133063	vLess-DILI-Concern	NaN
Ambrisentan	AZ13616209	Ambiguous DILI-concern	Neg
betaine	AZ10003728	vNo-DILI-Concern	Neg
Buspirone	AZ10047343	Ambiguous DILI-concern	Neg
cromoglicic acid (cromolyn)	AZ10005214	#N/A	Neg
Dexamethasone	AZ10168612	Ambiguous DILI-concern	Neg
Diphenhydramine	AZ10009895	vNo-DILI-Concern	Neg
Donepezil	AZ10087366	vLess-DILI-Concern	Neg
Entacapone	AZ13299485	vLess-DILI-Concern	Neg
epinephrine	AZ10453071	vNo-DILI-Concern	Neg
folic acid	AZ10013790	vNo-DILI-Concern	Neg
isoproterenol	AZ10064045	vNo-DILI-Concern	Neg
Oxybutynin	AZ10491901	vNo-DILI-Concern	Neg
Pargyline	AZ10065948	#N/A	Neg
Procyclidine	AZ10620821	vNo-DILI-Concern	Neg
streptomycin	AZ12121615	vNo-DILI-Concern	Neg
Acetylsalicylic acid	AZ10015436	#N/A	Pos
Alpidem	AZ11636409	vMost-DILI-Concern	Pos
Amiodarone	AZ10131427	vMost-DILI-Concern	Pos
Benzbromarone	AZ10132264	vMost-DILI-Concern	Pos
Bromfenac	AZ13432419	vMost-DILI-Concern	Pos
Busulfan	AZ10072216	vMost-DILI-Concern	Pos
Clofibrate	AZ10007325	vLess-DILI-Concern	Pos
Clozapine	AZ10030042	vMost-DILI-Concern	Pos
Coumarin	AZ10246257	#N/A	Pos
Dacarbazine	AZ10523577	vMost-DILI-Concern	Pos
Dantrolene	AZ11874538	vMost-DILI-Concern	Pos
Diclofenac	AZ10194317	vMost-DILI-Concern	Pos
Erythromycin	AZ12201437	vMost-DILI-Concern	Pos
Felbamate	AZ10130800	vMost-DILI-Concern	Pos
Fenofibrate	AZ10116192	vLess-DILI-Concern	Pos
Fluconazole	AZ10456348	vMost-DILI-Concern	Pos
Fluoxetine	AZ10166761	vLess-DILI-Concern	Pos
Furosemide	AZ10130507	Ambiguous DILI-concern	Pos

Drug Name	AZ Copound Name	FDA	Pos/Neg
Glimepiride	AZ13695398	vLess-DILI-Concern	Pos
haloperidol	AZ10047978	vLess-DILI-Concern	Pos
Ibuprofen	AZ10005713	vLess-DILI-Concern	Pos
Imipramine	AZ10120857	vLess-DILI-Concern	Pos
Indomethacin	AZ10003646	vMost-DILI-Concern	Pos
Iproniazid	AZ10013584	vMost-DILI-Concern	Pos
Labetalol	AZ10337779	vMost-DILI-Concern	Pos
Lapatinib	AZ10402704	vMost-DILI-Concern	Pos
leflunomide	AZ10042615	vMost-DILI-Concern	Pos
Lumiracoxib	AZ13112694	vMost-DILI-Concern	Pos
Mercaptopurine	AZ10184621	vMost-DILI-Concern	Pos
Metformin	AZ10046538	vLess-DILI-Concern	Pos
Methotrexate	AZ10403554	vMost-DILI-Concern	Pos
Naproxen	AZ10222853	vLess-DILI-Concern	Pos
Nefazodone	AZ10150878	vMost-DILI-Concern	Pos
Nevirapine	AZ12307889	vMost-DILI-Concern	Pos
Nimesulide	AZ10491890	vMost-DILI-Concern	Pos
nomifensine	AZ10154702	vMost-DILI-Concern	Pos
Perhexilene	AZ10466355	vMost-DILI-Concern	Pos
Phenytoin	AZ10246255	vMost-DILI-Concern	Pos
Pioglitazone	AZ10080838	vLess-DILI-Concern	Pos
Pravastatin	AZ10154396	vLess-DILI-Concern	Pos
Propylthiouracil	AZ10006157	vMost-DILI-Concern	Pos
Simvastatin	AZ10410259	vLess-DILI-Concern	Pos
Stavudine	AZ10129833	vMost-DILI-Concern	Pos
Sulindac	AZ10173856	vMost-DILI-Concern	Pos
sunitinib	AZ11755299	vMost-DILI-Concern	Pos
Tacrine	AZ10050561	#N/A	Pos
Tamoxifen	AZ10009015	vMost-DILI-Concern	Pos
Ticlopidine	AZ10025601	vMost-DILI-Concern	Pos
Tienilic acid/Ticrynafen	AZ10256496	#N/A	Pos
Troglitazone	AZ10308701	vMost-DILI-Concern	Pos
Ximelagatran	AZ11942255	vMost-DILI-Concern	Pos

Table 11. 384-well plate screen hit list. Compound hits obtained from the screening. To detect specificity and sensitivity our hits where compared with AstraZeneca's results as showed on the Pos/Neg column. The results of this screen were a sensitivity of 35.9% and a specificity of 84.2%. Pos = positive, Neg = Negative, NaN = No information available.

3.2.5 Disease modelling in 96-well plate format

In addition to drug toxicity studies, the semi-automated platform can be applied for disease modelling. Non-alcoholic fatty liver disease (NAFLD) is the most common cause of liver disease in developed countries. *In vitro* modelling of NAFLD would permit mechanistic studies to find therapies. I contributed to the development of an *in vitro* model of NAFLD by implementing the model into the semi-automated differentiation platform (67). In this study, HLCs were exposed to lactate, pyruvate and octanoic acid (LPO) for 48h or 96h to induce lipid accumulation. Following incubation, HLCs were stained with NucBlue for the nuclei, BODIPY green for lipids and Mitotracker for the mitochondrial activity. Imaging and analysis were performed as described before. Lipid accumulation and mitochondrial stress was quantified. LPO treated cells displayed a dose- and time-dependent increase in lipid vacuoles and mitochondrial stress.

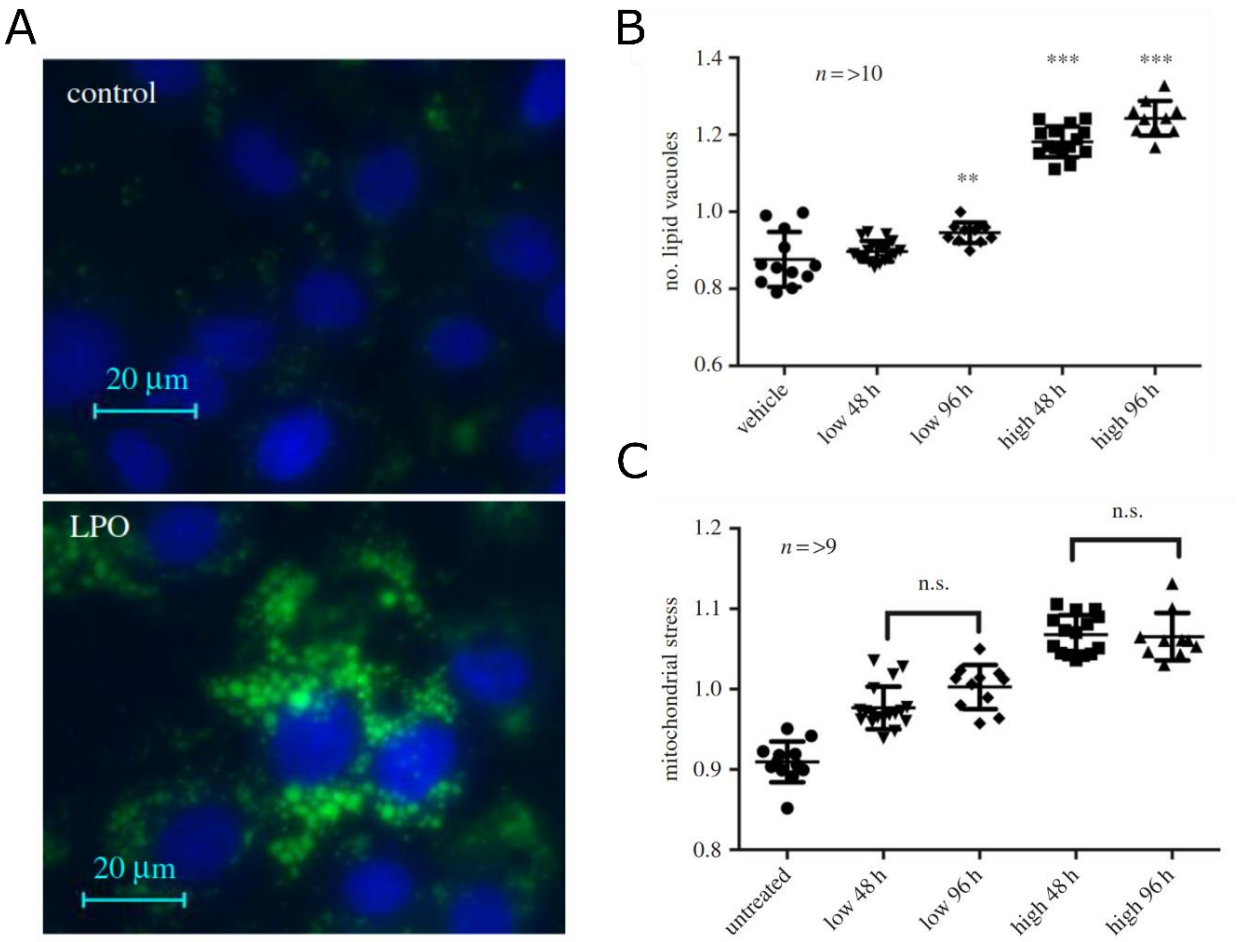

Figure 44. Incubation of HLCs with LPO at low or high dose for 48 or 96 h induces steatosis. (**A**) Fluorescence microscopy demonstrating BODIPY staining of neutral lipid vacuoles within HLC following exposure to LPO. (**B**) LPO induces a dose- and time-dependent increase in lipid vacuoles in HLCs. (**C**) Exposure to LPO increases mitochondrial stress in a dose-dependent manner at 48 and 96 h. Data was analysed by one-way ANOVA with Bonferroni correction. The minimum number of biological replicates is shown for each experiment. **p < 0.01, ***p < 0.001, n.s. = non-significant. Figure adapted from Lyall et al, 2018 (67).

3.3 Discussion

Biomedical research requires tools that better mimic and predict human liver biology. Traditionally, *in vitro* models relied heavily on immortalized cell lines. While these models demonstrate advantages, they offer limited biological relevance when compared to primary cells. Primary cells are considered the gold standard to study liver biology but due to batch-to-batch variations, rapid loss of phenotype and the scarcity of donor tissue more stable and reproducible models are required. Recent advances in stem cell technologies offer the possibility to develop more accurate models that better mimic hepatocyte physiology.

Our hepatocyte differentiation protocol consists of a stagewise approach where the stem cell populations are driven to definitive endoderm using Activin A and Wnt3a. This is followed by hepatic progenitor cell specification and hepatocyte maturation. HLCs express a battery of hepatocyte markers such as HNF4a, albumin. In addition, HLCs displayed cytochrome P450 including CYP P450, CYP1A2, CYP2C9, CYP2C19, CYP2D6, and CYP3A4 (**Figure 25**, **Figure 26**). These CYPs are responsible for the metabolism of approximately 90% of marketed drugs (173). Despite as the mixture of foetal and adult hepatocyte traits (90), HLCs provides a reproducible system to study hepatocyte biology for basic and translational research. HLCs produced in this protocol exhibit comparable metabolic activity and response to paracetamol toxicity to primary hepatocytes (66,150).

Over the last decade, researchers have demonstrated the potential of HLCs differentiation protocols as a tool to model human diseases or drug exposure. Several groups have applied HLCs for disease modelling or drug screening. Rashid et al. (70) and Cayo et al. (71) produced HLCs from patient-derived human iPSC cell lines which accurately modelled human metabolic liver disease. Similarly, Lyall et al. contributed to the

development of an *in vitro* model to study non-alcoholic fatty liver disease from human pluripotent stem cells, HLCs lipid accumulation, to recapitulate the transcriptional and metabolic dysregulation seen in NAFLD and additionally retain liver-like epigenome (67). Another model of non-alcoholic fatty liver disease was developed by Parafati et al. (174), in this study, induction of NAFLD was linked to an increase of endoplasmic reticulum stress. Following administration of both unsaturated and saturated fatty acids, there was an increase in endoplasmic reticulum stress, triglyceride accumulation as well as dysregulation of lipid metabolism without leading to cell apoptosis. Additionally, Lucendo-Villarin et al. (92) showed how HLCs can be used to study foetal hepatotoxicity when exposed to tobacco derivatives.

Relative to other types of hepatocyte sources, HLCs were found to be more sensitive than the cancer cell line HepG2 (175) and exhibit a comparable response to primary hepatocytes when challenged with toxins (150,175). While continued research into the cell niche is required to further improve the HLC phenotype, the studies described above evidence the power of stem cell-derived HLCs to model human disease and improve drug discovery.

The semi-automated procedure of HLCs differentiation is efficient, reliable and economical, allowing the production of HLCs at scale. As seen in the validation drug screen, the semi-automation workflow enables the user to produce large numbers of plates at once, for the 96-well plate screen, 60 plates were differentiated at once. This was not possible using traditional cell culture. Importantly, the automation process did not impact on differentiation yields, with the majority of cells expressing HNF4α and ALB. HLCs also exhibited metabolic activity comparable to previous reported experiments (66,87). Despite the standardization of the protocol, cell confluency prior to the differentiation is critical for pure HLC differentiation. Cell number and confluency needs to be empirically optimised for different hPSC.

In its current form, this platform is not suitable to produce large quantities of HLCs for clinical applications, and this will most likely be achieved through the use of cell factories and bioreactors. However, the methodology developed does allow for the rapid generation of human liver cells for basic and translational research.

An example of current limitations of *in vitro* models can be noticed during the different phases of drug development. Although high-throughput screening platforms permit the testing of large compound libraries during drug development, the high attrition rates demonstrate the need for improved screening platforms and more reliable pre-clinical models. The percentage of drug failure at phase II and phase III is high and the main reasons for failure are the lack of efficacy, 48% in phase II and 55% in phase III, and safety, 25% in phase II and 14% in phase III (176), with hepatotoxicity (18%) representing the first reason for drug withdrawal (177). Because of that, there is a need to improve current screening models to improve the early detection of hepatotoxic drugs. By combining the semi-automated production of stem cell-derived hepatocytes with high content analysis, alternative tools that better predict liver physiology could be developed delivering safer medicines for the patient.

Drug metabolism and hepatotoxic compound detection was tested onto the HLCs produced with the semi-automated platform in collaboration with AstraZeneca. A combination of commercial assays were combined with the cell painting staining (141). The main advantages of using high content analysis are that it generates a multiparametric data set instead of a single readout. In addition, by using the cell paint assay, it is possible to determine effects in the different stained organelles. Both 96 and 384-well plate were tested with the compound library.

Data analysis was performed using several data mining tools. First Python programming was used for data formatting and file merging. By

using Python, high quantities of files can be processed at once reducing time and minimising manual errors. Next, I used Spotfire for data visualisation. This software allows rapid data visualisation and analysis of large data sets. Similar visualisations can be achieved with Python but Spotfire allows a user-friendly interface allowing non-specialised programmers to work with big data. Analysis could be performed using Spotfire. The main disadvantage of using Spotfire for data mining is that normalisations, transformations or hit picking have to be programmed one by one. Due to the large quantity of features extracted from the analysis analysis with Spotfire would be time consuming and its use requires advance programming skills. Therefore, HC Stratominer was used for data analysis. HC Stratominer, allows a rapid analysis of big data sets to users with no previous programming experience. Due to its intractability, different thresholds or methods can be applied at every step of the analysis facilitating data exploration.

After analysis, 96-well plate assay detected 26 compounds as hits, see table **Table 10** for details. Results produced from the screen was validated with AstraZeneca's screen results. The sensitivity and specificity of the assay were 35.9% and 84.2% respectively. From the 26 hits, three compounds: Clotrimazole, Oxybutynin, Colchicine; were detected as negative in AstraZeneca's screen. Interestingly, on the FDA compound annotation (**Table 9**), only Oxybutynin was marked as a non-DILI concern compound. Clotrimazole and Colchicine presented less-DILI and ambiguous-DILI concerns respectively. Detection of Clotrimazole and Colchicine as hits could be explained due to a phenotype improvement. Changes in the AstraZeneca screen design could explain the reduced specificity. Our compound incubation was 48h versus 72h from AstraZeneca. In addition, we limited DMSO concentration to 1% due to its toxicity. This limited our higher concentration to 200 µM, while several compounds displayed toxicity

at higher concentrations. Further work could be focused on increasing assay sensitivity.

For the 384-well screen higher concentration was kept at 200 µM to maintain 1% DMSO concentration but compound incubation was extended to 72h. Following data analysis, 66 compounds were called a hit. See **Table 11** for details. Despite the increase in sensitivity (79.7%) 15 compounds annotated as negative were detected as a hit. FDA compound annotation showed 8 of the 15 compounds: Betaine, Diphenhydramine, epinephrine, folic acid, isoproterenol, Oxybutynin, Procyclidine, streptomycin were annotated as non-DILI related on the FDA. These results make 384-well plate more prone to false positives limiting its use as a drug exposure model.

In summary, development of high-throughput generation of HLCs in 96 and 384-well plate can be achieved by the implementation of automation. By using liquid handling systems and high content imaging standardisation and reproducibility from the differentiation to the analysis can be achieved. After comparing both multi-well systems, 96-well plate format displayed a higher specificity. In addition, 96-well plate format allows sample acquisition for other downstream applications such as protein or gene expression analysis. We used this system for modelling human drug exposure in the subsequent chapter.

CHAPTER FOUR

INVESTIGATING THE PROTECTIVE PROPERTIES OF DIMETHYL FUMARATE AND Nrf2 SIGNALLING DURING DRUG-INDUCED HEPATOTOXICITY

4.1 Introduction

4.1.1 Liver disease

Liver disease is a major cause of death. It is increasing every year in the UK with a four-fold increase in mortality rates since 1970 (178). Drug-induced liver injury (DILI) is the most common cause of acute liver failure (ALF) (179). Drugs and their metabolites can expose the organ to adverse events such as endoplasmic reticulum and mitochondrial stress. This can alter cellular homeostasis, inducing the generation of reactive oxygen species (ROS) and the triggering of cell death (180–182). Paracetamol-induced injury is the most common cause of DILI (183). It is characterised by hepatocyte death and organ failure. Phase II enzymes are responsible for a non-toxic paracetamol metabolism. During an overdose, non-toxic metabolism is saturated and paracetamol is then metabolised by CYP P450 proteins generating a toxic intermediate metabolite N-acetyl-p-benzoquinone imine (NAPQI). NAPQI is a highly reactive toxic metabolite that will induce hepatocyte death. Following the first injury insult, spreading of hepatocyte senescence occurs via TGF-b activation reducing liver regeneration which can results in organ failure and possible death (57,58).

N-Acetylcysteine (NAC) is the only current treatment for paracetamol overdose. Following treatment, NAC increases the production and availability of hepatic glutathione. This neutralises NAPQI reducing the hepatocyte death (58–60). To be an effective therapy, NAC has to be administrated within the first 8-10 h following paracetamol overdose consumption (58). Therefore, new treatments that can improve patient outcome or prolong the window of effective treatment are required.

4.1.2 Nrf2 stimulation as a tissue repair therapy

Anti-inflammatory and antioxidant therapies have been proposed in the past as a powerful approach to reduce the severity of acute injury and enhance organ regeneration. The transcription factor 'nuclear factor erythroid-derived 2-like 2' (Nrf2) is a transcription factor involved in the defence mechanism against ROS. Therefore, the clinical activation of Nrf2 activation may provide a successful therapy for acute disorders (184,185).

Nrf2 regulates multiple antioxidant genes involved in glutathione synthesis, ROS elimination, detoxification, drug excretion and NADPH synthesis that are activated following injury. In the absence of stress, Nrf2 is bound to its inhibitor 'kelch-like ECH-associated protein 1' (Keap1) promoting the ubiquitination and degradation of Nrf2. Keap1 is a cysteine-rich protein. These cysteine residues are highly reactive and can act as stress sensor. Oxidative stress and electrophile compounds can interact and modify covalently cysteine residues reducing its binding capacity with Nrf2 (101,186). Among all the cysteine residues, Cys-151, Cys-226, Cys-273, Cys-288 and Cys-613 are the most common modified residues with Cys-151 the preferable residue for electrophile compounds (101). Upon cell stress, Keap1 losses its capacity to bind Nrf2; Nrf2 translocates into the nucleus, forms an heterodimer with MafG and binds to the Antioxidant Response Element (ARE) - a promoter motif of multiple genes. This initiates the antioxidant and anti-inflammatory gene response (**Figure 8**) (94,117,187).

Several studies suggest that the activation of the Nrf2 pathway can have cytoprotective and anti-inflammatory effects (188–190). Therefore, pharmacological activation of Nrf2 could represent a promising therapeutic option to limit acute tissue injury and inhibit detrimental loss of function and scarring (184). A recent study also

showed that the activation of Nrf2 suppresses the macrophage inflammatory response by blocking the transcription of pro-inflammatory cytokines (IL6, IL1b, IL1a and Nos2) via an ARE non-dependent mechanism (109). Consequently, the activation of Nrf2 as a therapy could provide a dual protective role by reducing organ injury inflammation and enhancing regeneration.

4.1.3 Pharmacological activation of Nrf2 by dimethyl fumarate

Dimethyl fumarate (DMF) is a drug approved by the food and drug administration (FDA) and the European Medicines Agency (EMA) for some forms of multiple sclerosis and psoriasis (191). The full mechanism of DMF is not completely understood. *In vivo*, DMF is metabolised by hydrolysis to monoethyl fumarate (MMF) by esterases (123). Both DMF and MMF can interact with the Cys-151 residue of Keap1 allowing the activation of Nrf2 and its anti-oxidative and anti-inflammatory responses (**Figure 45**). Therefore pharmaceutical repurposing of the use of DMF could potentially lead to a successful treatment to reduce the severity of acute liver injury (192). By understanding the effects of DMF in the modulation of the Nrf2 pathway in liver injury, this research may provide a platform for translation to patients with acute liver disease.

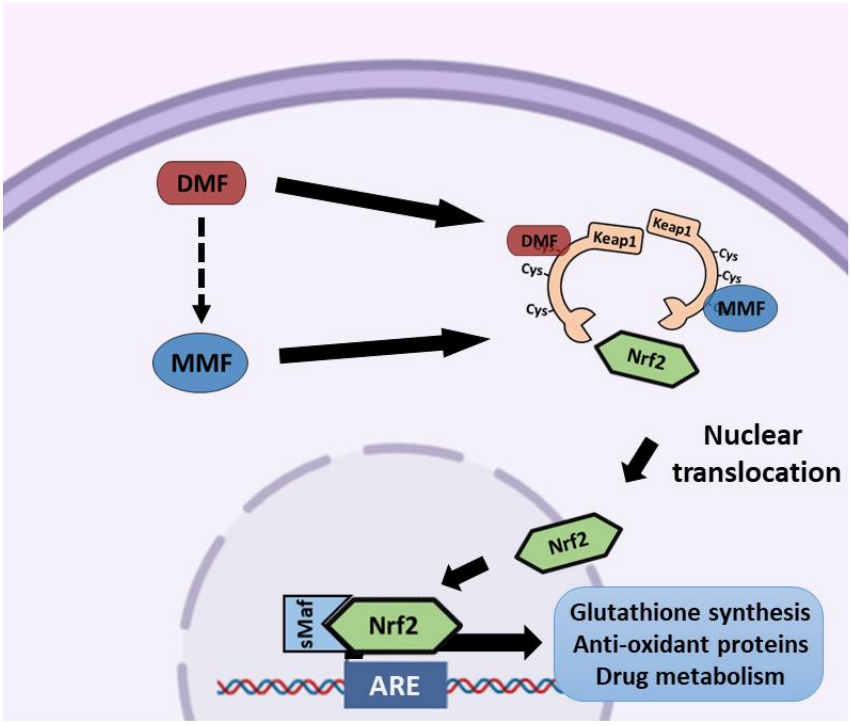

Figure 45. Schematic representation of the mechanism of action of dimethyl fumarate. DMF interacts with KEAP1 blocking the binding capacity to Nrf2. Nrf2 can then undergo nuclear translocation and induce gene expression. Figure drawn by author.

4.1.4 Cytoprotective effects of DMF in *in vitro* and *in vivo* models

Both *in vitro* and *in vivo* systems were used to study the cytoprotective properties of DMF in the context of paracetamol injury. For the *in vitro* work, HLCs were used as a human, defined and reproducible model to recapitulate human hepatocyte drug metabolism (91). In combination with our semi-automated differentiation platform, HLCs are an excellent tool to study the cytoprotective effects of DMF. A zebrafish model of paracetamol injury was chosen as an *in vivo* model. The advantages of working with zebrafish are: rapid liver development, 72 – 96 hours postfertilization, easy scalability, reduced costs, overlap with 82% of disease-associated targets and drug metabolism pathways and transparent embryos with transgenic reporter lines (193). This makes zebrafish an interesting *in vivo* model with translational potential to bring *in vitro* results into the clinic.

4.2 Results

4.2.1 Dimethyl fumarate in HLCs

4.2.1.1 Dimethyl fumarate safety

Before investigating the cytoprotective effects of DMF, compound toxicity was assessed. HLCs at day 18 were treated with DMF (dissolved in DMSO) in a concentration range of 5 µM, 10 µM, 20 µM, 50 µM, 150 µM; concentrations based on the literature (193). Compounds were incubated for 48 h with drug replenishing at 24 h. Following incubation, ATP depletion was quantified (CellTiter-Glo, Promega). After 48 h, no significant reduction of ATP was detected in any of the tested concentrations (**Figure 46**). Apoptosis induction following DMF 50 µM administration was tested for further validation. A caspase 3/7 induction assay (Caspase 3/7 - Glo, Promega) was performed at time 0, 30 min, 90 min and 6 hours post administration of DMF 50 µM. DMF 50 µM was selected as a starting concentration as no toxicity was observed in HLCs as well as being reported to induce cytoprotective effects via Nrf2 activation (123,131,195). No significant induction of apoptosis was detected between conditions from the same time point (**Figure 47**). Based on the literature, 50 µM and 10 µM were selected as working concentrations (196).

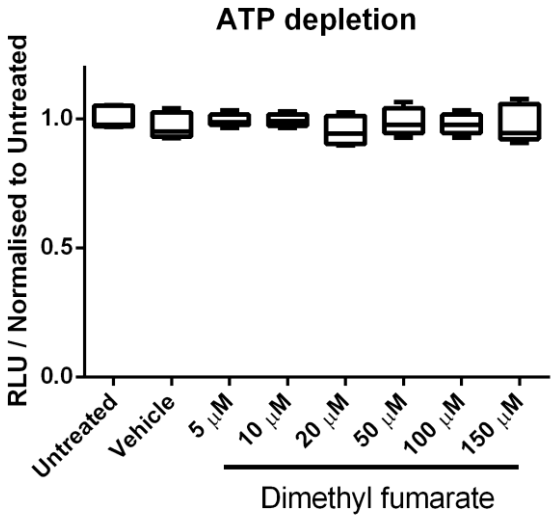

Figure 46. Assessment of DMF toxicity in HLCs. HLCs were incubated with DMF for 48 h in a concentration range of 5 µM, 10 µM, 20 µM, 50 µM, 150 µM. Following incubation, total ATP was quantified. No significant changes were detected. A One-way ANOVA with Tukey's post-hoc statistical tests was employed. Box plot, whiskers represents Min-Max. n=8 replicates of one plate.

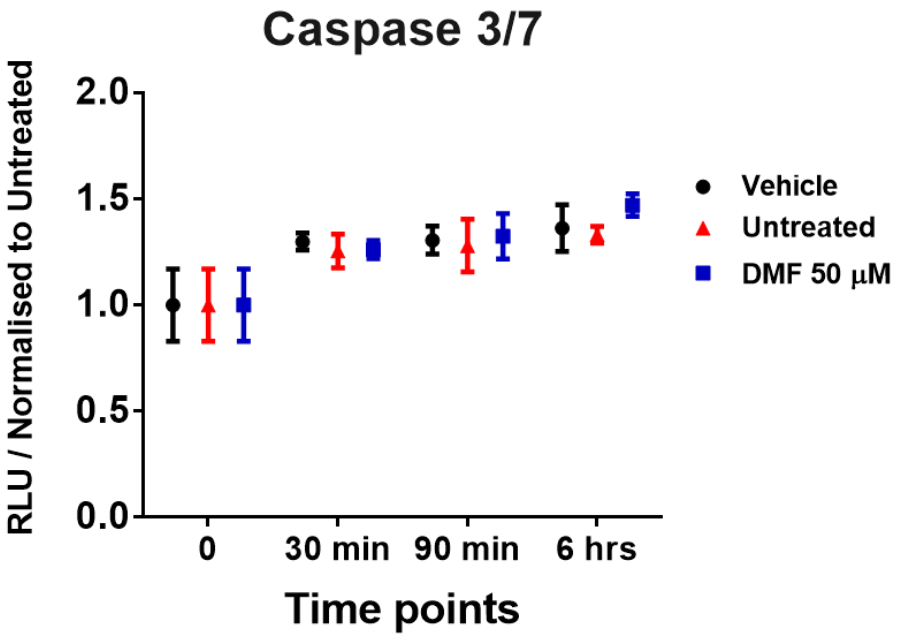

Figure 47. Caspase 3/7 induction following DMF incubation. Time course experiment to assess potential apoptosis induction from DMF. There was no significant increase between conditions from within the same point. A One-way ANOVA with Tukey's post-hoc statistical tests was employed. Dot plot, with mean and SD. n=16 replicates of one plate.

4.2.1.2 High content imaging of Nrf2 nuclear translocation

Antibody optimisation

Next, DMF potential to induce Nrf2 nuclear translocation was assessed. Two Nrf2 antibodies commonly used in the literature were tested. First, a rabbit polyclonal anti-Nrf2 ab31163 (Abcam) (197) and a mouse monoclonal anti-Nrf2 sc-365949 (Santa Cruz Biotechnology) (198). From the antibodies used, Nrf2 staining was only detected with the Abcam antibody (**Figure 48**). For subsequent studies, the anti-Nrf2 ab31163 antibody was used.

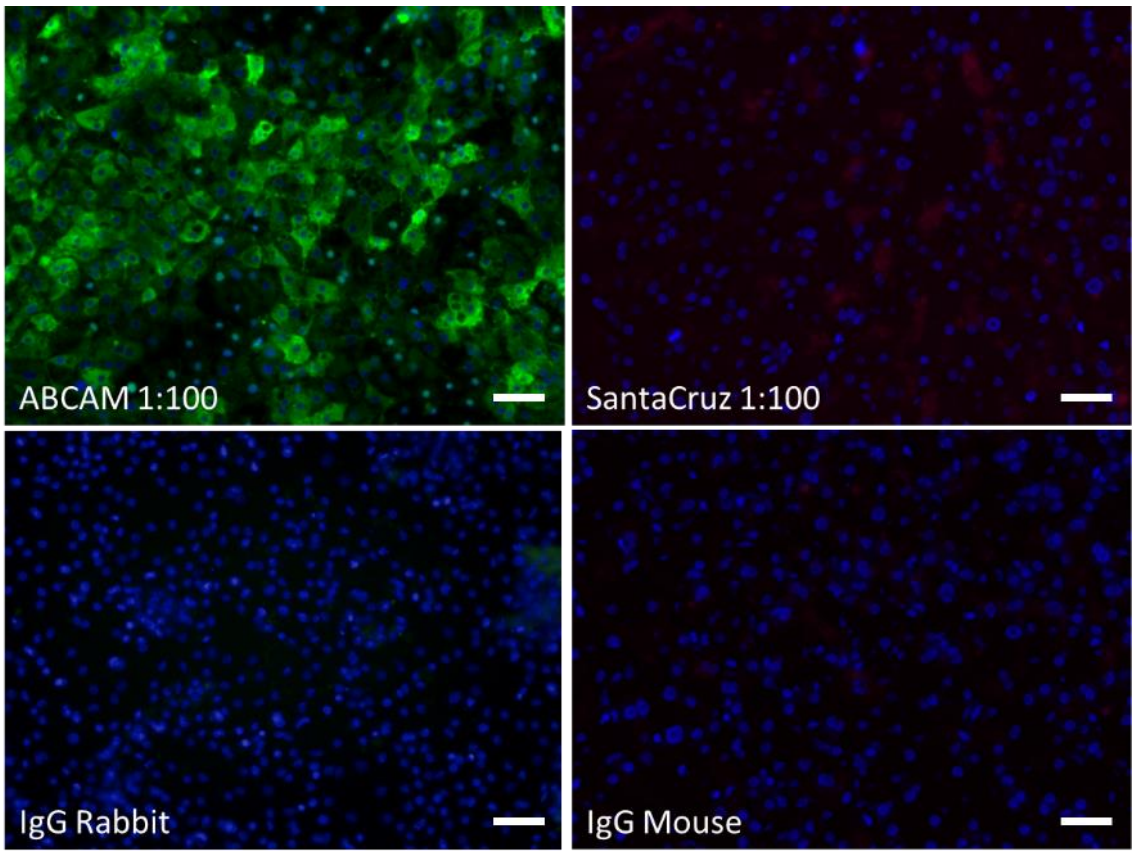

Figure 48. Nrf2 antibody optimisation. Representative staining of HLCs at day 18 were stained with the anti-Nrf2 antibodies. Reactivity was only observed on the Abcam antibody, three fields of view were imaged per antibody. Scale bar = 50 µM.

Following this, a time course experiment was designed to determine the capacity of DMF to induce Nrf2 nuclear translocation. HLCs at day 18 were administered with DMF 50 µM. Parallel plates were prepared and fixed at time 0, 0.5 h, 2 h, 6 h and 24 h. Plates were stained for Nrf2 on the red channel (568 nm), cytoplasm (CellMask green 488 nm) and nuclei (Hoechst 361 nm).

Nrf2 nuclear translocation by high content imaging

Following staining, plates were imaged using the Operetta high content microscope and cell segmentation was performed. Hoechst and Cellmask stain were used for cell identification. After the quality control step, Nrf2 intensity was calculated.

Nuclei and cytoplasm intensity were quantified separately, this allowed Nrf2 localisation as well as nuclear/cytoplasmatic staining ratio to assess Nrf2 nuclear translocation. After image quantification, an intensity threshold was applied to separate nuclear Nrf2 positive cells (Nrf2+) from nuclear Nrf2 negative cells (Nrf2-) (**Figure 49**). The value obtained represents the percentage of Nrf2+ cells per well. At time 0, the majority of the HLCs displayed cytoplasmic staining of Nrf2 (**Figure 50**), with only 31.2% Nrf2+ cells (**Figure 51**).

At 0.5 h following DMF administration, most of the cells displayed a marked Nrf2 nuclear staining (**Figure 50**), this change was quantified with an increase of Nrf2+ cells up to 71.2% (**Figure 51**). This was maintained at two hours, with 74.1% of Nrf2+ cells, followed by a decrease down to 58.4% Nrf2+ cells at 6 h and acquiring basal levels of 35.2% after 24 h of DMF administration (**Figure 51**, **Figure 50**). This result highlights the sensitivity of the Nrf2 pathway. DMF treatment induced Nrf2 nuclear translocation as early as 30 minutes.

This pipeline allows an automatic quantification of Nrf2 nuclear translocation following stimuli. The only limitation of this approach is the manual thresholding for Nrf2+ quantification.

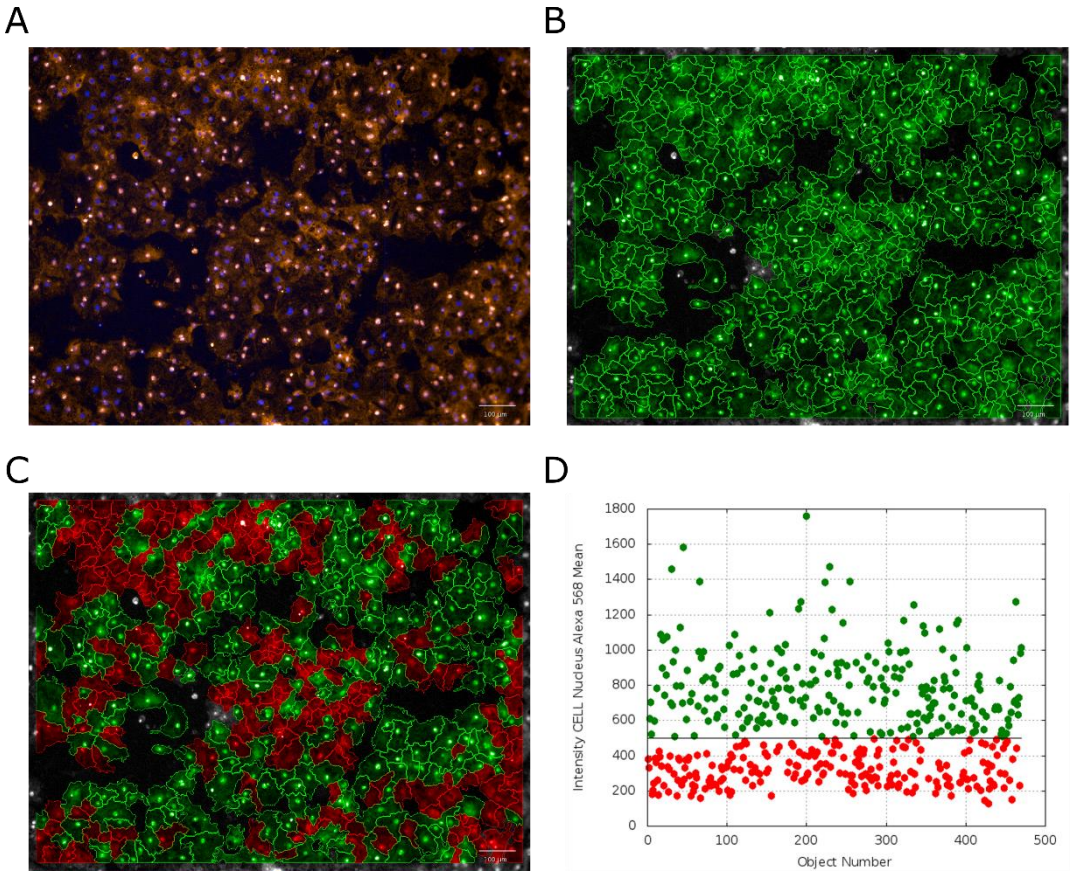

Figure 49. Example of the thresholding for Nrf2+ selection. (**A**) HLCs treated with DMF 50 µM for 2 hours, HLCs were stained for Nrf2 in orange and nuclei in blue. (**B**) Cell segmentation for HLCs detection. (**C**) Selection of Nrf2 nuclear positive cells. (**D**) Threshold applied to select Nrf2 nuclear positive cells based on Nrf2 nuclear intensity. Scale bar = 100 µm.

Further improvement on the quantification process was required to develop an unbiased quantification of Nrf2 dynamics. Previous data analysis was performed using well level data, as shown on **Figure 49**. Values obtained represented the average from all the cells within a well. This approach requires a manual thresholding to determine what a Nrf2+ cell is. This process is time consuming and it has to be adjusted for each plate due to batch-to-batch staining variations. To improve this, single cell level information was extracted.

This approach is referred to as image cytometry (166,199). Single cell level data allows an easy visualisation and quantification of protein localisation. For each cell, nuclear, cytoplasmic and the ratio of nuclear/ cytoplasmic Nrf2 staining were calculated.

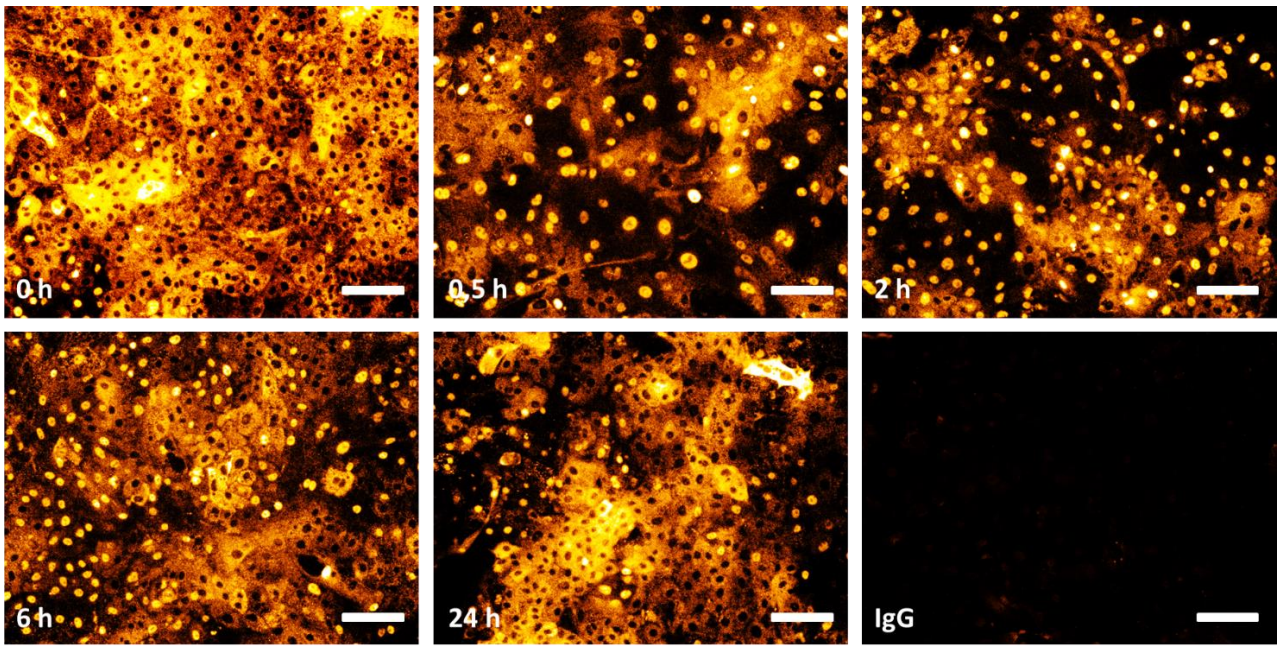

Figure 50. Nrf2 nuclear translocation following DMF administration. HLCs at day 18 were treated with 50 µM for 0, 0.5 ,2, 6 and 24 h. After treatment cells were stained for Nrf2. Representative images from each time point. Scale bar 100 µm. For each replicate, eight wells of a 96-well plate were imaged, n=3 biological replicates.

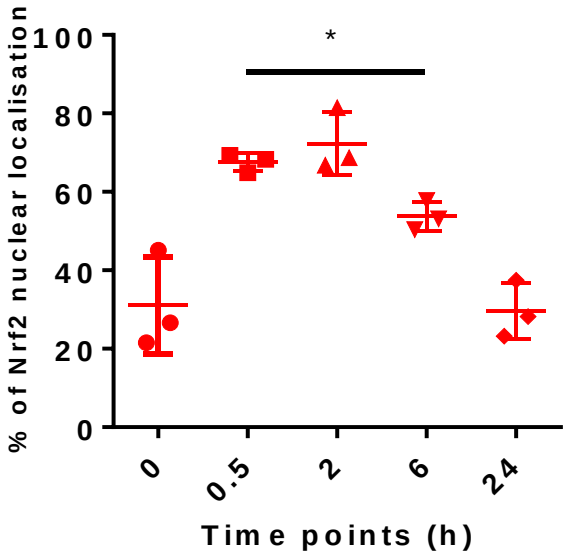

Figure 51. Time course quantification of Nrf2+ cells. Nrf2 positive cells were quantified using cell segmentation. Nrf2+ cells threshold was adjusted empirically to correct for staining variation. A One-way ANOVA with Tukey's post-hoc statistical tests was employed. Dot plot, where each dot represents a replicate with whiskers as SD, n=3 biological replicates.

By using single cell level data, the dataset size obtained was increased from one value per well to several thousand values per well. Data visualisation and normalisation was performed using Spotfire software as explained in Chapter 3. The advantage of using single cell data can be seen in **Figure 52**. In **Figure 52A**, data is plotted in a scatter plot, where each dot represents a cell, the X-axis represents the amount of Cytoplasmatic Nrf2 signal and the Y-axis represents the amount of Nuclear Nrf2 signal. Each scatter plot represents a time point in the time course. By using this method, it is possible to visualise Nrf2 dynamics upon time. In addition, this method allows detection of subpopulations that would be missing by using well level data. Moreover, by calculating the ratio of nuclear/cytoplasmic Nrf2, data can be visualised in a histogram as shown in **Figure 52B**. The histogram can help in visualising the shifts of the Nrf2+ cell populations upon treatment and time. Finally, this can be quantified in a box plot. **Figure 52C** shows each time point represented in a box plot with a histogram to show the sample distribution. The white line represents the median of the sample, the white semi-dotted line represents the average and the black bar next to the box plot represents the 95% confidence interval.

In addition, significance differences between time points can be seen in the comparison circles on the right, where alpha = 0.01 was applied (200). The centre of the circle is located at the same level as the average value of each time point. The size of the circle reflects the degree of the variability, the more variability of the sample the higher the circle. Circles that do not overlap indicate a significance difference.

A

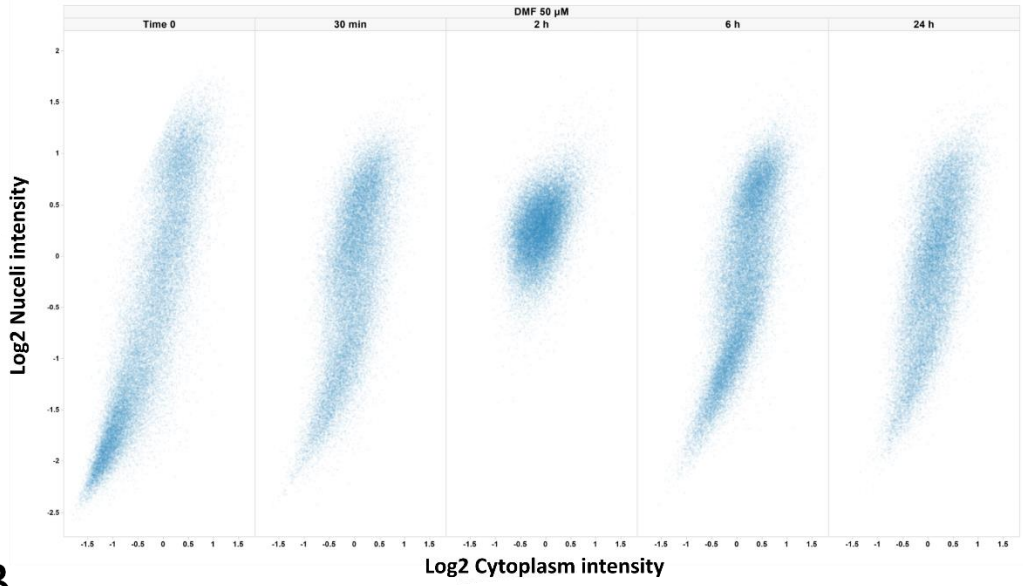

B

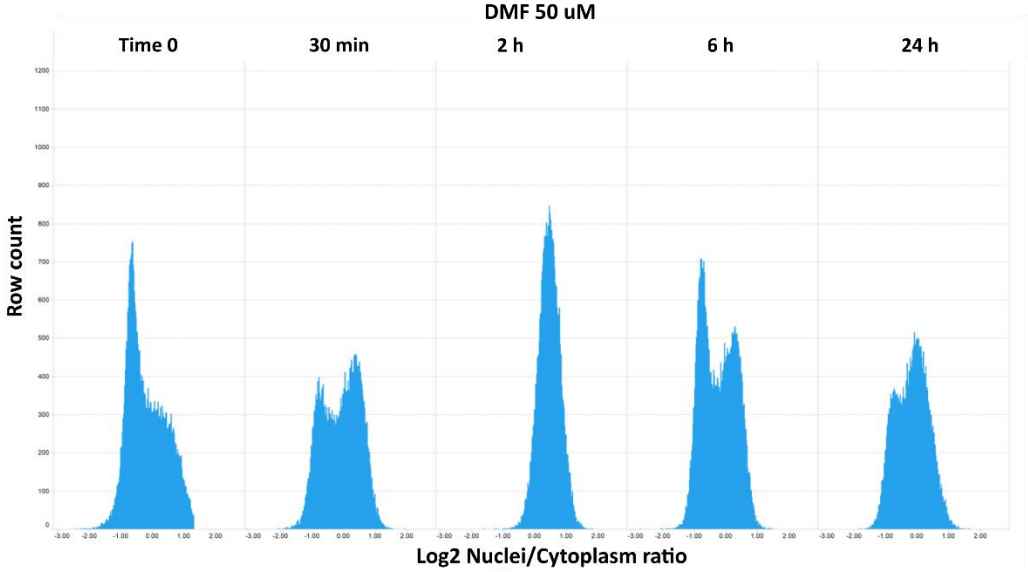

C

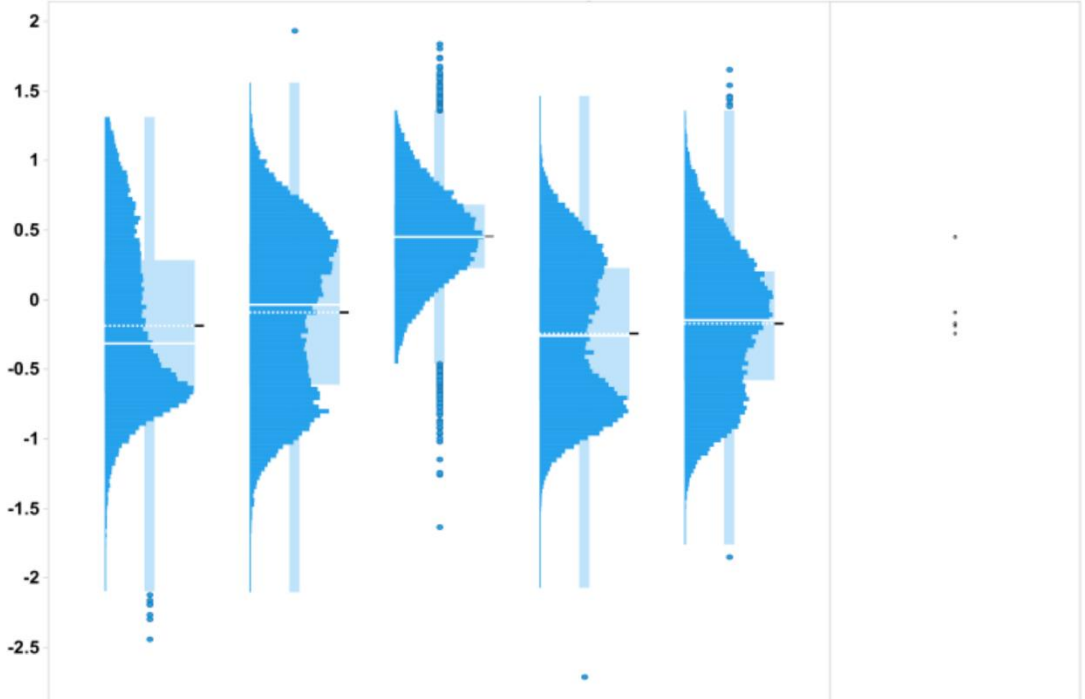

	Time 0	30 min	2 h	6 h	24 h
Count	38300	34178	33816	42319	32964
Median	-0.310615	-0.0322411	0.45252	-0.262259	-0.142716
Outliers	7	2	265	2	8
Avg	-0.185393	-0.0902148	0.452824	-0.242898	-0.17015
MedianAbsoluteDeviation	0.428829	0.493025	0.227625	0.471918	0.389137

Alpha level = 0.01
Root MSE = 0.533
sqrt(2)q* = 4.603

Figure 52. Single cell analysis of Nrf2 dynamics upon DMF 50 µM administration. (**A**) Scatter plot of single cell level data, where each dot represents a cell, the X-axis represents the amount of cytoplasmatic Nrf2 signal, Y-axis represents the amount of Nuclear Nrf2 signal. Each plot represents a time point (**B**) Histogram showing the ratio of nuclear/cytoplasmic Nrf2 intensity over time. (**C**) Box plot where each time point is represented in a box plot with a histogram to show the sample distribution. The white line represents the median of the sample, the black semi-dotted line represents the average and the black bar next to the box plot represents the 95% confidence interval. Comparison circles on the right show significant difference. Alpha = 0.01. n= 4 replicates from one plate.

This improved approach allows an unbiased image processing and data analysis to study Nrf2 dynamics. Comparison of **Figure 51** and **Figure 52** showed a similar trend: there is a significant increase of nuclear Nrf2 as early as 30 minutes with a peak at 2 hours, with a decrease after 6 hours of treatment.

In addition, vehicle and untreated groups were added as negative controls; H_2O_2 1 mM was used as a positive control. H_2O_2 is an Nrf2 inducer via oxidative stress injury (52).

Surprisingly, all conditions, positive and negative controls, showed similar patterns on Nrf2 dynamics. These results suggested that the increase of Nrf2 was not specific to the effects from DMF but to the medium change (**Figure 53**).

This could be explained by medium sock change. Changes in temperature or incorrected medium buffering could affect oxygen levels, triggering oxidative stress and Nrf2 nuclear translocation (201). To reduce this, further improvements were incorporated and a new time course experiment was performed. Media change was performed using the Viaflow automatic pipette. To minimise heat shock, the plate holder and tips from the Viaflow were preincubated at 37 °C overnight. In addition, culture medium containing the different treatments were prepared in a 96-well deep-well plate and preincubated for at least 6 hours in the same incubator as the HLCs. The same time points were chosen. Following compound incubation, staining and imaging,

unbiased data analysis was performed as before. Both untreated and vehicle did not show major population shifts over time (**Figure 54 A-B**). On the other hand, both DMF and H_20_2 showed an increase of Nrf2 at 2 hours. In the DMF group, Nrf2 stimuli decreased after 6 h, whereas in the H_2O_2 group, Nrf2 nuclear translocation was visible up to 24 hours (**Figure 54 C-E**). By minimising the cell stress from medium change, it is possible to study accurately Nrf2 dynamics following compound administration.

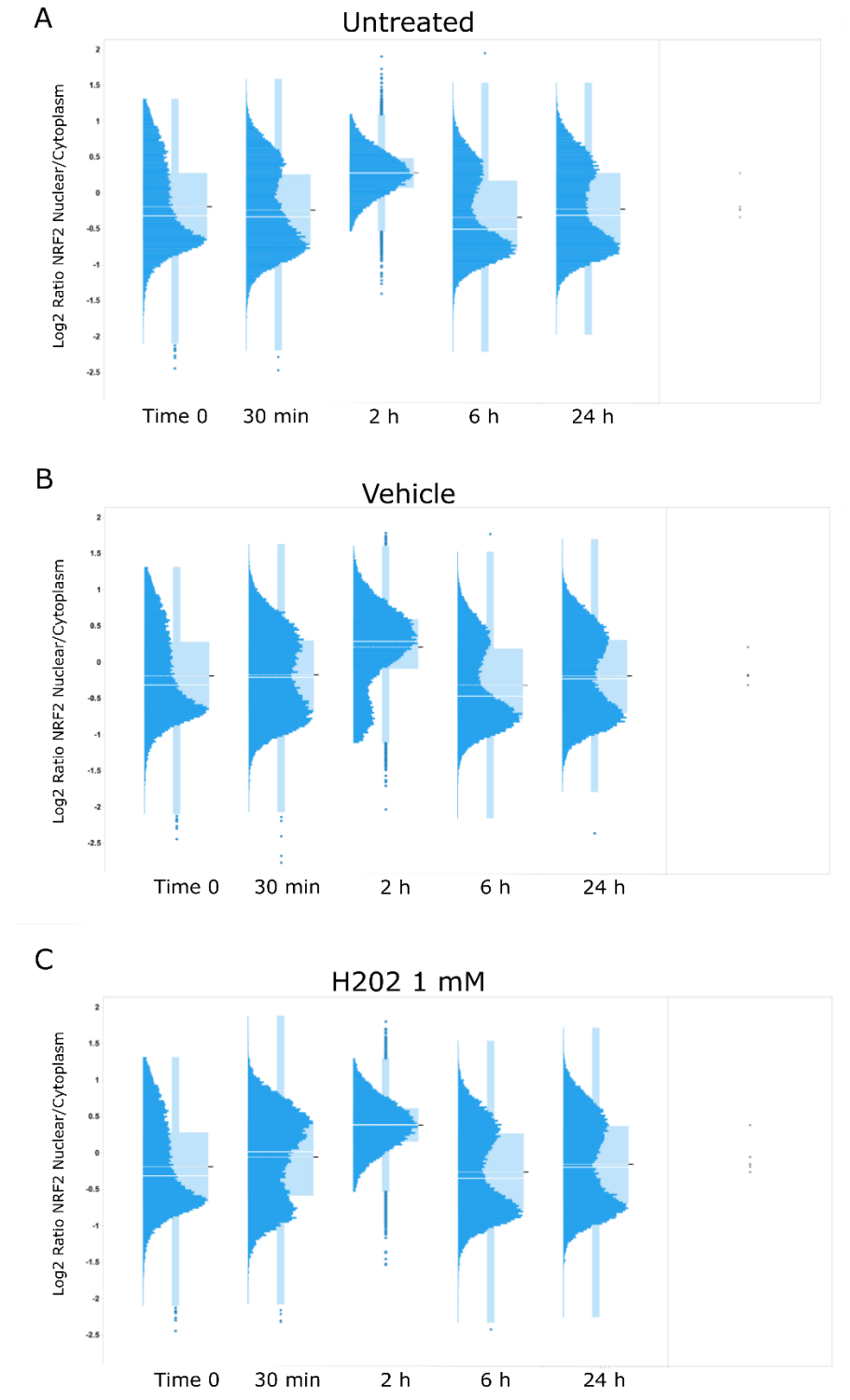

Figure 53. Medium induced Nrf2 stimulation. Analysis from Nrf2 nuclear translocation time course using single cell data form (**A**) untreated, (**B**) vehicle and (**C**) H_2O_2 1 mM. Box plots show similar trends in all conditions, implying that the effect on Nrf2 nuclear translocation is unsepecific to DMF (Figure 52) or H_2O_2. n=4. Alpha = 0.01. n= 4 replicates from a plate.

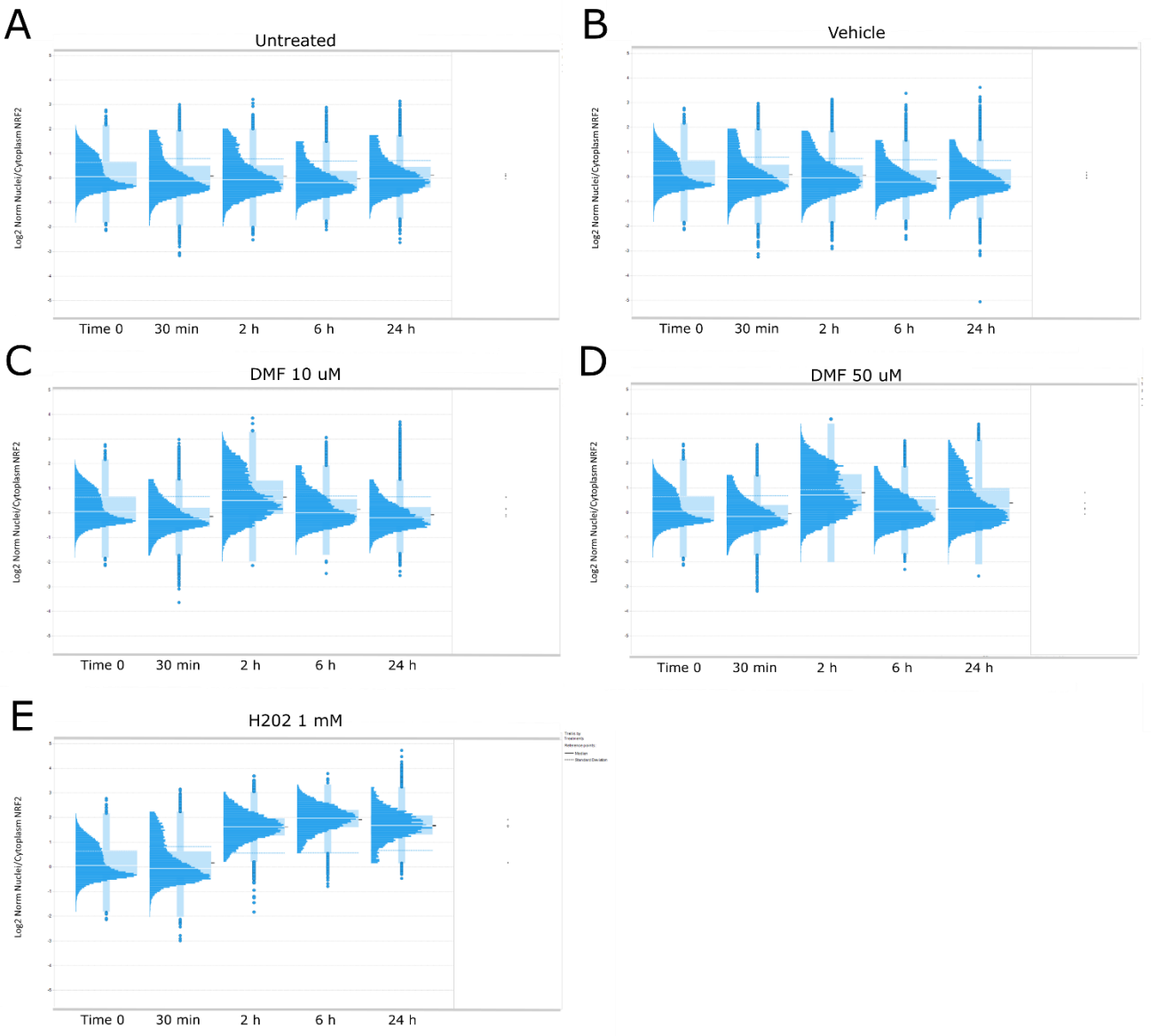

Figure 54. Assay optimisation leads to a specific Nrf2 nuclear translocation quantification. Following assay optimisation, Nrf2 nuclear/cytoplasmic ratio was maintained on (**A**) untreated and (**B**) vehicle during the time course. (**C**) DMF 10 µM and (**D**) DMF 50 µM showed an increase in Nrf2 nuclear population at 2 h post administration followed by a decrease of Nrf2+ at 24 h. (**E**) H_2O_2 1 mM showed an increase of Nrf2+ at 2 h which it was maintained at 6 and 24 h post administration. n=3. Alpha = 0.01. n= 4 replicates from a plate.

4.2.1.3 DMF drives Nrf2 gene transcription

After confirmation of Nrf2 nuclear translocation following DMF administration, the potential of DMF to induce Nrf2 target genes expression was tested. HLCs at day 18 were treated for 3 hours with dimethyl fumarate (50 µM), H_2O_2 (1 mM) and compared to controls. 3 hours post compound administration was selected to study the initial gene response following Nrf2 nuclear translocation.

Nrf2-driven gene expression was examined using three representative Nrf2 target genes (**Figure 55**): Glutathione-Disulfide Reductase (*GSR*), NADPH dehydrogenase quinone 1 (*NQO1*) and Heme oxygenase 1 (*HMOX1*) (94).

Both dimethyl fumarate and H_2O_2 induced expression of the three Nrf2 target genes (**Figure 55**). To determine whether there is a distinct gene response from a pro-injury Nrf2 activation such as H_2O_2 versus a cytoprotection activation from DMF, a RT² Profiler Oxidative Stress Plus PCR Array (Qiagen) was used. This array measures 84 genes related to oxidative stress and Nrf2 (**Figure 56A**). Pathway enrichment analysis from the subset of genes differentially expressed from DMF versus H_2O_2 showed that DMF increases the detoxification of ROS, and increases cell response to stress, metabolism and glutathione synthesis recycling (**Figure 56B**). On the other hand, pathway enrichment analysis from the set of genes differentially expressed only in H_2O_2 group showed an increase in the TP53 Metabolic Genes and decrease in Glutathione metabolism and decrease in drug metabolism in cytochrome P450 proteins (**Figure 56C**).

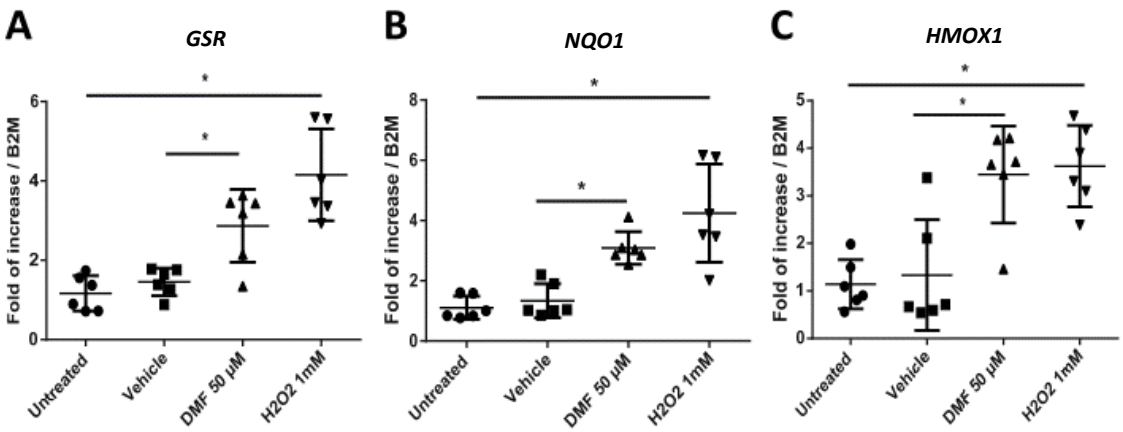

Figure 55. Nrf2 target genes expression following DMF 50 µM or H_2O_2 1mM treatment for 3h. The three target genes tested, (**A**) HMOX1, (**B**) NQO1 and (**C**) GSR were upregulated following treatment of wither DMF 50 µM or H2O2 1mM. HMOX1= Heme Oxygenase 1, NQO1= NAD(P)H Quinone Dehydrogenase 1, GSR= Glutathione-Disulfide Reductase. (n=6) * $p < 0.05$, n= 6 biological replicates.

A

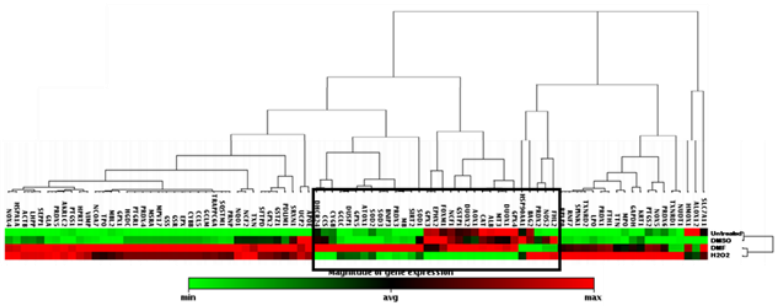

B

DMF Upregulated genes		DMF Downregulated genes
AKR1C2	LHPP	HSP90AA1
ATOX1	MBL2	BAG2
BNIP3	NCOA7	
CCS	NQO1	
CYGB	PRDX3	
DHCR24	SFTPD	
DUSP1	SOD1	
GCLC	SOD2	
GCLM	SOD3	
GPX1	TPO	
GPX5	HMOX1	

C

H_2O_2 Upregulated genes	H_2O_2 Downregulated genes
PRDX2	DUOX1
TXNRD1	DUOX2
FHL2	GPX3
NOS2	CAT
NUDT1	GPX4
	ALB
	EPHX2
	GSTP1
	AOX1
	MT3
	NCF1
	FOXM1

D

DMF Upregulated pathways	DMF Downregulated pathways
Detoxification of Reactive Oxygen Species_Homo sapiens_R-HSA-3299685	Cellular response to heat stress_Homo sapiens_R-HSA-3371556
Cellular responses to stress_Homo sapiens_R-HSA-2262752	Cellular responses to stress_Homo sapiens_R-HSA-2262752
Metabolism_Homo sapiens_R-HSA-1430728	
Glutathione synthesis and recycling_Homo sapiens_R-HSA-174403	

E

H2O2 Upregulated pathways	H2O2 Downregulated pathways
Detoxification of Reactive Oxygen Species_Homo sapiens_R-HSA-3299685	Metabolism_Homo sapiens_R-HSA-1430728
TP53 Regulates Metabolic Genes_Homo sapiens_R-HSA-5628897	Detoxification of Reactive Oxygen Species_Homo sapiens_R-HSA-3299685
Metabolism of nucleotides_Homo sapiens_R-HSA-15869	Thyroxine biosynthesis_Homo sapiens_R-HSA-209968
Regulation of lipid metabolism by Peroxisome proliferator-activated receptor alpha (PPARalpha)_	Amine-derived hormones_Homo sapiens_R-HSA-209776
	Cellular responses to stress_Homo sapiens_R-HSA-2262752

Figure 56. Human Oxidative Stress Plus RT² Profiler PCR Array was used to investigate differential expression of an injury stimulus (H_2O_2) or a cytoprotective stimulus (DMF). (**A**) Heatmap of the PCR array, a subset of genes differentially expressed from DMF versus H_2O_2. (**B**) List of genes up and down regulated in the DMF group versus H_2O_2. (**C**) List of genes up and down regulated in the H_2O_2 group versus DMF. (**D**) Pathway enrichment analysis of the genes up and down regulated in the DMF group. (**E**) Pathway enrichment analysis of the genes up and down regulated in the H_2O_2 group.

4.2.1.4 Role of Nrf2 in paracetamol-induced hepatotoxicity

The cytoprotective properties of DMF were tested in HLCs in an established model of paracetamol-induced hepatotoxicity (91). First, a concentration response was employed to test the paracetamol toxicity and determine IC50. HLCs at day 18 were incubated with 10 mM, 20 mM, 30 mM, 40 mM, 50 mM, 100 mM for 24 h. After treatment, total ATP was quantified (CellTiter-Glo – Promega). All the concentrations apart from 10 mM showed a significant decrease of ATP content when compared to vehicle (DMSO) (**Figure 57A**). Following quantification, IC50 was determined to be 35.58 mM (**Figure 57B**). Paracetamol 30mM was selected to induce hepatotoxicity as it is close to the IC50 concentration and it can be prepared with increased reproducibility than 35.58 mM.

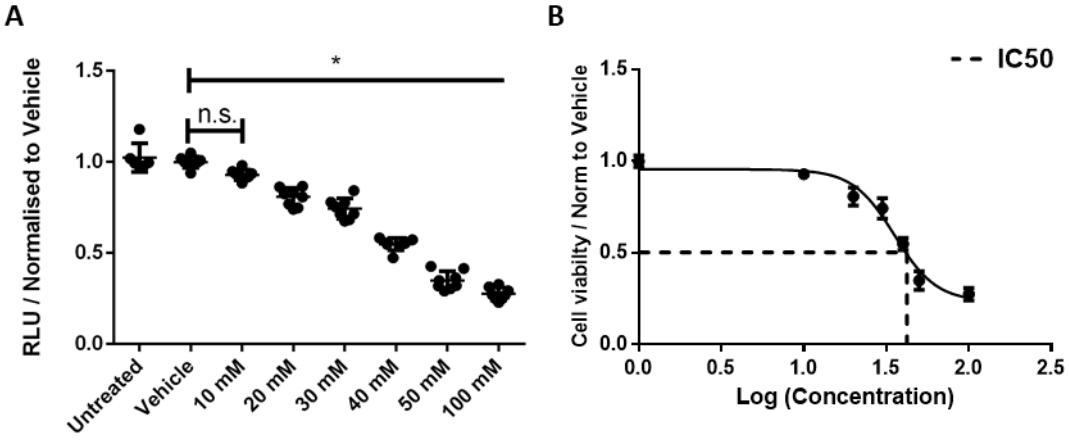

Figure 57. Paracetamol dose response toxicity following 24 h treatment. HLCs were treated with 10 mM, 20 mM, 30 mM, 40 mM, 50 mM, 100 mM for 24 h. Following treatment, (**A**) total ATP content was quantified and (**B**) IC50 was calculated. N=8 replicates from a plate, n.s.=non-significant, *=$p < 0.05$. Vehicle was kept at DMSO 1%, paracetamol concentrations from 40 to 100 mM contained > 1% DMSO.

Next, the cytoprotective properties of dimethyl fumarate were tested in HLCs in an established paracetamol-induced hepatotoxicity (91). To counteract drug-induced hepatotoxicity two concentrations of DMF were used, 10 µM and 50 µM. The concentrations were chosen due to recent studies showing a dose dependent DMF efficacy (196). HLCs at

day 18 were treated with DMF or vehicle for 24 hours. Following pre-incubation with DMF, HLCs were treated with paracetamol 30 mM for a further 24h. Total ATP and Caspase 3/7 induction were quantified. Pre-treatment with both DMF 10 µM and 50 µM significantly reduced ATP loss when compared to paracetamol 30 mM alone. Interestingly, DMF exhibited a concentration-dependent response. HLCs pre-treated with DMF 10 µM displayed a higher level of protection against paracetamol toxicity when compared with pre-treatment DMF at 50 µM (**Figure 58A**). Similar results were obtained after Caspase 3/7 induction quantification. Pre-treatment with DMF 10 µM inhibited the induction of Caspase 3/7 more profoundly than pre-treatment with DMF 50 µM (**Figure 58B**).

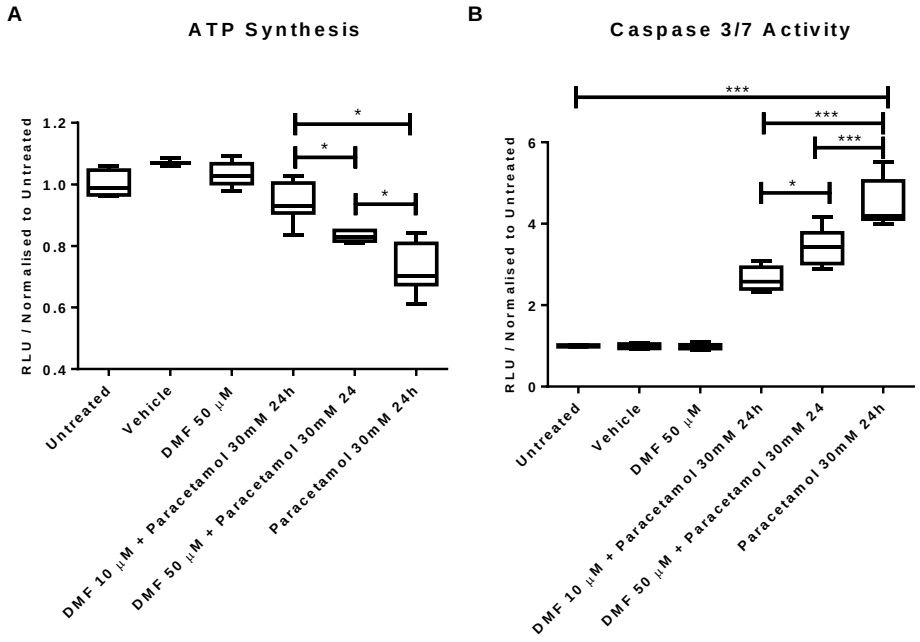

Figure 58. DMF exhibits protective effects upon paracetamol exposure in concentration dependent manner. Pre-treatment of either DMF 10 µM or 50 µM 24 h before paracetamol 30mM treatment prevented a decrease of (**A**) ATP or (**B**) caspase 3/7 induction. DMF 10 µM was more effective than in DMF 50 µM in both ATP and caspase 3/7 induction. n= 6 replicates from a plate, ***=$p < 0.001$, *=$p < 0.05$.

Based on these results, DMF 10 µM exhibits increased cytoprotective properties than DMF 50 µM. Therefore DMF 10 µM was chosen for the subsequent experiments.

To assess whether the cytoprotective properties of DMF were dependent of the Nrf2 pathway a combination of pharmacological inhibition of Nrf2 with DMF were tested in a paracetamol injury model. Brusatol was chosen as a Nrf2 inhibitor as it produces a rapid and transient inhibition of Nrf2 (202). Protein translation inhibition is the proposed mechanism of action of Brusatol (203). First, viability of the drug in HLCs was tested. HLCs at day 18 were treated with 150 nM, 250 nM, 500 nM, 1 µM or vehicle for 24 h, concentrations chosen based on the literature (202). Following compound treatment, total ATP was quantified. No significant changes were detected in any of the concentrations used after 24 h (**Figure 59**). Therefore 1 µM was chosen as a working concentration to ensure efficacy.

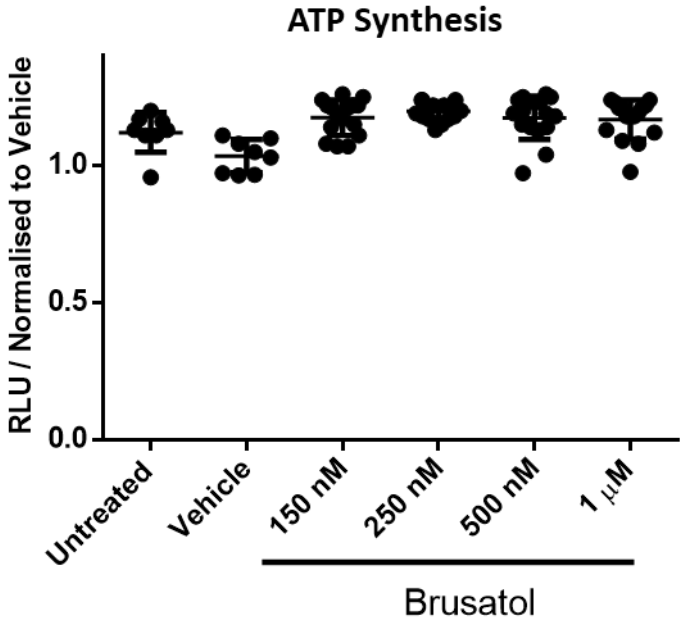

Figure 59. Brusatol showed no depletion of ATP synthesis in HLCs after 24h incubation. HLCs at day 18 were treated with 150 nM, 250 nM, 500 nM, 1 µM or vehicle for 24 h. Following compound treatment, total ATP was quantified. No significant changes were detected. n=8 replicates from a plate.

Next, inhibition of Nrf2 upon Brusatol administration was tested. HLCs were treated with Brusatol 1 µM. Total protein was collected at 0, 0.5, 2, 6 and 24 h after treatment. Western blot shows a decrease in Nrf2 at 2 h followed by a complete loss of Nrf2 at 6 and 24 h (**Figure 60**).

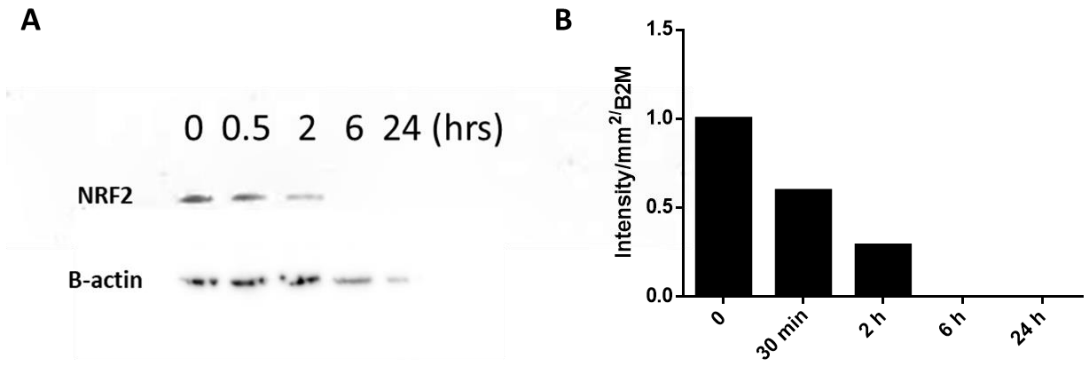

Figure 60. Inhibition of Nrf2 upon Brusatol treatment. Total protein was collected from HLCs. (**A**) Western Blot shows a rapid inhibition of Nrf2 upon Brusatol administration. 2 h after treatment, there is a partial reduction in Nrf2. 6 h following brusatol administration no Nrf2 is detected, this is maintained 24 h after administration. B-actin variability could be due to changes in protein concentrations as not the same amount of protein was loaded to perform the wester blot or by side effects of Brusatol treatment (**B**) Densitometry quantification of Nrf2, calculation was normalised by B-actin expression, quantification performed using ImageJ.

Finally, to test whether Nrf2 is required for the cytoprotective properties of DMF, HLCs were pre-treated with a combination of DMF and Brusatol for 24h prior to paracetamol 30 mM incubation for 24 h. Following treatment, total ATP was quantified. The protective effect of the pre-treatment of DMF was lost when DMF was combined with Brusatol (**Figure 61**). These results demonstrate the requirement of Nrf2 in the cytoprotective properties of DMF.

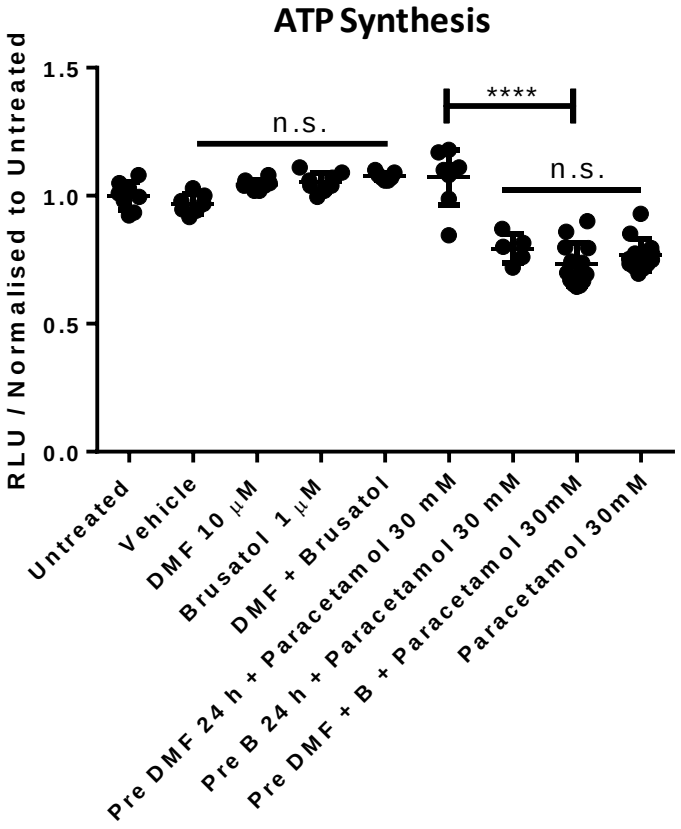

Figure 61. Nrf2 is required for DMF to protect HLCs from paracetamol. HLCs at day 18 were pre-treated with DMF 10 μM, Brusatol 1 μM or a combination of the two for 24h, prior to paracetamol 30mM administration. Nrf2 is required for DMF to protect HLCs as the combination of DMF and Brusatol blocks the protective effects of DMF. n>6 replicates from a plate. ****=p < 0.0001, n.s.= non-significant, B = Brustol.

4.2.1.5 Cytoprotective studies of DMF in a paracetamol-induced toxicity model

The efficacy of DMF to protect hepatocytes from paracetamol-induced toxicity was compared with the current clinical treatment for paracetamol-induced injury, N-acetylcysteine 1 mM (60). In addition, a combination of DMF + NAC was performed to determine any potential synergic effects. First, a 24 h pre-treatment of dimethyl fumarate 10 µM, NAC 1mM or combination followed by 24 h of paracetamol 30mM was performed (**Figure 62A**). Secondly a co-treatment of paracetamol 30mM with DMF, NAC or in combination for 24 h was performed (**Figure 62B**). Lastly, HLCs were treated with paracetamol 30mM for 24 h followed by 24 h of dimethyl fumarate 10 µM, NAC 1 mM or a combination of the two. (**Figure 62C**). Assessment of the cytoprotective effects were analysed by total ATP production.

In all cases, DMF showed a significant increase in ATP content when compared to paracetamol. NAC showed a significant ATP increase when compared to paracetamol in pre-treatment and co-treatment but not in the post-treatment. Combination of DMF with NAC showed a

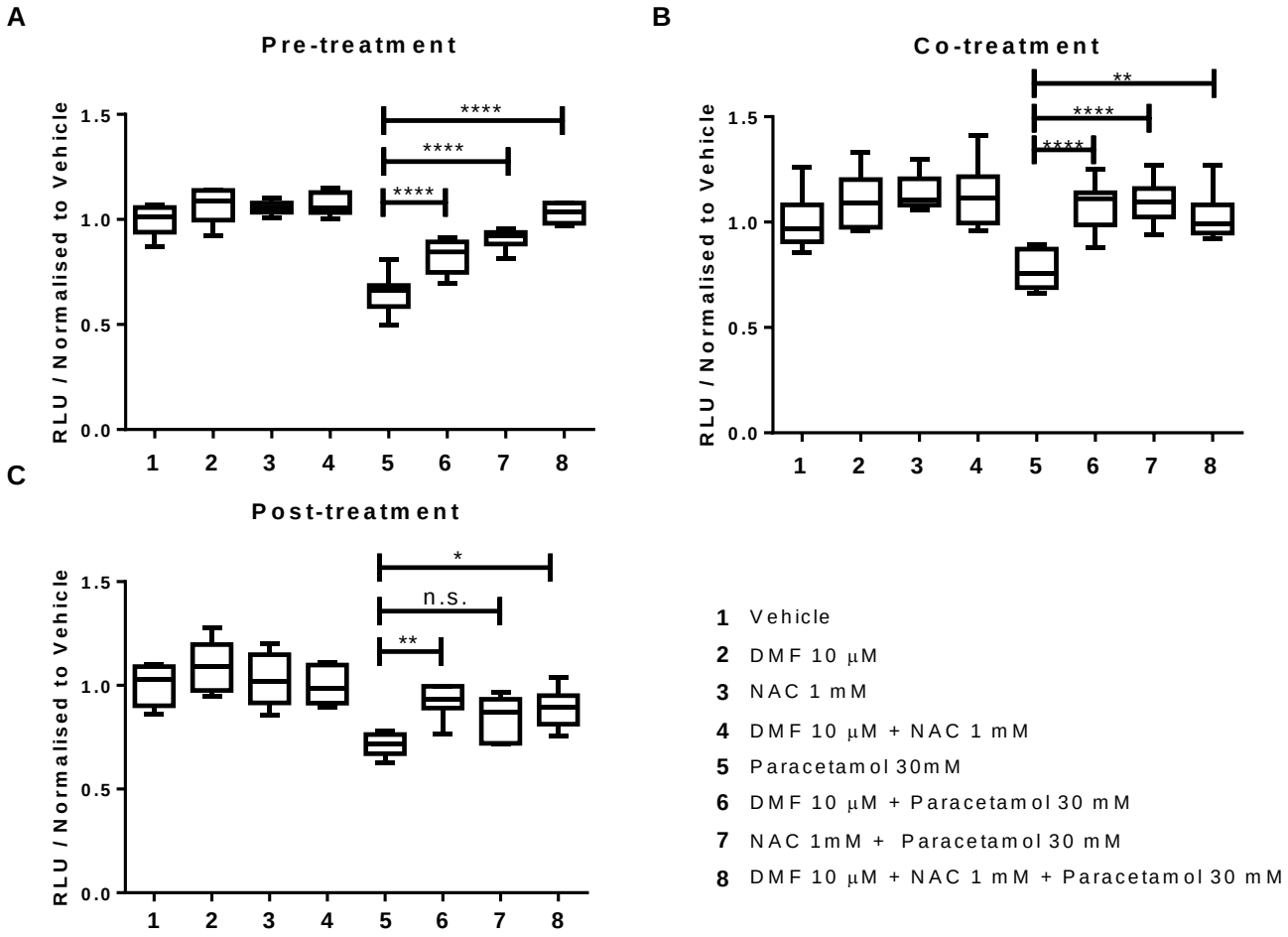

Figure 62. DMF 10 µM protects HLCs from paracetamol-induced hepatoxicity. (**A**) Pre-treatment of 10 µM DMF, NAC 1 mM or combination of the two for 24 h prior to the administration with 30mM of Paracetamol for 24 h shows a reduced loss of ATP in HLCs when compared to 30 mM paracetamol alone. (**B**) Co-treatment of DMF 10 µM, NAC 1 mM or combination of the two with paracetamol 30mM for 24 h shows a reduced loss in total ATP when compared to paracetamol 30 mM alone (**C**). Post-treatment of DMF 10 µM after a 24 h incubation with paracetamol 30mM shows a reduced loss of total ATP when compared to paracetamol 30 mM alone. * $p < 0.05$, ** $p < 0.01$, **** $p < 0.0001$ n=6 replicates from a plate.

significant increase in ATP in the pre- and post- treatments groups but not in the co-treatment group (**Figure 62**).

Cell painting assay was used for further validation of the cytoprotective effects of dimethyl fumarate. Pre-, co- and post- treatment were stained and imaged using the operetta microscope. Using cell segmentation, 86 different image-based features were used to create a morphological profile (**Figure 63**), a python code was used for data normalisation and sample clustering. Un-biased clustering of the different treatments was done based on the morphological profiling (**Figure 64A**). Principal Component Analysis (PCA) was performed for data reduction (**Figure 64B**). Both sample clustering graph and PCA plot paracetamol-treated group showed a distinct profile when compared with the dimethyl fumarate-treated groups or vehicle (**Figure 64**).

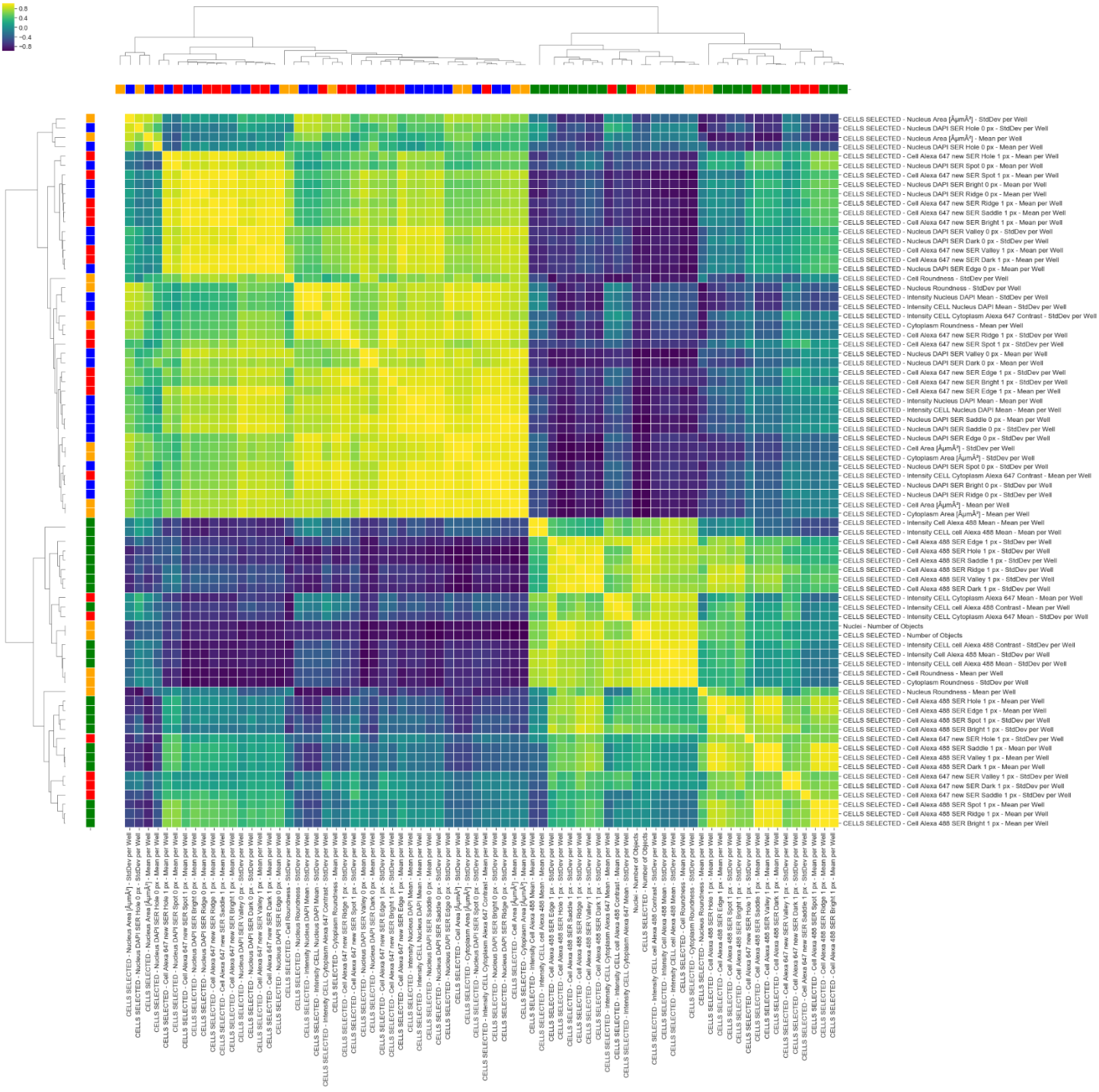

Figure 63. Correlation map of the DMF cytoprotection quantification by Cell Paint profiling. Correlation map of the different features extracted from each cell.

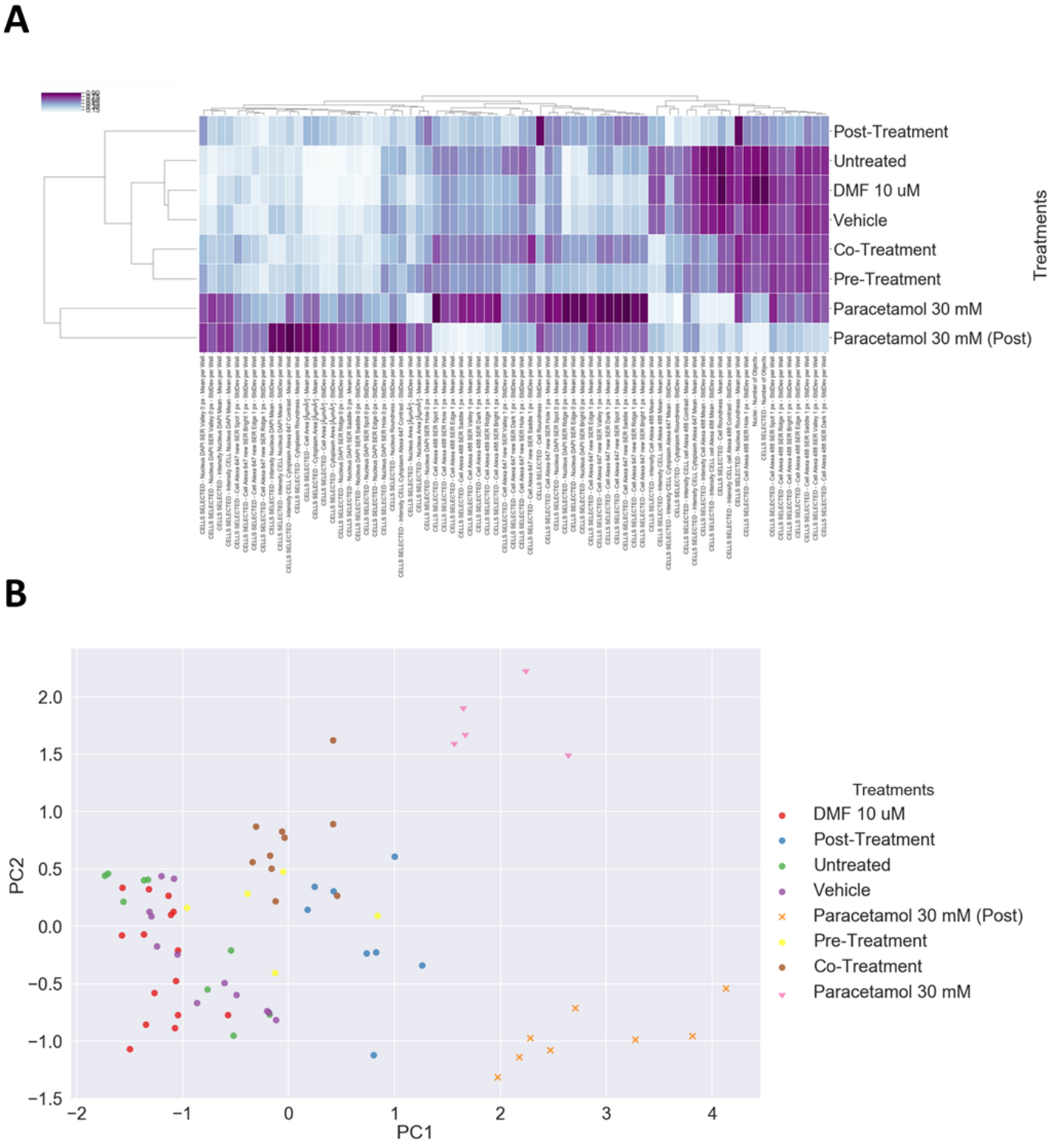

Figure 64. DMF cytoprotection quantification by Cell Paint profiling. (**A**) Cluster of the different populations based on similarities between the profiling of the different features. (**B**) PCA plot of all the different features comparing the different populations. n = 8 replicates from a plate.

4.2.2 Assessment of DMF effects in a Zebrafish paracetamol injury *in vivo* model

4.2.2.1 Zebrafish lines

Zebrafish larvae were used to validate the efficacy of DMF in an *in vivo* situation. Two different lines were used for these studies. First a wild-type WIK line was used for concentration and assay optimisation. Following this, a zebrafish liver GFP reporter line (Tg(-2.8lfabp:GFP)) was used to quantify changes in GFP fluorescence due to liver injury (146,147). This is a GFP reporter line for the liver-type fatty acid-binding protein (LFABP) which is only expressed in the hepatocytes. The zebrafish experiments were performed at 3 days post fertilisation (d.p.f) following zebrafish hatching. Experiments were stopped 5 d.p.f. in accordance with Home Office Regulations.

4.2.2.2 Cytoprotection studies with DMF in a zebrafish model of paracetamol injury

The cytoprotective properties of DMF were tested with the wild-type WIK line. Zebrafish embryos at 3 d.p.f. were pre-treated with DMF 2.5 µM for 6 h prior to paracetamol treatment 10 mM for 42 h. After treatment, survival was determined by both mobility test and heartbeat of the larvae. An embryo was marked as dead if no mobility and lack of heartbeat were detected upon magnification lenses observation. Dimethyl fumarate 2.5 µM exhibited significant larvae survival when compared to Paracetamol 10 mM alone (**Figure 65**)

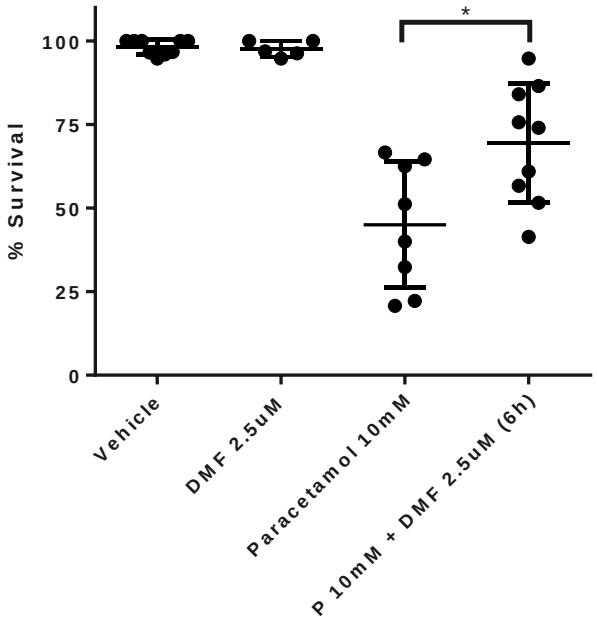

Figure 65. Protective effects of DMF in a zebrafish model of liver injury. WiK-larvae were treated with paracetamol 10mM (P 10 mM) for 42 hours or with a pre-treatment of 2.5uM of dimethyl fumarate for 6 hours, vehicle and dimethyl fumarate (DMF) alone were used as controls. Each dot represents the survival percentage of a biological replicate containing 30-35 zebrafish. Following treatment, survival was determined calculating the number of alive fish versus the initial population. * =p < 0.05. n>5.

4.2.2.3 Development of quantitative analysis to liver injury

Following this, a zebrafish liver GFP reporter line (Tg(-2.8lfabp:GFP)) was used to quantify changes in GFP fluorescence upon liver injury (146,147). Two different methods were developed for fluorescence acquisition, first a live imaging high throughput platform using the Operetta microscope; Secondly, a total larva fluorescence acquisition using a fluorescence plate reader.

For the live imaging, after paracetamol exposure, single larvae were embedded in agarose 0.75% wt/vol in a 96-well plate. Following embedding, imaging was performed to assess system performance. Due to the high variability in terms of orientation and plane focusing (**Figure 66**), an orientation tool developed by Wittbrodt et al was 3D

printed by CNCvac 3D Printing (**Figure 10**) (148). Briefly, 0.75%, wt/vol agar was added into the 96-well plate following the positioning of the orientation tool (**Figure 10**). Once the agar solidified, removal of the orientation tool creating an agar 'V' shape where the larvae could be position, increasing reproducibility in terms of focus plane and orientation (**Figure 66**).

Following zebrafish positioning standardisation, a supervised machine learning algorithm was developed for automatic zebrafish larva detection following automatic GFP+ liver segmentation and fluorescence quantification (**Figure 67**). A similar texture-based method as discussed in chapter 3 was used. First, manual annotation of both fish and background was uploaded into the algorithm. Following fish identification, selection of the fish ROI was performed based on shape and intensity features. After fish segmentation, liver detection was performed using a similar approach with and increase reproducibility. This system allows a fast and unbiased quantification of liver intensity. On the other hand, a plate reader was used to detect GFP fluorescence. Following paracetamol exposure, single embryos per well were placed into a black 96-well plate and green fluorescence was measured. Fluorescence quantification using both methods allows a detection of fluorescence loss upon paracetamol exposure for 48 h (**Figure 68**).

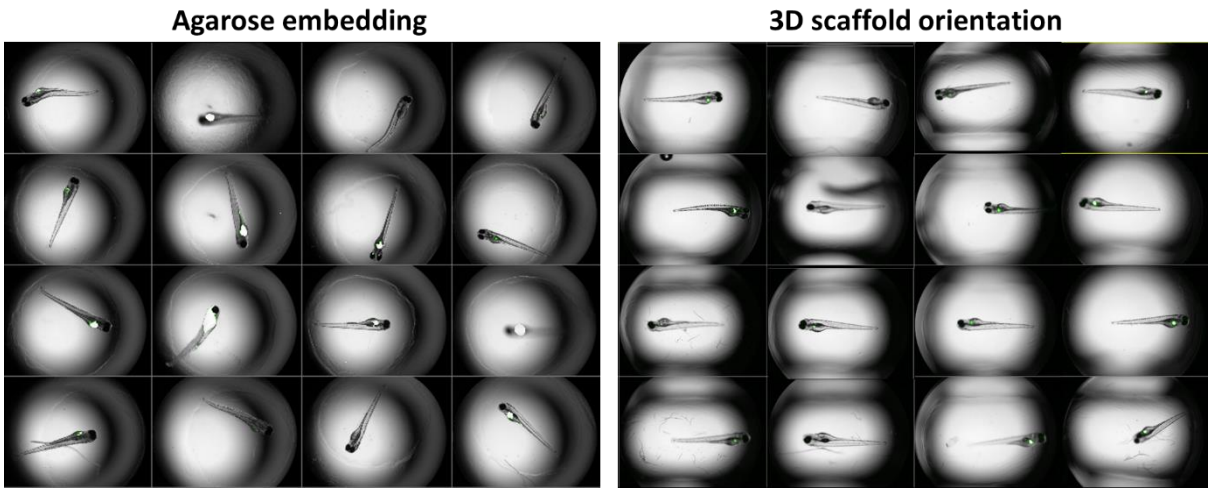

Figure 66. Methods for larvae orientation for live imaging. Left, manual agarose embedding. Right, 3D scaffold orientation tool. 3D orientation allows a reproducible position in terms of focus plane and orientation.

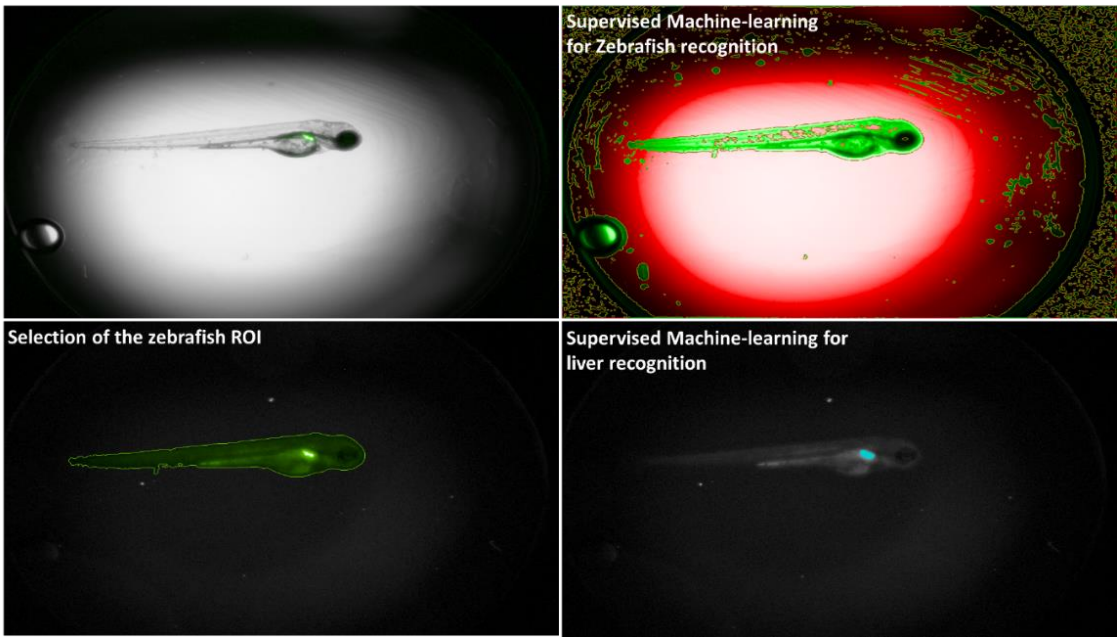

Figure 67. Automatic zebrafish segmentation for image analysis. Supervised machine learning for automatic zebrafish recognition using pixel texture was used to exclude background (red) from zebrafish (green) following zebrafish of region of interest refinement by size and shape. Next, supervised machine learning was used for GFP+ liver recognition.

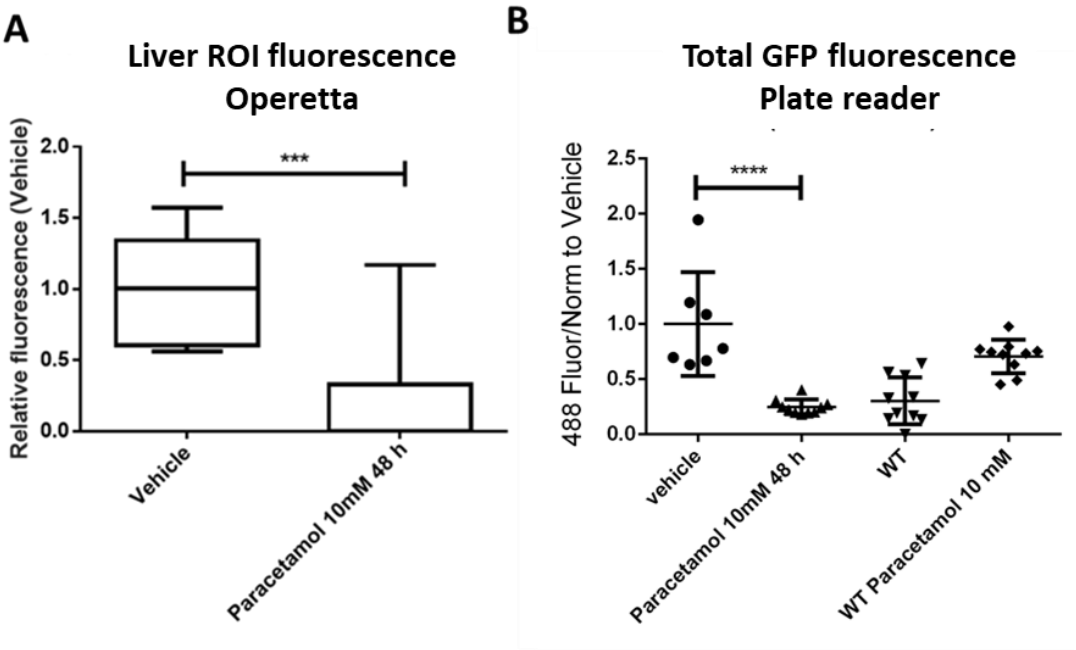

Figure 68. Loss of GFP upon paracetamol 10 mM treatment for 48 h was detected in both platforms. Quantification of the GFP signal loss after paracetamol 10 mM was quantified using (**A**) high content imaging or (**B**) total fish fluorescence using the plate reader. Wild type lines were used to detect any potential fish autofluorescence. n > 6 zebrafish embryo. ***=p < 0.001, ****=p < 0.0001. WT = wild type.

4.2.2.4 Quantification of DMF cytoprotection upon paracetamol-induced injury

Larvae were pre-treated with dimethyl fumarate 2.5 µM for 6 h followed by paracetamol treatment for 42 h. This was compared to vehicle and DMF 2.5 µM and paracetamol alone. Wild-type larvae were used to subtract larvae autofluorescence. In both systems, GFP fluorescence was significantly increased in the DMF pre-treatment group when compared to a paracetamol group; In addition, DMF 2.5 µM treatment for 6 h did not affect GFP levels when compared to vehicle (**Figure 69**).

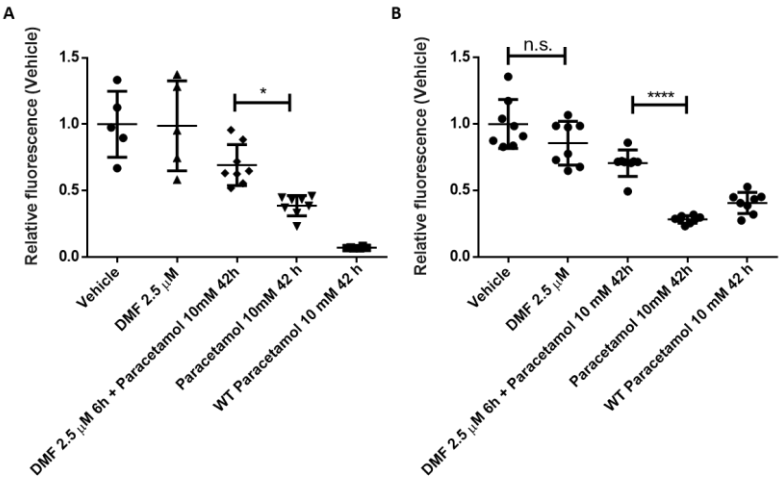

Figure 69. Pre-treatment with DMF 2.5 µM protects zebrafish from paracetamol 10 mM induced injury. Quantification of the GFP from (**A**) high content imaging or (**B**) total fish fluorescence using the plate reader shows a reduction on GFP loss on the DMF pre-treated group when compared to paracetamol 10 mM. n > 3 each dot represents a zebrafish embryo.

4.3 Discussion

Despite advances in liver biology and human liver injury management, DILI is maintained as the leading cause of acute liver failure (178). Paracetamol-induced hepatotoxicity is one of the most common causes of DILI (179), and it is characterised by major hepatocyte death due to an excess in NAPQI production. Recent reports indicate that following the initial injury, the remaining hepatocytes enter into cellular senescence via TGB-b1 activation (57). This prevents the hepatocytes from restoring organ homeostasis leading to liver failure. Current treatments include supportive treatments such as activated charcoal or gastric emptying or therapeutic agents that detoxify the liver such as N-acetylcysteine (60). Despite its efficacy, NAC has to be administrated within the first 8-10 h following paracetamol overdose (183). In the absence of treatments that restore liver function, organ transplant is the only treatment to overcome liver failure. Despite its success, liver transplant is not a scalable alternative for acute

diseases. Therefore, novel approaches are needed to overcome acute liver failure. Nrf2 activation upon injury has been proposed as potential therapy to treat DILI and induce tissue repair.

Nrf2 is a transcription factor which plays a key role in the regulation and modulation of key pathways involved in oxidative stress management, cell proliferation and inflammation modulation (117,187). Consequently, pharmacological activation of Nrf2 following DILI might represent a novel therapy to restore liver homeostasis. Nrf2 has been shown to be essential for managing paracetamol overdose. Nrf2-knockout mice exhibited a higher degree of injury or even death when treated with non-lethal doses of paracetamol (106,110,111). Opposite effects were observed when hepatocyte Keap1-knockout mice exhibited increased resistance to toxic doses of paracetamol (112). Moreover, a different study showed Nrf2 nuclear translocation following paracetamol administration in a mouse model of paracetamol overdose, where Nrf2 nuclear translocation was observed in both toxic and non-toxic concentrations (113). Interestingly, upregulation of Nrf2 target genes was not detected at the toxic concentration despite detection of Nrf2 nuclear translocation. More recently, the potential interaction of NAPQI and Nrf2 during paracetamol overdose was investigated (114). Authors report how NAPQI can activate Nrf2 nuclear translocation by either modifying cysteine residues of Keap1 or by depleting cellular glutathione. While NAPQI can activate Nrf2, during a paracetamol overdose Nrf2 gene upregulation is stopped (113,114). The absence of gene upregulation might be due to the level of injury developed by the paracetamol overdose, resulting in a disruption of cellular processes involved in gene transcription or cell metabolism.

Therefore, pharmacological activation of Nrf2 might represent a promising approach to prevent liver failure following paracetamol overdose. Recent work has reported the beneficial effects of the pharmacological activation of Nrf2 in the context of liver disease

(189,190). Within the different Nrf2 inducers, fumaric acid esters have been proposed as potent Nrf2 inducers due to their electrophilic activity (204). Electrophilic compounds react with Cys-151 in Keap1 activating Nrf2 (6,18). Dimethyl fumarate is a fumaric acid compound approved for the treatment of psoriasis and relapsing-remitting multiple sclerosis (121,192). DMF has been shown to induce gene expression of Nrf2 target genes such as glutathione transferases (*GST*), *NQO1* or *HMOX1* (194,205,206).

In this chapter, the potential protective effects of DMF in a paracetamol-induced hepatotoxicity model were investigated. This was first tested *in vitro* using stem cell-derived hepatocyte-like cells. Findings from the *in vitro* work were validated *in vivo* using a zebrafish model of liver injury.

In HLCs, Nrf2 nuclear translocation analysis following DMF administration was performed by using high content imaging. By implementing single cell imaging analysis, it was possible to perform an unbiased analysis of single cell dynamics. The use of single cell analysis allows for visualisation of cell population shifts upon time and treatment. This single cell imaging analysis pipeline could be applied to any protein upon pharmacological treatment or gene alteration, providing a powerful tool for biomedical research.

Following analysis, it was possible to detect Nrf2 nuclear translocation upon time, detecting Nrf2 nuclear accumulation as early as 30 minutes upon administration, with a peak at 2 hours and returning to basal levels 24 h post administration. Surprisingly, negative controls showed a similar trend in Nrf2 nuclear translocation dynamics upon time (**Figure 52**, **Figure 53**). These results suggested that Nrf2 nuclear translocation upon time was not a specific effect of any of the treatments but from medium change. This highlights the sensitivity of the Nrf2 pathway as a master regulator of cell stress where minor

changes in the culture homeostasis can trigger Nrf2 nuclear translocation (207). Medium shock change could explain this phenomena, where culture medium not buffered properly can induce both heat shock effects and the Nrf2 pathway (207). By preincubating the medium, tips and plate holder prior to administration, Nrf2 pathway activation from medium changes were minimised (**Figure 54**). A recent study by Bischoff et al showed similar results using HepG2 cells (208). In this study Nrf2 was tagged with GFP and Nrf2 dynamics were investigated following xenobiotic exposure. Nuclear translocation reached its peak at 2 h following compound administration.

Following assay optimisation, single cells analysis showed a transient Nrf2 nuclear translocation peaking at 2h post administration of DMF. In contrast, H_2O_2 1 mM displayed a marked increase on nuclear Nrf2 positive cell population up to 24 hours post treatment (**Figure 54**). These results reflect changes of Nrf2 dynamics upon a cytoprotective Nrf2 activation by DMF versus a stress response Nrf2 activation by H_2O_2. It has been shown than DMF not only activates Nrf2 but it also inhibits Nf-kb activation (131,194); an injury stimulus such as H_2O_2 would trigger multiple pathways for cell stress management such as NF-κB and Nrf2 (209). These differences could explain changes in Nrf2 nuclear translocation dynamics from DMF and H_2O_2.

Gene transactivation upon Nrf2 nuclear translocation was analysed following exposure to DMF and H_2O_2. Gene expression was analysed 3 h post administration to detect the early gene response after Nrf2 nuclear translocation. *GSR*, *NQO1* and *HMOX1* were selected as representative Nrf2 target genes. DMF and H_2O_2 induced the gene expression of the three target genes (**Figure 55**). *GSR* is a central enzyme of cellular antioxidant defence replenishing glutathione. *NQO1* reduces quinones to hydroquinones, accumulation of quinones results in the production of radical species. Finally, *HMXO1* catabolises the free heme and produces carbon monoxide (CO) and up-regulates an

anti-inflammatory cytokine interleukin 10 (IL-10). To understand the differences in Nrf2 gene regulation between DMF and H_2O_2, an oxidative Stress PCR Array was used. This array measures 84 genes related to ROS metabolism, antioxidants, pathway activity signature genes involved in oxidative stress and oxygen transporters. Heatmap visualisation of the results (**Figure 56**), shows a subset of genes differentially expressed from DMF vs H_2O_2. Changes in the Nrf2 nuclear translocation dynamics between DMS and H_2O_2 also translate in gene response. HLCs treated with DMF displayed an increase in metabolism and anti-oxidative stress-related functions (**Figure 56B**) (196). On the other hand, HLCs treated with H_2O_2 displayed an increase in TP53 and a decrease in drug metabolism (**Figure 56C**). These changes could be related to an increase in inflammation during the Nrf2 activation (59).

In this study, paracetamol was solubilised in DMSO, this could increase cell toxicity as low concentrations of DMSO (>1%) can induce cell toxicity (171). In addition, DMSO is a direct substrate of CYP 2E1 (210). This could potentially alter paracetamol metabolism in HLCs. Higher concentrations than 1 % of DMSO were used in the paracetamol IC50 assay (**Figure 57**). Here, the paracetamol concentrations from 40 to 100 mM contained > 1% DMSO. As result, increased cell toxicity could have been observed in the higher paracetamol concentrations. Further work could be focused to investigate the relationship of DMSO-induced toxicity in combination to paracetamol-induced toxicity. To do so, a comparison of paracetamol-induced toxicity resuspended in DMSO and H_2O could be performed. Another possibility would be to use a CYP P450 inhibitor such as 1-aminobenzotriazole to test the toxicity of DMSO as a vehicle for paracetamol (211). To minimise DMSO-induced toxicity, the maximum DMSO concentration used in the rest of the studies was kept at 1 %.

Cytoprotective properties of DMF were tested in a paracetamol-induced toxicity model. First, HLCs were pre-treated with DMF for 24 h followed by paracetamol for 24 h. Both DMF concentrations showed an increase in HLCs survival. Interestingly, DMF showed a dose dependent efficacy where DMF 10 µM had higher cytoprotective effects than DMF 50 µM. These results coincide with a recent work published by Saidu et al (196) where they showed how DMF concentrations higher than 25 µM induced oxidative stress-reducing Nrf2 pathway activation and leading to a reduced cytoprotection.

The role of Nrf2 in the cytoprotective properties of DMF was tested by inhibiting Nrf2 with Brusatol. Brusatol provokes a rapid inhibition of Nrf2 (202). Nrf2 inhibition could be achieved as a result of protein translation inhibition as Nrf2 is constantly produced in the cell. Potential off-target effects of protein inhibition should be investigated in the future. In HLCs, reduction of Nrf2 was detected as early as 2 h following Brusatol administration. There was no Nrf2 protein detection at 6 or 24 h post administration. Coadministration of DMF and Brusatol for 24 h prior to paracetamol injury obliterated the protective effects of DMF (**Figure 61**). This might indicate the requirement of Nrf2 for the protective effects of DMF.

Following DMF concentration optimisation, DMF efficacy was compared with the current clinical treatment for paracetamol-induced injury, N-acetylcysteine. The efficacy was tested in three different combinations: pre-treatment, co-treatment and post-treatment following paracetamol injury.

In all cases, DMF showed a significant increase in ATP content when compared to paracetamol. NAC showed a significant ATP increase when compared to paracetamol in pre-treatment and co-treatment but not in the post-treatment group (**Figure 62**). Combination of DMF with NAC showed a significant increase in ATP in the pre and post

treatments but not in the co-treatment. Even though DMF treatment showed an increase in cell viability in both pre and co treatments, these scenarios have a reduced clinical relevance in the context of paracetamol overdose. The clinical scenario for a paracetamol overdose would require a post-treatment intervention. Notably, post-treatment with DMF after paracetamol treatment showed a significant increase in cell survival, which was not detected in the NAC treated group; with similar results in the combination of DMF+NAC. Current guidelines suggest administering NAC within the first 8-10 h following paracetamol overdose consumption (182). These results could open a new opportunity to treat paracetamol overdose patients by expanding the treatment window. On the other hand, pre and co treatment results could be applied in other clinical contexts as shown by Takasu et al where pre-treatment of DMF ameliorated liver ischemia reperfusion injury in mice (212).

The relevance of the *in vitro* findings were tested in an *in vivo* zebrafish model of paracetamol injury. The zebrafish model was selected because it allows a rapid assessment of liver damage and has overlapping targets and drug metabolism pathways found in humans. In zebrafish, Nrf2a and Nrf2b are paralog genes to the human Nrf2 (213). Nrf2a seems to be regulated similarly to Nrf2 upon oxidative stress whereas Nrf2b might be a negative regulator during embryonic development (214). Expression of Nrf2 paralog genes make zebrafish a good model to study the protective effects of DMF during liver disease. By working with the Tg(-2.8lfabp:GFP) zebrafish line, it is possible to quantify hepatocyte damage due to GPF fluorescence changes (147). In a recent study, Vliegenthart et al, showed how GFP loss was linked with hepatocyte injury in a DILI model (147).

In this study, I developed two different methods to detect GFP changes upon paracetamol injury. First, a high content imaging method was developed for single embryo live imaging and liver fluorescence

quantification. Secondly, total fluorescence was quantified in live single embryos using a fluorescence plate reader. DMF treatment for 6 h did not affect normal liver development as no significant changes in fluorescence were detected (**Figure 69**). In addition, paracetamol treatment reduced zebrafish survival (**Figure 65**) and GFP fluorescence (**Figure 68**). Pre-treatment of DMF for 6 h prior to paracetamol administration showed an increase in GFP fluorescence (**Figure 69**). This was quantified using both plate reader fluorescence quantification and by high content imaging.

By moving the *in vitro* findings into a more translational model, it was possible to test the protective effects of DMF in a whole organism where multiple cell types are involved in the generation and resolution of the injury. Further work is required to develop a post-treatment scenario to validate the *in vitro* findings, and NAC comparison would be necessary for efficacy comparison.

In summary, this chapter showed the cytoprotective properties of DMF in the context of a paracetamol injury in both *in vitro* and *in vivo* models. These effects are Nrf2 dependent. The following chapter will describe RNA sequencing analysis performed in the different treatments of DMF and paracetamol to further understand the mechanism involved in the cell protection *in vitro* and *in vivo*.

CHAPTER FIVE

TRANSCRIPTOMIC ANALYSIS OF DRUG-INDUCED HEPATOTOXICITY WITH AND WITHOUT DIMETHYL FUMARATE TREATMENT

5.1 Introduction

Dimethyl fumarate exhibited cytoprotective effects in HLCs challenged with paracetamol. DMF was administered pre- paracetamol exposure, during paracetamol exposure and following paracetamol exposure. The *in vitro* findings were corroborated on a Zebrafish model of paracetamol-induced toxicity. In these studies, the fish were pre-treated with DMF prior to paracetamol exposure, and displayed reduced liver damage. RNA sequencing (RNA-seq) analysis was performed to dissect the underlying mechanism of cell protection in each scenario.

5.1.1 Transcriptomic analysis of DMF cytoprotection

Recent advances in Next Generation Sequencing (NGS) allow the sequencing of the transcriptome in a high throughput manner at a reduced cost (215). Therefore RNA-seq has become a widely used tool to study biological changes. Following RNA acquisition, cDNA library preparation from the transcript is required prior to sequencing. The protocol used for library preparation (QuantSeq 3′ mRNA-Seq Library Prep Kit - Lexogen) generates Illumina-compatible libraries from polyadenylated RNA. This protocol generated only one fragment per mRNA transcript with sample-specific adapters to allow sample multiplexing. After sequencing, raw reads were mapped onto their transcripts using a genome of reference. As the library used only produced one fragment per transcript, gene expression counting can be more accurate. This pipeline generated a file containing gene counts for all the genes per sample.

Following data preparation, differential expression genes (DEGs) identification between conditions was performed. DESeq2 was used for DEGs identification. DESeq2 is an easy-to-use tool for RNA-seq analysis (216). Finally, biological relevance from the identified DEGs

was evaluated. For this gene set enrichment analysis tools were used to identify the relevant biological process involved with the expression changes obtained from the analysis (217,218).

5.1.2 Dimethyl fumarate in the context of liver disease

To date, a few studies have been published on the cytoprotective effects of DMF in liver disease. Brennan et al, showed that DMF effects in mice are tissue specific (205). In the liver, several Nrf2 target genes: *Cdkn1a*, *sqstm1*, *gclc*, *Nqo1*, *Srxn1*, *Akr1b8* were upregulated upon DMF (100 mg/kg) administration. These effects were time dependent with peak stimulation from 6 to 12 hrs.

In the pre-treatment context, Takasu et al showed that DMF pre-treatment ameliorates liver ischemia/reperfusion injury in rats (212). In this study, DMF 25 mg/kg was orally administrated twice a day two days prior to ischemia/reperfusion injury. The DMF treated group showed a significant reduction of several liver injury markers such as aminotransferase (ALT) and malondialdehyde (MDA) as well as an increase of liver ATP. DMF treatment reduced Nf-kb expression as well as several inflammatory mediators such as IL-6, IL-10 or TNF-a. Finally, Sun et al, showed that DMF pre-treatment mitigated ethanol-induced liver injury in mice. In this study, pre-treatment with 25 mg/kg of DMF twice a day for five days prior to ethanol administration showed an increase in survival as well as an increase in blood glucose levels compared to vehicle. This was in part mediated by upregulation of several Nrf2 target genes: *GCLC*, *NQO1* and *HMOX1*.

In the post-treatment scenario, Giustina et al showed that post-administration of DMF 15 mg/kg in rats reduced sepsis-induced inflammation and oxidative stress in the liver (219). Finally, a recent study from Abdelrahman et al, showed that post-administration of DMF 100 mg/kg protected mice from paracetamol-induced injury (220). DMF-treated mice showed a serum decrease in several injury

markers when compared to a paracetamol-treated group. These markers include: serum glutamic oxaloacetic transaminase (SGOT), serum glutamic pyruvic transaminase (SGPT), gamma-glutamyl transferase (GGT) and alkaline phosphatase (ALP). These were linked with a reduction of hepatic Nf-kb activity and TNFa stimulation as well as an increase in HMOX-1 expression. This study was mainly descriptive rather than investigating the mechanism of protection.

Finally, only two studies use DMF in zebrafish models. First, García-Caballero et al showed that DMF inhibits angiogenesis in zebrafish (221). In this study, zebrafish embryos were used at 24 h postfertilization for a further 24 hrs using from 5 to 25 µM of DMF. In our work, we used DMF at a lower concentration (2,5 µM). In our model, no transcriptional changes involved in angiogenesis were detected (**Table 18 and Table 19**). The likely explanation for this is that the zebrafish were used at 72 h post postfertilization instead of 24 h as reported by García-Caballero et al. In addition, effects observed in this study could be due to DMF concentration. This could differ in our model as DMF presents dose-dependent protective effects (196). In addition, Kulkarni et al developed a model of experimental autoimmune encephalomyelitis in adult zebrafish and used dimethyl fumarate validate the model (222) where DMF-treated zebrafish were able to reverse the clinical signs of the encephalomyelitis. Validation of the clinical recovery was focused in clinical assays such as mobility, survival and body weight rather than on mechanistic studies.

This chapter will present the transcriptional changes that take place during hepatocyte exposure to paracetamol and how DMF mediates its protective effects *in vitro* and *in vivo*.

5.2 Results

5.2.1 RNA extraction & Library preparation

The objective was to understand the cytoprotective effects of DMF in the context of paracetamol injury in both HLCs and ZF. In HLCs, pre, co and post treatments were used to investigate any time dependent treatment mechanism. To do so, mRNA sequencing of these models was performed.

DMF cytoprotection was assessed by ATP production. This method is an end-point assay which requires cell lysis hindering RNA collection. To solve this, mirror plates for each treatment were prepared. One plate was used for ATP quantification and the other one for RNA collection.

For zebrafish, total GFP was quantified using the plate reader as shown in the previous chapter. As GFP quantification is not an end-point assay, single embryos were collected for RNA isolation following fluorescence quantification.

Following treatment, mRNA from HLCs was extracted using the Dynabeads mRNA direct kit (ThermoFisher). This kit allows simple and fast isolation of intact polyadenylated mRNA. For zebrafish, RNA was isolated from single embryos using the MIRneasy micro kit (Qiagen). This kit permits the extraction of RNA from reduced starting cell population.

RNA quality was measured by the RNA integrity number (RIN) using the TapeStation system. RIN is an algorithm used to assess RNA integrity by gel electrophoresis (**Figure 70**). Only samples that displayed RIN score > 7 were used for subsequent applications (223).

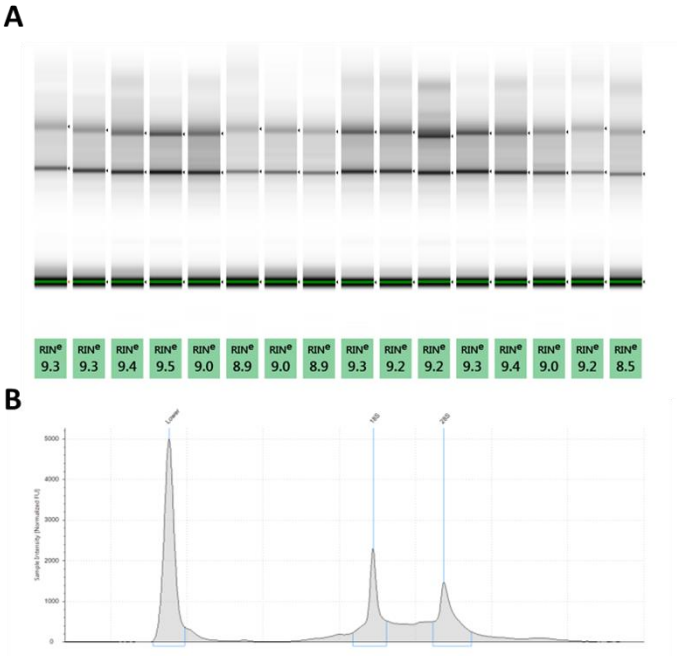

Figure 70. Example from RIN score quantification. (**A**) Images from a RNA electrophoresis with RIN score calculations. (**B**). Example of a RNA spectrum with a high RIN score >9.

Library preparation was performed using Lexogen's QuantSeq kit FWD HT. This kit allows a high-throughput library preparation and sample multiplexing generating Illumina-compatible libraries. Library size generated from this kit should be between 200 and 350 base pairs (bp). After sample multiplexing, a final library was generated. Library size was measured by TapeStation DNA electrophoresis (**Figure 71**). Library size was within the recommended size with a mean of 262 bp. Sequencing was performed using Illumina NextSeq 500 System with NextSeq 500/550 high output kit of 75 cycles. Library preparation and sequencing was performed during a three weeks internship at Novo Nordisk Research Centre Oxford (NNRCO).

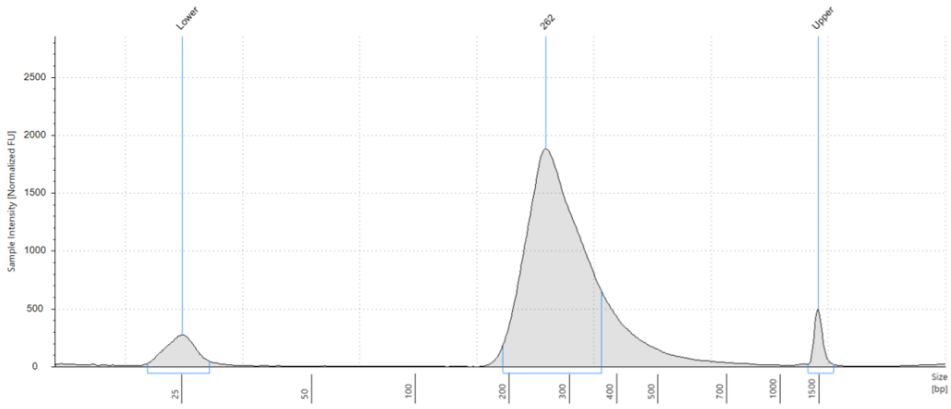

Sample Table

Well	Conc. [pg/µl]	Sample Description	Alert	Observations
B1	5900			

Peak Table

Size [bp]	Calibrated Conc. [pg/µl]	Assigned Conc. [pg/µl]	Peak Molarity [pmol/l]	% Integrated Area	Peak Comment	Observations
25	495	-	30500	-		Lower Marker
262	5900	-	34700	100.00		
1500	250	250	256	-		Upper Marker

Figure 71. Assessment of library size quantification after multiplexing. Prior to sequencing, a combination of the different samples into a master library was performed and library size quantified.

5.2.2 Differential expression analysis

Following sequencing, mapping and gene counting was performed by our collaborators at NNRCO. Next, differential expression and pathway enrichment analysis were performed using R programming. DEseq2 package was used for DEGs quantification and pathway viewer package for pathway enrichment (216). Analysis was performed comparing paracetamol + DMF versus paracetamol, p adjusted value > 0.05 was chosen as a threshold to detect DEGs. Then, only genes that displayed log2 Fold Change ± 0.58 were selected for downstream analysis; ±0.58 log2 Fold Change equals a 1.5 fold change gene expression (224). In addition, EnrichR, a web-based tool for gene list enrichment analysis was used (217). Gene expression analysis was focused on the DMF + paracetamol versus paracetamol in the different treatments to facilitate the analysis.

Finally, Gene Set Enrichment Analysis (GSEA) from the analysed data after DEseq2 was performed. GSEA evaluates gene expression changes at the level of gene sets to identify the relevant biological process involved with the expression changes (218). In combination with GSEA, the molecular signatures database (MSigDB) hallmarks gene sets were used for the enrichment analysis (225). MSigDB hallmarks consist of 50 refined gene sets involved in key biological processes involved in metabolism, proliferation, cell signalling, immune response, DNA damage, development, cell singling pathways and cellular components. By using MSigDB, RNA-seq results can be refined from gene lists into biological changes.

5.2.2.1 HLCs pre-treatment transcriptomic analysis

Before performing gene expression analysis, sample variability of the pre-treatment was examined and visualised by performing principal component analysis and heatmap visualisation of the top 200 genes. For the PCA plot, two factors were created using R and samples were clustered by treatment and shaped by replicates (**Figure 72**). Replicate-to-replicate variations were observed. Heatmap of the top 200 most variable genes was performed for sample hierarchical clustering (**Figure 73**). Notably, paracetamol-treated versus vehicle clustered separately, facilitating analysis.

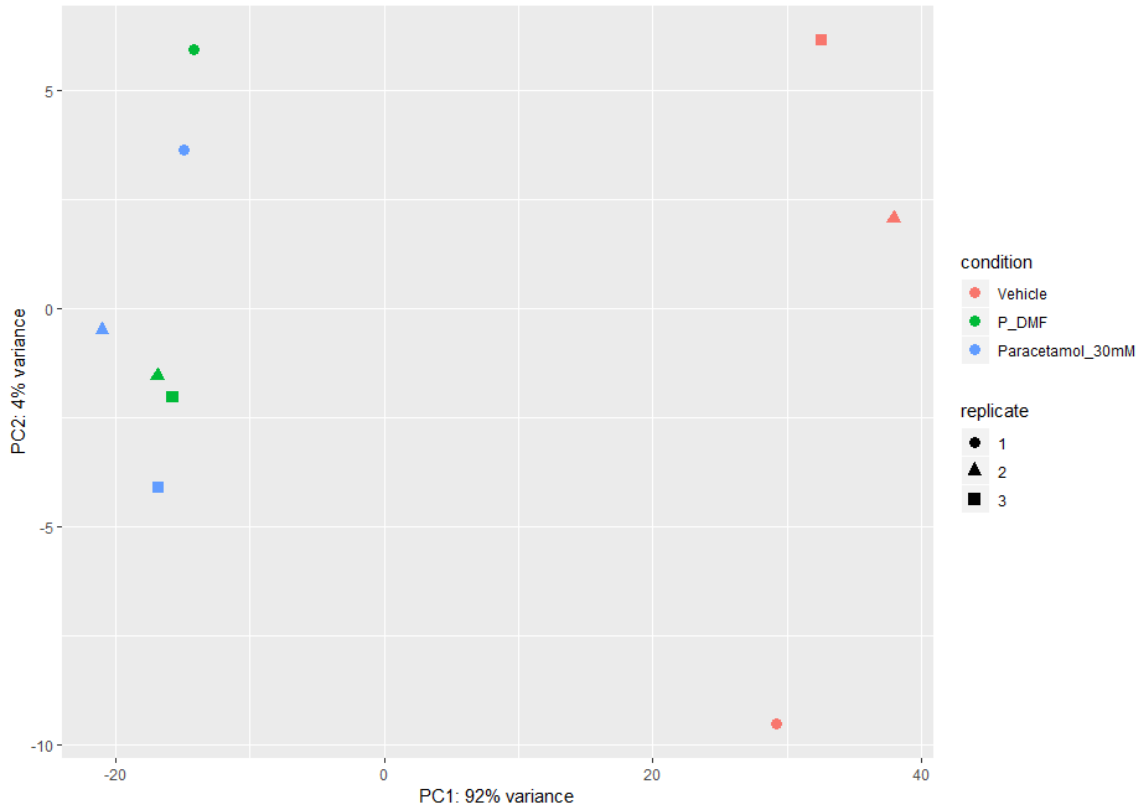

Figure 72. PCA plot of HLCs pre-treatment clusters the different treatments differently. PCA plot from HLCs pre-treatment, colours were used for the different conditions, shape for replicates. P_DMF = paracetamol + DMF.

Following further analysis, differential gene expression analysis was performed using DESeq2 (216). Threshold applied for DEGs detection was p adjusted value > 0.05 and log2 Fold Change ± 0.58. From all the genes, 76% (14010) displayed a low count value and they were omitted from the detection analysis. DEseq2 analysis from DMF + paracetamol treated group versus paracetamol showed an upregulation of 22 genes (**Table 12A**) and downregulation of 12 genes (**Table 12B**).

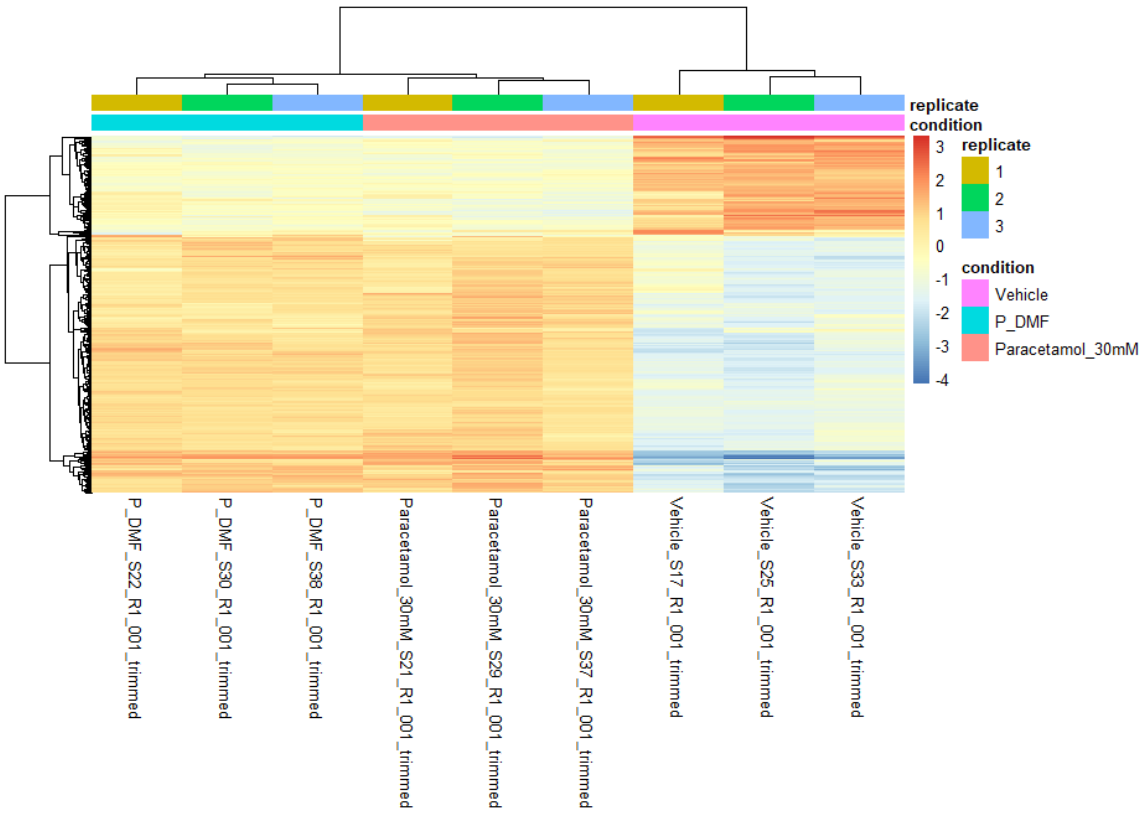

Figure 73. Replicate variability assessment using heatmap visualisation. Heatmap with the top 200 most variable genes clusters the replicates from the different conditions together.

The top 5 upregulated DEGs from DMF treatment included enzymes involved in cell protection such as phase I drug metabolism enzymes: prostaglandin reductase 1 (PTGR1) and NQO1, as well as phase II proteins glutathione S-transferase alpha 1 (GSTA1) and glutathione S-transferase alpha 2 (GSTA2) and the Electron Transfer Flavoprotein Subunit Beta (ETFB) (**Table 12A**).

On the other hand, downregulated DEGs included transcripts that are involved in cytoskeleton maintenance and cell-to-cell contact including claudin 6 (CLDN6), cell metabolism solute carrier family 2 member 3 (SLC2A3), a member of the short chain dehydrogenases/reductases family Dehydrogenase/Reductase 7 (DHRS7), Tropomyosin 1 (TPM1) and Neurogranin (NRGN) (**Table 12B**).

A

Gene Name	baseMean	log2FoldChange	lfcSE	pvalue	padj
PTGR1	911.0608	1.272486	0.127419	8.40E-25	3.80E-21
GSTA2	811.2315	1.26809	0.136508	5.53E-22	1.25E-18
GSTA1	530.7982	1.086071	0.15379	7.35E-14	1.11E-10
ETFB	351.7488	0.933055	0.161774	3.87E-10	2.91E-07
NQO1	548.9379	0.928922	0.152759	5.37E-11	6.07E-08
APOC3	269.9286	0.872558	0.197433	4.03E-07	0.000122
HGD	254.488	0.825786	0.197871	1.26E-06	0.000248
MT1H	237.9697	0.793595	0.261699	7.33E-05	0.006756
DUSP9	379.3415	0.77465	0.160505	6.54E-08	3.70E-05
TTN	162.2048	0.747947	0.29652	0.000381	0.025681
CHAC1	636.4172	0.734153	0.158965	1.64E-07	7.43E-05
PER1	466.6753	0.71376	0.157606	2.64E-07	9.94E-05
AK4	357.9543	0.697369	0.164386	1.02E-06	0.000231
MT1F	521.524	0.666587	0.177103	6.72E-06	0.00098
MLLT11	134.2237	0.665018	0.254615	0.000324	0.022227
SEPT9	460.1329	0.641653	0.170593	7.22E-06	0.000989
C2orf72	244.4756	0.635055	0.198485	5.60E-05	0.005477
S100A16	1336.004	0.629924	0.122695	1.42E-08	9.15E-06
NUPR1	907.2515	0.617522	0.147267	1.24E-06	0.000248
S100P	1045.176	0.616031	0.166832	9.00E-06	0.001197
TMEM141	512.8864	0.601183	0.150211	2.94E-06	0.000493
STOML2	292.7543	0.599431	0.179309	3.63E-05	0.003998

B

Gene Name	baseMean	log2FoldChange	lfcSE	pvalue	padj
NRGN	176.1492	-0.87921	0.235473	7.00E-06	0.000988
CLDN6	430.7649	-0.76242	0.166474	2.00E-07	8.21E-05
SLC2A3	799.089	-0.74165	0.171346	5.72E-07	0.000152
TPM1	1273.229	-0.69862	0.163399	7.42E-07	0.000186
DHRS7	220.7108	-0.69833	0.248381	0.00017	0.013692
KRT19	2596.852	-0.68819	0.114423	8.41E-11	7.60E-08
SPON2	721.8794	-0.65178	0.14468	3.01E-07	0.000105
PLEKHO1	462.8413	-0.63449	0.15318	1.63E-06	0.000306
CLU	1067.668	-0.60927	0.154848	3.50E-06	0.000565
GDF11	155.5532	-0.596	0.241361	0.000487	0.030177
CETN3	956.237	-0.59296	0.147858	2.66E-06	0.000463
SQSTM1	4552.491	-0.58536	0.124209	1.17E-07	5.87E-05

Table 12. Differential expressed genes in DMF + Paracetamol versus paracetamol in pre-treatment HLCs. (**A**) Top 25 upregulated genes (**B**) Downregulated genes. lfcSE = standard error value.

To help elucidate the protective mechanism of the DEGs in HLCs protection, DEG gene list was uploaded into EnrichR and Wikipathways (226) and pathway enrichment analysis was performed. Pathway enrichment analysis of the upregulated DEGs showed interaction in several pathways such as Nrf2 pathway wikipathway (WP) 2884, estrogen metabolism WP697, transcriptional activation by Nrf2 WP3, aryl hydrocarbon receptor pathway WP2873 and zinc homeostasis WP3529 (**Table 13A**).

In the downregulated DEGs, pathway enrichment analysis showed an interaction with several pathways including Nrf2 pathway WP2884, IL-1 signalling pathway WP37/WP195, striated muscle contraction WP383, RANKL/RANK signalling pathway WP2018 and glycolysis and gluconeogenesis WP534 (Table 13**B**).

Finally, GSEA-MSigDB analysis shows a positive enrichment in multiple pathways including adipogenesis, xenobiotic metabolism, oxidative phosphorylation or fatty acid metabolism. It also shows a reduction in TNFA signalling via Nf-kb, epithelial mesenchymal transition, apical junction or apoptosis (**Figure 74**).

Enrichment analysis from both wikipathways and GSEA-MSigDB suggests that DMF pre-treatment increased the metabolic capacity of the cell via Nrf2 activation prior to paracetamol administration. This prevented the development of pro-injury mechanisms such as Nf-kb activation or apoptosis.

A

Term	P-value	Adjusted P-value	Z-score	Combined Score	Genes
NRF2 pathway_Homo sapiens_WP2884	1.8E-05	0.000486	-2.00157	21.86787	NQO1;GSTA2;GSTA1;PTGR1
Estrogen metabolism_Homo sapiens_WP697	0.000175	0.001574	-1.96485	16.99907	NQO1;GSTA1
Transcriptional activation by NRF2_Homo sapiens_WP3	0.00012	0.001574	-1.75087	15.8035	NQO1;GSTA2
Aryl Hydrocarbon Receptor Pathway_Homo sapiens_WP2873	0.001161	0.006269	-1.97258	13.33169	NQO1;GSTA2
Zinc homeostasis_Homo sapiens_WP3529	0.000752	0.005073	-1.83974	13.23399	MT1F;MT1H
Copper homeostasis_Homo sapiens_WP3286	0.001597	0.007185	-1.93967	12.49121	MT1F;MT1H
Glutathione metabolism_Homo sapiens_WP100	0.02501	0.051949	-1.65253	6.095342	GSTA1
PPAR Alpha Pathway_Homo sapiens_WP2878	0.028228	0.051949	-1.37456	4.903695	APOC3
Oxidative Stress_Homo sapiens_WP408	0.033568	0.051949	-1.36243	4.624333	NQO1
Dopamine metabolism_Homo sapiens_WP2436	0.01421	0.041297	-0.95792	4.074782	NQO1

B

Term	P-value	Adjusted P-value	Z-score	Combined Score	Genes
NRF2 pathway_Homo sapiens_WP2884	0.00333	0.046613	-2.00157	11.41882	SLC2A3;SQSTM1
IL-1 Signaling Pathway_Mus musculus_WP37	0.021393	0.054197	-2.07489	7.977279	SQSTM1
Striated Muscle Contraction_Homo sapiens_WP383	0.022569	0.054197	-1.80803	6.854521	TPM1
RANKL/RANK Signaling Pathway_Homo sapiens_WP2018	0.032514	0.054197	-1.94452	6.662092	SQSTM1
IL-1 signaling pathway_Homo sapiens_WP195	0.032514	0.054197	-1.92144	6.583	SQSTM1
Glycolysis and Gluconeogenesis_Mus musculus_WP157	0.028431	0.054197	-1.82825	6.509082	SLC2A3
Glycolysis and Gluconeogenesis_Homo sapiens_WP534	0.029015	0.054197	-1.82752	6.469304	SLC2A3
Apoptosis-related network due to altered Notch3 in ovarian cancer_Homo sapiens_WP2864	0.031349	0.054197	-1.8639	6.453874	SQSTM1
Complement and Coagulation Cascades_Homo sapiens_WP558	0.034841	0.054197	-1.67158	5.611433	CLU

Table 13. Pre-treatment pathway enrichment analysis using Wikipathways. (**A**) pathways enrich from the upregulated DEGs. (**B**) Pathways enriched from the downregulated DEGs.

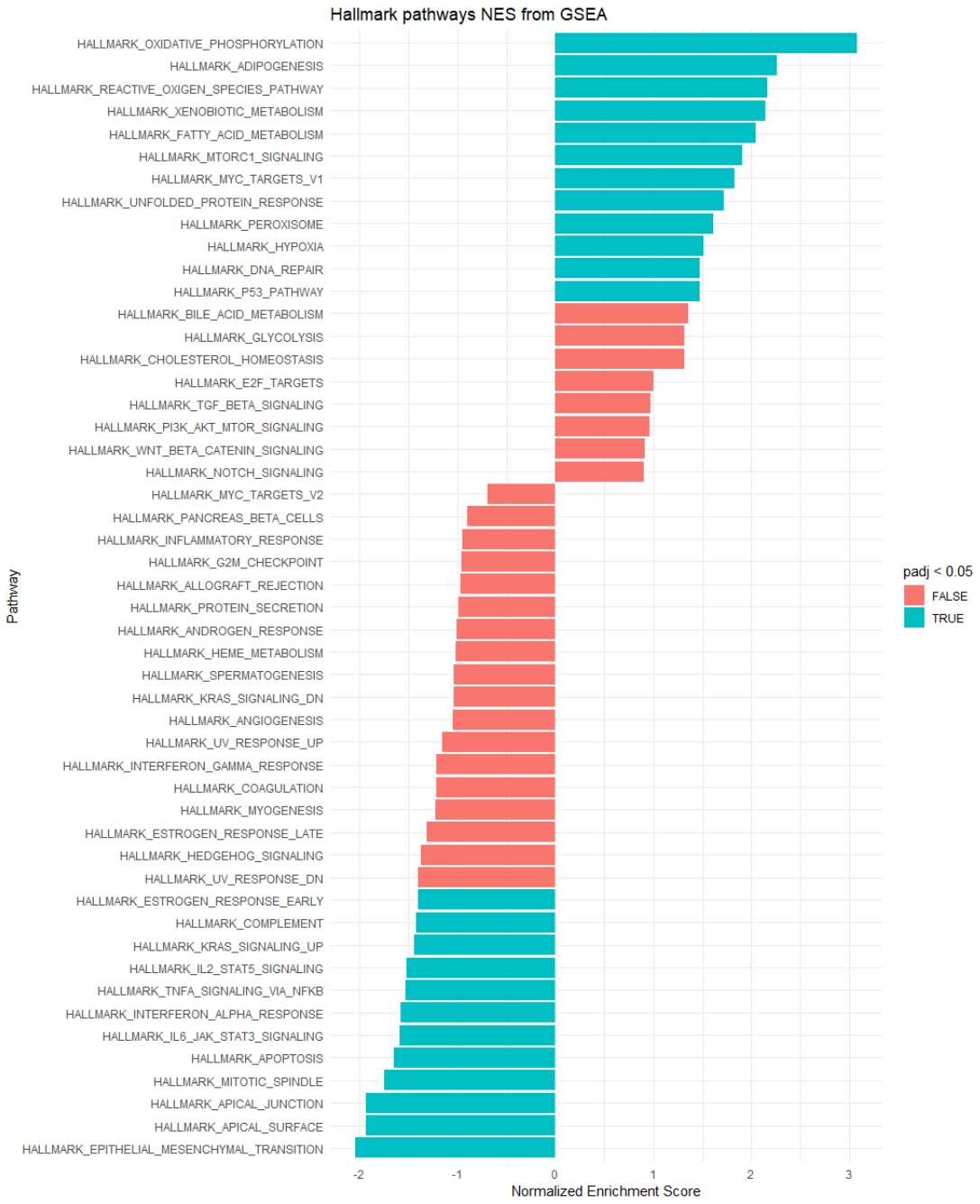

Figure 74. GSEA-MSigDB enrichment analysis from HLCs pre-treatment RNA-seq dataset. Graph represents the normalized enrichment score from the 50 hallmarks, these hallmarks are representative of important biological processes. In blue are labelled the hallmarks with an adjusted p value < 0.05.

5.2.2.2 HLCs co-treatment transcriptomic analysis

Prior to gene expression analysis, data exploration of the co-treatment was visualised by performing PCA and heatmap visualisation of the top 200 genes with higher variability. For the PCA plot, two factors were created and samples were clustered by treatment and shaped by replicates (**Figure 75**). Replicate-to-replicate variations were observed but conditions were separated based on the two components. Heatmap visualisation of the top 200 most variable genes showed a clear difference between vehicle treated HLCs and the other two treatments, paracetamol or DMF + paracetamol (**Figure 76**).

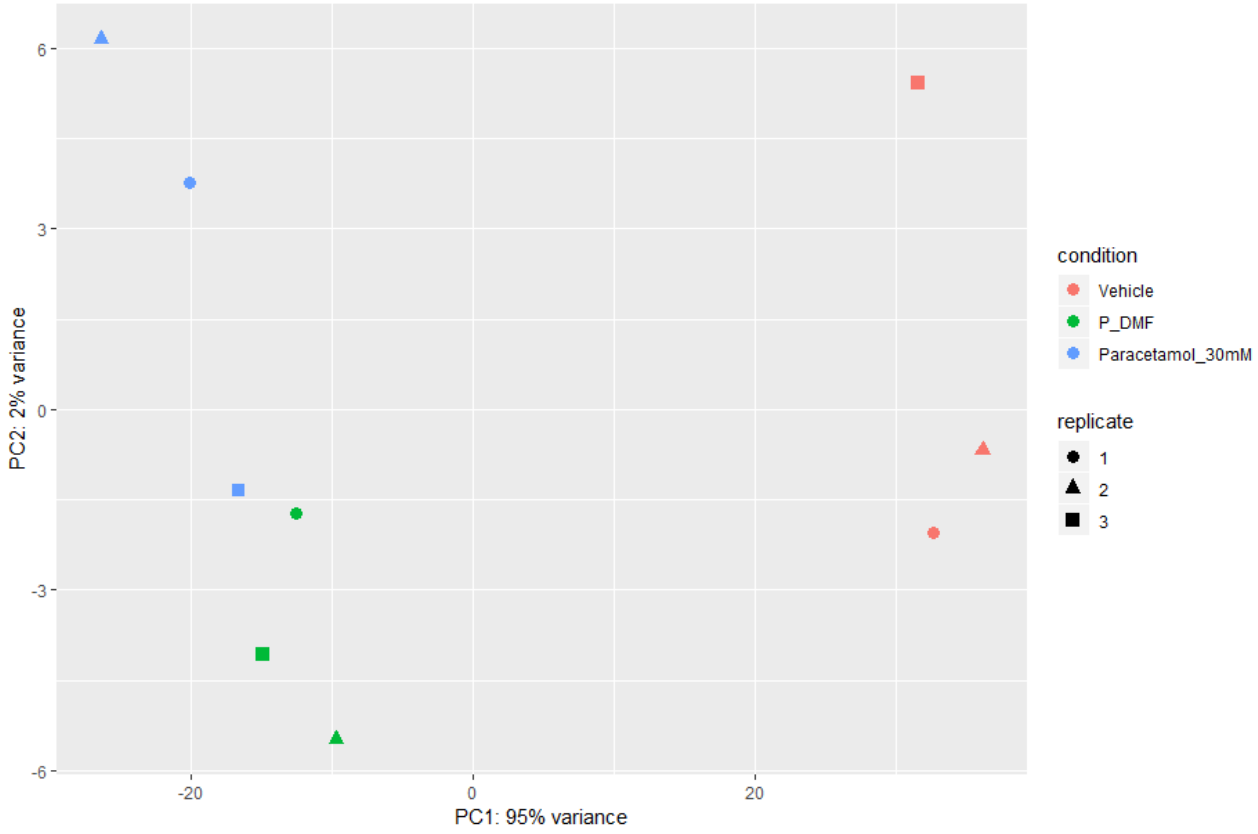

Figure 75. PCA plot of HLCs co-treatment clusters the different treatments differently. PCA plot from HLCs co-treatment, colours were used for the different conditions, shape for replicates. P_DMF = paracetamol + DMF.

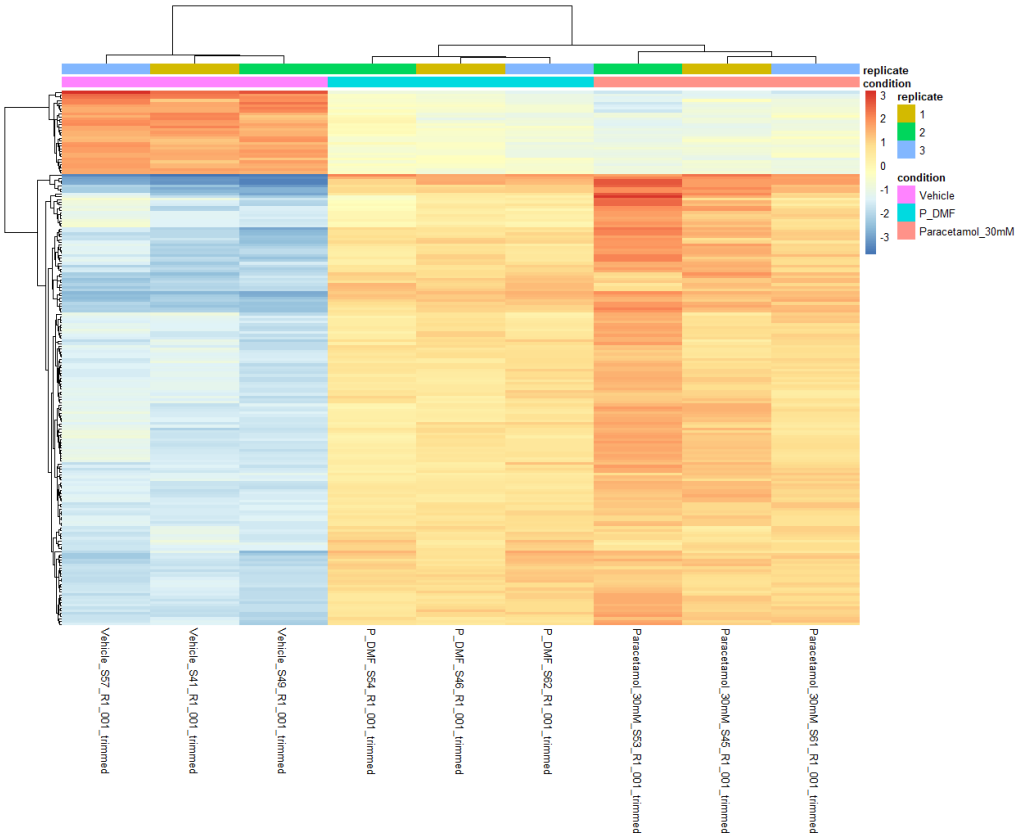

Figure 76. Replicate variability assessment using heatmap visualisation. Heatmap with the top 200 most variable genes clusters the replicates from the different conditions together.

Following data exploration, differential expression analysis was performed using DESeq2 as explained before. The detection threshold applied was p adjusted value > 0.05 and log2 Fold Change ± 0.58. From all the genes, 79% (16444 genes) displayed a low count value and they were omitted from the detection analysis. DEseq2 analysis from DMF + Paracetamol treated group versus paracetamol showed an upregulation of 9 genes (**Table 14A**) and a downregulation of 37 genes (**Table 14B** shows top 25 genes**,** for full list see supplementary information).

A

Gene Name	baseMean	log2FoldChange	lfcSE	pvalue	padj
UBR5	517.4942	0.741003	0.190105	4.70E-06	0.002846
NID1	382.7241	0.730912	0.235122	7.33E-05	0.015604
DUOX2	892.983	0.662857	0.187177	1.85E-05	0.007126
ABCA1	321.0358	0.655037	0.267391	0.000482	0.030968
TTC37	395.8516	0.626011	0.242216	0.000368	0.025881
UBR4	1058.952	0.613457	0.233124	0.000306	0.025797
TNRC6B	356.816	0.610498	0.214936	0.0002	0.021746
TRIM71	353.4599	0.602846	0.274969	0.000926	0.044168
TRIP11	441.0969	0.581967	0.218913	0.00034	0.025797

B

Gene Name	baseMean	log2FoldChange	lfcSE	pvalue	padj
TFPI2	261.6677	-1.08036	0.261259	1.23E-06	0.001502
TACSTD2	267.5707	-1.06425	0.259239	1.42E-06	0.001502
SERPINB8	270.9469	-0.9036	0.287292	4.97E-05	0.013178
CHST8	258.919	-0.85907	0.318414	0.000183	0.021526
NPPB	1027.292	-0.83766	0.215754	3.81E-06	0.002692
SMOX	452.0769	-0.77327	0.253153	7.59E-05	0.015604
SNHG8	1058.67	-0.76366	0.178234	8.42E-07	0.001502
IER2	1668.114	-0.75288	0.234789	4.39E-05	0.012405
ETV5	621.8365	-0.73807	0.255455	0.000124	0.017016
NGFR	259.1061	-0.73396	0.248353	0.000121	0.017016
SEMA7A	240.5932	-0.72986	0.271044	0.000247	0.023015
GAS5	1267.109	-0.70516	0.165374	9.67E-07	0.001502
HES6	431.8835	-0.70293	0.263752	0.00025	0.023015
MSX1	281.4012	-0.67829	0.292548	0.000621	0.034224
PBX3	900.9591	-0.65693	0.212706	7.98E-05	0.015604
TUBB4B	645.6846	-0.65502	0.226651	0.000145	0.018808
SNHG6	1337.182	-0.65297	0.16323	3.14E-06	0.002669
GCA	429.9702	-0.64972	0.234696	0.00022	0.022459
RPL18A	612.7302	-0.63968	0.206739	8.47E-05	0.015604
CDR2L	788.3575	-0.6307	0.207182	9.44E-05	0.015604
PMAIP1	501.639	-0.62729	0.27813	0.000713	0.037328
RPS12	43780.08	-0.62663	0.168181	9.18E-06	0.003899
IER5	1671.919	-0.62492	0.228937	0.000225	0.022459
CD59	4042.655	-0.62105	0.188671	4.20E-05	0.012405
MFSD12	1473.693	-0.61992	0.235708	0.000289	0.025546

Table 14. Differential expressed genes in DMF + Paracetamol versus paracetamol in co-treatment HLCs. (**A**) Upregulated genes (**B**) Top 25 downregulated genes. lfcSE = standard error value.

DEGs upregulated by the co-treatment of DMF + paracetamol versus paracetamol include: ATP Binding Cassette Subfamily A Member 1 (ABCA1), a cholesterol transporter, Ubiquitin Protein Ligase E3 Component N-Recognin 4 (UBR4) and UBR5 which form part of the N-end rule pathway, Nidogen 1 (NID1), dual oxidase 2 (DUOX2) and Tetratricopeptide Repeat Domain 37 (TTC37) (**Table 14A**).

Downregulated DEGs include Tissue Factor Pathway Inhibitor 2 (TFPI2), Tumor Associated Calcium Signal Transducer 2 (TACSTD2), Serpin Family B Member 8 (SERPINB8), Natriuretic Peptide B (NPPB) and Spermine Oxidase (SMOX) (**Table 14B**).

Pathway enrichment analysis of the upregulated DEGs include SREBF and miR33 in cholesterol and lipid homeostasis WP2011, Nuclear Receptors in Lipid Metabolism and Toxicity WP299, Tryptophan metabolism WP79, Statin Pathway WP430 and Tryptophan metabolism

WP465. On the other hand, pathway enrichment from the downregulated DEGs include Cytoplasmic Ribosomal Proteins WP477, Pathogenic Escherichia coli infection WP2272, EGFR1 Signaling Pathway WP572, Quercetin and Nf-kb/ AP-1 Induced Cell Apoptosis WP2435 and TP53 Network WP1742 (**Table 15**).

Finally, GSEA-MSigDB analysis shows a positive enrichment in multiple pathways including mitotic spindle, protein secretion, G2M checkpoint and fatty acid metabolism. In addition, there was a reduction in several hallmark pathways including TNFA signalling via Nf-kb, P53 pathway, UV response, KRAS signalling, inflammatory response and apoptosis (**Figure 77**).

Enrichment analysis from both pathway enrichment analyses suggests that in the co-treatment scenario, DMF cytoprotection was driven by a dual mechanism. This was mainly due to an increase in the metabolic capacity of the HLCs as well as by stopping the progression of pro-injury pathway activation.

A

Term	P-value	Adjusted P-value	Z-score	Combined Score	Genes
SREBF and miR33 in cholesterol and lipid homeostasis_Homo sapiens_WP2011	0.008073	0.033336	-1.73706	8.371416	ABCA1
Nuclear Receptors in Lipid Metabolism and Toxicity_Homo sapiens_WP299	0.016087	0.033336	-1.84295	7.61091	ABCA1
Tryptophan metabolism_Mus musculus_WP79	0.019188	0.033336	-1.88133	7.437755	UBR5
Statin Pathway_Homo sapiens_WP430	0.013867	0.033336	-1.65835	7.094862	ABCA1
Tryptophan metabolism_Homo sapiens_WP465	0.020515	0.033336	-1.79868	6.990782	UBR5
NOD pathway_Homo sapiens_WP1433	0.018303	0.033336	-1.73883	6.956533	DUOX2
Vitamin B12 Metabolism_Homo sapiens_WP1533	0.023603	0.034094	-1.72305	6.455185	ABCA1
Selenium Micronutrient Network_Homo sapiens_WP15	0.039786	0.04702	-1.73821	5.604396	ABCA1
Folate Metabolism_Homo sapiens_WP176	0.030193	0.039251	-1.56978	5.494455	ABCA1
PodNet: protein-protein interactions in the podocyte_Mus musculus_WP2310	0.129193	0.139959	-1.87267	3.832322	NID1

B

Term	P-value	Adjusted P-value	Z-score	Combined Score	Genes
Cytoplasmic Ribosomal Proteins_Homo sapiens_WP477	2.16E-05	0.000443	-1.98222	21.29218	RPL18A;RPL13A;RPL28;RPS12
Pathogenic Escherichia coli infection_Homo sapiens_WP2272	0.004649	0.063542	-1.91288	10.27412	KRT18;TUBB4B
EGFR1 Signaling Pathway_Mus musculus_WP572	0.039811	0.158362	-1.9869	6.405022	KRT18;KRT8
Quercetin and Nf-kB/ AP-1 Induced Cell Apoptosis_Homo sapiens_WP2435	0.029204	0.158362	-1.66706	5.890486	COX1
TP53 Network_Homo sapiens_WP1742	0.034586	0.158362	-1.55323	5.225546	PMAIP1
Hypertrophy Model_Homo sapiens_WP516	0.036374	0.158362	-1.55264	5.145289	ANKRD1
Effects of Nitric Oxide_Homo sapiens_WP1995	0.014707	0.150748	-1.05663	4.458352	COX1
Selenium Micronutrient Network_Mus musculus_WP1272	0.041718	0.158362	-1.40022	4.448255	COX1
Nanoparticle-mediated activation of receptor signaling_Homo sapiens_WP2643	0.05056	0.158362	-1.44487	4.312339	AREG
FSH signaling pathway_Homo sapiens_WP2035	0.048798	0.158362	-1.26126	3.809079	AREG

Table 15. Co-treatment pathway enrichment analysis using Wikipathways. (**A**) Pathways enriched by from the upregulated DEGs. (**B**) Pathways enriched by the downregulated DEGs.

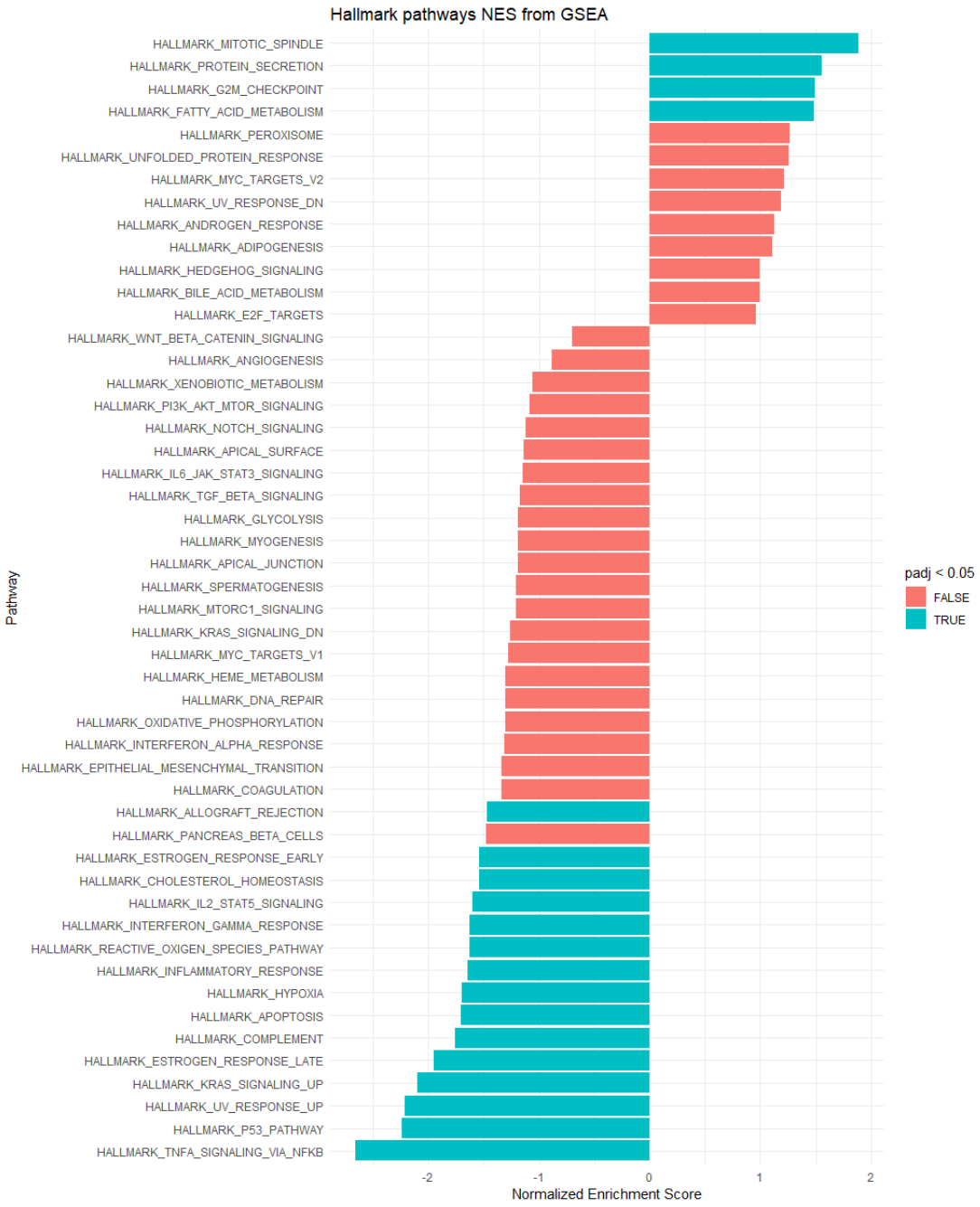

Figure 77. GSEA-MSigDB enrichment analysis from HLCs co-treatment RNA-seq dataset. Graph represents the normalized enrichment score from the 50 hallmarks, these hallmarks are representative of important biological processes. In blue are labelled the hallmarks with an adjusted p value < 0.05.

5.2.2.3 HLCs post-treatment transcriptomic analysis

For the post treatment group, only two biological replicates were sequenced due to time limitations, an extra replicate will be performed in the future. Despite the reduced replicate number, it is still possible to perform quantitative analysis from two replicates with reduced biological variability. By using a lower number of replicates, only genes with the largest effect size will be detected (227). In addition, sequencing of an extra biological replicate is planned in the near future.

Data exploration was performed as explained before, and a PCA plot was created to visualise condition variation. All three conditions showed a clear separation in the PCA plot (**Figure 78**). In addition, a heatmap of the top 200 genes with higher variation was created.

Similar clustering was observed, where vehicle-treated HLCs cluster separately from the post-treated groups and the replicates cluster together (**Figure 79**). These results highlight a reduced variability between replicates permitting subsequent analysis.

Following data exploration, differential expression analysis was performed using DESeq2 as explained before. The detection threshold applied was p adjusted value > 0.05 and log2 Fold Change ± 0.58.

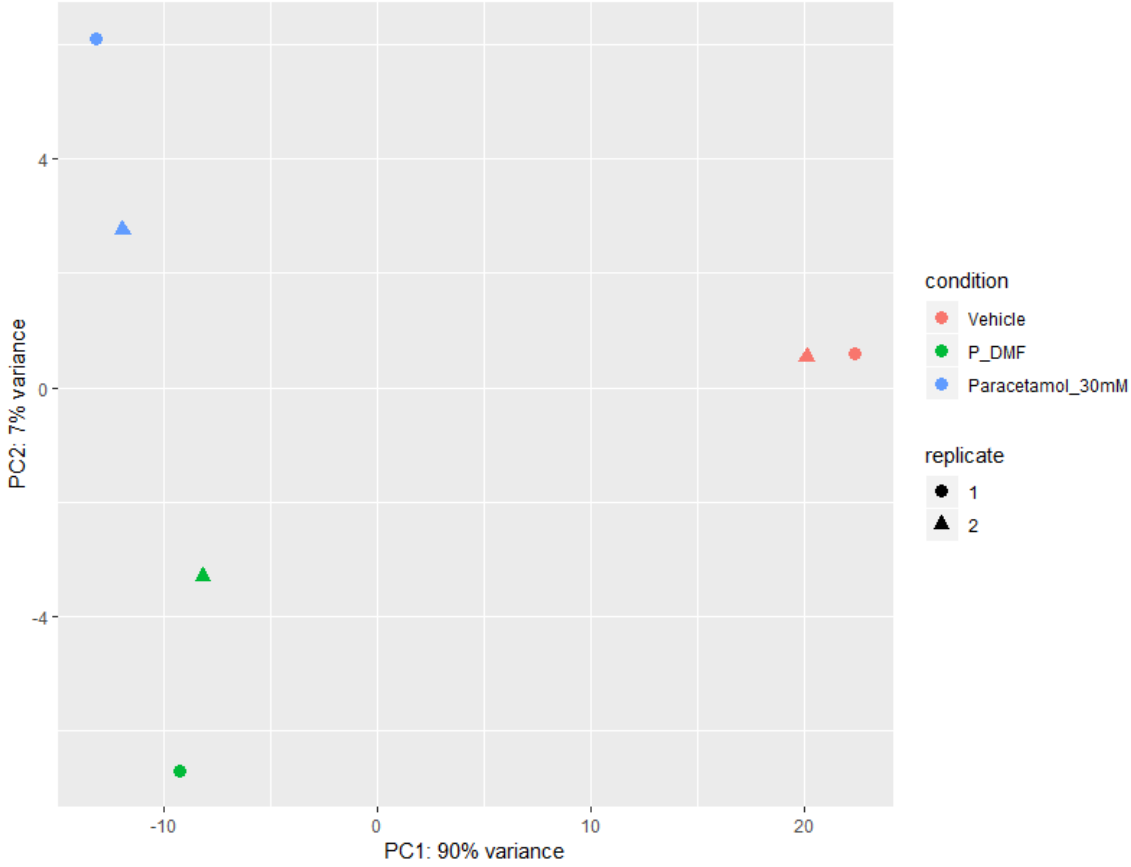

Figure 78. PCA plot of HLCs post-treatment clusters the different treatments differently. PCA plot from HLCs post-treatment, colours were used for the different conditions, shape for replicates. P_DMF = paracetamol + DMF.

During the analysis, 13380 genes displayed low counts and it was not

possible to include them into the analysis. Only 21% of the total counts passed the quality control required for DEseq2 analysis. From the DEGs obtained from the analysis from DMF + Paracetamol treated group versus paracetamol, 5 genes were upregulated (**Table 16A**) and 32 were downregulated (**Table 16B** shows top 25 genes**,** for full list see supplementary information).

DEGs upregulated by the post-treatment of DMF+paracetamol versus paracetamol included DUOX2, Sodium Channel Epithelial 1 Alpha Subunit (SCNN1A), Tripartite Motif Containing 71 (TRIM71) or Nuclear Enriched Abundant Transcript 1 (NEAT1) and Nuclear Protein 1 (NUPR1) (**Table 16A**).

Downregulated DEGs include: C-C Motif Chemokine Ligand 3 Like 1 (CCL3L1), CD44, Cytoskeleton Regulator RNA (CYTOR), MIR4435-2GH and ETS Proto-Oncogene 1 Factor (ETS1) (**Table 16B**).

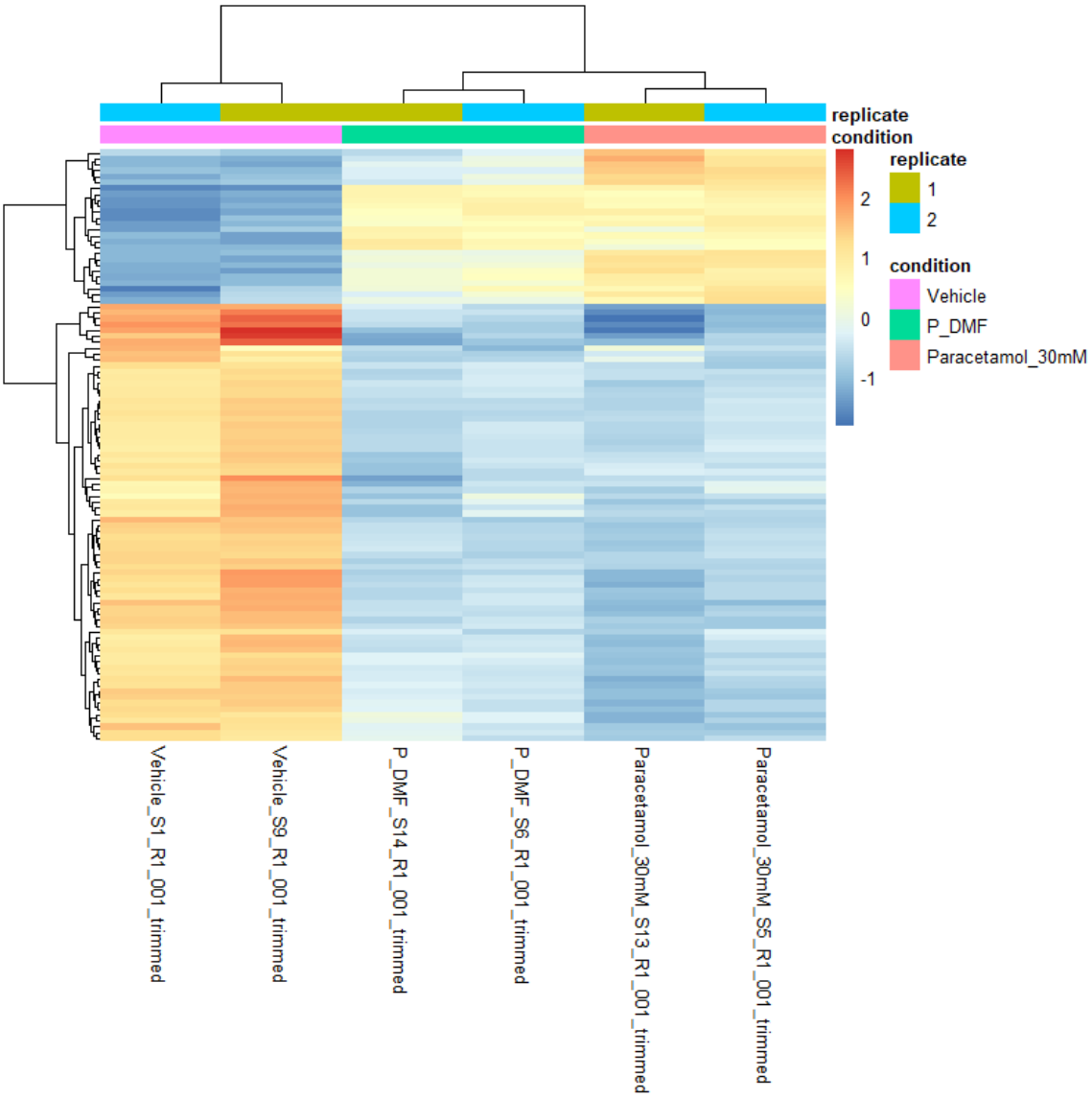

Figure 79. Replicate variability assessment using heatmap visualisation. Heatmap with the top 200 most variable genes clusters the replicates from the different conditions together.

Following DEGs acquisition, pathway enrichment of the upregulated DEGs showed an increase in several pathways including NOD pathway WP1433, endochondral ossification WP474 and spinal cord injury WP2431. Pathway enrichment analysis from the downregulated DEGs showed interactions with several pathways including: focal adhesion-PI3K-Akt-mTOR-signaling pathway WP2841, TGF-beta signalling pathway WP366 and Nrf2 pathway WP2884 (**Table 17**).

A

Gene Name	baseMean	log2FoldChange	lfcSE	pvalue	padj
NEAT1	12920.73	0.946268	0.173667	3.88E-09	2.23E-06
SCNN1A	543.1801	0.809522	0.281977	0.000127	0.016872
TRIM71	522.3106	0.772307	0.237238	4.39E-05	0.006584
DUOX2	771.5025	0.740942	0.219261	2.91E-05	0.005024
NUPR1	453.7334	0.736752	0.271945	0.000225	0.024824
MEGF9	428.9418	0.664578	0.270105	0.000456	0.042512
COL2A1	544.9756	0.607067	0.260094	0.000632	0.046427
GSR	1124.282	0.542446	0.220829	0.000503	0.043433

B

Gene Name	baseMean	log2FoldChange	lfcSE	pvalue	padj
CCL3L1	214.0358	-1.90757	0.298406	7.39E-12	1.28E-08
CD44	320.7262	-1.48105	0.273237	2.33E-09	1.61E-06
CYTOR	1491.51	-1.39564	0.560638	0.000291	0.030453
MIR4435-2HG	5036.48	-1.33168	0.199259	8.15E-13	2.82E-09
ETS1	294.5387	-1.27715	0.2681	8.03E-08	3.47E-05
ITGA2	2152.881	-1.12809	0.184412	4.18E-11	4.82E-08
KRT6A	432.2669	-1.11016	0.266388	1.10E-06	0.000346
MAFF	230.5556	-1.10327	0.294964	7.17E-06	0.001684
TAGLN	292.1205	-1.07995	0.32768	2.77E-05	0.005024
AKAP12	3599.472	-1.06989	0.180657	1.49E-10	1.28E-07
DUSP5	971.9109	-1.05339	0.202684	9.03E-09	4.45E-06
LAMC2	321.8058	-1.0221	0.27468	7.69E-06	0.001684
AREG	773.8499	-0.96762	0.230979	1.05E-06	0.000346
LIMA1	539.4222	-0.94899	0.234615	2.11E-06	0.000607
COTL1	523.6473	-0.94247	0.242423	3.82E-06	0.001013
SLC2A3	1759.993	-0.924	0.196697	1.11E-07	4.25E-05
RPL22L1	209.9762	-0.87975	0.361753	0.000404	0.03985
SEC61G	325.8817	-0.81446	0.305091	0.00023	0.024824
S100A11	481.9524	-0.80986	0.286971	0.000142	0.018186
ABL2	474.3977	-0.79826	0.243811	4.34E-05	0.006584
GSTO1	1469.689	-0.79782	0.2238	1.29E-05	0.002627
SFN	215.3717	-0.77658	0.330192	0.000558	0.04546
VIM	1393.804	-0.74408	0.198897	7.80E-06	0.001684
PMAIP1	371.2127	-0.72725	0.266189	0.000218	0.024824
FHL2	454.6041	-0.71283	0.263053	0.00023	0.024824

Table 16. Differential expressed genes in DMF + Paracetamol versus paracetamol in post-treatment HLCs. (**A**) Upregulated genes (**B**) Top 25 downregulated genes. lfcSE = standard error value.

Finally, GSEA-MSigDB analysis shows a positive enrichment in multiple pathways, including interferon alpha response, bile acid and fatty acid metabolism and xenobiotic metabolism. In addition, there was a reduction in several hallmark pathways including TNFA signalling via Nf-kb, MYC targets, TGF-b signalling pathway, P53 pathway, inflammatory response and apoptosis (**Figure 80**).

In the post-treatment scenario, enrichment analysis from both wikipathways and GSEA-MSigDB suggests that DMF protection was achieved from the downregulation of genes involved in multiple pro-injury pathways. In addition, DMF increased the xenobiotic metabolism capacity of the cells.

A

Term	P-value	Adjusted P-value	Z-score	Combined Score	Genes
NOD pathway_Homo sapiens_WP1433	0.014264	0.06138	-1.95213	8.296553	DUOX2
Endochondral Ossification_Mus musculus_WP1270	0.020471	0.06138	-1.9201	7.466757	COL2A1
Endochondral Ossification_Homo sapiens_WP474	0.022189	0.06138	-1.88886	7.193049	COL2A1
Spinal Cord Injury_Mus musculus_WP2432	0.033125	0.06138	-1.79741	6.124616	COL2A1
Neural Crest Differentiation_Homo sapiens_WP2064	0.034824	0.06138	-1.81744	6.101966	COL2A1
Spinal Cord Injury_Homo sapiens_WP2431	0.04092	0.06138	-1.84969	5.911865	COL2A1
Focal Adhesion_Homo sapiens_WP306	0.064974	0.073096	-1.99049	5.441526	COL2A1
Focal Adhesion_Mus musculus_WP85	0.06299	0.073096	-1.95562	5.406853	COL2A1
Focal Adhesion-PI3K-Akt-mTOR-signaling pathway_Mus musculus_WP2841	0.101364	0.101364	-2.15232	4.926737	COL2A1

B

Term	P-value	Adjusted P-value	Z-score	Combined Score	Genes
Focal Adhesion-PI3K-Akt-mTOR-signaling pathway_Mus musculus_WP2841	0.003242	0.107223	-2.3775	13.62662	ITGA2;LAMC2;SLC2A3
TGF-beta Signaling Pathway_Homo sapiens_WP366	0.007599	0.107223	-1.98704	9.696244	ITGA2;ETS1
NRF2 pathway_Homo sapiens_WP2884	0.009226	0.107223	-1.94928	9.133857	MAFF;SLC2A3
Focal Adhesion_Homo sapiens_WP306	0.015396	0.107223	-2.06983	8.638709	ITGA2;LAMC2
PodNet: protein-protein interactions in the podocyte_Mus musculus_WP2310	0.03676	0.107223	-1.89905	6.273233	TAGLN;ITGA2
Nanoparticle-mediated activation of receptor signaling_Homo sapiens_WP2643	0.027644	0.107223	-1.71585	6.157091	AREG
XPodNet - protein-protein interactions in the podocyte expanded by STRING_Mus musculus_WP2309	0.044878	0.107223	-1.9057	5.914917	TAGLN;ITGA2;LAMC2
Inflammatory Response Pathway_Homo sapiens_WP453	0.02959	0.107223	-1.67249	5.887689	LAMC2
Alpha 6 Beta 4 signaling pathway_Homo sapiens_WP244	0.032503	0.107223	-1.65629	5.675149	LAMC2
FSH signaling pathway_Homo sapiens_WP2035	0.026669	0.107223	-1.51797	5.501507	AREG

Table 17. Post-treatment pathway enrichment analysis using Wikipathways. (**A**) Pathways enriched by the upregulated DEGs. (**B**) Pathways enriched by the downregulated DEGs.

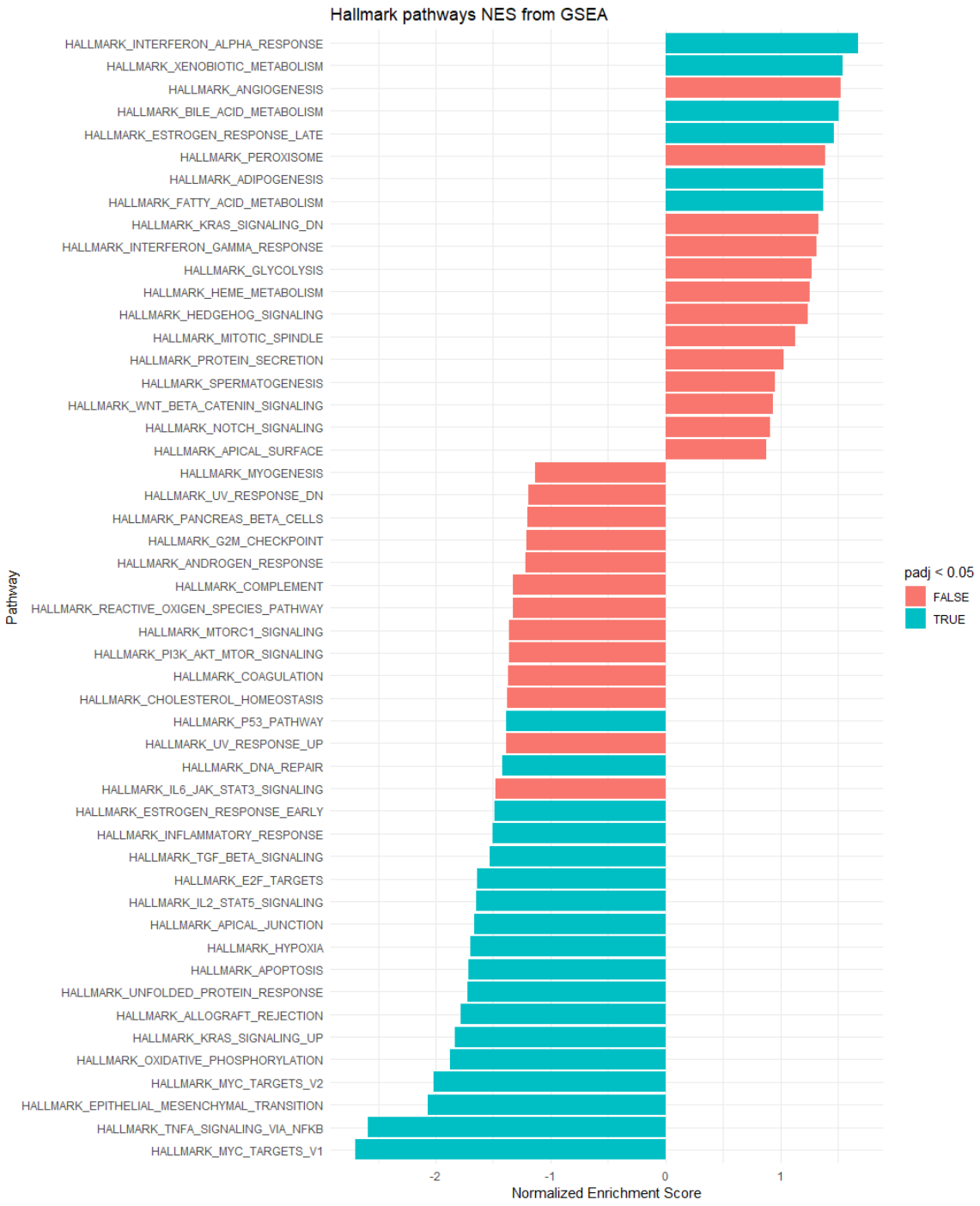

Figure 80. GSEA-MSigDB enrichment analysis from HLCs post-treatment RNA-seq dataset. Graph represents the normalized enrichment score from the 50 hallmarks, these hallmarks are representative from important biological processes. In blue are labelled the hallmarks with an adjusted p value < 0.05.

5.2.2.4 Zebrafish transcriptomic analysis

Data variability from the zebrafish data was assessed using PCA. Total gene counts from the sequencing was transformed into two components. The PCA plot on **Figure 81** shows conditions by colours and replicates by shape. Different conditions are separated in the PCA plot but there is variability between replicates. Heatmap of the top 200 most variable genes was performed for sample hierarchical clustering. Heatmap shows some variability between clustering replicates of the same condition together: one of the replicates from the paracetamol treated group was clustered with the vehicle group and one of the DMF + paracetamol group was clustered alone (**Figure 82**). This variability reduces the power of the DEseq2 analysis.

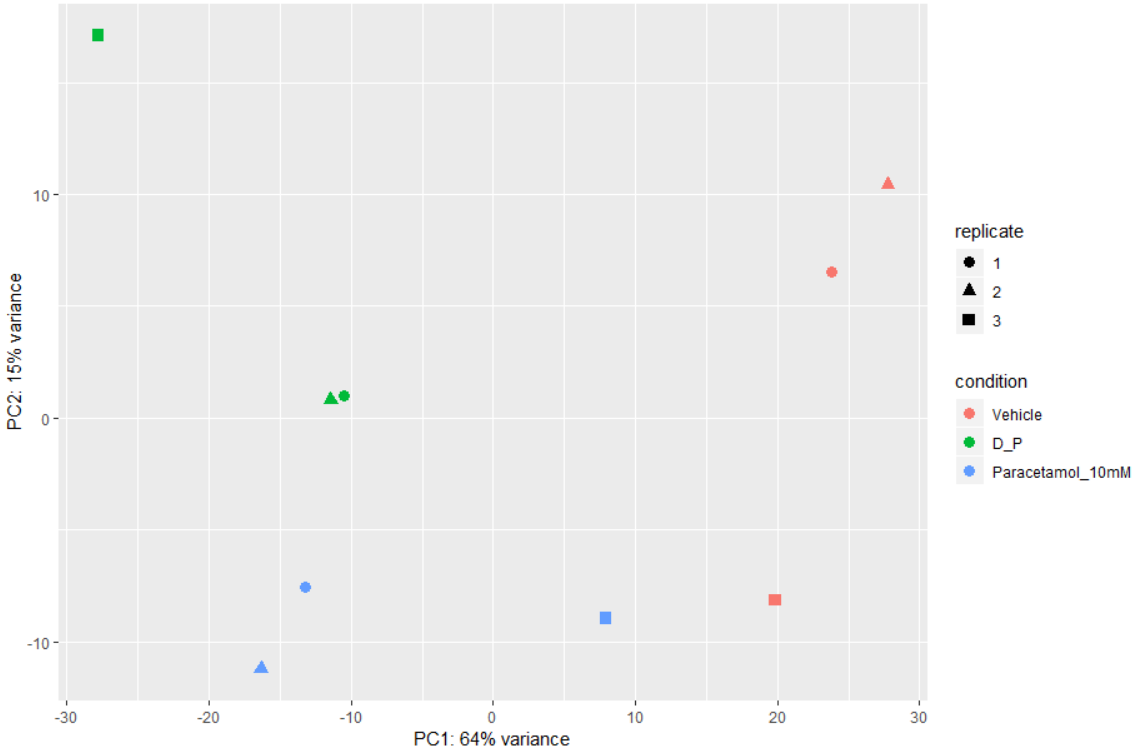

Figure 81. PCA plot zebrafish clusters the different treatments differently. PCA plot from zebrafish, colours were used for the different conditions, shape for replicates. D_P = paracetamol + DMF.

Following data exploration, differential expression analysis was performed using DESeq2 as explained before. The detection threshold applied was p adjusted value > 0.05 and log2 Fold Change ± 0.58. During the analysis, 9395 genes displayed low counts and it was not possible to include them into the analysis. Only 53% of the total counts passed the quality control required for DEseq2 analysis. From the DEGs obtained from the analysis from DMF + Paracetamol treated group versus Paracetamol, 30 genes were upregulated and 10 were downregulated (**Table 18**)

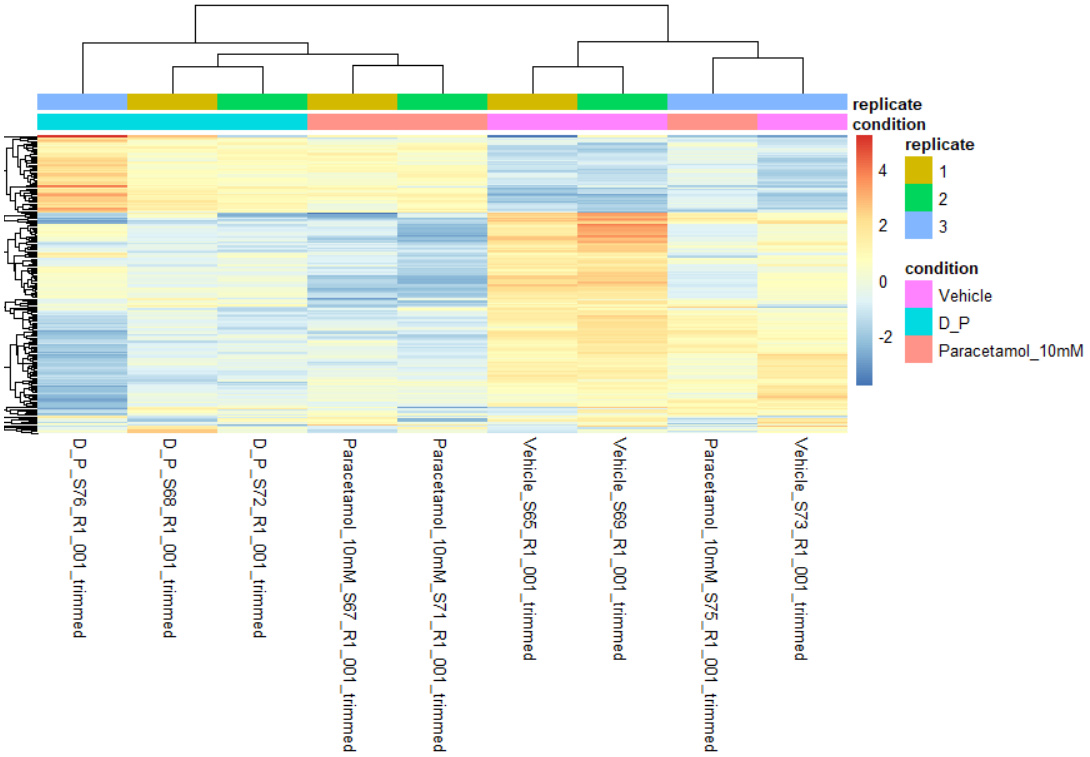

Figure 82. Replicate variability assessment using heatmap visualisation. Heatmap with the top 200 most variable genes clusters the replicates from the different conditions together.

From the upregulated DEGs, the top 5 include: transcobalamin beta a (tcnba), several members of the crystallin family (crygm), structural protein of eye lens and the cornea and the sequencing conting, CABZ01080568.1. Nucleoporin 160 (nup160) is expressed within the CABZ01080568 conting (**Table 18A**).

Downregulated DEGs included 3-hydroxyanthranilate 3, 4-dioxygenase (haao), the LOC100149563 which is homologous to the human gene HtrA serine peptidase 2 (HTRA2), F-Box Protein 32 (fbxo32) and apolipoprotein Da, duplicate 1 (apoda.1), Retinoid Isomerohydrolase (rpe65a) (**Table 18B**)

A

Gene Name	baseMean	log2FoldChange	lfcSE	pvalue	padj
tcnba	516.4075	2.442286	0.455423	8.14E-10	8.78E-06
CABZ01080568.1	142.5607	2.280092	0.724905	7.95E-06	0.004169
crygm2d15	869.9748	1.969861	0.37134	2.66E-09	1.40E-05
crygm2d5	1462.791	1.96209	0.475719	2.67E-07	0.000288
crygm2d17	1101.928	1.880228	0.411323	7.15E-08	0.000129
crygm2d14	1126.493	1.850981	0.366916	1.05E-08	2.84E-05
crygm2d7	1460.899	1.829098	0.411178	1.30E-07	0.000176
crybgx	252.9114	1.817982	0.703129	9.93E-05	0.03057
crygm2d11	861.6477	1.778383	0.394003	1.25E-07	0.000176
crygm2d4	1330.222	1.701993	0.320238	3.89E-09	1.40E-05
uchl1	109.6245	1.658356	0.588584	0.000109	0.031699
hspb1	2123.578	1.643173	0.49371	8.11E-06	0.004169
crygm2d18	949.22	1.584292	0.372289	5.51E-07	0.000496
crygm2d16	1300.437	1.507166	0.424185	6.65E-06	0.003986
crygm2d21	922.5474	1.502262	0.550307	5.65E-05	0.021028
crygm2d6	145.094	1.466385	0.509446	0.000128	0.035543
crygm2d20	1448.156	1.439415	0.433016	1.50E-05	0.00704
crygn2	1623.658	1.420965	0.489586	4.86E-05	0.018755
crygm2d2	2608.659	1.418607	0.356581	1.79E-06	0.001139
crygm2d1	1594.418	1.402341	0.431299	1.94E-05	0.00874
crygm2d9	1055.253	1.38857	0.341225	1.55E-06	0.001117
crygm2d3	3607.863	1.374161	0.326547	8.12E-07	0.000626
crygm2d19	1794.111	1.353566	0.396182	1.40E-05	0.006864
crygm2d13	2232.34	1.343253	0.372181	7.47E-06	0.004169
cryba1l1	872.6952	1.286035	0.469858	0.000119	0.033919

B

Gene Name	baseMean	log2FoldChange	lfcSE	pvalue	padj
haao	29.05509	-6.35336	1.584918	7.52E-07	0.000625
LOC100149563	28.46049	-5.44275	1.2896	4.94E-07	0.000485
rpe65a	100.2075	-2.81829	0.649972	2.02E-07	0.000242
fbxo32	352.1749	-1.85764	0.371364	2.12E-08	4.58E-05
apoda.1	112.819	-1.8496	0.682785	9.38E-05	0.02978
arr3a	2120.804	-1.6904	0.445434	1.70E-06	0.001139
calcoco1b	210.4044	-1.48855	0.534133	0.000102	0.03057
si:dkey-183i3.5	1247.315	-1.37855	0.485747	6.22E-05	0.022371
si:dkey-14d8.6	1749.698	-1.25324	0.443516	7.05E-05	0.024551

Table 18. Differential expressed genes in DMF + Paracetamol versus paracetamol in zebrafish. (**A**) Top 25 upregulated genes and (**B**) Downregulated genes. lfcSE = standard error value.

Pathway enrichment of the upregulated DEGs showed an increase in several pathways including IL-3 Signaling Pathway WP373, 6 signaling Pathway WP387, IL-7 Signaling Pathway WP205 and p38 MAPK Signaling Pathway WP350. Pathway enrichment analysis from the downregulated DEGs showed interactions with several pathways including NAD biosynthesis II WP2485, tryptophan metabolism WP79 and monoamine transport WP727 (**Table 19**).

A

Term	P-value	Adjusted P-value	Z-score	Combined Score	Genes
IL-3 Signaling Pathway_Mus musculus_WP373	0.009271	0.194027	-2.09891	9.824791	HSPB1;PIK3R2
IL-6 signaling Pathway_Mus musculus_WP387	0.009271	0.194027	-2.05238	9.606973	HSPB1;PIK3R2
IL-7 Signaling Pathway_Homo sapiens_WP205	0.036854	0.194027	-2.07847	6.860579	PIK3R2
IL-9 Signaling Pathway_Homo sapiens_WP22	0.025206	0.194027	-1.62698	5.988352	PIK3R2
p38 MAPK Signaling Pathway_Mus musculus_WP350	0.046936	0.194027	-1.80051	5.507715	HSPB1
Bladder Cancer_Homo sapiens_WP2828	0.045502	0.194027	-1.78131	5.504246	PIK3R2
Alpha 6 Beta 4 signaling pathway_Homo sapiens_WP244	0.048368	0.194027	-1.80472	5.46634	PIK3R2
p38 MAPK Signaling Pathway_Homo sapiens_WP400	0.049798	0.194027	-1.80445	5.412964	HSPB1
FAS pathway and Stress induction of HSP regulation_Mus musculus_WP571	0.052651	0.194027	-1.64609	4.846197	HSPB1
IL-5 Signaling Pathway_Homo sapiens_WP127	0.058333	0.194027	-1.68427	4.786006	PIK3R2

B

Term	P-value	Adjusted P-value	Z-score	Combined Score	Genes
NAD Biosynthesis II (from tryptophan)_Homo sapiens_WP2485	0.003994	0.015975	-1.67873	9.271678	HAAO
Tryptophan metabolism_Mus musculus_WP79	0.021298	0.022768	-2.06157	7.935288	HAAO
Monoamine Transport_Homo sapiens_WP727	0.015889	0.022768	-1.88898	7.824411	FBXO32
Tryptophan metabolism_Homo sapiens_WP465	0.022768	0.022768	-1.96429	7.429694	HAAO

Table 19. Zebrafish pathway enrichment analysis using Wikipathways. (**A**) pathways enriched by the upregulated DEGs. (**B**) pathways enriched by the downregulated DEGs.

Finally, zebrafish gene names were converted into human homologues and GSEA-MSigDB analysis was performed. There was a positive enrichment in multiple pathways including MYC targets, oxidative phosphorylation, reactive oxygen species pathway, DNA repair, apoptosis and G2M checkpoint. There were no significant hallmark decreases (**Figure 83**).

In zebrafish, enrichment analysis from both Eikipathways and GSEA-MSigDB highlights an increase in several cellular stress mechanisms as well as a reduction in the zebrafish metabolic capacity.

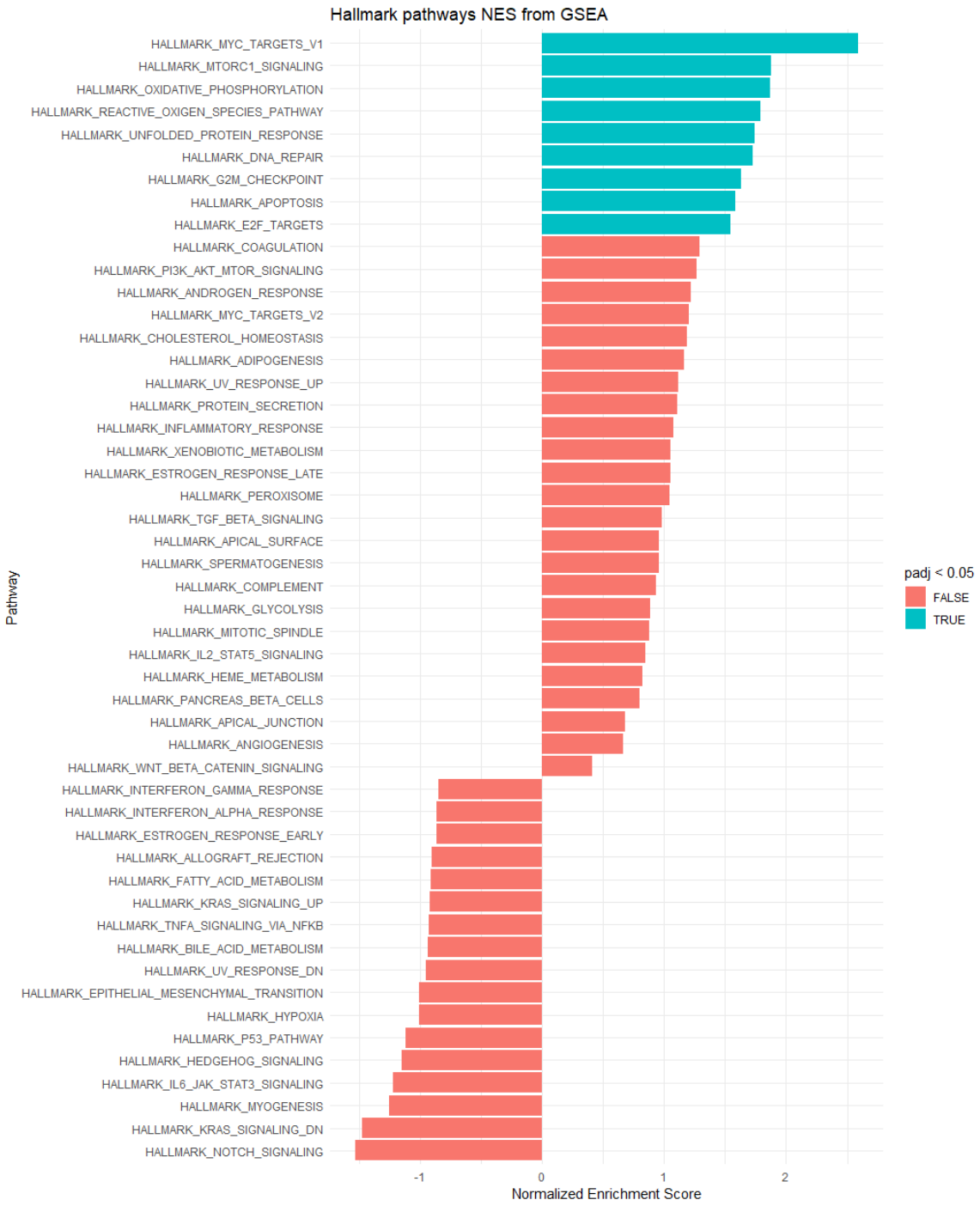

Figure 83. GSEA-MSigDB enrichment analysis from the zebrafish RNA-seq dataset. Graph represents the normalized enrichment score from the 50 hallmarks, these hallmarks are representative of important biological processes. In blue are labelled the hallmarks with an adjusted p value < 0.05.

5.3 Discussion

In the previous chapter we investigated the cytoprotective effects of DMF in the context of paracetamol hepatotoxicity. To try to elucidate the mechanism of action of DMF, mRNA sequencing was performed in both HLCs and zebrafish. RNA-seq analysis was focused in the differences between paracetamol + DMF versus paracetamol alone. In HLCs, gene regulation changes following DMF treatment were assessed in the three different scenarios pre, co and post treatment. This approach would elucidate any potential time-dependent effect of the DMF treatment. Finally, translation of these findings to a zebrafish *in vivo* model was performed. Gene function of the DEGs in the context of liver disease was investigated.

5.3.1 HLCs pre-treatment gene expression

HLCs pre-treated with DMF displayed an increase in antioxidant capacity as shown by the upregulation of several enzymes from phase I drug metabolism such as NQO1 or prostaglandin reductase 1 (PTGR1). The function of NQO1 is to reduce quinones to hydroquinones. This prevents the production of radical species by preventing the one electron reduction of quinones (228). Whereas PTGR1 encodes an oxidoreductase involved in the inactivation of the chemotactic factor, leukotriene B4 by converting leukotriene B4 to 12-oxo-leukotriene B4. PTGR1 is regulated by Nrf2 promoting cell proliferation and resistance to oxidative stress (229). In addition, there was an increase in glutathione metabolism as shown by the upregulation of glutathione S-transferase alpha 2 (GSTA2) and glutathione S-transferase alpha 1 (GSTA1). GSTA1 and GSTA2 are detoxification enzymes, part of the glutathione S-transferase (GST) alpha families, highly expressed in the liver (230). Cytoprotective effects of GSTs are based on the conjugation of reduced glutathione to xenobiotics (231,232). Expression of GSTs is regulated in part by Nrf2

(94). Upregulation of these enzymes prior to paracetamol-induced hepatotoxicity could explain the protective effects of DMF.

Moreover, there was an upregulation of several genes responsible for cell metabolism and lipid metabolism. Genes involved in cell metabolism include homogentisate 1,2-dioxygenase (HGD) and electron transfer flavoprotein subunit beta (ETFB) (233,234). In contrast, Dual specificity phosphatase 9 (DUSP9) and apolipoprotein C3 (APOC3) are involved lipid metabolism (235,236). These results indicate that DMF pre-treatment induced cell metabolism, which could improve cell health following paracetamol administration.

However, HLCs treated without DMF exhibited an upregulation of genes involved in several injury pathways including apoptosis, tumourgenesis, TGF-b activation or inducing inflammation.

CLDN6 is a tight junction membrane protein. Upregulation of CLDN6 has been shown to induce apoptosis and stop cell growth (237,238). In addition, changes in claudins expression can affect hepatocyte polarity leading to tumour formation (239–241). In addition, several genes that were identified in this dataset are involved in hepatocellular carcinoma development. These genes include SLC2A3, DHRS7, NRGN and KRT19.

First, SLC2A3 forms part of the glucose transporter family, upregulation of glucose transporters are linked to some cases of hepatocellular carcinoma (242). Interestingly, DHRS7 expression has been reported to be upregulated during rat liver regeneration process as well as downregulated in advanced HCC (243,244). Next, TPM1 is considered a tumour suppressor gene, TPM1 aberrant regulation is controlled by TGF-b induced epithelial–mesenchymal transition (EMT) (245). TPM1 downregulation has been linked with poor cancer prognosis (246). Despite NRGN being a neuron specific gene, Daust et all showed an upregulation of NRGN in liver progenitor cells from rats that were exposed to polychlorinated biphenyls (PCBs), tumour-

promoting compounds (247). In this work NRGN was only reported not investigated. Further work would be required to fully understand the effect of NRGN expression in liver biology. To conclude, KRT19 is a member of the keratin family. KRT19 is expressed in hepatic progenitor cells (HPCs) (248) as well as a marker of hepatocellular carcinoma (249).

Finally, SQSTM1 or p62/SQSTM1 is a stress-inducible scaffold protein that regulates autophagy. p62/SQSTM1 is involved in multifunctional processes including apoptosis, inflammation, regulation of endosomal trafficking as well as activating Nrf2 via KEAP1 degradation (250,251). These results suggest that the gene response triggered by the DMF pre-treatment stopped the development of a pro-injury gene response.

These findings were further validated by GSEA analysis. DMF-treated group showed an increase in several hallmarks involved in protein secretion, G2M checkpoint or fatty acid metabolism. In addition, there was a reduction in several pro-injury hallmarks such as TNFA signalling via Nf-kb, apoptosis or epithelial mesenchymal transition (**Figure 74**).

From these results, I hypothesise that pre-treatment of DMF drove an upregulation of the drug metabolism and antioxidative stress machinery in HLCs prior to paracetamol administration. This led to an improved ROS management resulting in an increased cell survival and higher metabolic activity of the cell. This would be achieved by stopping the excessive generation of NAPQI due to the upregulation of Phase I and Phase II enzymes. By doing this, the development of a pro-injury environment was stopped as evidenced by the decrease in the different pro-inflammatory hallmarks shown in the GSEA analysis (**Figure 84**).

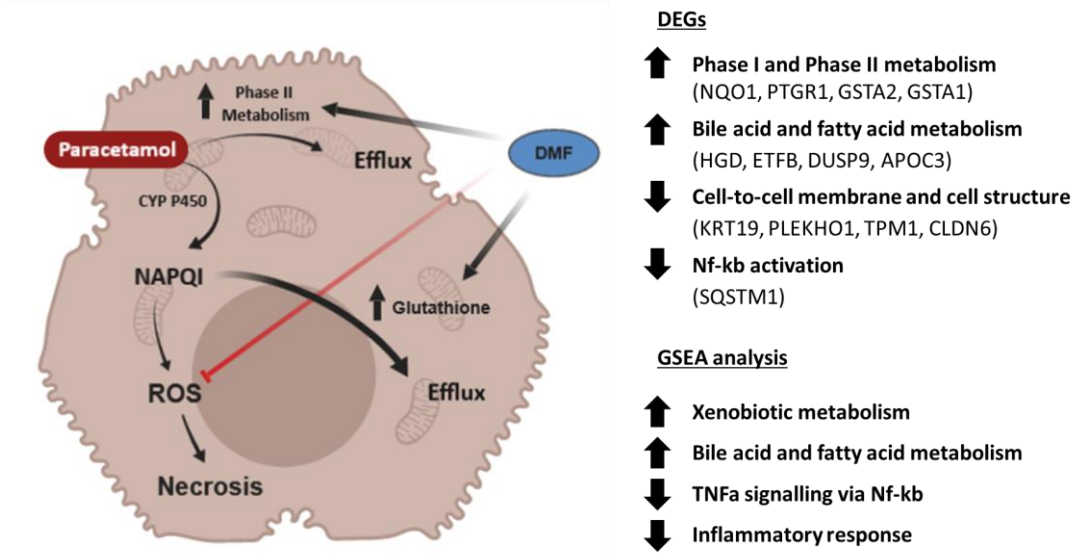

Figure 84. Proposed mechanism of action of DMF cytoprotection in the pre-treatment. During DMF pre-treatment, Nrf2 activation upregulates phase I and phase II genes. This leads to a better stress management after paracetamol administration and NAPQI generation. Figure drawn by author.

5.3.2 HLCs co-treatment gene expression

In the co-treatment scenario, DMF treatment upregulated genes involved in lipid metabolism (ABCA1), cell survival (UBR4 and UBR5) or NADPH metabolism (DUOX2). In hepatocytes, ABCA1 depletion impairs lipogenesis and insulin signalling (252) and is regulated by Nrf2 (253). UBR4 it has been found to be essential for membrane morphogenesis and cell survival. Loss of UBR4 induces cells to undergo apoptosis by cell detachment (254). UBR5 is involved in multiple processes such as progesterone-regulated cell proliferation, DNA repair and tumorigenesis (255,256). NID1 is a basement membrane glycoprotein involved in cell interactions with the extracellular matrix. NID1 methylation has been shown in gastrointestinal cancer (257). Finally, DUOX2 has been shown to be upregulated during alcohol hepatitis and as a marker of hepatocellular carcinoma after hepatectomy (258,259).

Moreover, TTC37 was upregulated. Whilst little is known about the function of TTC37, its function might be involved in mediating protein-to-protein interactions or chaperone activity. TTC37 mutations are the cause of trichohepatoenteric syndrome, an untreatable disorder with multiple organ defects such as life-threatening diarrhoea during infancy, immunodeficiency or liver disease among other symptoms (260). TTC37 mutations might cause changes in transporter proteins. Further research would be necessary to understand the TTC37 function during paracetamol injury.

But the main effect detected from DMF co-treatment was not an upregulation of a battery of xenobiotic metabolic enzymes as shown in the pre-treatment scenario but to block the development of a pro-injury pathway activation. HLCs treated with paracetamol only exhibited an upregulation of genes involved in TGF-b activation, inflammation or tumour progression.

Indications of TGF-b activation were observed by the detection of SERPINB8 and SEMA7A. SERPINB8 is a member of the serine proteases family and is mainly expressed in platelets (261). SERPIN proteins inhibit target proteins by conformational changes. SERPINB8 inhibits furin, a serine protease involved in platelet activity. SERPINB8 upregulation has been detected during a TGF-b/TNFa induction of EMT in lung cancer cells (262). In addition, SERPINB8 upregulation was included in a molecular fibrosis signature dataset from a non-alcoholic steatohepatitis (NASH) mouse model (263). Next, Semaphorin7A (SEMA7A) expression indicates an induction of a pro-fibrotic environment. SEMA7A is a membrane protein involved in inflammatory responses and fibrosis and its expression can be induced via TGF-b (264). In mice, SEMA7A overexpression induced a profibrotic response in liver. These findings were corroborated in human liver samples where SEMA7A expression was increased in patients with liver fibrosis (265).

Development of a pro-inflammatory response was observed by SMOX expression. SMOX upregulation is induced during cell stress and inflammation (266). SMOX catalyses the oxidation of spermine to spermadine and hydrogen peroxide as a secondary product.

Finally, HLCs treated with paracetamol only expressed genes involved in tumour development. These genes include TACSTD2, NPPB and TFPI2. TACSTD2 is a carcinoma-associated antigen. TACSTD2 expression has been detected in KRT19-positive HCC (267). NPPB is a cardiac hormone secreted by cardiomyocytes. Upregulation of NPPB in non-cardiomyocyte cell types has been linked with an aggressive osteosarcoma and it is also expressed in cancer-associated fibroblasts in ovarian tumours (268,269). Interestingly, TFPI2 has tumour repressor activities by inhibiting plasmin- and trypsin-matrix metalloproteinases, and this leads to reduced tumour progression and metastasis. TFPI2 methylation has been found in some forms of HCC (270,271).

Results from the GSEA analysis from the co-treatment show a similar trend as the one described from the DEGs. DMF-treated cells displayed hallmarks involved in cell homeostasis such as mitotic spindle or G2M checkpoint and hallmarks involved in cell metabolism like fatty acid metabolism or protein secretion. Most of the changes detected from the GSEA analysis were from downregulation of pro-injury hallmarks. These hallmarks include TNFA signalling via Nf-kb activation, apoptosis, P53 pathway, IL2 STAT5 signalling or reactive oxygen species response.

From these results, I hypothesise that DMF co-treatment protection is due to a dual mechanism of action. On the one hand, DMF induced the expression of several Nrf2 target genes involved in cell metabolism and survival (ABCA1, UBR4, UBR5 and DUOX2). On the other hand, dimethyl fumarate inhibited Nf-kb and TGF-b activation (**Figure 85**).

Dimethyl fumarate has been shown to block Nf-kb activation by a covalent modification of p65, a subunit of Nf-kb transcription complex. DMF inhibits the nuclear translocation blocking the DNA binding activity of phosphorylated p65 (130,131). In addition, DMF mediated Nrf2 activation has been shown to block TGF-b1 activation by interacting and blocking Smad3 protein activity in a model of renal fibrosis (206). Similar results have been shown in hepatocytes. Oh et al showed a TGF-b 1 inhibition in hepatocytes via a reduction of Smad3 phosphorylation following exposure to sulforaphane which is a Nrf2 inducer (272). In addition, Nrf2 activation reduced hepatic stellate cell activation into myofibroblasts via Smad3 inhibition (273) .

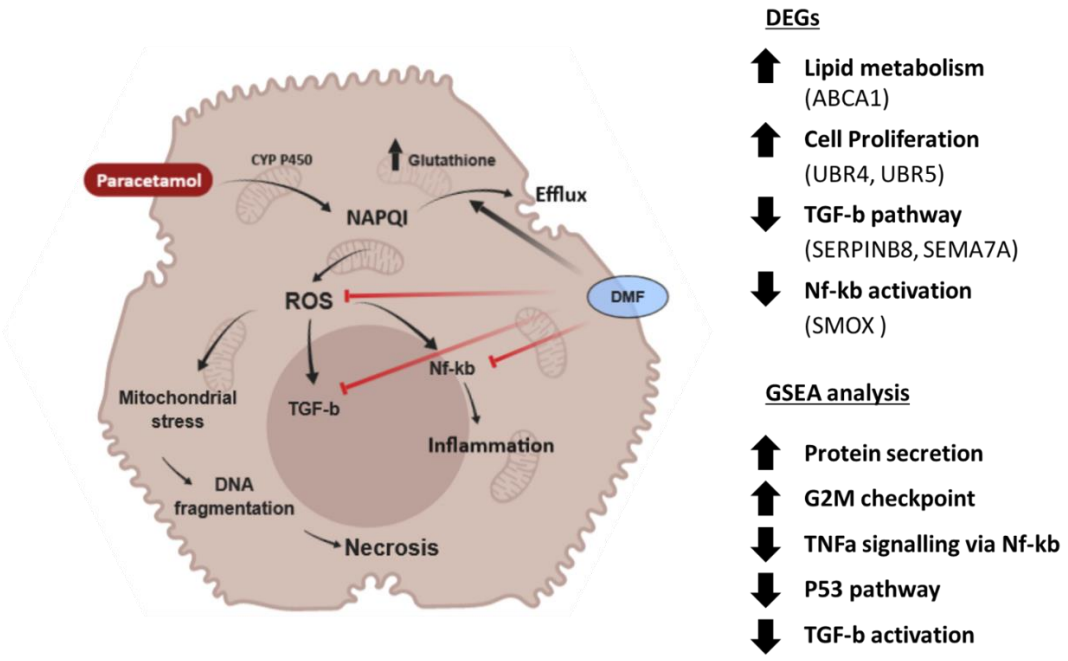

Figure 85. Proposed mechanism of action of DMF cytoprotection in the co-treatment. During DMF co-treatment, Nrf2 activation induces cell metabolism as well as blocking phase I and phase II genes. This leads to a better stress management after paracetamol administration and NAPQI generation. Moreover, DMF inhibited Nf-kb and TGF-b activation reducing necrosis and inflammation. Figure drawn by author.

5.3.3 HLCs post-treatment gene expression

DMF post-treatment induced the expression of genes involved in cell proliferation and xenobiotic metabolism. Genes involved in cell proliferation include NEAT1, TRIM71 and NUPR1. Firstly, NEAT1 upregulation promotes cell proliferation by reducing apoptosis in hepatocellular carcinomas (274,275). Next, TRIM71 has been shown to target p53 to stop cell death and promote differentiation (276). Lastly, NUPR1 is a stress inducible protein and it has been shown to be essential for cell survival and proliferation of HCC (277,278).

Moreover, an increase in xenobiotic metabolism was observed by the upregulation of GSR. GSR is an antioxidant enzyme that reduces GSSG replenishing GSH and is regulated by Nrf2 (279). Therefore, NAPQI damage can be reduced by replenishing GSH (183). Finally, upregulation of SCNN1A was detected. SCNN1A is a sodium channel and its inhibition has been shown to reduce hepatitis B infection (280).

Similar to co-treatment, the main effect observed from the post-treatment was not from the gene upregulation but from a downregulation of genes involved in multiple pro-injury pathways. HLCs treated with paracetamol only exhibited an upregulation of genes involved in Nf-kb and TGF-b activation, inflammation or tumour progression. From these genes, CD44 is a cell surface glycoprotein involved in cell-to-cell interactions. CD44 has been seen shown to be increased in paracetamol-induced hepatotoxicity and is regulated through Nf-kb activation (281).

Following this, TGF-b activation was observed by the detection of MIR4435-2GH, TAGLN and ITGA2. High expression of MIR4435-2GH has been linked with poor prognosis in several cancers by inducing cell proliferation via b-catenin activation (282,283). Moreover, a positive correlation was detected between MIR4435-2GH and TGF-b1 in

squamous cell carcinoma (284). In addition, transgelin (TAGLN) and integrin a2 (ITGA2) are regulated by the TGF-b pathway (285,286).

In addition, CYTOR and EST1 upregulation has been found in some cases of hepatocellular carcinoma. CYTOR is a long noncoding RNA, that has been shown to be upregulated in hepatocellular carcinoma (287,288). Finally EST1 is a transcription factor involved in many cell processes such as cell proliferation and angiogenesis (289). EST1 overexpression has been found in HCC (290). Interestingly, ETS1 has been reported to play a role in hepatic stellate cell activation during Non-alcoholic steatohepatitis (NASH) development (291). Lastly, CCL3L1 upregulation has been linked to an increased susceptibility to acute rejection following liver transplantation (292). GSEA analysis from the post-treatment data showed similar results. Analysis showed an enrichment in hallmarks involved in xenobiotic metabolism or bile acid and fatty acid metabolism. This was accompanied by a decrease in pro-injury hallmarks such as TNF-a signalling via Nf-kb, TGF beta signalling, apoptosis or epithelial mesenchymal transition (**Figure 80**).

In the post-treatment scenario, DMF was administrated after paracetamol and NAPQI-induced cell damage. Similar to the co-treatment, I hypothesise that DMF protection in the post-treatment scenario is due to a dual mechanism. This entails an induction of cell proliferation and oxidative stress management, whilst inhibiting the progression of Nf-kb and TGF-b activation.

In the previous chapter we observed that in the post-treatment scenario only DMF was able to recover cell viability. Cell recovery was not observed with NAC post-treatment (**Figure 62**). The combination of the proposed hypothesis obtained from the RNA-seq data with the cytoprotective effects observed in the previous chapter highlight a potential clinical therapy for acute liver diseases. DMF cytoprotection was achieved by a multi-factor response including Nrf2 activation and

the inhibition of Nf-kb and TGF-b response. The protective mechanism could be similar to a recent study by Bird et al (57) where they showed that TGF-b inhibition following paracetamol injury induces liver regeneration by blocking injury-induced senescence. Similar processes occur in our case where HLCs treated with DMF show an upregulation of proliferative markers and a reduction of senescence markers such as p53 or KRAS (293). Further work is required to validate the role of senescence inhibition in the cytoprotective properties of DMF (**Figure 86**).

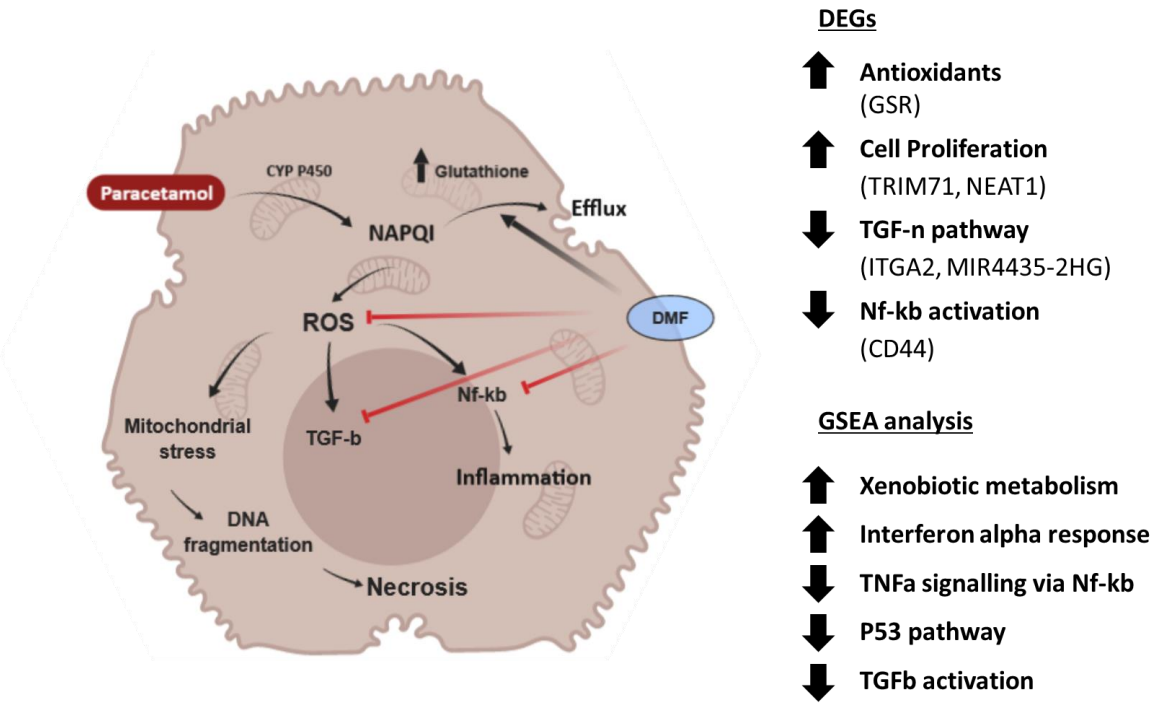

Figure 86. Proposed mechanism of action of DMF cytoprotection in the post-treatment. In the post-treatment scenario, DMF was administrated after paracetamol and NAPQI-induced cell damage. DMF cytoprotection was due to multiple-factors. First DMF increased the glutathione replenishing capacity of the HLCs. Moreover, DMF inhibited Nf-kb and TGF-b activation reducing necrosis and inflammation. Figure drawn by author.

5.3.4 Zebrafish cytoprotective gene regulation.

In the zebrafish scenario, DMF pre-treatment showed an increase in several genes including tcnba, nup160 and members of the crystallin family. In zebrafish, tcnba is expressed in the intestinal bulb and it plays a role in vitamin B12 transport (294). nup160 is expressed in the kidney, where nup160 knockdown in mice induced apoptosis and cell migration as well as inhibiting cell proliferation in podocytes, a member of the kidney glomerulus (295). In addition, abnormal development following paracetamol administration could explain the changes found in the crystallin family overexpression in the DMF-treated group. Pinto et al showed that liver X Receptors (LXRs) are responsible for crystallin expression during zebrafish development (296). In addition, Saini et al reported that LXR activation increases paracetamol clearance in mice (297). This could indicate that in the paracetamol-treated group the reduction of crystallin might be related to a reduction of LXR activity which might impair paracetamol clearance, inducing liver damage and reduction of GFP in our model. Yan et al showed how curcumin reduced steatosis in a NAFLD mice model via the activation of Nrf2 and LXRs pathways (298). Further validation is required to confirm this proposed mechanism.

In contrast, zebrafish treated with paracetamol only showed an increase in expression in several genes including haao, HTRA2, fbxo32, apoda.1 and rpe65a. Firstly, haao is an enzyme that catalyzes quinolinic acid (QUIN) synthesis from 3-hydroxyanthranilic acid Excessive production of QUIN can lead to oxidative stress and it has been shown to cause neurologic damage (299). Downregulation of haao is correlated with poor HCC prognosis due to alterations in nicotinamide adenine dinucleotide (NAD^+) metabolism (300).

Next, HTRA2 is a pro-apoptotic mitochondrial protein via caspase activation (301,302). fbxo32 is a novel TGF-beta/SMAD4 target gene and it is involved in phosphorylation-dependent ubiquitination (303). fbxo32 methylation silencing was observed in ovarian cancer and it was associated with poor prognosis (303).

In addition, apoda.1 encodes an apolipoprotein with lipid transport activity. apolipoprotein D (APOD) is its human homologue. APOD has been shown to be linked with several neurological disorders where ROS induced APOD expression (304). In addition, APOD expression has been shown to inhibit cell proliferation as well as being a direct target of p53 family members (305,306). Finally, rpe65a is a oxygenase member of the visual cycle of the retina (307).

Interestingly, GSEA analysis showed an increase in several pro-injury markers of apoptosis and reactive oxygen species pathways, as well as an enrichment of genes involved in cell proliferation and DNA repair. One limitation of the GSEA analysis in this scenario is due to analysing zebrafish data in a dataset designed to analyse human data (225).

From these results, we propose that the cytoprotective effects of DMF pre-treatment in zebrafish are due to the modulation of multiple pathways. Firstly, DMF-treated zebrafish showed an increase in metabolism and cell proliferation and this could be due to Nrf2 activation. Even though no Nrf2 target genes were detected, the possible induction of LXR pathway involved in the crystallin expression might involve Nrf2 activation (298). On the other hand, DMF pre-treatment reduced the development of cell apoptosis by the reduction of HTRA2, a pro-apoptotic mitochondrial protein. This mechanism could be mediated in part by p53 and TGF-b inhibition as shown by the reduction of fbxo32 and APOD expression (308,309). The lack of detection of Nrf2 target genes might be a result of the experimental design and due to timing of the sample acquisition. RNA acquisition

was performed 42 h post-administration of DMF. Further work is required to validate the mechanism proposed.

5.3.5 Conclusion

Findings from the RNA-seq highlight the protective mechanism of DMF shown in the previous chapter. DMF treatment not only activates Nrf2 target genes but is also able to stop the development of a pro-injury response by inhibiting Nf-kb and TGF-b activation. These findings are novel in the context of paracetamol-induced hepatotoxicity. Moreover, these results have translational relevance from HLCs to zebrafish as TGF-b inhibition was also observed in the zebrafish RNA-seq. Finally, results showing cytoprotection in the post-treatment scenario where NAC efficacy was lost have interesting clinical relevance. These results suggest that DMF could represent a novel therapy to treat patients with acute liver disease.

CHAPTER SIX

CONCLUSIONS AND FUTURE PERSPECTIVES

6.1 Conclusions

Drug-induced liver injury represents a major cause of acute liver failure, so to improve patient outcome it is necessary to develop new therapies (310). Nrf2 stimulation has been proposed as a potential therapy to reduce DILI severity. Nrf2 is a major regulator of cytoprotective genes involved in multiple processes such as oxidative stress management, glutathione synthesis, detoxification, drug excretion and NADPH synthesis (94). Dimethyl fumarate is a drug approved to treat relapsing multiple sclerosis and psoriasis; DMF beneficial effects are due in part to Nrf2 activation (191). The objective of this thesis was to investigate cytoprotective properties of dimethyl fumarate via Nrf2 stimulation during drug-induced hepatotoxicity. This was tested in both hepatocyte-like cells (HLCs) and in zebrafish.

During my project, I developed a semi-automated platform to produce HLCs in 96-well plate format to study liver biology and disease modelling (67,89). Following platform optimisation, the effects of DMF in HLCs were investigated. DMF induced Nrf2 nuclear translocation and upregulated Nrf2 target genes. In addition, DMF displayed cytoprotective properties in the context of paracetamol-induced injury. This protection was Nrf2 dependent. Interestingly, DMF showed an increase in cell viability where NAC treatment was not effective. These findings were translated into a zebrafish model of paracetamol injury where pre-treatment with DMF protected zebrafish from paracetamol-induced injury.

To understand the cytoprotective mechanisms, RNA-sequencing was performed in both systems. In HLCs, DMF exhibited a time-dependent mechanism. From these results, the proposed mechanism during the pre-treatment scenario is that DMF cytoprotection is due to an upregulation of the drug metabolism and reduced oxidative stress. Meanwhile in the co- and post-treatment scenarios cytoprotection was

due to a reduction of spreading senescence and inflammation as well as by the induction of Nrf2 target genes. In zebrafish, we hypothesised that the protection could be due to Nrf2 activation as well as TGF-b inhibition. Further validation is required to confirm the mechanism proposed.

Findings of this study are novel in the context of paracetamol-induced hepatotoxicity and could have clinical relevance providing a new therapy to treat patients with acute liver disease.

6.2 Future perspectives

Evidence from this project provides proof-of-concept for using DMF to reduce the severity of acute liver injuries. Further work is required to improve current *in vitro* models to better recapitulate human liver biology and this would allow a better understanding of DMF in the context of liver injury and provide better tools for regenerative medicine research. Going forward, further *in vivo* characterisation of these datasets is required to validate the proposed mechanisms of action of DMF. In addition, a mouse model of paracetamol induced liver injury could be used to study the effects on a mammal system. This would allow to study the immunomodulation effect of DMF in the immune system following the initial hepatocyte death caused by paracetamol overdose.

6.2.1 Improved HLCs disease modelling

Although the semi-automated differentiation platform allows a rapid and reproducible production of HLCs, further improvements could be implemented to better recapitulate situations in the clinic. This could be achieved by using panels of iPSC-derived lines that recapitulate genetic polymorphisms, CYP450 genotypes and sex differences. This work was performed using the female hESC line H9, by adding multiple lines from different donors, a better representation of human

variability could be achieved. By using iPSC derived HLCs, it might be possible to reduce significant sources of interindividual variability. In this regard, Takayama et al. generated 12 individual HLC lines that exhibited interindividual differences in drug metabolism that are similar to the ones found in the originating primary human hepatocytes (311). Drug-induced liver damage often occurs within pre-existing hepatic illnesses such as NAFLD (312). These could be easily modelled in HLCs by combining current NAFLD models in the context of paracetamol injury (67).

Nrf2 studies could also be improved by using an Nrf2 reporter line or an Nrf2 target gene reporter line. This would allow a real time quantification of Nrf2 dynamics upon treatment and time. Genome editing in hPSC could be performed using CRISPR/CAS technology (313,314). The potential of this approach can be seen by the recent work from Bischoff et al, (208), where HepG2 Nrf2 were tagged with GFP allowing a real time study of Nrf2 dynamics upon xenobiotic exposure. Finally, efficacy of DMF could be compared with recent compounds with slow and sustained release of MMF that would improve MMF bioavailability (96). These compounds include diroximel fumarate, currently in phase III clinical trial for MS (NCT03093324) or tepilamide fumarate, currently in phase II for psoriasis (NCT02173301) (96). Overall, the technology developed in this study provides an excellent tool to test the improvements suggested above.

6.2.2 Nf-kb and TGF-b regulation by DMF treatment

Here, we proposed that part of the cytoprotective properties of DMF was through the inhibition of both Nf-kb and TGF-b signalling pathways. Several studies have provided insights that DMF treatment inhibits Nf-kb activation via covalent modification of p65. DMF treatment blocks the nuclear translocation and DNA binding activity of p65 (130,131). In addition, TGF-b1 inhibition from DMF-mediated

Nrf2 activation has been reported in a model of renal fibrosis, where inhibition was due to an interaction between Nrf2 and Smad3 leading to a Smad3 inhibition (206).

Further work would be focused on investigating the interactions between DMF, p65 and Smad3 in HLCs. This could be performed using the high content analysis pipeline developed in this study to quantify p65 nuclear translocation dynamics upon DMF treatment. In addition, TGF-b inhibition following paracetamol injury could promote liver regeneration by blocking senescence (57). This could be validated by staining for both senescence (p21, p16 or p53) and cell proliferation (Ki67) markers in the post-treatment scenario (57,293,315).

Finally, the capacity of DMF to reduce the TGF-b induced fibrosis could be tested in an *in vitro* model of fibrosis by using stem cell-derived stellate cells (316). Recent work from Coll et al, developed a novel protocol to differentiate hepatic stellate cells from human pluripotent cells. These cells exhibit a quiescent phenotype but can develop a fibrogenic response secreting collagen and a-SMA expression in response to TGF-b (316). By using these cells, inhibition of TGF-b following DMF treatment in HLCs could be tested by culturing the stellate cells with the supernatant from the post-treatment.

6.2.3 Three-dimensional (3D) cellular aggregates

To date most of the work has been focused on monolayer differentiation of HLCs. Despite its advantages, monolayer HLCs do face some limitations including different cell-to-cell interactions, mixture of foetal and adult hepatocyte traits, lack of blood flow, and limited tissue organisation and as a consequence cannot recapitulate *in vivo* situations (78,90). To overcome these limitations, organoid and 3D aggregates have been developed showing promising results. Despite requiring more complex differentiation protocols, organoids and 3D systems better recapitulate human tissue structure and display a more

mature and functional phenotype such as improved cytochrome P450 3A4 activity, higher expression of Phase II and III enzymes, reduction of foetal gene expression and longer lifespan (317,318). Recent work from Takebe et al reported a protocol to generate 3D 'liver buds' formed by hepatic endoderm, endothelial and mesenchymal progenitor cells generated from the same iPSC line (319). In addition, a recent study from Rashidi et al developed a stem cell-derived self-aggregation protocol to produce 3D liver tissue under defined conditions. These 3D liver tissues displayed a stable phenotype for over one year in culture, providing an attractive tool for long-term *in vitro* studies. In addition, the liver tissue generated provided liver support in immune-competent or -deficient mice ($Fah^{-/-}$, $Rag2^{-/-}$ and $IL2rg^{-/-}$ mice) with compromised liver function (320).

Future work could be focused to study the cytoprotection of DMF in a 3D system that better mimics liver injury. Although stem cell-derived 3D liver models are promising, further work is required to determine the potential use of these systems for drug-induced liver injury prediction, repeated dosing or modelling human disease.

6.2.4 *In vivo* translational work

In this study, a zebrafish liver-GFP reporter line was used to validate the *in vitro* findings. Pre-treatment of DMF prevented GFP fluorescent loss. For the RNA sequencing, single embryos were used for total RNA preparation. To study the effect of DMF treatment in hepatocytes, hepatocyte sorting based on GFP intensity could be done in future experiments (321). One of the disadvantages of this approach could be the isolation of healthy hepatocytes expressing GFP, following injury, GFP expression could be altered leading into a hepatocyte underrepresentation. To solve this, whole embryo cell sorting could be performed. Further studies characterising the level of GFP loss upon injury at single cell level should be considered. In addition,

development of a post-treatment scenario in zebrafish would provide a more clinically relevant model to study DILI. Finally, these findings could be tested in a mouse model of paracetamol-induced hepatotoxicity. Mouse models are commonly used to study DILI. Their advantages are a better recapitulation of the human immune response following injury. In mouse models, paracetamol toxicity is characterised by the overproduction of NAPQI by CYP P450 proteins mimicking human physiology (322). With this, my studies might provide the foundation for a new clinical application of DMF to reduce acute liver injury.

6.2.5 Potential risks of DMF induced Nrf2 stimulation in the clinic

The safety of a potential DMF treatment for acute liver failure should be investigated prior drug repurposing into the clinic. DMF was approved by the FDA on 2013 as a treatment for multiple sclerosis and it has been used for more than 30 years for psoriasis treatment (121,122). Golf et al performed a long-term study called ENDROSE as a follow up study of the phase III clinical trial for DMF. ENDORSE focused on DMF treatment in patients with relapsing–remitting multiple sclerosis investigated the potential efficacy and safety (323). This study focused in a 14 years follow-up of patients treated with DMF. The main adverse events observed in patients were flushing and gastrointestinal alterations. These adverse events are common and tend to occur during within the first months after starting the treatment. The other main adverse event presented following long term DMF treatment is a reduction of neutrophils and lymphocytes counts. The clinical implications of the lymphopenia following DMF treatment are not completely understood. The immune response plays a key role during the initiation and resolution of acute liver

injury. Therefore, the interaction of DMF and the immune response during acute liver failure should be investigated to ensure safety.

Another potential risk from Nrf2 stimulation could be an increase risk in cancer development. Maintained expression of cytoprotective genes via Nrf2 stimulation can lead into increased cell growth in cancer cells as well as chemoresistance (324,325). Nrf2-induced tumorigenesis has been observed in mutations in both Nrf2 and Keap1. Nrf2 mutations that lead to overactivation of Nrf2 have been observed in primary lung cancers and neck tumours (326). In addition, Keap1 mutations that reduce the Keap1 repressor activity have been reported in lung cancer (327). Therefore, DMF patients with those mutations could be at risk of developing more aggressive cancers. The potential correlation of DMF patients and cancer development was investigated in the ENDORSE study. Increased risk of malignancy was not observed in DMF-treated patients compared with general multiple sclerosis patients; Results from the ENDORSE study suggest that the mutations in Nrf2 have more carcinogenesis potential than Nrf2 stimulation as long term stimulation of Nrf2 via DMF treatment did not increase carcinogenesis. A new clinical application of DMF to reduce acute liver injury should investigate any potential adverse effects involved in liver disease.

Bibliography

1. Si-Tayeb K, Lemaigre FP, Duncan SA. Organogenesis and development of the liver. Dev Cell. 2010 Feb 16;18(2):175–89.

2. Godoy P, Hewitt NJ, Albrecht U, Andersen ME, Ansari N, Bhattacharya S, et al. Recent advances in 2D and 3D in vitro systems using primary hepatocytes, alternative hepatocyte sources and non-parenchymal liver cells and their use in investigating mechanisms of hepatotoxicity, cell signaling and ADME. Arch Toxicol. 2013;87(8):1315–530.

3. Gebhardt R, Matz-Soja M. Liver zonation: Novel aspects of its regulation and its impact on homeostasis. World J Gastroenterol WJG. 2014 Jul 14;20(26):8491–504.

4. Gordillo M, Evans T, Gouon-Evans V. Orchestrating liver development. Development. 2015 Jun 15;142(12):2094–108.

5. Birchmeier W. Orchestrating Wnt signalling for metabolic liver zonation. Nat Cell Biol. 2016 May;18(5):463–5.

6. Lawson KA, Meneses JJ, Pedersen RA. Clonal analysis of epiblast fate during germ layer formation in the mouse embryo. Dev Camb Engl. 1991 Nov;113(3):891–911.

7. Tremblay KD, Zaret KS. Distinct populations of endoderm cells converge to generate the embryonic liver bud and ventral foregut tissues. Dev Biol. 2005 Apr 1;280(1):87–99.

8. Grapin-Botton A, Constam D. Evolution of the mechanisms and molecular control of endoderm formation. Mech Dev. 2007 Apr;124(4):253–78.

9. Lickert H, Kutsch S, Kanzler B, Tamai Y, Taketo MM, Kemler R. Formation of multiple hearts in mice following deletion of beta-catenin in the embryonic endoderm. Dev Cell. 2002 Aug;3(2):171–81.

10. Bort R, Signore M, Tremblay K, Martinez Barbera JP, Zaret KS. Hex homeobox gene controls the transition of the endoderm to a pseudostratified, cell emergent epithelium for liver bud development. Dev Biol. 2006 Feb 1;290(1):44–56.

11. Matsumoto K, Yoshitomi H, Rossant J, Zaret KS. Liver Organogenesis Promoted by Endothelial Cells Prior to Vascular Function. Science. 2001 Oct 19;294(5542):559–63.

12. Kinoshita T, Miyajima A. Cytokine regulation of liver development. Biochim Biophys Acta BBA - Mol Cell Res. 2002 Nov 11;1592(3):303–12.

13. Calmont A, Wandzioch E, Tremblay KD, Minowada G, Kaestner KH, Martin GR, et al. An FGF response pathway that mediates hepatic gene induction in embryonic endoderm cells. Dev Cell. 2006 Sep;11(3):339–48.

14. Shin D, Shin CH, Tucker J, Ober EA, Rentzsch F, Poss KD, et al. Bmp and Fgf signaling are essential for liver specification in zebrafish. Dev Camb Engl. 2007 Jun;134(11):2041–50.

15. Zimmerman LB, De Jesús-Escobar JM, Harland RM. The Spemann organizer signal noggin binds and inactivates bone morphogenetic protein 4. Cell. 1996 Aug 23;86(4):599–606.

16. Poulain M, Ober EA. Interplay between Wnt2 and Wnt2bb controls multiple steps of early foregut-derived organ development. Dev Camb Engl. 2011 Aug 15;138(16):3557–68.

17. Goss AM, Tian Y, Tsukiyama T, Cohen ED, Zhou D, Lu MM, et al. Wnt2/2b and β-catenin signaling are necessary and sufficient to specify lung progenitors in the foregut. Dev Cell. 2009 Aug;17(2):290–8.

18. Suksaweang S, Lin C-M, Jiang T-X, Hughes MW, Widelitz RB, Chuong C-M. Morphogenesis of chicken liver: identification of localized growth zones and the role of beta-catenin/Wnt in size regulation. Dev Biol. 2004 Feb 1;266(1):109–22.

19. Berg T, Rountree CB, Lee L, Estrada J, Sala FG, Choe A, et al. Fibroblast growth factor 10 is critical for liver growth during embryogenesis and controls hepatoblast survival via beta-catenin activation. Hepatol Baltim Md. 2007 Oct;46(4):1187–97.

20. Lemaigre FP. Molecular mechanisms of biliary development. Prog Mol Biol Transl Sci. 2010;97:103–26.

21. Zong Y, Panikkar A, Xu J, Antoniou A, Raynaud P, Lemaigre F, et al. Notch signaling controls liver development by regulating biliary differentiation. Dev Camb Engl. 2009 May;136(10):1727–39.

22. Decaens T, Godard C, de Reyniès A, Rickman DS, Tronche F, Couty J-P, et al. Stabilization of beta-catenin affects mouse embryonic liver growth and hepatoblast fate. Hepatol Baltim Md. 2008 Jan;47(1):247–58.

23. Tan X, Yuan Y, Zeng G, Apte U, Thompson MD, Cieply B, et al. Beta-catenin deletion in hepatoblasts disrupts hepatic morphogenesis and survival during mouse development. Hepatol Baltim Md. 2008 May;47(5):1667–79.

24. Schmidt C, Bladt F, Goedecke S, Brinkmann V, Zschiesche W, Sharpe M, et al. Scatter factor/hepatocyte growth factor is essential for liver development. Nature. 1995 Feb 23;373(6516):699–702.

25. Asrani SK, Devarbhavi H, Eaton J, Kamath PS. Burden of liver diseases in the world. J Hepatol. 2019 Jan 1;70(1):151–71.

26. Pellicoro A, Ramachandran P, Iredale JP, Fallowfield JA. Liver fibrosis and repair: immune regulation of wound healing in a solid organ. Nat Rev Immunol. 2014 Mar;14(3):181–94.

27. Bataller R, Brenner DA. Liver fibrosis. J Clin Invest. 2005 Feb;115(2):209–18.

28. Hellerbrand C, Stefanovic B, Giordano F, Burchardt ER, Brenner DA. The role of TGFbeta1 in initiating hepatic stellate cell activation in vivo. J Hepatol. 1999 Jan;30(1):77–87.

29. Ying H-Z, Chen Q, Zhang W-Y, Zhang H-H, Ma Y, Zhang S-Z, et al. PDGF signaling pathway in hepatic fibrosis pathogenesis and therapeutics. Mol Med Rep. 2017 Dec;16(6):7879–89.

30. Bataller R, Sancho-Bru P, Ginès P, Lora JM, Al-Garawi A, Solé M, et al. Activated human hepatic stellate cells express the renin-angiotensin system and synthesize angiotensin II. Gastroenterology. 2003 Jul;125(1):117–25.

31. Thawley V. Acute Liver Injury and Failure. Vet Clin North Am Small Anim Pract. 2017 May 1;47(3):617–30.

32. Kerr JF, Wyllie AH, Currie AR. Apoptosis: a basic biological phenomenon with wide-ranging implications in tissue kinetics. Br J Cancer. 1972 Aug;26(4):239–57.

33. Russell SW, Rosenau W, Lee JC. Cytolysis induced by human lymphotoxin. Am J Pathol. 1972 Oct;69(1):103–18.

34. Jiang X, Wang X. Cytochrome C-mediated apoptosis. Annu Rev Biochem. 2004;73:87–106.

35. Malhi H, Gores GJ, Lemasters JJ. Apoptosis and necrosis in the liver: A tale of two deaths? Hepatology. 2006;43(S1):S31–44.

36. Hotchkiss RS, Strasser A, McDunn JE, Swanson PE. Cell death. N Engl J Med. 2009 Oct 15;361(16):1570–83.

37. Guicciardi ME, Malhi H, Mott JL, Gores GJ. Apoptosis and Necrosis in the Liver. Compr Physiol [Internet]. 2013 Apr [cited 2019 Apr 14];3(2). Available from: https://www.ncbi.nlm.nih.gov/pmc/articles/PMC3867948/

38. Larson AM, Polson J, Fontana RJ, Davern TJ, Lalani E, Hynan LS, et al. Acetaminophen-induced acute liver failure: results of a United States multicenter, prospective study. Hepatol Baltim Md. 2005 Dec;42(6):1364–72.

39. Tanne J. Paracetamol causes most liver failure in UK and US. BMJ. 2006 Mar 18;332(7542):628.

40. Sgro C, Clinard F, Ouazir K, Chanay H, Allard C, Guilleminet C, et al. Incidence of drug-induced hepatic injuries: a French population-based study. Hepatol Baltim Md. 2002 Aug;36(2):451–5.

41. Woodhead JL, Howell BA, Yang Y, Harrill AH, Clewell HJ, Andersen ME, et al. An analysis of N-acetylcysteine treatment for acetaminophen overdose using a systems model of drug-induced liver injury. J Pharmacol Exp Ther. 2012 Aug;342(2):529–40.

42. Karthivashan G, Arulselvan P, Fakurazi S. Pathways involved in acetaminophen hepatotoxicity with specific targets for inhibition/downregulation. RSC Adv. 2015 Jul 16;5(76):62040–51.

43. Gillette JR, Nelson SD, Mulder GJ, Jollow DJ, Mitchell JR, Pohl LR, et al. Formation of chemically reactive metabolites of phenacetin and acetaminophen. Adv Exp Med Biol. 1981;136 Pt B:931–50.

44. Dahlin DC, Miwa GT, Lu AY, Nelson SD. N-acetyl-p-benzoquinone imine: a cytochrome P-450-mediated oxidation product of acetaminophen. Proc Natl Acad Sci U S A. 1984 Mar;81(5):1327–31.

45. Patten CJ, Thomas PE, Guy RL, Lee M, Gonzalez FJ, Guengerich FP, et al. Cytochrome P450 enzymes involved in acetaminophen activation by rat and human liver microsomes and their kinetics. Chem Res Toxicol. 1993 Aug;6(4):511–8.

46. Chen Q, Cederbaum AI. Cytotoxicity and apoptosis produced by cytochrome P450 2E1 in Hep G2 cells. Mol Pharmacol. 1998 Apr;53(4):638–48.

47. Dong H, Haining RL, Thummel KE, Rettie AE, Nelson SD. Involvement of human cytochrome P450 2D6 in the bioactivation of acetaminophen. Drug Metab Dispos Biol Fate Chem. 2000 Dec;28(12):1397–400.

48. Anzenbacher P, Anzenbacherová E. Cytochromes P450 and metabolism of xenobiotics. Cell Mol Life Sci CMLS. 2001 May 1;58(5–6):737–47.

49. Lancaster EM, Hiatt JR, Zarrinpar A. Acetaminophen hepatotoxicity: an updated review. Arch Toxicol. 2015 Feb 1;89(2):193–9.

50. Rumack BH, Matthew H. Acetaminophen poisoning and toxicity. Pediatrics. 1975 Jun;55(6):871–6.

51. Eriksson LS, Broomé U, Kalin M, Lindholm M. Hepatotoxicity due to repeated intake of low doses of paracetamol. J Intern Med. 1992;231(5):567–70.

52. Du K, Ramachandran A, Jaeschke H. Oxidative stress during acetaminophen hepatotoxicity: Sources, pathophysiological role and therapeutic potential. Redox Biol. 2016 Oct 4;10:148–56.

53. Cohen SD, Pumford NR, Khairallah EA, Boekelheide K, Pohl LR, Amouzadeh HR, et al. Selective protein covalent binding and target organ toxicity. Toxicol Appl Pharmacol. 1997 Mar;143(1):1–12.

54. Blazka ME, Wilmer JL, Holladay SD, Wilson RE, Luster MI. Role of proinflammatory cytokines in acetaminophen hepatotoxicity. Toxicol Appl Pharmacol. 1995 Jul;133(1):43–52.

55. Gardner CR, Laskin JD, Dambach DM, Chiu H, Durham SK, Zhou P, et al. Exaggerated hepatotoxicity of acetaminophen in mice lacking tumor necrosis factor receptor-1. Potential role of inflammatory mediators. Toxicol Appl Pharmacol. 2003 Oct 15;192(2):119–30.

56. Reuben A, Tillman H, Fontana RJ, Davern T, McGuire B, Stravitz RT, et al. Outcomes in Adults With Acute Liver Failure Between 1998 and 2013. Ann Intern Med. 2016 Jun 7;164(11):724–32.

57. Bird TG, Müller M, Boulter L, Vincent DF, Ridgway RA, Lopez-Guadamillas E, et al. TGFβ inhibition restores a regenerative response in acute liver injury by suppressing paracrine senescence. Sci Transl Med. 2018 Aug 15;10(454).

58. Chun LJ, Tong MJ, Busuttil RW, Hiatt JR. Acetaminophen hepatotoxicity and acute liver failure. J Clin Gastroenterol. 2009 Apr;43(4):342–9.

59. Lauterburg BH, Corcoran GB, Mitchell JR. Mechanism of Action of *N*-Acetylcysteine in the Protection Against the Hepatotoxicity of Acetaminophen in Rats In Vivo. J Clin Invest. 1983 Apr 1;71(4):980–91.

60. Smilkstein MJ, Knapp GL, Kulig KW, Rumack BH. Efficacy of oral N-acetylcysteine in the treatment of acetaminophen overdose. Analysis of the national multicenter study (1976 to 1985). N Engl J Med. 1988 Dec 15;319(24):1557–62.

61. Castell JV, Jover R, Martínez-Jiménez CP, Gómez-Lechón MJ. Hepatocyte cell lines: their use, scope and limitations in drug metabolism studies. Expert Opin Drug Metab Toxicol. 2006 Apr;2(2):183–212.

62. Gómez-Lechón MJ, Tolosa L, Conde I, Donato MT. Competency of different cell models to predict human hepatotoxic drugs. Expert Opin Drug Metab Toxicol. 2014 Nov 1;10(11):1553–68.

63. Soldatow VY, LeCluyse EL, Griffith LG, Rusyn I. In vitro models for liver toxicity testing. Toxicol Res. 2013 Jan 1;2(1):23–39.

64. Burkhardt B, Martinez-Sanchez JJ, Bachmann A, Ladurner R, Nüssler AK. Long-term culture of primary hepatocytes: new matrices and microfluidic devices. Hepatol Int. 2014 Jan 1;8(1):14–22.

65. Gao X, Liu Y. A transcriptomic study suggesting human iPSC-derived hepatocytes potentially offer a better in vitro model of hepatotoxicity than most hepatoma cell lines. Cell Biol Toxicol. 2017 Jan 31;1–15.

66. Cameron K, Tan R, Schmidt-Heck W, Campos G, Lyall MJ, Wang Y, et al. Recombinant Laminins Drive the Differentiation and Self-Organization of hESC-Derived Hepatocytes. Stem Cell Rep. 2015 Dec 8;5(6):1250–62.

67. Lyall MJ, Cartier J, Thomson JP, Cameron K, Meseguer-Ripolles J, O'Duibhir E, et al. Modelling non-alcoholic fatty liver disease in human hepatocyte-like cells. Philos Trans R Soc Lond B Biol Sci. 2018 Jul 5;373(1750).

68. Kim DE, Jang M-J, Kim YR, Lee J-Y, Cho EB, Kim E, et al. Prediction of drug-induced immune-mediated hepatotoxicity using

hepatocyte-like cells derived from human embryonic stem cells. Toxicology. 2017 Jul 15;387(Supplement C):1–9.

69. Graffmann N, Ring S, Kawala M-A, Wruck W, Ncube A, Trompeter H-I, et al. Modeling Nonalcoholic Fatty Liver Disease with Human Pluripotent Stem Cell-Derived Immature Hepatocyte-Like Cells Reveals Activation of PLIN2 and Confirms Regulatory Functions of Peroxisome Proliferator-Activated Receptor Alpha. Stem Cells Dev. 2016 Jun 16;25(15):1119–33.

70. Rashid ST, Corbineau S, Hannan N, Marciniak SJ, Miranda E, Alexander G, et al. Modeling inherited metabolic disorders of the liver using human induced pluripotent stem cells. J Clin Invest. 2010 Sep 1;120(9):3127–36.

71. Cayo MA, Mallanna SK, Di Furio F, Jing R, Tolliver LB, Bures M, et al. A Drug Screen using Human iPSC-Derived Hepatocyte-like Cells Reveals Cardiac Glycosides as a Potential Treatment for Hypercholesterolemia. Cell Stem Cell. 2017 Apr 6;20(4):478-489.e5.

72. Hentze H, Soong PL, Wang ST, Phillips BW, Putti TC, Dunn NR. Teratoma formation by human embryonic stem cells: evaluation of essential parameters for future safety studies. Stem Cell Res. 2009 May;2(3):198–210.

73. Thomson JA, Itskovitz-Eldor J, Shapiro SS, Waknitz MA, Swiergiel JJ, Marshall VS, et al. Embryonic stem cell lines derived from human blastocysts. Science. 1998 Nov 6;282(5391):1145–7.

74. Takahashi K, Yamanaka S. Induction of pluripotent stem cells from mouse embryonic and adult fibroblast cultures by defined factors. Cell. 2006 Aug 25;126(4):663–76.

75. Schöler HR, Hatzopoulos AK, Balling R, Suzuki N, Gruss P. A family of octamer-specific proteins present during mouse embryogenesis: evidence for germline-specific expression of an Oct factor. EMBO J. 1989 Sep;8(9):2543–50.

76. Chambers I, Colby D, Robertson M, Nichols J, Lee S, Tweedie S, et al. Functional expression cloning of Nanog, a pluripotency sustaining factor in embryonic stem cells. Cell. 2003 May 30;113(5):643–55.

77. Avilion AA, Nicolis SK, Pevny LH, Perez L, Vivian N, Lovell-Badge R. Multipotent cell lineages in early mouse development depend on SOX2 function. Genes Dev. 2003 Jan 1;17(1):126–40.

78. Meseguer-Ripolles J, Khetani SR, Blanco JG, Iredale M, Hay DC. Pluripotent Stem Cell-Derived Human Tissue: Platforms to Evaluate Drug Metabolism and Safety. AAPS J. 2018 Jan 1;20(1):20.

79. D'Amour KA, Agulnick AD, Eliazer S, Kelly OG, Kroon E, Baetge EE. Efficient differentiation of human embryonic stem cells to definitive endoderm. Nat Biotechnol. 2005 Dec;23(12):1534–41.

80. Hay DC, Fletcher J, Payne C, Terrace JD, Gallagher RCJ, Snoeys J, et al. Highly efficient differentiation of hESCs to functional hepatic endoderm requires ActivinA and Wnt3a signaling. Proc Natl Acad Sci U S A. 2008 Aug 26;105(34):12301–6.

81. Song Z, Cai J, Liu Y, Zhao D, Yong J, Duo S, et al. Efficient generation of hepatocyte-like cells from human induced pluripotent stem cells. Cell Res. 2009 Nov;19(11):1233–42.

82. Basma H, Soto-Gutiérrez A, Yannam GR, Liu L, Ito R, Yamamoto T, et al. Differentiation and transplantation of human embryonic stem cell-derived hepatocytes. Gastroenterology. 2009 Mar;136(3):990–9.

83. Cai J, Zhao Y, Liu Y, Ye F, Song Z, Qin H, et al. Directed differentiation of human embryonic stem cells into functional hepatic cells. Hepatol Baltim Md. 2007 May;45(5):1229–39.

84. Sullivan GJ, Hay DC, Park I-H, Fletcher J, Hannoun Z, Payne CM, et al. Generation of functional human hepatic endoderm from human induced pluripotent stem cells. Hepatol Baltim Md. 2010 Jan;51(1):329–35.

85. Touboul T, Hannan NRF, Corbineau S, Martinez A, Martinet C, Branchereau S, et al. Generation of functional hepatocytes from human embryonic stem cells under chemically defined conditions that recapitulate liver development. Hepatology. 2010 May 1;51(5):1754–65.

86. Chen Y-F, Tseng C-Y, Wang H-W, Kuo H-C, Yang VW, Lee OK. Rapid generation of mature hepatocyte-like cells from human induced pluripotent stem cells by an efficient three-step protocol. Hepatol Baltim Md. 2012 Apr;55(4):1193–203.

87. Wang Y, Alhaque S, Cameron K, Meseguer-Ripolles J, Lucendo-Villarin B, Rashidi H, et al. Defined and Scalable Generation of Hepatocyte-like Cells from Human Pluripotent Stem Cells. JoVE J Vis Exp. 2017 Mar 2;(121):e55355–e55355.

88. Grimm FA, Iwata Y, Sirenko O, Bittner M, Rusyn I. High-Content Assay Multiplexing for Toxicity Screening in Induced Pluripotent Stem Cell-Derived Cardiomyocytes and Hepatocytes. Assay Drug Dev Technol. 2015 Nov;13(9):529–46.

89. Meseguer-Ripolles J, Lucendo-Villarin B, Wang Y, Hay DC. Semi-automated Production of Hepatocyte Like Cells from Pluripotent Stem Cells. JoVE J Vis Exp. 2018 Jul 27;(137):e57995–e57995.

90. Baxter M, Withey S, Harrison S, Segeritz C-P, Zhang F, Atkinson-Dell R, et al. Phenotypic and functional analyses show stem cell-derived hepatocyte-like cells better mimic fetal rather than adult hepatocytes. J Hepatol. 2015 Mar;62(3):581–9.

91. Szkolnicka D, Lucendo-Villarin B, Moore JK, Simpson KJ, Forbes SJ, Hay DC. Reducing Hepatocyte Injury and Necrosis in Response to Paracetamol Using Noncoding RNAs. Stem Cells Transl Med. 2016 Jun;5(6):764–72.

92. Lucendo-Villarin B, Filis P, Swortwood MJ, Huestis MA, Meseguer-Ripolles J, Cameron K, et al. Modelling foetal exposure to maternal smoking using hepatoblasts from pluripotent stem cells. Arch Toxicol. 2017 May 16;

93. Choi SM, Kim Y, Shim JS, Park JT, Wang R-H, Leach SD, et al. Efficient drug screening and gene correction for treating liver disease using patient-specific stem cells. Hepatology. 2013 Jun 1;57(6):2458–68.

94. Hayes JD, Dinkova-Kostova AT. The Nrf2 regulatory network provides an interface between redox and intermediary metabolism. Trends Biochem Sci. 2014 Apr 1;39(4):199–218.

95. Moi P, Chan K, Asunis I, Cao A, Kan YW. Isolation of NF-E2-related factor 2 (Nrf2), a NF-E2-like basic leucine zipper transcriptional activator that binds to the tandem NF-E2/AP1 repeat of the beta-globin locus control region. Proc Natl Acad Sci U S A. 1994 Oct 11;91(21):9926–30.

96. Cuadrado A, Rojo AI, Wells G, Hayes JD, Cousin SP, Rumsey WL, et al. Therapeutic targeting of the NRF2 and KEAP1 partnership in chronic diseases. Nat Rev Drug Discov. 2019 Apr;18(4):295.

97. Itoh K, Wakabayashi N, Katoh Y, Ishii T, Igarashi K, Engel JD, et al. Keap1 represses nuclear activation of antioxidant responsive elements by Nrf2 through binding to the amino-terminal Neh2 domain. Genes Dev. 1999 Jan 1;13(1):76–86.

98. Zhang DD, Lo S-C, Cross JV, Templeton DJ, Hannink M. Keap1 is a redox-regulated substrate adaptor protein for a Cul3-dependent ubiquitin ligase complex. Mol Cell Biol. 2004 Dec;24(24):10941–53.

99. Cullinan SB, Gordan JD, Jin J, Harper JW, Diehl JA. The Keap1-BTB protein is an adaptor that bridges Nrf2 to a Cul3-based E3 ligase: oxidative stress sensing by a Cul3-Keap1 ligase. Mol Cell Biol. 2004 Oct;24(19):8477–86.

100. McMahon M, Lamont DJ, Beattie KA, Hayes JD. Keap1 perceives stress via three sensors for the endogenous signaling molecules nitric oxide, zinc, and alkenals. Proc Natl Acad Sci U S A. 2010 Nov 2;107(44):18838–43.

101. Takaya K, Suzuki T, Motohashi H, Onodera K, Satomi S, Kensler TW, et al. Validation of the multiple sensor mechanism of the Keap1-Nrf2 system. Free Radic Biol Med. 2012 Aug 15;53(4):817–27.

102. Zhu R, Wang Y, Zhang L, Guo Q. Oxidative stress and liver disease. Hepatol Res Off J Jpn Soc Hepatol. 2012 Aug;42(8):741–9.

103. Jiang Y, Wang Y, Tan H, Yu T, Fan X, Chen P, et al. Schisandrol B protects against acetaminophen-induced acute hepatotoxicity in mice via activation of the NRF2/ARE signaling pathway. Acta Pharmacol Sin. 2016 Mar;37(3):382–9.

104. Reisman SA, Csanaky IL, Aleksunes LM, Klaassen CD. Altered Disposition of Acetaminophen in Nrf2-null and Keap1-knockdown Mice. Toxicol Sci. 2009 May;109(1):31–40.

105. Adachi T, Nakagawa H, Chung I, Hagiya Y, Hoshijima K, Noguchi N, et al. Nrf2-dependent and -independent induction of ABC transporters ABCC1, ABCC2, and ABCG2 in HepG2 cells under oxidative stress. J Exp Ther Oncol. 2007;6(4):335–48.

106. Chan K, Han XD, Kan YW. An important function of Nrf2 in combating oxidative stress: detoxification of acetaminophen. Proc Natl Acad Sci U S A. 2001 Apr 10;98(8):4611–6.

107. Thimmulappa RK, Lee H, Rangasamy T, Reddy SP, Yamamoto M, Kensler TW, et al. Nrf2 is a critical regulator of the innate immune response and survival during experimental sepsis. J Clin Invest. 2006 Apr;116(4):984–95.

108. Kim S-W, Lee H-K, Shin J-H, Lee J-K. Up-down regulation of HO-1 and iNOS gene expressions by ethyl pyruvate via recruiting

p300 to Nrf2 and depriving It from p65. Free Radic Biol Med. 2013 Dec;65:468–76.

109. Kobayashi EH, Suzuki T, Funayama R, Nagashima T, Hayashi M, Sekine H, et al. Nrf2 suppresses macrophage inflammatory response by blocking proinflammatory cytokine transcription. Nat Commun. 2016 May 23;7:11624.

110. Aleksunes LM, Manautou JE. Emerging role of Nrf2 in protecting against hepatic and gastrointestinal disease. Toxicol Pathol. 2007 Jun;35(4):459–73.

111. Enomoto A, Itoh K, Nagayoshi E, Haruta J, Kimura T, O'Connor T, et al. High Sensitivity of Nrf2 Knockout Mice to Acetaminophen Hepatotoxicity Associated with Decreased Expression of ARE-Regulated Drug Metabolizing Enzymes and Antioxidant Genes. Toxicol Sci. 2001 Jan 1;59(1):169–77.

112. Okawa H, Motohashi H, Kobayashi A, Aburatani H, Kensler TW, Yamamoto M. Hepatocyte-specific deletion of the keap1 gene activates Nrf2 and confers potent resistance against acute drug toxicity. Biochem Biophys Res Commun. 2006 Jan 6;339(1):79–88.

113. Goldring CEP, Kitteringham NR, Elsby R, Randle LE, Clement YN, Williams DP, et al. Activation of hepatic Nrf2 in vivo by acetaminophen in CD-1 mice. Hepatology. 2004;39(5):1267–76.

114. Copple IM, Goldring CE, Jenkins RE, Chia AJL, Randle LE, Hayes JD, et al. The hepatotoxic metabolite of acetaminophen directly activates the Keap1-Nrf2 cell defense system. Hepatology. 2008;48(4):1292–301.

115. Zou Y, Lee J, Nambiar SM, Hu M, Rui W, Bao Q, et al. Nrf2 Is Involved in Maintaining Hepatocyte Identity during Liver Regeneration. PLOS ONE. 2014 Sep 15;9(9):e107423.

116. Wakabayashi N, Shin S, Slocum SL, Agoston ES, Wakabayashi J, Kwak M-K, et al. Regulation of Notch1 Signaling by Nrf2: Implications for Tissue Regeneration. Sci Signal. 2010 Jul 13;3(130):ra52.

117. Cuadrado A, Manda G, Hassan A, Alcaraz MJ, Barbas C, Daiber A, et al. Transcription Factor NRF2 as a Therapeutic Target for Chronic Diseases: A Systems Medicine Approach. Pharmacol Rev. 2018 Apr 1;70(2):348–83.

118. Saito R, Suzuki T, Hiramoto K, Asami S, Naganuma E, Suda H, et al. Characterizations of Three Major Cysteine Sensors of Keap1 in Stress Response. Mol Cell Biol. 2016 15;36(2):271–84.

119. Rachakonda G, Xiong Y, Sekhar KR, Stamer SL, Liebler DC, Freeman ML. Covalent modification at Cys151 dissociates the electrophile sensor Keap1 from the ubiquitin ligase CUL3. Chem Res Toxicol. 2008 Mar;21(3):705–10.

120. Baird L, Dinkova-Kostova AT. Diffusion dynamics of the Keap1-Cullin3 interaction in single live cells. Biochem Biophys Res Commun. 2013 Mar 29;433(1):58–65.

121. Gold R, Kappos L, Arnold DL, Bar-Or A, Giovannoni G, Selmaj K, et al. Placebo-Controlled Phase 3 Study of Oral BG-12 for Relapsing Multiple Sclerosis. N Engl J Med. 2012 Sep 20;367(12):1098–107.

122. Mrowietz U, Christophers E, Altmeyer P. Treatment of severe psoriasis with fumaric acid esters: scientific background and guidelines for therapeutic use. The German Fumaric Acid Ester Consensus Conference. Br J Dermatol. 1999 Sep;141(3):424–9.

123. Al-Jaderi Z, Maghazachi AA. Utilization of Dimethyl Fumarate and Related Molecules for Treatment of Multiple Sclerosis, Cancer, and Other Diseases. Front Immunol [Internet]. 2016 [cited 2017 Feb 7];7. Available from: http://journal.frontiersin.org/article/10.3389/fimmu.2016.00278/abstract

124. Lin SX, Lisi L, Dello Russo C, Polak PE, Sharp A, Weinberg G, et al. The anti-inflammatory effects of dimethyl fumarate in astrocytes involve glutathione and haem oxygenase-1. ASN Neuro. 2011 Apr 7;3(2).

125. Drug Approval Package: Brand Name (Generic Name) NDA # [Internet]. [cited 2019 Apr 18]. Available from: https://www.accessdata.fda.gov/drugsatfda_docs/nda/2013/204063Orig1s000TOC.cfm

126. Wilms H, Sievers J, Rickert U, Rostami-Yazdi M, Mrowietz U, Lucius R. Dimethylfumarate inhibits microglial and astrocytic inflammation by suppressing the synthesis of nitric oxide, IL-1beta, TNF-alpha and IL-6 in an in-vitro model of brain inflammation. J Neuroinflammation. 2010 May 19;7:30.

127. Gold R, Linker RA, Stangel M. Fumaric acid and its esters: an emerging treatment for multiple sclerosis with antioxidative

mechanism of action. Clin Immunol Orlando Fla. 2012 Jan;142(1):44–8.

128. Linker RA, Lee D-H, Ryan S, van Dam AM, Conrad R, Bista P, et al. Fumaric acid esters exert neuroprotective effects in neuroinflammation via activation of the Nrf2 antioxidant pathway. Brain J Neurol. 2011 Mar;134(Pt 3):678–92.

129. Scannevin RH, Chollate S, Jung M, Shackett M, Patel H, Bista P, et al. Fumarates promote cytoprotection of central nervous system cells against oxidative stress via the nuclear factor (erythroid-derived 2)-like 2 pathway. J Pharmacol Exp Ther. 2012 Apr;341(1):274–84.

130. Kastrati I, Siklos MI, Calderon-Gierszal EL, El-Shennawy L, Georgieva G, Thayer EN, et al. Dimethyl Fumarate Inhibits the Nuclear Factor κB Pathway in Breast Cancer Cells by Covalent Modification of p65 Protein. J Biol Chem. 2016 Dec 2;291(7):3639–47.

131. Loewe R, Holnthoner W, Gröger M, Pillinger M, Gruber F, Mechtcheriakova D, et al. Dimethylfumarate inhibits TNF-induced nuclear entry of NF-kappa B/p65 in human endothelial cells. J Immunol Baltim Md 1950. 2002 May 1;168(9):4781–7.

132. Zhao G, Liu Y, Fang J, Chen Y, Li H, Gao K. Dimethyl fumarate inhibits the expression and function of hypoxia-inducible factor-1α (HIF-1α). Biochem Biophys Res Commun. 2014 Jun 6;448(3):303–7.

133. Schmidt MM, Dringen R. Fumaric acid diesters deprive cultured primary astrocytes rapidly of glutathione. Neurochem Int. 2010 Nov;57(4):460–7.

134. Brennan MS, Matos MF, Li B, Hronowski X, Gao B, Juhasz P, et al. Dimethyl Fumarate and Monoethyl Fumarate Exhibit Differential Effects on KEAP1, NRF2 Activation, and Glutathione Depletion In Vitro. PLOS ONE. 2015 Mar 20;10(3):e0120254.

135. Hoffmann C, Dietrich M, Herrmann A-K, Schacht T, Albrecht P, Methner A. Dimethyl Fumarate Induces Glutathione Recycling by Upregulation of Glutathione Reductase. Oxid Med Cell Longev. 2017;2017:6093903.

136. Krämer T, Grob T, Menzel L, Hirnet T, Griemert E, Radyushkin K, et al. Dimethyl fumarate treatment after traumatic brain injury prevents depletion of antioxidative brain glutathione and confers neuroprotection. J Neurochem. 2017;143(5):523–33.

137. Müller S, Behnen M, Bieber K, Möller S, Hellberg L, Witte M, et al. Dimethylfumarate Impairs Neutrophil Functions. J Invest Dermatol. 2016 Jan;136(1):117–26.

138. Hoffmann JHO, Schaekel K, Hartl D, Enk AH, Hadaschik EN. Dimethyl fumarate modulates neutrophil extracellular trap formation in a glutathione- and superoxide-dependent manner. Br J Dermatol. 2018;178(1):207–14.

139. Wu Q, Wang Q, Mao G, Dowling CA, Lundy SK, Mao-Draayer Y. Dimethyl Fumarate Selectively Reduces Memory T Cells and Shifts the Balance between Th1/Th17 and Th2 in Multiple Sclerosis Patients. J Immunol Baltim Md 1950. 2017 15;198(8):3069–80.

140. Longbrake EE, Ramsbottom MJ, Cantoni C, Ghezzi L, Cross AH, Piccio L. Dimethyl fumarate selectively reduces memory T cells in multiple sclerosis patients. Mult Scler Houndmills Basingstoke Engl. 2016;22(8):1061–70.

141. Bray M-A, Singh S, Han H, Davis CT, Borgeson B, Hartland C, et al. Cell Painting, a high-content image-based assay for morphological profiling using multiplexed fluorescent dyes. Nat Protoc. 2016 Sep;11(9):1757–74.

142. Wang Y, Tatham MH, Schmidt-Heck W, Swann C, Singh-Dolt K, Meseguer-Ripolles J, et al. Multiomics Analyses of HNF4α Protein Domain Function during Human Pluripotent Stem Cell Differentiation. iScience. 2019 Jun 28;16:206–17.

143. Kim S, Kim T. Selection of optimal internal controls for gene expression profiling of liver disease. BioTechniques. 2003 Sep;35(3):456–8, 460.

144. Narasimhan M, Riar AK, Rathinam ML, Vedpathak D, Henderson G, Mahimainathan L. Hydrogen Peroxide responsive miR153 targets Nrf2/ARE cytoprotection in paraquat induced dopaminergic neurotoxicity. Toxicol Lett. 2014 Aug 4;228(3):179–91.

145. Loseva P, Kostyuk S, Malinovskaya E, Clement N, Dechesne CA, Dani C, et al. Extracellular DNA oxidation stimulates activation of NRF2 and reduces the production of ROS in human mesenchymal stem cells. Expert Opin Biol Ther. 2012 May 1;12(sup1):S85–97.

146. Her GM, Chiang C-C, Chen W-Y, Wu J-L. In vivo studies of liver-type fatty acid binding protein (L-FABP) gene expression in

liver of transgenic zebrafish (Danio rerio). FEBS Lett. 2003 Mar 13;538(1–3):125–33.

147. Vliegenthart ADB, Wei C, Buckley C, Berends C, de Potter CMJ, Schneemann S, et al. Characterization of Triptolide-Induced Hepatotoxicity by Imaging and Transcriptomics in a Novel Zebrafish Model. Toxicol Sci Off J Soc Toxicol. 2017 Oct 1;159(2):380–91.

148. Wittbrodt JN, Liebel U, Gehrig J. Generation of orientation tools for automated zebrafish screening assays using desktop 3D printing. BMC Biotechnol. 2014 May 1;14:36.

149. Gerets HHJ, Tilmant K, Gerin B, Chanteux H, Depelchin BO, Dhalluin S, et al. Characterization of primary human hepatocytes, HepG2 cells, and HepaRG cells at the mRNA level and CYP activity in response to inducers and their predictivity for the detection of human hepatotoxins. Cell Biol Toxicol. 2012 Apr;28(2):69–87.

150. Szkolnicka D, Farnworth SL, Lucendo-Villarin B, Storck C, Zhou W, Iredale JP, et al. Accurate prediction of drug-induced liver injury using stem cell-derived populations. Stem Cells Transl Med. 2014 Feb;3(2):141–8.

151. Malik N, Rao MS. A Review of the Methods for Human iPSC Derivation. Methods Mol Biol Clifton NJ. 2013;997:23–33.

152. Unger C, Skottman H, Blomberg P, Sirac Dilber M, Hovatta O. Good manufacturing practice and clinical-grade human embryonic stem cell lines. Hum Mol Genet. 2008 Apr 15;17(R1):R48–53.

153. Kim K, Doi A, Wen B, Ng K, Zhao R, Cahan P, et al. Epigenetic memory in induced pluripotent stem cells. Nature. 2010 Sep 16;467(7313):285–90.

154. da Cruz L, Fynes K, Georgiadis O, Kerby J, Luo YH, Ahmado A, et al. Phase 1 clinical study of an embryonic stem cell–derived retinal pigment epithelium patch in age-related macular degeneration. Nat Biotechnol. 2018 Apr;36(4):328–37.

155. Barker RA, Parmar M, Studer L, Takahashi J. Human Trials of Stem Cell-Derived Dopamine Neurons for Parkinson's Disease: Dawn of a New Era. Cell Stem Cell. 2017 Nov 2;21(5):569–73.

156. Goutman SA, Brown MB, Glass JD, Boulis NM, Johe K, Hazel T, et al. Long-term Phase 1/2 intraspinal stem cell transplantation outcomes in ALS. Ann Clin Transl Neurol. 2018 Jun;5(6):730–40.

157. A Randomized, Double-Blind, Placebo-Controlled, Dose-Escalation Study of Intravenous Adult Human Mesenchymal Stem Cells (Prochymal) After Acute Myocardial Infarction - ScienceDirect [Internet]. [cited 2019 Jan 16]. Available from: https://www.sciencedirect.com/science/article/pii/S0735109709030927

158. Barker RA, Carpenter MK, Forbes S, Goldman SA, Jamieson C, Murry CE, et al. The Challenges of First-in-Human Stem Cell Clinical Trials: What Does This Mean for Ethics and Institutional Review Boards? Stem Cell Rep. 2018 May 8;10(5):1429–31.

159. Andrews PW, Bronson DL, Benham F, Strickland S, Knowles BB. A comparative study of eight cell lines derived from human testicular teratocarcinoma. Int J Cancer. 1980 Sep 15;26(3):269–80.

160. Bronson DL, Andrews PW, Solter D, Cervenka J, Lange PH, Fraley EE. Cell line derived from a metastasis of a human testicular germ cell tumor. Cancer Res. 1980 Jul;40(7):2500–6.

161. Müller F-J, Goldmann J, Löser P, Loring JF. A call to standardize teratoma assays used to define human pluripotent cell lines. Cell Stem Cell. 2010 May 7;6(5):412–4.

162. Martin GR, Evans MJ. Differentiation of clonal lines of teratocarcinoma cells: formation of embryoid bodies in vitro. Proc Natl Acad Sci U S A. 1975 Apr;72(4):1441–5.

163. Caicedo JC, Cooper S, Heigwer F, Warchal S, Qiu P, Molnar C, et al. Data-analysis strategies for image-based cell profiling. Nat Methods. 2017 Sep;14(9):849–63.

164. Bray M-A, Gustafsdottir SM, Ljosa V, Singh S, Sokolnicki KL, Bittker JA, et al. A dataset of images and morphological profiles of 30,000 small-molecule treatments using the Cell Painting assay. GigaScience [Internet]. [cited 2017 May 25]; Available from: https://academic.oup.com/gigascience/article/doi/10.1093/gigascience/giw014/2865213/A-dataset-of-images-and-morphological-profiles-of

165. Rohban MH, Singh S, Wu X, Berthet JB, Bray M-A, Shrestha Y, et al. Systematic morphological profiling of human gene and allele function via Cell Painting. eLife. 2017 Mar 18;6:e24060.

166. Carpenter AE, Jones TR, Lamprecht MR, Clarke C, Kang IH, Friman O, et al. CellProfiler: image analysis software for identifying and quantifying cell phenotypes. Genome Biol. 2006 Oct 31;7:R100.

167. Sommer C, Straehle C, Köthe U, Hamprecht FA. Ilastik: Interactive learning and segmentation toolkit. In: 2011 IEEE International Symposium on Biomedical Imaging: From Nano to Macro. 2011. p. 230–3.

168. Omta WA, van Heesbeen RG, Pagliero RJ, van der Velden LM, Lelieveld D, Nellen M, et al. HC StratoMineR: A Web-Based Tool for the Rapid Analysis of High-Content Datasets. Assay Drug Dev Technol. 2016 Oct;14(8):439–52.

169. Boutros M, Brás LP, Huber W. Analysis of cell-based RNAi screens. Genome Biol. 2006;7(7):R66.

170. Medine CN, Lucendo-Villarin B, Storck C, Wang F, Szkolnicka D, Khan F, et al. Developing High-Fidelity Hepatotoxicity Models From Pluripotent Stem Cells. Stem Cells Transl Med. 2013 Jul;2(7):505–9.

171. Galvao J, Davis B, Tilley M, Normando E, Duchen MR, Cordeiro MF. Unexpected low-dose toxicity of the universal solvent DMSO. FASEB J Off Publ Fed Am Soc Exp Biol. 2014 Mar;28(3):1317–30.

172. Costello AB, Osborne JW. Best Practices in Exploratory Factor Analysis : Four Recommendations for Getting the Most From Your Analysis. In 2005.

173. Lynch T, Price AL. The Effect of Cytochrome P450 Metabolism on Drug Response, Interactions, and Adverse Effects. Am Fam Physician. 2007 Aug 1;76(3):391–6.

174. Parafati M, Kirby RJ, Khorasanizadeh S, Rastinejad F, Malany S. A nonalcoholic fatty liver disease model in human induced pluripotent stem cell-derived hepatocytes, created by endoplasmic reticulum stress-induced steatosis. Dis Model Mech. 2018 25;11(9).

175. Kang S-J, Lee H-M, Park Y-I, Yi H, Lee H, So B, et al. Chemically induced hepatotoxicity in human stem cell-induced hepatocytes compared with primary hepatocytes and HepG2. Cell Biol Toxicol. 2016 Oct 1;32(5):403–17.

176. Harrison RK. Phase II and phase III failures: 2013-2015. Nat Rev Drug Discov. 2016 Diciembre;15(12):817–8.

177. Onakpoya IJ, Heneghan CJ, Aronson JK. Post-marketing withdrawal of 462 medicinal products because of adverse drug reactions: a systematic review of the world literature. BMC Med. 2016;14:10.

178. Williams R, Aspinall R, Bellis M, Camps-Walsh G, Cramp M, Dhawan A, et al. Addressing liver disease in the UK: a blueprint for attaining excellence in health care and reducing premature mortality from lifestyle issues of excess consumption of alcohol, obesity, and viral hepatitis. The Lancet. 2014 Nov;384(9958):1953–97.

179. Bernal W, Wendon J. Acute Liver Failure. N Engl J Med. 2013 Diciembre;369(26):2525–34.

180. Sano R, Reed JC. ER stress-induced cell death mechanisms. Biochim Biophys Acta. 2013 Dec;1833(12):3460–70.

181. Decker CW, Casian JG, Nguyen KT, Horton LA, Rao MP, Silkwood KH, et al. The Critical Role of Mitochondria in Drug-Induced Liver Injury. In: Molecules, Systems and Signaling in Liver Injury [Internet]. Springer, Cham; 2017 [cited 2017 Nov 5]. p. 159–81. (Cell Death in Biology and Diseases). Available from: https://link.springer.com/chapter/10.1007/978-3-319-58106-4_8

182. Yuan L, Kaplowitz N. Mechanisms of Drug Induced Liver Injury. Clin Liver Dis. 2013 Nov;17(4):507–18.

183. Athersuch TJ, Antoine DJ, Boobis AR, Coen M, Daly AK, Possamai L, et al. Paracetamol metabolism, hepatotoxicity, biomarkers and therapeutic interventions: a perspective. Toxicol Res. 2018 May 8;7(3):347–57.

184. Shin SM, Yang JH, Ki SH, Shin SM, Yang JH, Ki SH. Role of the Nrf2-ARE Pathway in Liver Diseases, Role of the Nrf2-ARE Pathway in Liver Diseases. Oxidative Med Cell Longev Oxidative Med Cell Longev. 2013 May 9;2013, 2013:e763257.

185. Baird L, Dinkova-Kostova AT. The cytoprotective role of the Keap1-Nrf2 pathway. Arch Toxicol. 2011 Apr;85(4):241–72.

186. Saito T, Fukai A, Mabuchi A, Ikeda T, Yano F, Ohba S, et al. Transcriptional regulation of endochondral ossification by HIF-2alpha during skeletal growth and osteoarthritis development. Nat Med. 2010 Jun;16(6):678–86.

187. Hirotsu Y, Katsuoka F, Funayama R, Nagashima T, Nishida Y, Nakayama K, et al. Nrf2–MafG heterodimers contribute globally to antioxidant and metabolic networks. Nucleic Acids Res. 2012 Sep 10;gks827.

188. Osburn WO, Yates MS, Dolan PD, Chen S, Liby KT, Sporn MB, et al. Genetic or pharmacologic amplification of nrf2 signaling

inhibits acute inflammatory liver injury in mice. Toxicol Sci Off J Soc Toxicol. 2008 Jul;104(1):218–27.

189. Jin F, Wan C, Li W, Yao L, Zhao H, Zou Y, et al. Formononetin protects against acetaminophen-induced hepatotoxicity through enhanced NRF2 activity. PLOS ONE. 2017 Feb 24;12(2):e0170900.

190. Sharma RS, Harrison DJ, Kisielewski D, Cassidy DM, McNeilly AD, Gallagher JR, et al. Experimental Nonalcoholic Steatohepatitis and Liver Fibrosis Are Ameliorated by Pharmacologic Activation of Nrf2 (NF-E2 p45-Related Factor 2). Cell Mol Gastroenterol Hepatol. 2018 Jan 1;5(3):367–98.

191. Ruggieri S, Tortorella C, Gasperini C. Pharmacology and clinical efficacy of dimethyl fumarate (BG-12) for treatment of relapsing–remitting multiple sclerosis. Ther Clin Risk Manag. 2014 Mar 27;10:229–39.

192. Fox RJ, Kita M, Cohan SL, Henson LJ, Zambrano J, Scannevin RH, et al. BG-12 (dimethyl fumarate): a review of mechanism of action, efficacy, and safety. Curr Med Res Opin. 2014 Feb 1;30(2):251–62.

193. MacRae CA, Peterson RT. Zebrafish as tools for drug discovery. Nat Rev Drug Discov. 2015 Oct;14(10):721–31.

194. Gillard GO, Collette B, Anderson J, Chao J, Scannevin RH, Huss DJ, et al. DMF, but not other fumarates, inhibits NF-κB activity in vitro in an Nrf2-independent manner. J Neuroimmunol. 2015 Jun 15;283:74–85.

195. Wierinckx A, Brevé J, Mercier D, Schultzberg M, Drukarch B, Van Dam A-M. Detoxication enzyme inducers modify cytokine production in rat mixed glial cells. J Neuroimmunol. 2005 Sep 1;166(1):132–43.

196. Saidu NEB, Noé G, Cerles O, Cabel L, Kavian-Tessler N, Chouzenoux S, et al. Dimethyl Fumarate Controls the NRF2/DJ-1 Axis in Cancer Cells: Therapeutic Applications. Mol Cancer Ther. 2017 Mar 1;16(3):529–39.

197. Denis M-C, Roy D, Yeganeh PR, Desjardins Y, Varin T, Haddad N, et al. Apple peel polyphenols: a key player in the prevention and treatment of experimental inflammatory bowel disease. Clin Sci Lond Engl 1979. 2016 Dec 1;130(23):2217–37.

198. Desvergne A, Ugarte N, Radjei S, Gareil M, Petropoulos I, Friguet B. Circadian modulation of proteasome activity and

accumulation of oxidized protein in human embryonic kidney HEK 293 cells and primary dermal fibroblasts. Free Radic Biol Med. 2016 May;94:195–207.

199. Bailey SN, Ali SM, Carpenter AE, Higgins CO, Sabatini DM. Microarrays of lentiviruses for gene function screens in immortalized and primary cells. Nat Methods. 2006 Feb;3(2):117–22.

200. Sall, J. Graphical Comparison of Means. Stat Comput Stat Graph Newsl. 1992;3:27–32.

201. Halliwell B. Oxidative stress in cell culture: an under-appreciated problem? FEBS Lett. 2003 Apr 10;540(1):3–6.

202. Olayanju A, Copple IM, Bryan HK, Edge GT, Sison RL, Wong MW, et al. Brusatol provokes a rapid and transient inhibition of Nrf2 signaling and sensitizes mammalian cells to chemical toxicity—implications for therapeutic targeting of Nrf2. Free Radic Biol Med. 2015 Jan 1;78:202–12.

203. Harder B, Tian W, La Clair JJ, Tan A-C, Ooi A, Chapman E, et al. Brusatol overcomes chemoresistance through inhibition of protein translation. Mol Carcinog. 2017;56(5):1493–500.

204. Spencer SR, Wilczak CA, Talalay P. Induction of glutathione transferases and NAD(P)H:quinone reductase by fumaric acid derivatives in rodent cells and tissues. Cancer Res. 1990 Dec 15;50(24):7871–5.

205. Brennan MS, Patel H, Allaire N, Thai A, Cullen P, Ryan S, et al. Pharmacodynamics of Dimethyl Fumarate Are Tissue Specific and Involve NRF2-Dependent and -Independent Mechanisms. Antioxid Redox Signal. 2016 Jun 20;24(18):1058–71.

206. Oh CJ, Kim J-Y, Choi Y-K, Kim H-J, Jeong J-Y, Bae K-H, et al. Dimethylfumarate attenuates renal fibrosis via NF-E2-related factor 2-mediated inhibition of transforming growth factor-β/Smad signaling. PloS One. 2012;7(10):e45870.

207. Gosslau A, Ruoff P, Mohsenzadeh S, Hobohm U, Rensing L. Heat Shock and Oxidative Stress-induced Exposure of Hydrophobic Protein Domains as Common Signal in the Induction ofhsp68. J Biol Chem. 2001 Jan 19;276(3):1814–21.

208. Bischoff LJM, Kuijper IA, Schimming JP, Wolters L, Braak B ter, Langenberg JP, et al. A systematic analysis of Nrf2 pathway activation dynamics during repeated xenobiotic exposure. Arch Toxicol. 2019 Feb 1;93(2):435–51.

209. Oliveira-Marques V, Marinho HS, Cyrne L, Antunes F. Role of hydrogen peroxide in NF-kappaB activation: from inducer to modulator. Antioxid Redox Signal. 2009 Sep;11(9):2223–43.

210. Yang M-X, Cederbaum AI. Characterization of Cytochrome P4502E1 Turnover in Transfected HepG2 Cells Expressing Human CYP2E1. Arch Biochem Biophys. 1997 May 1;341(1):25–33.

211. Watanabe A, Mayumi K, Nishimura K, Osaki H. In vivo use of the CYP inhibitor 1-aminobenzotriazole to increase long-term exposure in mice. Biopharm Drug Dispos. 2016 Sep;37(6):373–8.

212. Takasu C, Vaziri ND, Li S, Robles L, Vo K, Takasu M, et al. Treatment with dimethyl fumarate ameliorates liver ischemia/reperfusion injury. World J Gastroenterol. 2017 Jul 7;23(25):4508–16.

213. Hahn ME, Timme-Laragy AR, Karchner SI, Stegeman JJ. Nrf2 and Nrf2-Related Proteins in Development and Developmental Toxicity: Insights from studies in Zebrafish (Danio rerio). Free Radic Biol Med. 2015 Nov;88(0 0):275–89.

214. Timme-Laragy AR, Karchner SI, Franks DG, Jenny MJ, Harbeitner RC, Goldstone JV, et al. Nrf2b, Novel Zebrafish Paralog of Oxidant-responsive Transcription Factor NF-E2-related Factor 2 (NRF2). J Biol Chem. 2012 Feb 10;287(7):4609–27.

215. Costa-Silva J, Domingues D, Lopes FM. RNA-Seq differential expression analysis: An extended review and a software tool. PLoS ONE [Internet]. 2017 Dec 21 [cited 2019 Mar 27];12(12). Available from: https://www.ncbi.nlm.nih.gov/pmc/articles/PMC5739479/

216. Love MI, Huber W, Anders S. Moderated estimation of fold change and dispersion for RNA-seq data with DESeq2. Genome Biol. 2014 Dec 5;15(12):550.

217. Kuleshov MV, Jones MR, Rouillard AD, Fernandez NF, Duan Q, Wang Z, et al. Enrichr: a comprehensive gene set enrichment analysis web server 2016 update. Nucleic Acids Res. 2016 08;44(W1):W90-97.

218. Subramanian A, Tamayo P, Mootha VK, Mukherjee S, Ebert BL, Gillette MA, et al. Gene set enrichment analysis: A knowledge-based approach for interpreting genome-wide expression profiles. Proc Natl Acad Sci. 2005 Oct 25;102(43):15545–50.

219. Giustina AD, Bonfante S, Zarbato GF, Danielski LG, Mathias K, de Oliveira AN, et al. Dimethyl Fumarate Modulates Oxidative

Stress and Inflammation in Organs After Sepsis in Rats. Inflammation. 2018 Feb 1;41(1):315–27.

220. Abdelrahman RS, Abdel-Rahman N. Dimethyl fumarate ameliorates acetaminophen-induced hepatic injury in mice dependent of Nrf-2/HO-1 pathway. Life Sci. 2019 Jan 15;217:251–60.

221. García-Caballero M, Marí-Beffa M, Medina MÁ, Quesada AR. Dimethylfumarate Inhibits Angiogenesis In Vitro and In Vivo: A Possible Role for Its Antipsoriatic Effect? J Invest Dermatol. 2011 Jun;131(6):1347–55.

222. Kulkarni P, Yellanki S, Medishetti R, Sriram D, Saxena U, Yogeeswari P. Novel Zebrafish EAE model: A quick in vivo screen for multiple sclerosis. Mult Scler Relat Disord. 2017;11:32–9.

223. Schroeder A, Mueller O, Stocker S, Salowsky R, Leiber M, Gassmann M, et al. The RIN: an RNA integrity number for assigning integrity values to RNA measurements. BMC Mol Biol. 2006 Jan 31;7:3.

224. Quackenbush J. Microarray data normalization and transformation. Nat Genet. 2002 Dec;32 Suppl:496–501.

225. Liberzon A, Birger C, Thorvaldsdóttir H, Ghandi M, Mesirov JP, Tamayo P. The Molecular Signatures Database Hallmark Gene Set Collection. Cell Syst. 2015 Dec 23;1(6):417–25.

226. Slenter DN, Kutmon M, Hanspers K, Riutta A, Windsor J, Nunes N, et al. WikiPathways: a multifaceted pathway database bridging metabolomics to other omics research. Nucleic Acids Res. 2018 Jan 4;46(D1):D661–7.

227. Schurch NJ, Schofield P, Gierliński M, Cole C, Sherstnev A, Singh V, et al. How many biological replicates are needed in an RNA-seq experiment and which differential expression tool should you use? RNA. 2016 Jun;22(6):839–51.

228. Maher JM, Dieter MZ, Aleksunes LM, Slitt AL, Guo G, Tanaka Y, et al. Oxidative and electrophilic stress induces multidrug resistance–associated protein transporters via the nuclear factor-E2–related factor-2 transcriptional pathway. Hepatology. 2007 Nov 1;46(5):1597–610.

229. Sánchez-Rodríguez R, Torres-Mena JE, Quintanar-Jurado V, Chagoya-Hazas V, Rojas Del Castillo E, Del Pozo Yauner L, et al. Ptgr1 expression is regulated by NRF2 in rat hepatocarcinogenesis

and promotes cell proliferation and resistance to oxidative stress. Free Radic Biol Med. 2017;102:87–99.

230. Adachi Y, Horii K, Takahashi Y, Tanihata M, Ohba Y, Yamamoto T. Serum glutathione S-transferase activity in liver diseases. Clin Chim Acta Int J Clin Chem. 1980 Oct 9;106(3):243–55.

231. Hayes JD, Pulford DJ. The glutathione S-transferase supergene family: regulation of GST and the contribution of the isoenzymes to cancer chemoprotection and drug resistance. Crit Rev Biochem Mol Biol. 1995;30(6):445–600.

232. Chanas SA, Jiang Q, McMahon M, McWalter GK, McLellan LI, Elcombe CR, et al. Loss of the Nrf2 transcription factor causes a marked reduction in constitutive and inducible expression of the glutathione S-transferase Gsta1, Gsta2, Gstm1, Gstm2, Gstm3 and Gstm4 genes in the livers of male and female mice. Biochem J. 2002 Jul 15;365(Pt 2):405–16.

233. Rosen MB, Lee JS, Ren H, Vallanat B, Liu J, Waalkes MP, et al. Toxicogenomic Dissection of the Perfluorooctanoic Acid Transcript Profile in Mouse Liver: Evidence for the Involvement of Nuclear Receptors PPARα and CAR. Toxicol Sci. 2008 May 1;103(1):46–56.

234. van der Lee R, Szklarczyk R, Smeitink J, Smeets HJM, Huynen MA, Vogel R. Transcriptome analysis of complex I-deficient patients reveals distinct expression programs for subunits and assembly factors of the oxidative phosphorylation system. BMC Genomics [Internet]. 2015 Sep 15 [cited 2019 Mar 12];16. Available from: https://www.ncbi.nlm.nih.gov/pmc/articles/PMC4570683/

235. Cheng X, Yamauchi J, Lee S, Zhang T, Gong Z, Muzumdar R, et al. APOC3 Protein Is Not a Predisposing Factor for Fat-induced Nonalcoholic Fatty Liver Disease in Mice. J Biol Chem. 2017 03;292(9):3692–705.

236. Ye P, Xiang M, Liao H, Liu J, Luo H, Wang Y, et al. Dual-Specificity Phosphatase 9 Protects Against Nonalcoholic Fatty Liver Disease in Mice Through ASK1 Suppression. Hepatol Baltim Md. 2019 Jan;69(1):76–93.

237. Zhang X, Ruan Y, Li Y, Lin D, Quan C. Tight junction protein claudin-6 inhibits growth and induces the apoptosis of cervical carcinoma cells in vitro and in vivo. Med Oncol. 2015 May 1;32(5):148.

238. Guo Y, Lin D, Zhang M, Zhang X, Li Y, Yang R, et al. CLDN6-induced apoptosis via regulating ASK1-p38/JNK signaling in breast cancer MCF-7 cells. Int J Oncol. 2016 Jun 1;48(6):2435–44.

239. Zeisel MB, Dhawan P, Baumert TF. Tight junction proteins in gastrointestinal and liver disease. Gut. 2018 Oct 8;

240. Gissen P, Arias IM. Structural and functional hepatocyte polarity and liver disease. J Hepatol. 2015 Oct;63(4):1023–37.

241. Holczbauer Á, Gyöngyösi B, Lotz G, Törzsök P, Kaposi-Novák P, Szijártó A, et al. Increased Expression of Claudin-1 and Claudin-7 in Liver Cirrhosis and Hepatocellular Carcinoma. Pathol Oncol Res. 2014 Jul 1;20(3):493–502.

242. Karim S, Adams DH, Lalor PF. Hepatic expression and cellular distribution of the glucose transporter family. World J Gastroenterol WJG. 2012 Dec 14;18(46):6771–81.

243. Wang W-B, Fan J, Zhang X, Xu J, Yao W. Serial expression analysis of liver regeneration-related genes in rat regenerating liver. Mol Biotechnol. 2009 Nov;43(3):221–31.

244. Petrelli A, Perra A, Cora D, Sulas P, Menegon S, Manca C, et al. MicroRNA/gene profiling unveils early molecular changes and nuclear factor erythroid related factor 2 (NRF2) activation in a rat model recapitulating human hepatocellular carcinoma (HCC). Hepatology. 2014;59(1):228–41.

245. Kubo E, Shibata S, Shibata T, Kiyokawa E, Sasaki H, Singh DP. FGF2 antagonizes aberrant TGFβ regulation of tropomyosin: role for posterior capsule opacity. J Cell Mol Med. 2017 May;21(5):916–28.

246. Chen Y, Hong Z, Lu S, Zhang N, Rong G, Chang X, et al. Downregulated Expression of Tropomyosin 1 in Intrahepatic Cholangiocarcinoma: A Predictor of Recurrence and Prognosis. Med Sci Monit Int Med J Exp Clin Res. 2018 Nov 3;24:7875–82.

247. Faust D, Vondráček J, Krčmář P, Šmerdová L, Procházková J, Hrubá E, et al. AhR-mediated changes in global gene expression in rat liver progenitor cells. Arch Toxicol. 2013 Apr 1;87(4):681–98.

248. Raven A, Lu W-Y, Man TY, Ferreira-Gonzalez S, O'Duibhir E, Dwyer BJ, et al. Cholangiocytes act as Facultative Liver Stem Cells during Impaired Hepatocyte Regeneration. Nature. 2017 Jul 20;547(7663):350–4.

249. Uenishi T, Kubo S, Yamamoto T, Shuto T, Ogawa M, Tanaka H, et al. Cytokeratin 19 expression in hepatocellular carcinoma predicts early postoperative recurrence. Cancer Sci. 2003 Oct;94(10):851–7.

250. Manley S, Williams JA, Ding W-X. The Role of p62/SQSTM1 in Liver Physiology and Pathogenesis. Exp Biol Med Maywood NJ. 2013 May;238(5):525–38.

251. Sánchez-Martín P, Komatsu M. p62/SQSTM1 – steering the cell through health and disease. J Cell Sci. 2018 Nov 1;131(21):jcs222836.

252. Key C-CC, Liu M, Kurtz CL, Chung S, Boudyguina E, Dinh TA, et al. Hepatocyte ABCA1 deletion impairs liver insulin signaling and lipogenesis. Cell Rep. 2017 Jun 6;19(10):2116–29.

253. Lu Q, Tang S-L, Liu X-Y, Zhao G-J, Ouyang X-P, Lv Y-C, et al. Tertiary-butylhydroquinone upregulates expression of ATP-binding cassette transporter A1 via nuclear factor E2-related factor 2/heme oxygenase-1 signaling in THP-1 macrophage-derived foam cells. Circ J Off J Jpn Circ Soc. 2013;77(9):2399–408.

254. Nakatani Y, Konishi H, Vassilev A, Kurooka H, Ishiguro K, Sawada J, et al. p600, a unique protein required for membrane morphogenesis and cell survival. Proc Natl Acad Sci U S A. 2005 Oct 18;102(42):15093–8.

255. Saunders DN, Hird SL, Withington SL, Dunwoodie SL, Henderson MJ, Biben C, et al. Edd, the Murine Hyperplastic Disc Gene, Is Essential for Yolk Sac Vascularization and Chorioallantoic Fusion. Mol Cell Biol. 2004 Aug 15;24(16):7225–34.

256. Tasaki T, Sriram SM, Park KS, Kwon YT. The N-End Rule Pathway. Annu Rev Biochem. 2012;81(1):261–89.

257. Ulazzi L, Sabbioni S, Miotto E, Veronese A, Angusti A, Gafà R, et al. Nidogen 1 and 2 gene promoters are aberrantly methylated in human gastrointestinal cancer. Mol Cancer. 2007 Feb 28;6:17.

258. Lu C-L, Qiu J-L, Huang P-Z, Zou R-H, Hong J, Li B-K, et al. NADPH oxidase DUOX1 and DUOX2 but not NOX4 are independent predictors in hepatocellular carcinoma after hepatectomy. Tumour Biol J Int Soc Oncodevelopmental Biol Med. 2011 Dec;32(6):1173–82.

259. de Mochel NSR, Seronello S, Wang SH, Ito C, Zheng JX, Liang TJ, et al. Hepatocyte NAD(P)H oxidases as an endogenous source of reactive oxygen species during hepatitis C virus infection. Hepatol Baltim Md. 2010 Jul;52(1):47–59.

260. Hartley JL, Zachos NC, Dawood B, Donowitz M, Forman J, Pollitt RJ, et al. Mutations in TTC37 cause trichohepatoenteric syndrome (phenotypic diarrhea of infancy). Gastroenterology. 2010 Jun;138(7):2388–98, 2398.e1-2.

261. Dahlen JR, Jean F, Thomas G, Foster DC, Kisiel W. Inhibition of soluble recombinant furin by human proteinase inhibitor 8. J Biol Chem. 1998 Jan 23;273(4):1851–4.

262. Saito A, Suzuki HI, Horie M, Ohshima M, Morishita Y, Abiko Y, et al. An Integrated Expression Profiling Reveals Target Genes of TGF-β and TNF-α Possibly Mediated by MicroRNAs in Lung Cancer Cells. PLoS ONE [Internet]. 2013 Feb 20 [cited 2019 Mar 25];8(2). Available from: https://www.ncbi.nlm.nih.gov/pmc/articles/PMC3577886/

263. van Koppen A, Verschuren L, van den Hoek AM, Verheij J, Morrison MC, Li K, et al. Uncovering a Predictive Molecular Signature for the Onset of NASH-Related Fibrosis in a Translational NASH Mouse Model. Cell Mol Gastroenterol Hepatol. 2017 Oct 14;5(1):83-98.e10.

264. Kang H-R, Lee CG, Homer RJ, Elias JA. Semaphorin 7A plays a critical role in TGF-β1–induced pulmonary fibrosis. J Exp Med. 2007 May 14;204(5):1083–93.

265. De Minicis S, Rychlicki C, Agostinelli L, Saccomanno S, Trozzi L, Candelaresi C, et al. Semaphorin 7A Contributes to TGF-β–Mediated Liver Fibrogenesis. Am J Pathol. 2013 Sep;183(3):820–30.

266. Babbar N, Casero RA. Tumor necrosis factor-alpha increases reactive oxygen species by inducing spermine oxidase in human lung epithelial cells: a potential mechanism for inflammation-induced carcinogenesis. Cancer Res. 2006 Dec 1;66(23):11125–30.

267. Govaere O, Komuta M, Berkers J, Spee B, Janssen C, de Luca F, et al. Keratin 19: a key role player in the invasion of human hepatocellular carcinomas. Gut. 2014 Apr;63(4):674–85.

268. Lauvrak SU, Munthe E, Kresse SH, Stratford EW, Namløs HM, Meza-Zepeda LA, et al. Functional characterisation of osteosarcoma cell lines and identification of mRNAs and miRNAs

associated with aggressive cancer phenotypes. Br J Cancer. 2013 Oct;109(8):2228–36.

269. Lawrenson K, Grun B, Lee N, Mhawech-Fauceglia P, Kan J, Swenson S, et al. NPPB is a Novel Candidate Biomarker Expressed by Cancer-Associated Fibroblasts In Epithelial Ovarian Cancer. Int J Cancer J Int Cancer. 2015 Mar 15;136(6):1390–401.

270. Wong C-M, Ng Y-L, Lee JM-F, Wong CC-L, Cheung O-F, Chan C-Y, et al. Tissue factor pathway inhibitor-2 as a frequently silenced tumor suppressor gene in hepatocellular carcinoma. Hepatol Baltim Md. 2007 May;45(5):1129–38.

271. Sprecher CA, Kisiel W, Mathewes S, Foster DC. Molecular cloning, expression, and partial characterization of a second human tissue-factor-pathway inhibitor. Proc Natl Acad Sci U S A. 1994 Apr 12;91(8):3353–7.

272. Oh CJ, Kim J-Y, Min A-K, Park K-G, Harris RA, Kim H-J, et al. Sulforaphane attenuates hepatic fibrosis via NF-E2-related factor 2-mediated inhibition of transforming growth factor-β/Smad signaling. Free Radic Biol Med. 2012 Feb 1;52(3):671–82.

273. Prestigiacomo V, Suter-Dick L. Nrf2 protects stellate cells from Smad-dependent cell activation. PLoS ONE [Internet]. 2018 Jul 20 [cited 2019 Mar 25];13(7). Available from: https://www.ncbi.nlm.nih.gov/pmc/articles/PMC6054401/

274. Mang Y, Li L, Ran J, Zhang S, Liu J, Li L, et al. Long noncoding RNA NEAT1 promotes cell proliferation and invasion by regulating hnRNP A2 expression in hepatocellular carcinoma cells. OncoTargets Ther. 2017 Feb 20;10:1003–16.

275. Guo S, Chen W, Luo Y, Ren F, Zhong T, Rong M, et al. Clinical implication of long non-coding RNA NEAT1 expression in hepatocellular carcinoma patients. Int J Clin Exp Pathol. 2015;8(5):5395–402.

276. Nguyen DTT, Richter D, Michel G, Mitschka S, Kolanus W, Cuevas E, et al. The ubiquitin ligase LIN41/TRIM71 targets p53 to antagonize cell death and differentiation pathways during stem cell differentiation. Cell Death Differ. 2017 Jun;24(6):1063–78.

277. Emma MR, Iovanna JL, Bachvarov D, Puleio R, Loria GR, Augello G, et al. NUPR1, a new target in liver cancer: implication in controlling cell growth, migration, invasion and sorafenib resistance. Cell Death Dis. 2016 Jun;7(6):e2269.

278. Lee Y-K, Jee BA, Kwon SM, Yoon Y-S, Xu WG, Wang H-J, et al. Identification of a mitochondrial defect gene signature reveals NUPR1 as a key regulator of liver cancer progression. Hepatol Baltim Md. 2015 Oct;62(4):1174–89.

279. MacLeod AK, McMahon M, Plummer SM, Higgins LG, Penning TM, Igarashi K, et al. Characterization of the cancer chemopreventive NRF2-dependent gene battery in human keratinocytes: demonstration that the KEAP1–NRF2 pathway, and not the BACH1–NRF2 pathway, controls cytoprotection against electrophiles as well as redox-cycling compounds. Carcinogenesis. 2009 Sep;30(9):1571–80.

280. Zhang Z, Chen J, He Y, Zhan X, Zhao R, Huang Y, et al. miR-125b inhibits hepatitis B virus expression in vitro through targeting of the SCNN1A gene. Arch Virol. 2014 Dec;159(12):3335–43.

281. Harrill AH, Watkins PB, Su S, Ross PK, Harbourt DE, Stylianou IM, et al. Mouse population-guided resequencing reveals that variants in CD44 contribute to acetaminophen-induced liver injury in humans. Genome Res. 2009 Sep;19(9):1507–15.

282. Qian H, Chen L, Huang J, Wang X, Ma S, Cui F, et al. The lncRNA MIR4435-2HG promotes lung cancer progression by activating β-catenin signalling. J Mol Med Berl Ger. 2018 Aug;96(8):753–64.

283. Fu M, Huang Z, Zang X, Pan L, Liang W, Chen J, et al. Long noncoding RNA LINC00978 promotes cancer growth and acts as a diagnostic biomarker in gastric cancer. Cell Prolif. 2018 Feb;51(1).

284. Huang T, Huang W, Lu H, Zhang B, Ma J, Zhao D, et al. Identification and validation a TGF-β-associated long non-coding RNA of head and neck squamous cell carcinoma by bioinformatics method. J Transl Med. 2018 Feb 28;16(1):46.

285. Aldeiri B, Roostalu U, Albertini A, Behnsen J, Wong J, Morabito A, et al. Abrogation of TGF-beta signalling in TAGLN expressing cells recapitulates Pentalogy of Cantrell in the mouse. Sci Rep. 2018 Feb 26;8(1):3658.

286. Girgert R, Martin M, Kruegel J, Miosge N, Temme J, Eckes B, et al. Integrin α2-deficient mice provide insights into specific functions of collagen receptors in the kidney. Fibrogenesis Tissue Repair. 2010 Sep 22;3(1):19.

287. Cao L, Zhang Q, Cheng S, Chen Z, Hua Z, Yang J, et al. Long non-coding RNAs and genes contributing to the generation of

cancer stem cells in hepatocellular carcinoma identified by RNA sequencing analysis. Oncol Rep. 2016 Nov;36(5):2619–24.

288. Jovel J, Lin Z, O'keefe S, Willows S, Wang W, Zhang G, et al. A Survey of Molecular Heterogeneity in Hepatocellular Carcinoma. Hepatol Commun. 2018 Jul 12;2(8):941–55.

289. Fry EA, Mallakin A, Inoue K. Translocations involving ETS family proteins in human cancer. Integr Cancer Sci Ther [Internet]. 2018 Aug [cited 2019 Mar 25];5(4). Available from: https://www.ncbi.nlm.nih.gov/pmc/articles/PMC6287620/

290. Ma N, Chen F, Shen S-L, Chen W, Chen L-Z, Su Q, et al. MicroRNA-129-5p inhibits hepatocellular carcinoma cell metastasis and invasion via targeting ETS1. Biochem Biophys Res Commun. 2015 Jun 12;461(4):618–23.

291. Marcher A-B, Bendixen SM, Terkelsen MK, Hohmann SS, Hansen MH, Larsen BD, et al. Transcriptional regulation of Hepatic Stellate Cell activation in NASH. Sci Rep [Internet]. 2019 Feb 20 [cited 2019 Mar 25];9. Available from: https://www.ncbi.nlm.nih.gov/pmc/articles/PMC6382845/

292. Li H, Xie H-Y, Zhou L, Feng X-W, Wang W-L, Liang T-B, et al. Copy number variation in CCL3L1 gene is associated with susceptibility to acute rejection in patients after liver transplantation. Clin Transplant. 2012 Apr;26(2):314–21.

293. Wang AS, Dreesen O. Biomarkers of Cellular Senescence and Skin Aging. Front Genet [Internet]. 2018 Aug 23 [cited 2019 Mar 26];9. Available from: https://www.ncbi.nlm.nih.gov/pmc/articles/PMC6115505/

294. Benoit CR, Stanton AE, Tartanian AC, Motzer AR, McGaughey DM, Bond SR, et al. Functional and phylogenetic characterization of noncanonical vitamin B12–binding proteins in zebrafish suggests involvement in cobalamin transport. J Biol Chem. 2018 Sep 11;293(45):17606–21.

295. Wang P, Zhao F, Nie X, Liu J, Yu Z. Knockdown of NUP160 inhibits cell proliferation, induces apoptosis, autophagy and cell migration, and alters the expression and localization of podocyte associated molecules in mouse podocytes. Gene. 2018 Jul 20;664:12–21.

296. Pinto CL, Kalasekar SM, McCollum CW, Riu A, Jonsson P, Lopez J, et al. Lxr regulates lipid metabolic and visual perception pathways during zebrafish development. Mol Cell Endocrinol. 2016 Jan 5;419:29–43.

297. Saini SPS, Zhang B, Niu Y, Jiang M, Gao J, Zhai Y, et al. Activation of liver X receptor increases acetaminophen clearance and prevents its toxicity in mice. Hepatol Baltim Md. 2011 Dec;54(6):2208–17.

298. Yan C, Zhang Y, Zhang X, Aa J, Wang G, Xie Y. Curcumin regulates endogenous and exogenous metabolism via Nrf2-FXR-LXR pathway in NAFLD mice. Biomed Pharmacother Biomedecine Pharmacother. 2018 Sep;105:274–81.

299. Trescher WH, McDonald JW, Johnston MV. Quinolinate-induced injury is enhanced in developing rat brain. Brain Res Dev Brain Res. 1994 Dec 16;83(2):224–32.

300. Tummala KS, Gomes AL, Yilmaz M, Graña O, Bakiri L, Ruppen I, et al. Inhibition of De Novo NAD+ Synthesis by Oncogenic URI Causes Liver Tumorigenesis through DNA Damage. Cancer Cell. 2014 Dec 8;26(6):826–39.

301. Wang P, Hu Y, Yao D, Li Y. Omi/HtrA2 Regulates a Mitochondria-Dependent Apoptotic Pathway in a Murine Model of Septic Encephalopathy. Cell Physiol Biochem Int J Exp Cell Physiol Biochem Pharmacol. 2018;49(6):2163–73.

302. Yang Q-H, Church-Hajduk R, Ren J, Newton ML, Du C. Omi/HtrA2 catalytic cleavage of inhibitor of apoptosis (IAP) irreversibly inactivates IAPs and facilitates caspase activity in apoptosis. Genes Dev. 2003 Jun 15;17(12):1487–96.

303. Chou J-L, Su H-Y, Chen L-Y, Liao Y-P, Hartman-Frey C, Lai Y-H, et al. Promoter hypermethylation of FBXO32, a novel TGF-beta/SMAD4 target gene and tumor suppressor, is associated with poor prognosis in human ovarian cancer. Lab Investig J Tech Methods Pathol. 2010 Mar;90(3):414–25.

304. Muffat J, Walker DW. Apolipoprotein D. Cell Cycle Georget Tex. 2010 Jan 15;9(2):269–73.

305. López-Boado YS, Puente XS, Alvarez S, Tolivia J, Binderup L, López-Otín C. Growth inhibition of human breast cancer cells by 1,25-dihydroxyvitamin D3 is accompanied by induction of apolipoprotein D expression. Cancer Res. 1997 Sep 15;57(18):4091–7.

306. Sasaki Y, Negishi H, Koyama R, Anbo N, Ohori K, Idogawa M, et al. p53 family members regulate the expression of the apolipoprotein D gene. J Biol Chem. 2009 Jan 9;284(2):872–83.

307. Moiseyev G, Chen Y, Takahashi Y, Wu BX, Ma J-X. RPE65 is the isomerohydrolase in the retinoid visual cycle. Proc Natl Acad Sci U S A. 2005 Aug 30;102(35):12413–8.

308. Haupt S, Berger M, Goldberg Z, Haupt Y. Apoptosis - the p53 network. J Cell Sci. 2003 Oct 15;116(20):4077–85.

309. Song J. EMT or apoptosis: a decision for TGF-β. Cell Res. 2007 Apr 16;17:289–90.

310. Ahmad J, Odin JA. Epidemiology and Genetic Risk Factors of Drug Hepatotoxicity. Clin Liver Dis. 2017 Feb;21(1):55–72.

311. Takayama K, Morisaki Y, Kuno S, Nagamoto Y, Harada K, Furukawa N, et al. Prediction of interindividual differences in hepatic functions and drug sensitivity by using human iPS-derived hepatocytes. Proc Natl Acad Sci U S A. 2014 Nov 25;111(47):16772–7.

312. Hernaez R, Solà E, Moreau R, Ginès P. Acute-on-chronic liver failure: an update. Gut. 2017 Mar 1;66(3):541–53.

313. Murugan K, Babu K, Sundaresan R, Rajan R, Sashital DG. The Revolution Continues: Newly Discovered Systems Expand the CRISPR-Cas Toolkit. Mol Cell. 2017 Oct;68(1):15–25.

314. Mali P, Yang L, Esvelt KM, Aach J, Guell M, DiCarlo JE, et al. RNA-Guided Human Genome Engineering via Cas9. Science. 2013 Feb 15;339(6121):823–6.

315. Hubackova S, Krejcikova K, Bartek J, Hodny Z. IL1- and TGFβ-Nox4 signaling, oxidative stress and DNA damage response are shared features of replicative, oncogene-induced, and drug-induced paracrine 'Bystander senescence'. Aging. 2012 Dec 30;4(12):932–51.

316. Coll M, Perea L, Boon R, Leite SB, Vallverdú J, Mannaerts I, et al. Generation of Hepatic Stellate Cells from Human Pluripotent Stem Cells Enables In Vitro Modeling of Liver Fibrosis. Cell Stem Cell. 2018 Jul 5;23(1):101-113.e7.

317. Iii RLG, Hannan NRF, Bort R, Hanley NA, Drake RAL, Cameron GWW, et al. Maturation of Induced Pluripotent Stem Cell Derived Hepatocytes by 3D-Culture. PLOS ONE. 2014 Jan 22;9(1):e86372.

318. Guan Y, Xu D, Garfin PM, Ehmer U, Hurwitz M, Enns G, et al. Human hepatic organoids for the analysis of human genetic diseases. JCI Insight. 2017 Sep 7;2(17).

319. Takebe T, Sekine K, Kimura M, Yoshizawa E, Ayano S, Koido M, et al. Massive and Reproducible Production of Liver Buds Entirely from Human Pluripotent Stem Cells. Cell Rep. 2017 Dec 5;21(10):2661–70.

320. Rashidi H, Luu N-T, Alwahsh SM, Ginai M, Alhaque S, Dong H, et al. 3D human liver tissue from pluripotent stem cells displays stable phenotype in vitro and supports compromised liver function in vivo. Arch Toxicol. 2018;92(10):3117–29.

321. Wagner DE, Weinreb C, Collins ZM, Briggs JA, Megason SG, Klein AM. Single-cell mapping of gene expression landscapes and lineage in the zebrafish embryo. Science. 2018 Jun 1;360(6392):981–7.

322. Jaeschke H, Xie Y, McGill MR. Acetaminophen-induced Liver Injury: from Animal Models to Humans. J Clin Transl Hepatol. 2014 Sep 28;2(3):153–61.

323. Gold R, Arnold DL, Bar-Or A, Hutchinson M, Kappos L, Havrdova E, et al. Long-term effects of delayed-release dimethyl fumarate in multiple sclerosis: Interim analysis of ENDORSE, a randomized extension study. Mult Scler J. 2017 Feb 1;23(2):253–65.

324. Kensler TW, Wakabayashi N. Nrf2: friend or foe for chemoprevention? Carcinogenesis. 2010 Jan;31(1):90–9.

325. Mitsuishi Y, Motohashi H, Yamamoto M. The Keap1–Nrf2 system in cancers: stress response and anabolic metabolism. Mol Cell Oncol. 2012;2:200.

326. Shibata T, Ohta T, Tong KI, Kokubu A, Odogawa R, Tsuta K, et al. Cancer related mutations in NRF2 impair its recognition by Keap1-Cul3 E3 ligase and promote malignancy. Proc Natl Acad Sci U S A. 2008 Sep 9;105(36):13568–73.

327. Singh A, Misra V, Thimmulappa RK, Lee H, Ames S, Hoque MO, et al. Dysfunctional KEAP1-NRF2 interaction in non-small-cell lung cancer. PLoS Med. 2006 Oct;3(10):e420.

Supplementary information

Downregulated genes	baseMean	log2FoldChange	lfcSE	pvalue	padj	symbol
ENSG00000154146	176.1492	-0.87921	0.235473	7.00E-06	0.000988	NRGN
ENSG00000184697	430.7649	-0.76242	0.166474	2.00E-07	8.21E-05	CLDN6
ENSG00000059804	799.089	-0.74165	0.171346	5.72E-07	0.000152	SLC2A3
ENSG00000140416	1273.229	-0.69862	0.163399	7.42E-07	0.000186	TPM1
ENSG00000100612	220.7108	-0.69833	0.248381	0.00017	0.013692	DHRS7
ENSG00000171345	2596.852	-0.68819	0.114423	8.41E-11	7.60E-08	KRT19
ENSG00000159674	721.8794	-0.65178	0.14468	3.01E-07	0.000105	SPON2
ENSG00000023902	462.8413	-0.63449	0.15318	1.63E-06	0.000306	PLEKHO1
ENSG00000120885	1067.668	-0.60927	0.154848	3.50E-06	0.000565	CLU
ENSG00000135414	155.5532	-0.596	0.241361	0.000487	0.030177	GDF11
ENSG00000153140	956.237	-0.59296	0.147858	2.66E-06	0.000463	CETN3
ENSG00000161011	4552.491	-0.58536	0.124209	1.17E-07	5.87E-05	SQSTM1
ENSG00000198730	870.5006	-0.56766	0.137643	1.76E-06	0.000319	CTR9
ENSG00000148677	14628.68	-0.54212	0.129276	1.25E-06	0.000248	ANKRD1
ENSG00000221890	849.8509	-0.51825	0.142292	1.27E-05	0.001553	NPTXR
ENSG00000121060	220.4191	-0.48466	0.217785	0.000941	0.048888	TRIM25
ENSG00000170456	425.2846	-0.47743	0.162212	0.000145	0.011888	DENND5B
ENSG00000137070	235.1593	-0.47656	0.214939	0.00097	0.049805	IL11RA
ENSG00000176014	2418.556	-0.46366	0.126835	1.27E-05	0.001553	TUBB6
ENSG00000167772	463.9657	-0.46094	0.160644	0.000187	0.014789	ANGPTL4
ENSG00000153048	1004.467	-0.4321	0.12796	3.77E-05	0.004017	CARHSP1
ENSG00000175137	343.4006	-0.42641	0.179639	0.000754	0.041032	SH3BP5L
ENSG00000182985	947.9779	-0.41071	0.134181	0.000114	0.009928	CADM1
ENSG00000151233	1475.528	-0.38601	0.119227	6.18E-05	0.00582	GXYLT1
ENSG00000117298	778.273	-0.37681	0.137566	0.000316	0.022227	ECE1
ENSG00000125266	1400.448	-0.37581	0.151253	0.000583	0.035109	EFNB2
ENSG00000142089	1254.776	-0.37356	0.136804	0.000318	0.022227	IFITM3
ENSG00000225663	980.8937	-0.36671	0.133531	0.000325	0.022227	MCRIP1
ENSG00000164465	1988.957	-0.36392	0.114886	8.90E-05	0.00804	DCBLD1
ENSG00000160310	832.5637	-0.34943	0.138207	0.0006	0.035682	PRMT2
ENSG00000162734	3369.087	-0.34521	0.112813	0.000132	0.011068	PEA15
ENSG00000105993	1149.809	-0.34066	0.126914	0.000389	0.025835	DNAJB6
ENSG00000187514	3068.093	-0.33719	0.117952	0.000239	0.018341	PTMA
ENSG00000169976	2016.428	-0.30686	0.119964	0.00064	0.036364	SF3B5
ENSG00000166441	15370.79	-0.27885	0.110802	0.000792	0.042105	RPL27A
Upregulated genes	**baseMean**	**log2FoldChange**	**lfcSE**	**pvalue**	**padj**	**symbol**
ENSG00000106853	911.0608	1.272486	0.127419	8.40E-25	3.80E-21	PTGR1
ENSG00000244067	811.2315	1.26809	0.136508	5.53E-22	1.25E-18	GSTA2
ENSG00000243955	530.7982	1.086071	0.15379	7.35E-14	1.11E-10	GSTA1
ENSG00000105379	351.7488	0.933055	0.161774	3.87E-10	2.91E-07	ETFB
ENSG00000181019	548.9379	0.928922	0.152759	5.37E-11	6.07E-08	NQO1
ENSG00000110245	269.9286	0.872558	0.197433	4.03E-07	0.000122	APOC3
ENSG00000113924	254.488	0.825786	0.197871	1.26E-06	0.000248	HGD
ENSG00000205358	237.9697	0.793595	0.261699	7.33E-05	0.006756	MT1H
ENSG00000130829	379.3415	0.77465	0.160505	6.54E-08	3.70E-05	DUSP9
ENSG00000155657	162.2048	0.747947	0.29652	0.000381	0.025681	TTN
ENSG00000128965	636.4172	0.734153	0.158965	1.64E-07	7.43E-05	CHAC1
ENSG00000179094	466.6753	0.71376	0.157606	2.64E-07	9.94E-05	PER1

ENSG00000162433	357.9543	0.697369	0.164386	1.02E-06	0.000231	AK4
ENSG00000198417	521.524	0.666587	0.177103	6.72E-06	0.00098	MT1F
ENSG00000213190	134.2237	0.665018	0.254615	0.000324	0.022227	MLLT11
ENSG00000184640	460.1329	0.641653	0.170593	7.22E-06	0.000989	Sep-09
ENSG00000204128	244.4756	0.635055	0.198485	5.60E-05	0.005477	C2orf72
ENSG00000188643	1336.004	0.629924	0.122695	1.42E-08	9.15E-06	S100A16
ENSG00000176046	907.2515	0.617522	0.147267	1.24E-06	0.000248	NUPR1
ENSG00000163993	1045.176	0.616031	0.166832	9.00E-06	0.001197	S100P
ENSG00000244187	512.8864	0.601183	0.150211	2.94E-06	0.000493	TMEM141
ENSG00000165283	292.7543	0.599431	0.179309	3.63E-05	0.003998	STOML2
ENSG00000074800	3251.871	0.562303	0.128658	5.62E-07	0.000152	ENO1
ENSG00000051108	627.8994	0.550683	0.155298	1.77E-05	0.001998	HERPUD1
ENSG00000166136	400.125	0.548642	0.16445	3.82E-05	0.004017	NDUFB8
ENSG00000068615	233.4204	0.548451	0.206217	0.000309	0.022227	REEP1
ENSG00000008394	716.1526	0.539736	0.150493	1.57E-05	0.00187	MGST1
ENSG00000138207	2336.284	0.53767	0.12029	3.94E-07	0.000122	RBP4
ENSG00000143575	211.1934	0.508738	0.224584	0.000846	0.044433	HAX1
ENSG00000076770	330.4757	0.501908	0.214283	0.000678	0.03734	MBNL3
ENSG00000004779	352.2827	0.500239	0.187213	0.000313	0.022227	NDUFAB1
ENSG00000144136	1575.529	0.483909	0.129729	9.58E-06	0.001237	SLC20A1
ENSG00000105327	321.4598	0.48045	0.193017	0.000528	0.032229	BBC3
ENSG00000130208	1593.716	0.461142	0.120039	6.39E-06	0.000963	APOC1
ENSG00000125148	15127.21	0.457588	0.118531	5.74E-06	0.000894	MT2A
ENSG00000250479	441.49	0.449027	0.161142	0.000244	0.018407	CHCHD10
ENSG00000158874	6172.306	0.444126	0.103393	9.76E-07	0.000231	APOA2
ENSG00000177733	544.2009	0.440403	0.154288	0.000199	0.015506	HNRNPA0
ENSG00000178741	876.8116	0.437595	0.134039	5.70E-05	0.005477	COX5A
ENSG00000177156	713.1106	0.430635	0.170282	0.000483	0.030177	TALDO1
ENSG00000130522	1611.075	0.430228	0.119238	1.65E-05	0.001909	JUND
ENSG00000125144	3217.309	0.425566	0.128123	4.66E-05	0.004678	MT1G
ENSG00000169635	745.0314	0.417749	0.137551	0.000121	0.010322	HIC2
ENSG00000154277	977.675	0.399299	0.151444	0.000396	0.025913	UCHL1
ENSG00000169715	3521.445	0.394455	0.159491	0.000638	0.036364	MT1E
ENSG00000189334	1678.432	0.393898	0.159928	0.000611	0.035884	S100A14
ENSG00000127184	1868.739	0.357801	0.114745	0.000101	0.008993	COX7C
ENSG00000103363	675.9637	0.356096	0.147308	0.000773	0.041571	ELOB
ENSG00000087086	20918.04	0.343291	0.101014	4.61E-05	0.004678	FTL
ENSG00000112695	840.871	0.339853	0.135263	0.000652	0.036364	COX7A2
ENSG00000166165	1962.221	0.328942	0.124718	0.000445	0.02872	CKB
ENSG00000121274	1799.263	0.322542	0.122129	0.000484	0.030177	TENT4B
ENSG00000182774	4013.075	0.276809	0.108003	0.000645	0.036364	RPS17

Supplementary table 1. Differential expressed genes on the HLCs pre-treatment.
Differential expressed genes with padj >0.05.

Downregulated genes	baseMean	log2FoldChange	lfcSE	pvalue	padj	symbol
ENSG00000105825	261.6677	-1.08036	0.261259	1.23E-06	0.001502	TFPI2
ENSG00000184292	267.5707	-1.06425	0.259239	1.42E-06	0.001502	TACSTD2
ENSG00000166401	270.9469	-0.9036	0.287292	4.97E-05	0.013178	SERPINB8
ENSG00000124302	258.919	-0.85907	0.318414	0.000183	0.021526	CHST8
ENSG00000120937	1027.292	-0.83766	0.215754	3.81E-06	0.002692	NPPB
ENSG00000088826	452.0769	-0.77327	0.253153	7.59E-05	0.015604	SMOX
ENSG00000269893	1058.67	-0.76366	0.178234	8.42E-07	0.001502	SNHG8
ENSG00000160888	1668.114	-0.75288	0.234789	4.39E-05	0.012405	IER2
ENSG00000244405	621.8365	-0.73807	0.255455	0.000124	0.017016	ETV5
ENSG00000064300	259.1061	-0.73396	0.248353	0.000121	0.017016	NGFR
ENSG00000138623	240.5932	-0.72986	0.271044	0.000247	0.023015	SEMA7A
ENSG00000234741	1267.109	-0.70516	0.165374	9.67E-07	0.001502	GAS5
ENSG00000144485	431.8835	-0.70293	0.263752	0.00025	0.023015	HES6
ENSG00000163132	281.4012	-0.67829	0.292548	0.000621	0.034224	MSX1
ENSG00000167081	900.9591	-0.65693	0.212706	7.98E-05	0.015604	PBX3
ENSG00000188229	645.6846	-0.65502	0.226651	0.000145	0.018808	TUBB4B
ENSG00000245910	1337.182	-0.65297	0.16323	3.14E-06	0.002669	SNHG6
ENSG00000115271	429.9702	-0.64972	0.234696	0.00022	0.022459	GCA
ENSG00000105640	612.7302	-0.63968	0.206739	8.47E-05	0.015604	RPL18A
ENSG00000109089	788.3575	-0.6307	0.207182	9.44E-05	0.015604	CDR2L
ENSG00000141682	501.639	-0.62729	0.27813	0.000713	0.037328	PMAIP1
ENSG00000112306	43780.08	-0.62663	0.168181	9.18E-06	0.003899	RPS12
ENSG00000162783	1671.919	-0.62492	0.228937	0.000225	0.022459	IER5
ENSG00000085063	4042.655	-0.62105	0.188671	4.20E-05	0.012405	CD59
ENSG00000161091	1473.693	-0.61992	0.235708	0.000289	0.025546	MFSD12
ENSG00000111057	4893.181	-0.61917	0.188944	5.43E-05	0.013548	KRT18
ENSG00000173334	738.5834	-0.61271	0.234589	0.000334	0.025797	TRIB1
ENSG00000198804	3510.582	-0.61132	0.158626	6.48E-06	0.003437	COX1
ENSG00000115756	1076.253	-0.60522	0.202452	0.000118	0.017016	HPCAL1
ENSG00000253368	1671.67	-0.60053	0.233393	0.000353	0.025797	TRNP1
ENSG00000178585	486.7062	-0.60029	0.226562	0.000328	0.025797	CTNNBIP1
ENSG00000142541	7360.029	-0.59807	0.159899	9.19E-06	0.003899	RPL13A
ENSG00000148677	21957.93	-0.59056	0.191931	8.32E-05	0.015604	ANKRD1
ENSG00000109321	555.7752	-0.58772	0.207573	0.000197	0.021746	AREG
ENSG00000170421	1704.135	-0.58702	0.191104	9.56E-05	0.015604	KRT8
ENSG00000108107	2337.985	-0.58077	0.165222	2.30E-05	0.008138	RPL28
ENSG00000224032	1013.183	-0.58006	0.185657	8.36E-05	0.015604	EPB41L4A-AS1
ENSG00000249992	352.3268	-0.57148	0.236596	0.000614	0.034224	TMEM158
ENSG00000143947	50720.52	-0.57048	0.190975	0.000121	0.017016	RPS27A
ENSG00000184515	541.2307	-0.56652	0.245746	0.000695	0.036836	BEX5
ENSG00000266402	3268.263	-0.56416	0.206962	0.000245	0.023015	SNHG25
ENSG00000182580	1113.056	-0.56403	0.255468	0.000888	0.04364	EPHB3
ENSG00000177410	3541.361	-0.56219	0.168534	4.38E-05	0.012405	ZFAS1
ENSG00000088986	2003.421	-0.5571	0.214841	0.000372	0.025881	DYNLL1
ENSG00000197989	434.1653	-0.55707	0.259874	0.001103	0.048576	SNHG12
ENSG00000255198	518.7972	-0.55698	0.265768	0.001206	0.04927	SNHG9
ENSG00000277075	274.1023	-0.55281	0.256334	0.001131	0.048972	HIST1H2AE
ENSG00000197756	29857.5	-0.55087	0.188845	0.000155	0.018855	RPL37A
ENSG00000197019	1255.63	-0.5462	0.246071	0.000895	0.04364	SERTAD1
ENSG00000185022	663.8621	-0.54502	0.214462	0.000465	0.030858	MAFF
ENSG00000130255	8212.797	-0.54309	0.175012	9.17E-05	0.015604	RPL36
ENSG00000102096	966.752	-0.53908	0.213212	0.000473	0.030858	PIM2
ENSG00000128311	1047.822	-0.53578	0.238874	0.000847	0.042805	TST
ENSG00000233016	607.7003	-0.53228	0.209082	0.000492	0.031154	SNHG7

ENSG00000211459	28720.17	-0.52542	0.18348	0.000192	0.021746	MT-RNR1
ENSG00000132002	6732.186	-0.52392	0.20942	0.000556	0.033898	DNAJB1
ENSG00000189325	639.7264	-0.52162	0.215078	0.000653	0.035506	C6orf222
ENSG00000189077	512.094	-0.51901	0.208257	0.000565	0.033898	TMEM120A
ENSG00000171858	6377.68	-0.50788	0.180065	0.000224	0.022459	RPS21
ENSG00000171863	2543.412	-0.50784	0.165163	0.000111	0.017016	RPS7
ENSG00000189143	1806.707	-0.50511	0.202659	0.000548	0.033898	CLDN4
ENSG00000143933	1741.947	-0.4931	0.176206	0.000259	0.02336	CALM2
ENSG00000133818	558.8907	-0.49032	0.195514	0.000578	0.034034	RRAS2
ENSG00000231500	6648.419	-0.4896	0.159365	0.000156	0.018855	RPS18
ENSG00000169567	4322.211	-0.48547	0.185603	0.000434	0.02925	HINT1
ENSG00000145592	6911.284	-0.48348	0.175963	0.000297	0.025689	RPL37
ENSG00000196937	898.6864	-0.47676	0.190701	0.000599	0.034224	FAM3C
ENSG00000099804	1643.701	-0.47655	0.218678	0.001188	0.04927	CDC34
ENSG00000075618	2575.555	-0.47396	0.17859	0.000404	0.027641	FSCN1
ENSG00000168002	1232.994	-0.45868	0.203267	0.00111	0.048576	POLR2G
ENSG00000105193	5919.662	-0.45541	0.182555	0.000617	0.034224	RPS16
ENSG00000110700	5111.901	-0.45351	0.196515	0.000952	0.044371	RPS13
ENSG00000105372	18430.03	-0.43627	0.188252	0.000947	0.044371	RPS19
ENSG00000163682	4325.1	-0.43249	0.1879	0.001037	0.046554	RPL9
ENSG00000089157	15728.21	-0.43233	0.174032	0.000694	0.036836	RPLP0
ENSG00000117410	2517.668	-0.42902	0.190001	0.001202	0.04927	ATP6V0B
ENSG00000136942	3530.71	-0.42245	0.177208	0.000906	0.043673	RPL35
ENSG00000213741	21920.03	-0.42093	0.186449	0.00119	0.04927	RPS29
ENSG00000133639	4443.254	-0.41166	0.176117	0.001042	0.046554	BTG1
ENSG00000167526	4896.005	-0.4059	0.172152	0.001001	0.045901	RPL13
ENSG00000210082	179937.4	-0.39343	0.165492	0.001006	0.045901	MT-RNR2
ENSG00000198886	10165.78	-0.3772	0.16083	0.001208	0.04927	ND4
Upregulated genes	**baseMean**	**log2FoldChange**	**lfcSE**	**pvalue**	**padj**	**symbol**
ENSG00000104517	517.4942	0.741003	0.190105	4.70E-06	0.002846	UBR5
ENSG00000116962	382.7241	0.730912	0.235122	7.33E-05	0.015604	NID1
ENSG00000140279	892.983	0.662857	0.187177	1.85E-05	0.007126	DUOX2
ENSG00000165029	321.0358	0.655037	0.267391	0.000482	0.030968	ABCA1
ENSG00000198677	395.8516	0.626011	0.242216	0.000368	0.025881	TTC37
ENSG00000127481	1058.952	0.613457	0.233124	0.000306	0.025797	UBR4
ENSG00000100354	356.816	0.610498	0.214936	0.0002	0.021746	TNRC6B
ENSG00000206557	353.4599	0.602846	0.274969	0.000926	0.044168	TRIM71
ENSG00000100815	441.0969	0.581967	0.218913	0.00034	0.025797	TRIP11
ENSG00000122299	374.0185	0.575035	0.215921	0.000343	0.025797	ZC3H7A
ENSG00000171316	467.9534	0.568548	0.215603	0.000359	0.0258	CHD7
ENSG00000054118	792.9844	0.567535	0.192042	0.000146	0.018808	THRAP3
ENSG00000038427	1125.683	0.566572	0.215176	0.00034	0.025797	VCAN
ENSG00000187498	1118.726	0.542228	0.192925	0.000228	0.022459	COL4A1
ENSG00000186951	577.2873	0.522842	0.221617	0.000764	0.039548	PPARA
ENSG00000011114	498.0748	0.510569	0.215697	0.000787	0.040207	BTBD7
ENSG00000084674	5348.217	0.498255	0.186529	0.000349	0.025797	APOB
ENSG00000102024	1312.153	0.496447	0.198403	0.000567	0.033898	PLS3
ENSG00000244067	1248.57	0.491888	0.197842	0.000594	0.034224	GSTA2
ENSG00000141252	367.8466	0.482994	0.216176	0.001171	0.04927	VPS53
ENSG00000108861	818.7747	0.462999	0.193906	0.000878	0.04364	DUSP3
ENSG00000171560	25873.67	0.46225	0.169575	0.00034	0.025797	FGA

Supplementary table 2. Differential expressed genes on the HLCs co-treatment.
Differential expressed genes with padj >0.05.

Downregulated	baseMean	log2FoldChange	lfcSE	pvalue	padj	symbol
ENSG00000241794	51.01052	-2.12689	0.603346	1.31E-05	NA	SPRR2A
ENSG00000122641	78.932	-1.97629	0.500934	2.26E-06	NA	INHBA
ENSG00000276085	214.0358	-1.90757	0.298406	7.39E-12	1.28E-08	CCL3L1
ENSG00000274012	58.20267	-1.69323	0.535591	5.55E-05	NA	RN7SL2
ENSG00000026508	320.7262	-1.48105	0.273237	2.33E-09	1.61E-06	CD44
ENSG00000226380	58.65134	-1.46174	0.557825	0.000258	NA	LINC-PINT
ENSG00000222041	1491.51	-1.39564	0.560638	0.000291	0.030453	CYTOR
ENSG00000172965	5036.48	-1.33168	0.199259	8.15E-13	2.82E-09	MIR4435-2HG
ENSG00000149564	99.45685	-1.32098	0.453763	0.000102	NA	ESAM
ENSG00000134954	294.5387	-1.27715	0.2681	8.03E-08	3.47E-05	ETS1
ENSG00000164171	2152.881	-1.12809	0.184412	4.18E-11	4.82E-08	ITGA2
ENSG00000205420	432.2669	-1.11016	0.266388	1.10E-06	0.000346	KRT6A
ENSG00000185022	230.5556	-1.10327	0.294964	7.17E-06	0.001684	MAFF
ENSG00000149591	292.1205	-1.07995	0.32768	2.77E-05	0.005024	TAGLN
ENSG00000131016	3599.472	-1.06989	0.180657	1.49E-10	1.28E-07	AKAP12
ENSG00000138166	971.9109	-1.05339	0.202684	9.03E-09	4.45E-06	DUSP5
ENSG00000058085	321.8058	-1.0221	0.27468	7.69E-06	0.001684	LAMC2
ENSG00000109321	773.8499	-0.96762	0.230979	1.05E-06	0.000346	AREG
ENSG00000050405	539.4222	-0.94899	0.234615	2.11E-06	0.000607	LIMA1
ENSG00000103187	523.6473	-0.94247	0.242423	3.82E-06	0.001013	COTL1
ENSG00000059804	1759.993	-0.924	0.196697	1.11E-07	4.25E-05	SLC2A3
ENSG00000163584	209.9762	-0.87975	0.361753	0.000404	0.03985	RPL22L1
ENSG00000132432	325.8817	-0.81446	0.305091	0.00023	0.024824	SEC61G
ENSG00000163191	481.9524	-0.80986	0.286971	0.000142	0.018186	S100A11
ENSG00000143322	474.3977	-0.79826	0.243811	4.34E-05	0.006584	ABL2
ENSG00000148834	1469.689	-0.79782	0.2238	1.29E-05	0.002627	GSTO1
ENSG00000175793	215.3717	-0.77658	0.330192	0.000558	0.04546	SFN
ENSG00000026025	1393.804	-0.74408	0.198897	7.80E-06	0.001684	VIM
ENSG00000141682	371.2127	-0.72725	0.266189	0.000218	0.024824	PMAIP1
ENSG00000115641	454.6041	-0.71283	0.263053	0.00023	0.024824	FHL2
ENSG00000136167	1898.231	-0.68956	0.192989	1.45E-05	0.002774	LCP1
ENSG00000102317	396.1198	-0.68513	0.299396	0.000631	0.046427	RBM3
ENSG00000181649	365.2326	-0.67825	0.287802	0.000566	0.04546	PHLDA2
ENSG00000136810	1038.034	-0.61834	0.265885	0.000581	0.045589	TXN
ENSG00000253368	1537.668	-0.60463	0.201769	0.000123	0.016872	TRNP1
ENSG00000111057	6457.431	-0.59548	0.181213	4.20E-05	0.006584	KRT18
ENSG00000142871	1666.391	-0.5927	0.249433	0.000516	0.04347	CYR61
ENSG00000172115	810.391	-0.58592	0.234298	0.000425	0.040731	CYCS
ENSG00000147065	847.0252	-0.56989	0.24169	0.000605	0.046427	MSN
ENSG00000067082	2720.955	-0.56289	0.194969	0.000152	0.018714	KLF6
ENSG00000072110	1845.467	-0.54918	0.207807	0.000304	0.030853	ACTN1
ENSG00000184009	15273.92	-0.54727	0.184734	0.000125	0.016872	ACTG1
ENSG00000132341	1763.957	-0.51188	0.204768	0.000487	0.043433	RAN
ENSG00000176014	4625.958	-0.46554	0.192705	0.000491	0.043433	TUBB6
Upregulated genes	**baseMean**	**log2FoldChange**	**lfcSE**	**pvalue**	**padj**	**symbol**
ENSG00000162981	152.1544	1.02568	0.354092	0.000129	NA	FAM84A
ENSG00000245532	12920.73	0.946268	0.173667	3.88E-09	2.23E-06	NEAT1
ENSG00000111319	543.1801	0.809522	0.281977	0.000127	0.016872	SCNN1A
ENSG00000206557	522.3106	0.772307	0.237238	4.39E-05	0.006584	TRIM71
ENSG00000140279	771.5025	0.740942	0.219261	2.91E-05	0.005024	DUOX2
ENSG00000176046	453.7334	0.736752	0.271945	0.000225	0.024824	NUPR1
ENSG00000106780	428.9418	0.664578	0.270105	0.000456	0.042512	MEGF9
ENSG00000139219	544.9756	0.607067	0.260094	0.000632	0.046427	COL2A1
ENSG00000104687	1124.282	0.542446	0.220829	0.000503	0.043433	GSR

Supplementary table 3. Differential expressed genes on the HLCs post-treatment.
Differential expressed genes with padj >0.05.

sDownregulated genes	baseMean	log2FoldChange	lfcSE	pvalue	padj	symbol
ENSDARG00000076487	29.05509	-6.35336	1.584918	7.52E-07	0.000625	haao
ENSDARG00000069909	28.46049	-5.44275	1.2896	4.94E-07	0.000485	LOC100149563
ENSDARG00000007480	100.2075	-2.81829	0.649972	2.02E-07	0.000242	rpe65a
ENSDARG00000040277	352.1749	-1.85764	0.371364	2.12E-08	4.58E-05	fbxo32
ENSDARG00000060345	112.819	-1.8496	0.682785	9.38E-05	0.02978	apoda.1
ENSDARG00000056511	2120.804	-1.6904	0.445434	1.70E-06	0.001139	arr3a
ENSDARG00000016391	210.4044	-1.48855	0.534133	0.000102	0.03057	calcoco1b
ENSDARG00000056248	1247.315	-1.37855	0.485747	6.22E-05	0.022371	si:dkey-183i3.5
ENSDARG00000045835	1749.698	-1.25324	0.443516	7.05E-05	0.024551	si:dkey-14d8.6
ENSDARG00000103543	1871.383	-0.98687	0.372678	0.000195	0.049073	gngt2b
ENSDARG00000002593	104.2687	-0.00494	0.030043	0.000134	0.03613	slc45a2
ENSDARG00000077652	51.83696	-0.00327	0.029709	3.60E-05	0.014733	lratb.2
ENSDARG00000070057	115.6232	-0.0031	0.029677	7.31E-05	0.024666	si:dkey-69o16.5
Upregulated genes	**baseMean**	**log2FoldChange**	**lfcSE**	**pvalue**	**padj**	**symbol**
ENSDARG00000068088	516.4075	2.442286	0.455423	8.14E-10	8.78E-06	tcnba
ENSDARG00000051762	142.5607	2.280092	0.724905	7.95E-06	0.004169	CABZ01080568.1
ENSDARG00000069826	869.9748	1.969861	0.37134	2.66E-09	1.40E-05	crygm2d15
ENSDARG00000069792	1462.791	1.96209	0.475719	2.67E-07	0.000288	crygm2d5
ENSDARG00000069817	1101.928	1.880228	0.411323	7.15E-08	0.000129	crygm2d17
ENSDARG00000087301	1126.493	1.850981	0.366916	1.05E-08	2.84E-05	crygm2d14
ENSDARG00000076572	1460.899	1.829098	0.411178	1.30E-07	0.000176	crygm2d7
ENSDARG00000036140	252.9114	1.817982	0.703129	9.93E-05	0.03057	crybgx
ENSDARG00000069827	861.6477	1.778383	0.394003	1.25E-07	0.000176	crygm2d11
ENSDARG00000087164	1330.222	1.701993	0.320238	3.89E-09	1.40E-05	crygm2d4
ENSDARG00000026871	109.6245	1.658356	0.588584	0.000109	0.031699	uchl1
ENSDARG00000041065	2123.578	1.643173	0.49371	8.11E-06	0.004169	hspb1
ENSDARG00000073750	949.22	1.584292	0.372289	5.51E-07	0.000496	crygm2d18
ENSDARG00000076790	1300.437	1.507166	0.424185	6.65E-06	0.003986	crygm2d16
ENSDARG00000086658	922.5474	1.502262	0.550307	5.65E-05	0.021028	crygm2d21
ENSDARG00000073874	145.094	1.466385	0.509446	0.000128	0.035543	crygm2d6
ENSDARG00000091148	1448.156	1.439415	0.433016	1.50E-05	0.00704	crygm2d20
ENSDARG00000030411	1623.658	1.420965	0.489586	4.86E-05	0.018755	crygn2
ENSDARG00000086917	2608.659	1.418607	0.356581	1.79E-06	0.001139	crygm2d2
ENSDARG00000087324	1594.418	1.402341	0.431299	1.94E-05	0.00874	crygm2d1
ENSDARG00000115701	1055.253	1.38857	0.341225	1.55E-06	0.001117	crygm2d9
ENSDARG00000088823	3607.863	1.374161	0.326547	8.12E-07	0.000626	crygm2d3
ENSDARG00000109861	1794.111	1.353566	0.396182	1.40E-05	0.006864	crygm2d19
ENSDARG00000057460	2232.34	1.343253	0.372181	7.47E-06	0.004169	crygm2d13
ENSDARG00000032929	872.6952	1.286035	0.469858	0.000119	0.033919	cryba1l1
ENSDARG00000024746	4206.144	1.222288	0.435766	8.49E-05	0.027761	hsp90aa1.2
ENSDARG00000018060	878.645	1.180174	0.466394	0.000191	0.049015	pik3r2
ENSDARG00000116164	2501.711	1.141518	0.351502	3.15E-05	0.0136	crygm2d8
ENSDARG00000016793	1456.38	1.108596	0.340958	3.68E-05	0.014733	crybb1l2
ENSDARG00000102004	3696.718	0.945817	0.340642	0.000155	0.040767	apoea

Supplementary table 4 Differential expressed genes on the zebrafish group.
Differential expressed genes with padj >0.05.